

**Computational Studies of Electronic Excited States, or:
How I Learned to Stop Worrying
and Love Multireference Methods**

by

Meagan Oakley

A thesis submitted in partial fulfillment of the requirements for the degree of

Doctor of Philosophy

Department of Chemistry

University of Alberta

©Meagan Oakley, 2019

Abstract

Modelling electronic excited states is important in the search to understand molecular properties. Vacuum ultraviolet (VUV) spectroscopy can be used to identify different isomers in complicated mixtures of many molecules. In this Thesis, calculated VUV spectra were compared with spectra of experimental mixtures to benchmark appropriate computational methods. Because the benchmark molecule, 1-bromo-1-propene, contains a heavy atom, both all-electron and model core potential basis sets were investigated. Time-dependent density functional theory (TD-DFT) can accurately compute electronic excited states at low-energy excitations and was cross-checked at higher energies against results from the symmetry adapted cluster-configuration interaction (SAC-CI) method. TD-DFT was determined to be satisfactory at low energies; however, excitation energies can deviate by 0.5 eV at high energies. TD-DFT with both all-electron and model core potential basis sets produced satisfactory excitation energies for the lower excited states. This method was also able to predict spectra produced experimentally, including a mixture of isomers (cis- and trans-1-bromo-1-propene), even if the oscillator strengths were underestimated.

The potential energy surface for the thermal decomposition reaction $P_4 \rightarrow 2P_2$ was computed along the C_{2v} reaction trajectory. Single-reference methods were not suitable for describing this complex bond-breaking process, so two multiconfigurational methods, namely, multi-state complete active space second-order perturbation theory (MS-CASPT2) and multiconfiguration pair-density functional theory (MC-PDFT), were used with the aim of determining the accuracy and efficiency of these methods for this process. Several active spaces and basis sets were explored. It was found that the MC-PDFT method was up to 900 times faster than MS-CASPT2 while

providing similar accuracy.

A new method, Δ DFT/MIX, was proposed and calibrated for use in calculating core electron binding energies. Chemically relevant test sets were used to determine the most accurate functionals out of the 70 density functionals included in GAMESS. The best three functionals, B3LYP, TPSSm, and BLYP, were used to calculate the 1s electron binding energies of nucleic acid base tautomers, and the results were compared to experimental values to demonstrate accuracy and sensitivity of the method. Previously suggested methods such as ADC(4) and Δ MP2/MIX are as accurate as the new method; the overall mean absolute deviation of Δ DFT/MIX is 0.19 eV. Comparing calculation time shows that using DFT instead of MP2 is much less computationally costly for larger molecules.

Lastly, a study in designing chemosensors for the detection of heavy metals was done using numerous crown structures for preferential binding to Hg^{2+} . Binding affinity was calculated with respect to other hydrated metal ions in order to incorporate explicit solvent effects (water and acetonitrile). The ionophore binding affinity was selective to highly charged metal ions (3+, 4+), but a narrowed metal ion study (Zn^{2+} , Cd^{2+} , Hg^{2+}) and the full chemosensor structure showed that binding to Hg^{2+} is preferential. Electronic excited states of the full chemosensor were calculated to determine the metal complex with a bright state with the largest difference compared to the excited states of the parent ligand. Ultimately, the chemosensor with the best binding affinity and the largest difference in excitation energy ($\Delta\Delta E$) was 18C-O₄S₂-meta-a, with a binding affinity for Hg^{2+} of -67 kJ/mol with respect to Zn^{2+} , and -56 kJ/mol with respect to Cd^{2+} and a $\Delta\Delta E$ of 1.4 eV compared to the parent ligand.

Preface

A version of Chapter 2 has been published as “Computing UV-vis spectra of 1-bromo-1-propene: a comparison of model core potential and all-electron basis sets” in *Canadian Journal of Chemistry*, **2017**, *95*, 627-631 by M. S. Oakley and M. Klobukowski. The experimental vacuum ultraviolet spectrum of 1-bromo-1-propene isomers was provided by Justin Stoesz and Dr. James Harynuk. The calculations and analysis were performed by M. S. Oakley. Scripts to extract excitation data and plot spectra were written by M. Klobukowski.

Chapter 3 was published in *The Journal of Physical Chemistry A*, **2018**, *122*, 5742-5749 as “Multireference Methods for Calculating the Dissociation Enthalpy of Tetrahedral P₄ to Two P₂” by M. S. Oakley, J. J. Bao, M. Klobukowski, D. Truhlar, and L. Gagliardi. M. S. Oakley completed the potential energy surface calculations with multireference methods and wrote the majority of the manuscript. J. J. Bao performed all geometry optimization calculations of P₄ and P₂, the ground-state orbital analysis and wrote the respective sections in the manuscript. M. Klobukowski performed preliminary calculations of the potential energy surface (with single and multireference methods) and provided scripts for quadratic fitting and extraction of data. D. Truhlar and L. Gagliardi provided guidance and editing of the manuscript.

The research presented in Chapter 4 was published as “ Δ DFT/MIX: A reliable and efficient method for calculating core electron binding energies of large molecules” in *Journal of Electron Spectroscopy and Related Phenomena*, **2018**, *227*, 44-50 by M. S. Oakley and M. Klobukowski. M. Klobukowski wrote scripts for generating

input files and extracting data, as well as carried out preliminary calculations. M. S. Oakley extended the preliminary work to include all functionals available in GAMESS, added new relevant molecules to the test set, performed data analysis, and wrote the manuscript.

In Chapter 5, S. Azimi performed all preliminary geometry optimizations with RHF and DFT, as well as excitations of the free ligand and complex with CIS, data analysis of these calculations, and wrote the introduction to this chapter. WISEST summer research program student R. Ferrao, supervised by S. Azimi, performed preliminary excited state calculations on the above compounds with TD-DFT. WISEST student A. de Costa, supervised by M. S. Oakley, performed a frozen rotational energy profile and excitation calculations with TD-DFT and CIS, data analysis of the free ligand, as well as the the complex with Hg^{2+} and Ba^{2+} . M. Klobukowski wrote scripts to automate rotation of the molecule and to extract data. M. S. Oakley performed extended metal ion analysis with ionophores, calculated binding affinities associated with the heat maps, extended excited state calculations of the full chemosensor with metal ions to include bright states, extended rotations to include Cd^{2+} and Zn^{2+} , and performed analysis of the difference in excitation energies of the parent ligand and metal complex. M. S. Oakley introduced the computational methods, and wrote the discussion and conclusions to the chapter.

Not included in this thesis is a collaborative project published as “Engaging dual donor sites within an N-heterocyclic olefin phosphine ligand” in *Dalton Transactions*, **2017**, *46*, 5946-5954 by M. W. Lui, O. Shynkaruk, M. S. Oakley, R. Sinelnikov, R. McDonald, M. J. Ferguson, A. Meldrum, M. Klobukowski, and E. Rivard. M. S. Oakley was responsible for all geometry optimization and excited state calculations done in the paper.

Another collaborative project, which is currently in revision, was submitted as “Mechanochemical Synthesis of 3D and 0D Cesium Lead Mixed Halide Perovskite Solid Solutions” in *Chemical Communications*, **2019** by A. Karmakar, M. Dodd, X.

Zhang, M. S. Oakley, M. Klobukowski, and V. K. Michaelis. M. S. Oakley performed all NMR calculations in the paper.

In memory of June and Myron Weeks.

Acknowledgements

First and foremost, I would like to thank my supervisor, Dr. Mariusz Klobukowski. I have learned so much from you over the past few years, mostly because our short, science discussions turned into long, off-topic digressions.^a Your guidance and mentorship have been central to my success and I am truly blessed to have you as someone I can reach out to. On more than one occasion, these visits have kept me motivated instead of giving up completely, especially on **FFFF**ridays. I could not ask for a better supervisor.

I would like to extend my gratitude to my supervisory committee. Thank you to Dr. Alex Brown for always thoughtfully examining my science and making me answer “Why?”. This has made me a better scientist, and better at defending my decisions. My appreciation also goes to Dr. James Harynuik for inspiring our work in Chapter 2 and for reading my theory-heavy progress reports year after year. To candidacy examination committee, Dr. Jonathan Veinot and Dr. Sarah Styler, I appreciated your time and insightful questions. I am especially grateful to my external examiner, Dr. Bess Vlasisavljevich, for your expertise and taking the time to read a stranger’s thesis.

I am grateful to the members of the Klobukowski and Brown research groups,

^aOnce we somehow got on the topic of pre-drinking, the act of drinking as much as you can at home before you go out to the bar to save money. I commented that at some point I would like to be able to afford a whole night out at the bar. Mariusz said, “You know what I did with my first big paycheque?” and followed with this story. When he was a child, his grandmother would give him a slice of white bread with butter and sugar on it as a treat, and he remembered it fondly. He said once he got his first pay, he went down to the store and bought a loaf of bread, butter, and some sugar. He cut a slice, spread lots of butter over it and sprinkled on the sugar. Mariusz said, “I didn’t like it”. Not only did this make me re-think how I would spend my first paycheque, but I remember laughing so hard I almost cried.

especially Dr. Cassandra Churchill, Dr. Shuai Sun, and Dr. Melis Gedik. Thank you so much for your friendship and openness that helped me feel at home when I was so far from it. And of course for sharing resources and debugging input files (I am always missing a `$end` somewhere).

During my time at the University of Alberta, I was part of many committees and societies, but WIC is the one that is the closest to my heart. You all have accomplished so much and I am so proud of all of you. I can't wait to see what you do next.

I would also like to thank the following funding agencies for their support of the work reported in this Thesis: the Natural Sciences and Engineering Research Council (NSERC), the University of Alberta, and the Government of Alberta. As well, I would like to thank Compute Canada for their seemingly endless computational resources.

None of the work in this Thesis could have been done without the time spent to unwind away from my computer. Special thanks goes to Dr. Aleks Popowich and Dr. Melanie Lui for letting me be myself and discovering new outlets for creativity. I want to thank Anis Fahandej-Sadi, MSc, for much needed coffee breaks and relentless dog photos, and Dr. Chris Fetterly for additional coffee breaks and interesting discussions revolving around the old Gods.

It was not easy leaving the East coast because of the following five people. Thank you to my Mom for showing me that women can do anything and everything, my Dad for teaching me math well ahead of when I was actually supposed to learn it, and my sister for always being there for me. I would also like to thank my other parents, my Aunt Beryl and Uncle Donald, for their unconditional love and support. I miss and love you all so much.

Lastly, there is Aaron. I would need an infinite basis set to express my love for you.¹ Thank you for being a constant in my life when I needed it the most.

Table of Contents

1 Chapter 1: Introduction	1
1.1 Scope	1
1.2 Wave Function Theory	1
1.3 Density Functional Theory	5
1.4 Basis Functions	8
1.5 Some Advanced Computational Methods	10
1.5.1 Configuration Interaction	10
1.5.2 Coupled Cluster	11
1.5.3 Multiconfigurational Self-Consistent Field	12
1.5.4 Møller-Plesset Perturbation Theory	14
1.5.5 Time-Dependent Density Functional Theory	16
1.5.6 Multiconfigurational Pair-Density Functional Theory	16
1.6 Electronic Excited States	17
1.7 Overview	20
2 Chapter 2: Computing UV-Vis Spectra of 1-Bromo-1-Propene: A Comparison of Model Core Potential and All-Electron Approaches	21
2.1 Introduction	21
2.2 Computational Details	23
2.3 Discussion	23
2.3.1 Major Peaks #1 and #2	25
2.3.2 Major Peak #3	26
2.3.3 Major Peaks #4 and #5	28
2.3.4 Major Peak #6	29
2.3.5 Comparison with Experimental Spectra	33
2.4 Conclusion	37
3 Chapter 3: Multireference Methods for Calculating the Dissociation Enthalpy of Tetrahedral P₄ to Two P₂	38
3.1 Introduction	38
3.2 Computational Details	39
3.3 Discussion	43

3.3.1	Equilibrium Geometry of P ₂	43
3.3.2	Equilibrium Geometry of P ₄	45
3.3.3	Reaction Enthalpies	45
3.3.4	Potential Energy Curves	46
3.3.5	Computational Considerations	48
3.3.6	Change of Valence Orbital Shape Along the Dissociation Path	49
3.4	Conclusion	53
4	Chapter 4: ΔDFT/MIX: A reliable and efficient method for calculating core electron binding energies of large molecules	54
4.1	Introduction	54
4.2	Computational Details	56
4.3	Discussion	57
4.3.1	Calibration of Δ DFT/MIX method	57
4.3.2	Application to Nucleic Acid Bases	57
4.3.3	Sensitivity of the Δ B3LYP/MIX Method to Nucleic Acid Base Tautomers	61
4.3.4	Timing	66
4.4	Conclusion	68
5	Chapter 5: Designing Fluorescent Chemosensors with Metal-Complexed Crown Ethers	70
5.1	Introduction	70
5.2	Computational Details	72
5.3	Discussion	73
5.3.1	Selectivity of the Ionophores	73
5.3.2	Binding Affinity of Crown Ethers	75
5.3.3	Introducing the Fluorophore	80
5.3.4	Excitation Energies of Chemosensors	82
5.4	Conclusion	89
6	Conclusions	91
6.1	Summary of Thesis Research	91
6.2	Future Work	93
	Bibliography	95
A	Appendix to Chapter 2	106
A1	Legend of Individual Contributions	106
A2	Experimental and Calculated Spectra with a Triple-zeta Basis Set . .	107
A3	Analysis of Major Peaks for <i>cis</i> -1-bromo-1-propene	108

B	Appendix to Chapter 3	110
B1	Decomposition Pathways Calculated with Single-Reference Methods .	110
B2	Z3PolP Basis Set for Phosphorus	111
B3	Reaction Enthalpies	113
B4	Frozen Decomposition Pathways	113
B5	Coordinates Along the Decomposition Pathway	114
C	Appendix to Chapter 4	143
C1	Core Electron Binding Energies of the Test Set Calculated with Other Density Functionals	144
D	Appendix to Chapter 5	209
D1	Relative Energies of Flat and Bent Ionophores	209
D2	Relative Energies of Ionophore Isomers	210
D3	Binding Affinities of Ionophores with Metal Incorporated	210
D4	Relative Energies of Chemosensor Isomers	213
D5	Rotation of BODIPY	215

List of Tables

2.1	trans-1B1P: Analysis of Major Peak #1	25
2.2	trans-1B1P: Analysis of Major Peak #2 ^(a)	26
2.3	trans-1B1P: Analysis of Major Peak #3 ^(a)	27
2.4	trans-1B1P: Analysis of Major Peak #4 ^(a)	27
2.5	trans-1B1P: Analysis of Major Peak #5 ^(a)	28
2.6	trans-1B1P: Analysis of Major Peak #6 ^(a)	30
3.1	Equilibrium P ₂ Bond Lengths, $R(\text{P-P})$, (Å) and Signed Errors of Multireference Methods Compared to Experimental Bond Lengths	44
3.2	Equilibrium Bond Length $[R(\text{P-P})]$ (Å) of P ₄ and Signed Errors of Multireference Methods Compared to Experiment	45
3.3	Reaction Enthalpy (kcal/mol) at 298 K Calculated with Multireference Methods ^a	46
3.4	Average Computer Time Using the (6442) Active Space (in Minutes) ^a	50
4.1	The Chong test set used to benchmark density functionals for evaluating core electron binding energy (eV); the ionized atom is in bold font.	59
4.2	Experimental and theoretical values of 1s core electron binding energy (eV) in adenine A.	60
4.3	Experimental and theoretical values of 1s core electron binding energy (eV) in uracil.	60
4.4	Experimental and theoretical values of 1s core electron binding energy (eV) in thymine.	61
4.5	Experimental and theoretical values of core electron binding energies show method sensitivity for detecting small energetic differences within cytosine tautomers.	63
4.6	Experimental and theoretical values of core electron binding energies show method sensitivity for detecting small energetic differences within guanine tautomers.	65
A1	<i>cis</i> -1B1P: Analysis of Major Peak #1	108
A2	<i>cis</i> -1B1P: Analysis of Major Peak #2 ^(a)	108
A3	<i>cis</i> -1B1P: Analysis of Major Peak #3 ^(a)	109

A4	<i>cis</i> -1B1P: Analysis of Major Peak #4 ^(a)	109
B1	MS-CASPT2 Reaction Enthalpy with Frozen P-P distance (kcal/mol) ^a	113
C1	CEBE results (eV) from density functional SVWN; the Chong test set is used and the ionized atom is in bold font.	144
C2	CEBE results (eV) from density functional SVWN1RPA; the Chong test set is used and the ionized atom is in bold font.	145
C3	CEBE results (eV) from density functional BOP; the Chong test set is used and the ionized atom is in bold font.	146
C4	CEBE results (eV) from density functional BP86; the Chong test set is used and the ionized atom is in bold font.	147
C5	CEBE results (eV) from density functional GLYP; the Chong test set is used and the ionized atom is in bold font.	148
C6	CEBE results (eV) from density functional GP86; the Chong test set is used and the ionized atom is in bold font.	149
C7	CEBE results (eV) from density functional GVWN; the Chong test set is used and the ionized atom is in bold font.	150
C8	CEBE results (eV) from density functional GPW91; the Chong test set is used and the ionized atom is in bold font.	151
C9	CEBE results (eV) from density functional PBEVWN; the Chong test set is used and the ionized atom is in bold font.	152
C10	CEBE results (eV) from density functional PBEOP; the Chong test set is used and the ionized atom is in bold font.	153
C11	CEBE results (eV) from density functional OLYP; the Chong test set is used and the ionized atom is in bold font.	154
C12	CEBE results (eV) from density functional PW91; the Chong test set is used and the ionized atom is in bold font.	155
C13	CEBE results (eV) from density functional PBE; the Chong test set is used and the ionized atom is in bold font.	156
C14	CEBE results (eV) from density functional EDF1; the Chong test set is used and the ionized atom is in bold font.	157
C15	CEBE results (eV) from density functional revPBE; the Chong test set is used and the ionized atom is in bold font.	158
C16	CEBE results (eV) from density functional RPBE; the Chong test set is used and the ionized atom is in bold font.	159
C17	CEBE results (eV) from density functional PBEsol; the Chong test set is used and the ionized atom is in bold font.	160
C18	CEBE results (eV) from density functional HCTH93; the Chong test set is used and the ionized atom is in bold font.	161
C19	CEBE results (eV) from density functional HCTH120; the Chong test set is used and the ionized atom is in bold font.	162

C20	CEBE results (eV) from density functional HCTH147; the Chong test set is used and the ionized atom is in bold font.	163
C21	CEBE results (eV) from density functional HCTH407; the Chong test set is used and the ionized atom is in bold font.	164
C22	CEBE results (eV) from density functional SOGGA; the Chong test set is used and the ionized atom is in bold font.	165
C23	CEBE results (eV) from density functional MOHLYP; the Chong test set is used and the ionized atom is in bold font.	166
C24	CEBE results (eV) from density functional B97-D; the Chong test set is used and the ionized atom is in bold font.	167
C25	CEBE results (eV) from density functional BHHLYP; the Chong test set is used and the ionized atom is in bold font.	168
C26	CEBE results (eV) from density functional B3PW91; the Chong test set is used and the ionized atom is in bold font.	169
C27	CEBE results (eV) from density functional B3LYP1; the Chong test set is used and the ionized atom is in bold font.	170
C28	CEBE results (eV) from density functional B97; the Chong test set is used and the ionized atom is in bold font.	171
C29	CEBE results (eV) from density functional B97-1; the Chong test set is used and the ionized atom is in bold font.	172
C30	CEBE results (eV) from density functional B97-2; the Chong test set is used and the ionized atom is in bold font.	173
C31	CEBE results (eV) from density functional B97-3; the Chong test set is used and the ionized atom is in bold font.	174
C32	CEBE results (eV) from density functional B97-K; the Chong test set is used and the ionized atom is in bold font.	175
C33	CEBE results (eV) from density functional B98; the Chong test set is used and the ionized atom is in bold font.	176
C34	CEBE results (eV) from density functional PBE0; the Chong test set is used and the ionized atom is in bold font.	177
C35	CEBE results (eV) from density functional X3LYP; the Chong test set is used and the ionized atom is in bold font.	178
C36	CEBE results (eV) from density functional VS98; the Chong test set is used and the ionized atom is in bold font.	179
C37	CEBE results (eV) from density functional PKZB; the Chong test set is used and the ionized atom is in bold font.	180
C38	CEBE results (eV) from density functional tHCTH; the Chong test set is used and the ionized atom is in bold font.	181
C39	CEBE results (eV) from density functional tHCTHhyb; the Chong test set is used and the ionized atom is in bold font.	182
C40	CEBE results (eV) from density functional BMK; the Chong test set is used and the ionized atom is in bold font.	183

C41	CEBE results (eV) from density functional TPSS; the Chong test set is used and the ionized atom is in bold font.	184
C42	CEBE results (eV) from density functional revTPSS; the Chong test set is used and the ionized atom is in bold font.	185
C43	CEBE results (eV) from density functional M05; the Chong test set is used and the ionized atom is in bold font.	186
C44	CEBE results (eV) from density functional M05-2X; the Chong test set is used and the ionized atom is in bold font.	187
C45	CEBE results (eV) from density functional BPBE; the Chong test set is used and the ionized atom is in bold font.	188
C46	CEBE results (eV) from density functional M06; the Chong test set is used and the ionized atom is in bold font.	189
C47	CEBE results (eV) from density functional M06-L; the Chong test set is used and the ionized atom is in bold font.	190
C48	CEBE results (eV) from density functional M06-2X; the Chong test set is used and the ionized atom is in bold font.	191
C49	CEBE results (eV) from density functional M06-HF; the Chong test set is used and the ionized atom is in bold font.	192
C50	CEBE results (eV) from density functional M08-HX; the Chong test set is used and the ionized atom is in bold font.	193
C51	CEBE results (eV) from density functional M08-SO; the Chong test set is used and the ionized atom is in bold font.	194
C52	CEBE results (eV) from density functional CAMB3LYP; the Chong test set is used and the ionized atom is in bold font.	195
C53	CEBE results (eV) from density functional ω B97; the Chong test set is used and the ionized atom is in bold font.	196
C54	CEBE results (eV) from density functional ω B97X; the Chong test set is used and the ionized atom is in bold font.	197
C55	CEBE results (eV) from density functional ω B97X-D; the Chong test set is used and the ionized atom is in bold font.	198
C56	CEBE results (eV) from density functional BPW91; the Chong test set is used and the ionized atom is in bold font.	199
C57	CEBE results (eV) from density functional TPSSh; the Chong test set is used and the ionized atom is in bold font.	200
C58	CEBE results (eV) from density functional M11; the Chong test set is used and the ionized atom is in bold font.	201
C59	CEBE results (eV) from density functional M11-L; the Chong test set is used and the ionized atom is in bold font.	202
C60	CEBE results (eV) from density functional SOGGA11; the Chong test set is used and the ionized atom is in bold font.	203
C61	CEBE results (eV) from density functional SOGGA11X; the Chong test set is used and the ionized atom is in bold font.	204

C62	CEBE results (eV) from density functional B3LYPV1R; the Chong test set is used and the ionized atom is in bold font.	205
C63	CEBE results (eV) from density functional B3LYPV3; the Chong test set is used and the ionized atom is in bold font.	206
C64	CEBE results (eV) from density functional B3P86V1R; the Chong test set is used and the ionized atom is in bold font.	207
C65	CEBE results (eV) from density functional B3P86V5; the Chong test set is used and the ionized atom is in bold font.	208
D1	Relative energies (in kJ/mol) of flat and bent geometries of crown ether ionophores.	209
D2	Relative energies (in kJ/mol) of crown ether ionophore isomers.	210

List of Figures

1.1	The methods used in this Thesis as related to parent quantum mechanical methods.	2
1.2	The potential energy curve of Cl_2 as a function of the bond distance, r , calculated with two methods, Hartree-Fock and Complete Active Space Self-Consistent Field using a polarized triple-zeta valence basis set, TZVP.	6
1.3	The xenon 5s orbital as described by all-electron (AE), large-core model core potential (MCP), and large-core effective core potential (ECP) basis sets. The blue MCP orbital closely follows the structure of the green AE orbital, whereas the purple ECP orbital maintains the proper valence structure only.	9
1.4	Distribution of electrons in active space orbitals. On the left, the CASSCF wave function where the CAS allows all excitations within the orbitals circled. All other occupied molecular orbitals are frozen at the Hartree-Fock level. On the right is a representation of the RASSCF wave function, where the RAS2 space is equivalent to CAS, and all excitations are allowed within this space. The RAS1 space restricts the occupancy by specifying how many holes are allowed in that space at one time. Likewise, RAS3 occupancies are restricted by specifying how many electrons are allowed in that space at one time. The rest of the occupied orbitals below RAS1 must always have double occupancy, but can be partitioned into inactive (MC-SCF level) or frozen (Hartree-Fock level).	13
1.5	The Jabłoński diagram depicts radiative and non-radiative pathways involved in excitations. Energy is absorbed in a vertical excitation by the ground-state molecule, S_0 , and ends up in an excited state, S_1 . De-excitation pathway a shows fluorescence, and pathway b shows phosphorescence through internal conversion. For both de-excitation pathways, the internal conversion to the lowest vibrational state is omitted for clarity.	18

1.6	The vibrational state wave function overlap predicts the intensity of the vertical transition: a) a good vibrational wave function overlap between ground state $v''=0$ and excited $v'=0, 2,$ and $4.$ b) a poor vibrational wave function overlap except for $v''=0$ and $v'=3.$	19
2.1	Labelling six major peaks on the electronic excitation spectra for CAM-B3LYP, PBE0 and SAC-CI with acct basis set. In simulating spectra from excitation energies and intensities we used Cauchy-Lorentz band shape with a 0.3 eV half-width.	24
2.2	Computed excitation energies for the 9 to 12 eV spectral range using the acct basis set.	31
2.3	Contributions from individual states explicitly shown for results from CAM-B3LYP/acct.	32
2.4	Experimental spectrum compared to computed electronic excitations of <i>trans</i> -1B1P with SAC-CI(30,30)/acct and CAM-B3LYP/amcp3-Br.	34
2.5	Weighted calculated spectra of <i>trans</i> -1B1P and <i>cis</i> -1B1P with SAC-CI/acct compared to experimental spectrum.	35
2.6	Weighted calculated spectra of <i>trans</i> -1B1P and <i>cis</i> -1B1P with CAM-B3LYP/amcp3-Br compared to experimental spectrum.	36
3.1	Tetrahedral P_4 structure and coordinate system for calculating the potential energy hypersurface of the dissociation of $P_4.$	41
3.2	MS-CASPT2 potential energy curves of the decomposition pathway of P_4 to $2 P_2$ with varying distances between the P_2 subunits, $R(P_2-P_2).$ The Opt $R(P-P)$ pathway allows the distance within the subunits, $R(P-P)$ to relax. The equilibrium geometry of P_4 was calculated with B3LYP/6-31G(d). The curves were calculated with two active spaces, (4332) and (6442), and two basis sets. Top: Curve calculated with the all-electron, cc-pVTZ basis set. Bottom: Curve calculated with the model potential MCP-TZP basis set. Both the ground state (Root 1) and the first excited state (Root 2) are shown in each case.	47
3.3	MC-PDFT potential energy curves of the decomposition pathway of P_4 to $2 P_2$ with varying distances between the P_2 subunits, $R(P_2-P_2).$ The Opt $R(P-P)$ pathway allows the distance within the subunits, $R(P-P)$ to relax. The equilibrium geometry of P_4 was calculated with B3LYP/6-31G(d). The curves were calculated with two active spaces, (4332) and (6442), and two basis sets. Top: Curve calculated with the all-electron, cc-pVTZ basis set. Bottom: Curve calculated with the model potential MCP-TZP basis set. Both the ground state (Root 1) and the first excited state (Root 2) are shown in each case.	49

3.4	MC-PDFT potential energy curves of the decomposition pathway of P_4 to 2 P_2 with varying distances between the P_2 subunits, $R(P_2-P_2)$. The Opt $R(P-P)$ pathway allows the distance within the subunits, $R(P-P)$ to relax. The equilibrium geometry of P_4 was calculated with B3LYP/6-31G(d). The curves were calculated with two active spaces, (4332) and (6442), and two basis sets. Top: Curve calculated with the all-electron, cc-pVQZ basis set. Bottom: Curve calculated with the all-electron cc-pV5Z basis set. Both the ground state (Root 1) and the first excited state (Root 2) are shown in each case.	50
3.5	Ground state P_4 natural valence orbitals of symmetry a_1 and a_2 for P_2-P_2 distances of 1.59, 2.49, and 3.71 Å. The natural orbital occupation number is shown below the orbital.	52
3.6	Ground state P_4 natural valence orbitals of symmetry b_1 and b_2 for P_2-P_2 distances of 1.59, 2.49, and 3.71 Å. The natural orbital occupation number is shown below the orbital.	52
4.1	Structural formulas of the four new additions to the Chong test set, a) OCNH b) NCNH ₂ c) NH ₂ CHO d) OC(NH ₂) ₂	58
4.2	Structural formulas of nucleic acid bases used to compare calculated core electron binding energies to experimentally measured values. . .	58
4.3	Structures of cytosine A, C, and D, with unique atomic environments highlighted.	62
4.4	Structures of guanine A, B, and C, with unique atomic environments highlighted.	64
4.5	Deviation of Δ B3LYP/MIX core electron binding energies (eV) from experiment, per carbon, nitrogen, and oxygen atom. The results are split into the Chong test set results and NAB results.	66
4.6	Correlation between calculated (x-axis) and experimental (y-axis) 1s core electron binding energies (in eV)	67
4.7	Timing study of B3LYP and MP2 calculations by increasing molecular size by number of units, n, on one core on the WestGrid Altix XE 1300 cluster.	68
5.1	Free BODIPY-benzothiacrown chemosensor proposed by Kim et al. .	72
5.2	The naming of all possible combinations of the positions of oxygen and sulfur atoms in the ionophore considered in this chapter.	74
5.3	An example of the two minimum energy structures of the ionophores. Top: flat 18C-O ₀ S ₆ . Bottom: bent 18C-O ₀ S ₆	75
5.4	Heat map of binding affinity (in kJ/mol) of metal ions of varying size and charge with the 18C-O ₆ S ₀ crown. Negative values (yellow to green) indicate that M_1 binds with greater affinity to the crown than M_2 . . .	77

5.5	Heat map of binding affinity (in kJ/mol) of metal ions of varying size and charge with the 18C-O ₄ S ₂ -para crown. Negative values (yellow to green) indicate that M ₁ binds with greater affinity to the crown than M ₂	78
5.6	A heat map of binding affinity (in kJ/mol) of metal ions of varying size and charge with the 18C-O ₀ S ₆ crown. Negative values (yellow to green) indicate that M ₁ binds with greater affinity to the crown than M ₂	79
5.7	64 structural combinations of the crowns from Figure 5.2, with varying positions of fluorophore. a) 18C-O ₆ S ₀ and 18C-O ₀ S ₆ have just one isomer each. b) 18C-O ₅ S ₁ and 18C-O ₁ S ₅ have six isomers. c) 18C-O ₄ S ₂ -ortho and -meta have six isomers and -para has three possible isomers, similar to 18C-O ₂ S ₄ in d). e) 18C-O ₃ S ₃ -1,1,1 has two possible isomers, and 18C-O ₃ S ₃ -3 has six, while with 18C-O ₃ S ₃ -2,1 all 12 linker positions and fluorophore binding sites are considered.	81
5.8	Binding affinity for Hg ²⁺ versus Zn ²⁺ . A negative value ($\Delta\Delta E$) indicates that Hg ²⁺ has a higher affinity for the chemosensor than Zn ²⁺	82
5.9	Binding affinity for Hg ²⁺ versus Cd ²⁺ . A negative value ($\Delta\Delta E$) indicates that Hg ²⁺ has a higher affinity for the crown than Cd ²⁺	83
5.10	A relative RHF energy profile as a function of dihedral angle rotating BODIPY in relation to the benzene linker. At 54° and 234°, the highest energy structures have steric interactions between the hydrogens on BODIPY and on the linker. At 174° and 0° (or 360°, the initial optimized geometry), the most stable structures are highlighted, with the position of the linker slightly rotated to avoid the unfavorable hydrogen interactions.	85
5.11	A plot of excitation energy as a function of BODIPY-linker dihedral angle. The energies of the brightest three singlet excited states, calculated with TD-DFT(PBE0)/6-31G(d), for the free ligand (top left), ligand with Hg ²⁺ (top right), ligand with Zn ²⁺ (bottom right), and ligand with Cd ²⁺ (bottom left).	86
5.12	A plot of oscillator strength as a function of BODIPY-linker dihedral angle. The oscillator strengths of the brightest three singlet excited states, calculated with TD-DFT(PBE0)/6-31G(d), for the free ligand (top left), ligand with Hg ²⁺ (top right), ligand with Zn ²⁺ (bottom right), and ligand with Cd ²⁺ (bottom left).	87
5.13	Heat map of the difference in excitation energies, ΔE (in eV), of the free ligand and the metal complex. Red squares represent little to no difference with respect to the excitation energy of the parent ligand, and green squares indicate a difference of at least 1 eV.	88

5.14	The 18C-O ₄ S ₂ -meta-A chemosensor for Hg ²⁺ . Left: Two-dimensional structure. Right: Three-dimensional structure optimized at the PBE0/6-31G(d)/LANL2DZ level of theory.	89
A1	Legend of individual contributions from CAM-B3LYP/amcp3-Br. Labels represent excitation energy, symmetry of the state and oscillator strength, respectively.	106
A2	Experimental spectra compared to computed electronic excitations of <i>cis</i> -1B1P with SAC-CI(30,30)/acct and CAM-B3LYP/amcp3.	107
B1	Single-reference thermal decomposition pathway of P ₄ to 2 P ₂ calculated with the Z3PolP basis set. Hartree-Fock, density functional theory, Møller-Plesset perturbation theory, coupled cluster theory, and configuration interaction were all used to describe the reaction barrier.	110
B2	MS-CASPT2 potential energy curves of the decomposition of P ₄ to 2 P ₂ by varying the distance between P ₂ subunits, R(P ₂ -P ₂) and keeping the distance within the P ₂ subunits, R(P-P), frozen. The optimized geometry from B3LYP/6-31G(d) was used as the equilibrium geometry of P ₄ . The top plot was calculated with the double zeta cc-pVDZ basis set, and the bottom plot was calculated with MCP-DZP. Both show results with two different active spaces: (4332) and (6442) and two roots: the ground state (Root 1) and first excited state (Root 2).	113
B3	MC-PDFT potential energy curves of the decomposition of P ₄ to 2 P ₂ by varying the distance between P ₂ subunits, R(P ₂ -P ₂) and keeping the distance within the P ₂ subunits, R(P-P), frozen. The optimized geometry from B3LYP/6-31G(d) was used as the equilibrium geometry of P ₄ . The top plot was calculated with the double zeta cc-pVDZ basis set, and the bottom plot was calculated with MCP-DZP. Both plots show results with two different active spaces: (4332) and (6442) and two roots: the ground state (Root 1) and first excited state (Root 2).	114
D1	Binding affinity for Cd ²⁺ over Zn ²⁺ . A negative binding affinity ($\Delta\Delta E_{rxn}$) indicates that Cd has a higher affinity for the crown than Zn.	210
D2	Binding affinity for Hg ²⁺ over Zn ²⁺ . A negative binding affinity ($\Delta\Delta E$) indicates that Hg has a higher affinity for the crown than Zn.	211
D3	Binding affinity for Hg ²⁺ over Cd ²⁺ . A negative binding affinity ($\Delta\Delta E$) indicates that Hg has a higher affinity for the crown than Cd.	212
D4	The relative energy (kJ/mol) for each isomer is compared to the position of the benzene linker for 18C-O ₅ S ₁ and 18C-O ₁ S ₅ . The lowest energy compounds are 18C-O ₅ S ₁ - B and -E , and 18C-O ₁ S ₅ - F	213

D5	The relative energy (kJ/mol) for each isomer is compared to the position of the benzene linker for 18C-O ₂ S ₄ . The lowest energy compounds are 18C-O ₂ S ₄ -meta- D , 18C-O ₂ S ₄ -ortho- A , and 18C-O ₂ S ₄ -para- C and - A	213
D6	The relative energy (kJ/mol) for each isomer is compared to the position of the benzene linker for 18C-O ₃ S ₃ . The lowest energy compounds are 18C-O ₂ S ₄ -3- E , 18C-O ₂ S ₄ -2,1- L , and 18C-O ₂ S ₄ -1,1,1- A and - B . . .	214
D7	The relative energy (kJ/mol) for each isomer is compared to the position of the benzene linker for 18C-O ₄ S ₂ . The lowest energy compounds are 18C-O ₄ S ₂ -meta- E , 18C-O ₄ S ₂ -ortho- B , and 18C-O ₂ S ₄ -para- B . . .	214
D8	A plot of excitation energy as a function of BODIPY-linker angle. a) Energies of the lowest three singlet excited states, calculated with CIS and the MCP-DZP basis set for light atoms and MCP-TZP for any metal ions and TD-DFT(PBE0) with the same basis set, for the free ligand (top), ligand with Ba ²⁺ (middle), and ligand with Hg ²⁺ (bottom). b) Energies of the lowest three triplet excited states, calculated with CIS/6-31G(d) and TD-DFT(PBE0)/6-31G(d), for the free ligand (top), ligand with Ba ²⁺ (middle), and ligand with Hg ²⁺ (bottom). . .	215
D9	A plot of oscillator strength as a function of BODIPY-linker angle. a) Oscillator strengths of the lowest three singlet excited states, calculated with CIS and the MCP-DZP basis set for light atoms and MCP-TZP for any metal ions and TD-DFT(PBE0) with the same basis set, for the free ligand (top), ligand with Ba ²⁺ (middle), and ligand with Hg ²⁺ (bottom). b) Oscillator strengths of the lowest three triplet excited states, calculated with CIS and TD-DFT(PBE0), for the free ligand (top), ligand with Ba ²⁺ (middle), and ligand with Hg ²⁺ (bottom). . .	216

List of Abbreviations and Acronyms

1B1P	<i>1-bromo-1-propene</i>
6-31G(d)	<i>Double-zeta valence basis set with d polarization functions on heavy atoms ($>H$)</i>
6-311G(d,p)	<i>Triple-zeta valence basis set with d polarization functions on heavy atoms and p polarization functions on hydrogen</i>
6-311G++(d,p)	<i>Triple-zeta valence basis set with polarization and diffuse functions on heavy and light atoms</i>
acct	<i>see aug-cc-pVTZ</i>
ADC(4)	<i>Fourth-order algebraic diagrammatic construction method</i>
AE	<i>All-electron basis set</i>
amcp3	<i>see MCP-aTZP</i>
amcp3-Br	<i>A mixed basis set; a triple-zeta model core potential basis set was used for the bromine atom only and all electron basis set aug-cc-pVTZ were used on carbon and hydrogen atoms</i>
aug-cc-pVnZ	<i>An n-tuple correlation consistent basis set with diffuse functions</i>
B3LYP	<i>Density functional with Becke's 3 parameters and 1988 exchange B88 with Lee, Yang, Parr correlation</i>
B88-P86	<i>Density functional with Becke's 1988 exchange B88 with Perdew's 1986 correlation</i>
BLYP	<i>Gradient corrected density functional with Becke's 1988 exchange B88 with Lee, Yang, Parr correlation</i>

BODIPY	<i>4,4-difluoro-4-bora-3a,4a-diaza-s-indacene</i>
CAM-B3LYP	<i>Long-range corrected hybrid density functional</i>
CAS	<i>Complete active space</i>
CASPT2	<i>Complete active space second order perturbation theory</i>
CASSCF	<i>Complete active space self-consistent field method</i>
CC	<i>Coupled cluster theory</i>
cc-pCV _n Z	<i>An n-tuple zeta correlation consistent basis set with core polarization functions</i>
cc-pV _n Z	<i>An n-tuple zeta valence correlation consistent basis set</i>
CEBE	<i>Core electron binding energy</i>
CHEF	<i>Chelation enhanced fluorescence</i>
CISD	<i>Configuration interaction with single and double excitations</i>
CPU	<i>Central processing unit</i>
DFT	<i>Density functional theory</i>
ECP	<i>Effective core potential basis set</i>
eV	<i>Electron volt</i>
GAMESS	<i>General Atomic and Molecular Electronic Structure System, a quantum chemistry program</i>
GC VUV	<i>Gas chromatograph with vacuum ultra violet detector attachment</i>
GF	<i>Gaussian-type function</i>
HF	<i>Hartree-Fock</i>
IPEA	<i>Ionization potential electron affinity shift</i>
KS-DFT	<i>Kohn-Sham density functional theory</i>
M06	<i>Truhlar's Minnesota 2006 hybrid meta gradient generalized approximation density functional</i>
MAD	<i>Mean absolute deviation</i>
MCSCF	<i>Multi-configuration self consistent field</i>
MCP	<i>Model core potential basis set</i>
MCP-nZP	<i>An n-tuple zeta valence model core potential basis set</i>

MCP-aTZP	<i>Augmented triple-ζ model core potential basis set</i>
MC-PDFT	<i>Multi-configuration pair-density functional theory</i>
MIX	<i>Mixture of model core potential and all-electron basis sets for calculating core electron binding energies</i>
MOM	<i>Maximum overlap method</i>
MP2	<i>Second-order Møller-Plesset perturbation theory</i>
MRCI	<i>Multi-reference configuration interaction method</i>
MRCI+Q	<i>Multireference configuration interaction method with Davidson correction</i>
MS-CASPT2	<i>Multi-state complete active space second order perturbation theory</i>
NAB	<i>Nucleic acid bases</i>
NOON	<i>Natural orbital occupation numbers</i>
PBE0	<i>Parameter-free and hybrid version of Perdew-Burke-Ernzerhof density functional</i>
PT2	<i>Second-order perturbation theory</i>
PW86x-PW91c	<i>Density functional with Perdew-Wang 1986 exchange and Perdew-Wang 1991 correlation</i>
RAS	<i>Restricted active space</i>
SA-CASSCF	<i>State-averaged complete active space self-consistent field method</i>
SAC-CI SD-R	<i>Symmetry adapted cluster/configuration interaction method with single and double excitations</i>
SCF	<i>Self-consistent field method</i>
SE	<i>Signed error</i>
SS-CASPT2	<i>State-specific Complete active space second order perturbation theory</i>
tPBE	<i>Translated PBE on-top density functional</i>
TPSSm	<i>Tao-Perdew-Staroverov-Scuseria meta-generalized gradient approximated density functional, with modified parameter from the original TPSS functional</i>
TD-DFT	<i>Time dependent density functional theory</i>

uGTS	<i>Unrestricted generalized transition-state model</i>
VUV	<i>Vacuum ultra-violet</i>
ZPE	<i>Zero point energy</i>

List of Symbols

\AA	<i>angstrom</i>
e	<i>Electron charge</i>
f	<i>Oscillator strength</i>
\hat{H}	<i>Hamiltonian</i>
\hat{H}_e	<i>Electronic Hamiltonian</i>
$\hat{H}^{(0)}$	<i>Unperturbed Hamiltonian</i>
\hbar	<i>Reduced Planck's constant</i>
m_e	<i>Electron mass</i>
Λ	<i>Spatial overlap between ground and excited states</i>
Ψ	<i>Wave function</i>
Φ	<i>Trial wave function</i>
ϕ	<i>Orbital</i>
ψ	<i>Spin orbital</i>
χ	<i>Basis function</i>
\hat{f}	<i>Fock operator</i>
\hat{J}	<i>Coulomb operator</i>
\hat{K}	<i>Exchange operator</i>
\hat{T}	<i>Cluster operator</i>
\hat{V}	<i>Perturbation operator</i>
ρ	<i>Electron density</i>
Π	<i>On-top pair density</i>
ν	<i>Frequency</i>
μ	<i>Transition dipole</i>

$\delta(X)$ *Difference between calculated and experimental results,
where X stands for the method used*

Δ *Shift parameter*

Chapter 1

Introduction

1.1 Scope

Electronic excited states of small systems are studied in this Thesis using a number of quantum chemistry methods. The main focus is to provide insight to experimental processes which may not yet be fully understood. Generating *in-silico* spectra may be essential to understanding and assigning electronic transitions. If we can reproduce experimental results, we may have a good theoretical grasp on the chemical system and can begin digging deeper, and also can apply the same method to a similar but unknown chemical system. There are many computational methods available to study electronic excited states, and those that were used in the course of the Thesis are briefly described in the following sections of this chapter.^a

1.2 Wave Function Theory

Computational chemistry focuses on calculating properties of matter. Quantum mechanics allows us to do this through rigorous equations and approximations to them. Shown in Figure 1.1 is the relationship between the current methods described in this Thesis for calculating properties of molecular systems.

The governing postulates let us describe the state of any system with a wave function, Ψ , which contains everything we could know about an atomic or molecu-

^aAn excellent introduction to those methods may be found in Quantum Chemistry by Ira N. Levine.²

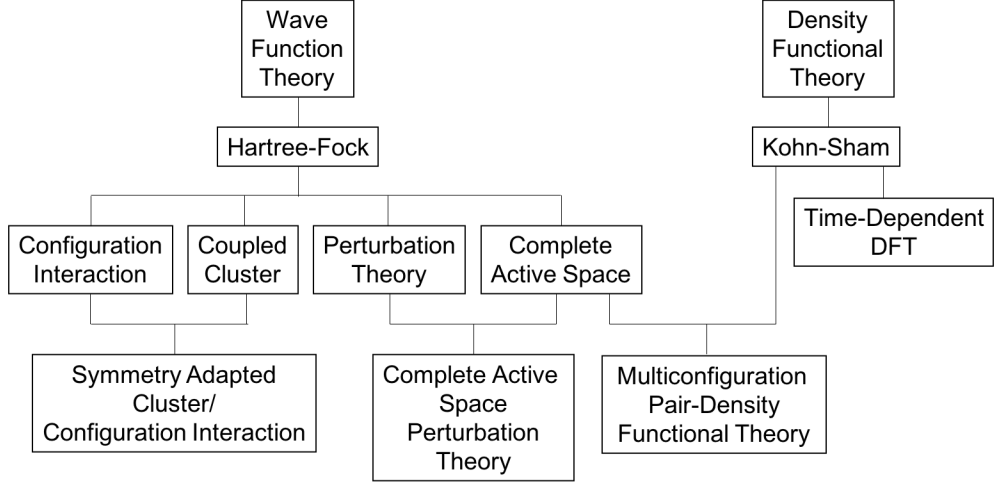


Figure 1.1: *The methods used in this Thesis as related to parent quantum mechanical methods.*

lar system. Energy levels can be calculated by solving the Schrödinger eigenvalue equation:

$$\hat{H}\Psi = E\Psi, \quad (1.1)$$

where \hat{H} is the Hamiltonian (energy) operator, which gives both energy E and the eigenfunction Ψ . The form of the non-relativistic Hamiltonian operator (in atomic units) is

$$\begin{aligned} \hat{H} = & -\frac{1}{2} \sum_{i=1}^N \nabla_i^2 - \sum_{A=1}^P \frac{1}{2M_A} \nabla_A^2 - \sum_{i=1}^N \sum_{A=1}^P \frac{Z_A}{|\mathbf{r}_i - \mathbf{R}_A|} \\ & + \sum_{i=1}^{N-1} \sum_{j>i}^N \frac{1}{|\mathbf{r}_i - \mathbf{r}_j|} + \sum_{A=1}^{P-1} \sum_{B>A}^P \frac{Z_A Z_B}{|\mathbf{R}_A - \mathbf{R}_B|} \end{aligned} \quad (1.2)$$

where the first term accounts for kinetic energy of N electrons and the second is kinetic energy of P nuclei, where M_A is the atomic mass of nucleus A . The third term describes attractive interactions between electrons and nuclei, where Z_A is the atomic number of nucleus A , and the distance between electron i and nucleus A is the denominator. The fourth stands for the repulsive interactions between electrons i and j , and the fifth term describes nuclear-nuclear repulsion, with \mathbf{r}_i and \mathbf{R}_A representing the position vectors of electrons and nuclei, respectively.

The difficulty of solving the Schrödinger equation increases with the number of electrons, therefore approximations are used for larger systems.

First, the mass of electrons is at least three orders of magnitude smaller than that of nuclei, so it may be assumed that nuclei would be stationary compared to the motion of electrons (the Born-Oppenheimer approximation). This allows simplification of the Hamiltonian so that the nuclear kinetic energy term is neglected and the nuclear repulsion term becomes a constant. We can describe this new operator as the electronic Hamiltonian:

$$\hat{H}_e = -\frac{1}{2} \sum_{i=1}^N \nabla_i^2 - \sum_{i=1}^N \sum_{A=1}^P \frac{Z_A}{r_{Ai}} + \sum_{i=1}^{N-1} \sum_{j>i}^N \frac{1}{r_{ij}} + \sum_{A=1}^{P-1} \sum_{B>A}^P \frac{Z_A Z_B}{|\mathbf{R}_A - \mathbf{R}_B|} \quad (1.3)$$

The postulates of quantum mechanics state that possible wave functions must be limited to functions which are continuous, integrable, and one-to-one (well behaved), and the integral of the product of the wave function with its complex conjugate must equal one. Unfortunately, even with all these restrictions, we are not given the recipe to build the exact wave function. We can manipulate the Schrödinger equation by multiplying both sides by the complex conjugate of Ψ , integrating, and solving for energy:

$$E_0 = \frac{\langle \Psi | \hat{H} | \Psi \rangle}{\langle \Psi | \Psi \rangle} \quad (1.4)$$

The Variational Theorem guarantees that if we use a trial wave function, Φ , to guess the total energy, E_G , of a chemical system, the energy value obtained will be always greater than or equal to the exact energy, E_0 .

$$E_G = \frac{\langle \Phi | \hat{H} | \Phi \rangle}{\langle \Phi | \Phi \rangle} \geq E_0 \quad (1.5)$$

This allows us to systematically alter the trial wave function (via adjustable parameters) to produce a lower energy, in turn generating a better wave function.

The wave function must also obey antisymmetry and Pauli exclusion principles. The simplest such function for a closed-shell system containing N electrons is the Hartree-Fock wave function in the form of a Slater determinant:

$$\Phi^{HF}(1, 2, \dots, N) = \frac{1}{\sqrt{N!}} \begin{vmatrix} \phi_1^{HF}(r_1) & \bar{\phi}_1^{HF}(r_1) & \phi_2^{HF}(r_1) & \dots & \bar{\phi}_n^{HF}(r_1) \\ \phi_1^{HF}(r_2) & \bar{\phi}_1^{HF}(r_2) & \phi_2^{HF}(r_2) & \dots & \bar{\phi}_n^{HF}(r_2) \\ \dots & \dots & \dots & \dots & \dots \\ \phi_1^{HF}(r_N) & \bar{\phi}_1^{HF}(r_N) & \phi_2^{HF}(r_N) & \dots & \bar{\phi}_n^{HF}(r_N) \end{vmatrix}$$

where each ϕ_i orbital is associated with a spin up function (ϕ_i) or a spin down function ($\bar{\phi}_i$), and where $n = N/2$ is the number of doubly occupied orbitals.

In Hartree-Fock theory the problematic exact electron-electron repulsion term is eliminated by using a mean-field method instead of evaluating each interaction pairwise, consequently simplifying a many-body problem to several one-body problems. The Fock operator:

$$\hat{f}^{HF}(\mathbf{r}) = \hat{h}(\mathbf{r}) + \sum_{j=1}^{N/2} [2\hat{J}_j(\mathbf{r}) - \hat{K}_j(\mathbf{r})] \quad (1.6)$$

where $\hat{h}(\mathbf{r})$ is the one-electron Hamiltonian for any electron at position \mathbf{r} and the second term takes care of electron-electron interaction. The Coulomb repulsion term, $\hat{J}_j(\mathbf{r})$ represents repulsion between electrons, while the exchange term, $\hat{K}_j(\mathbf{r})$, which is a consequence of using the antisymmetric wave function, exists only between electrons of the same spin. We can now use the Fock operator to solve the Hartree-Fock equation for multi-electron systems:

$$\hat{f}^{HF}(\mathbf{r})\phi_a^{HF}(\mathbf{r}) = \varepsilon_a^{HF}\phi_a^{HF}(\mathbf{r}) \quad (1.7)$$

The Hartree-Fock method has limitations, mostly due to the error arising from the mean-field approximation. The difference between the exact energy and the energy calculated with the Hartree-Fock method is called correlation energy. Physically, movement of electrons is correlated because each electron interacts with all remaining electrons via the electron repulsion term. The Hartree-Fock method assumes each electron feels an average cloud of all other $N - 1$ electrons. While the correlation energy makes up only about 1% of the total energy, it is crucial for properly describing

molecular properties. Figure 1.2 shows the dissociation of Cl_2 as calculated using the Hartree-Fock method and a correlated method, Complete Active Space (CAS), using the TZVP basis set.³ The CAS results (in green) show the correct dissociation behaviour, where at longer distances the two atoms are no longer interacting. The Hartree-Fock results (in purple) show an inflated dissociation energy. The Hartree-Fock method for closed-shell systems uses one Slater determinant to describe the wave function, which does not afford the flexibility needed to describe how electron configurations change along the potential energy surface. A number of post-Hartree-Fock methods use many Slater determinants to capture the correlation energy, and they will be briefly explained below. Density functional theory (DFT) is another method, similar in methodology to the Hartree-Fock approach, but it includes correlation energy. DFT is a popular method among experimentalists and computational chemists since it is more computationally efficient and is less technical than most post-Hartree-Fock methods.

1.3 Density Functional Theory

Density functional theory is an alternate methodology to wave function theory and was introduced by Hohenberg and Kohn.⁴ They showed that it is possible to calculate the exact ground state energy, E , of a system in a non-degenerate ground state if we knew the exact electron density, $\rho(\mathbf{r})$. Subsequently, Kohn and Sham⁵ proposed a procedure for finding an orbital representation of the density by using the variational theorem via the Kohn-Sham (KS) equation:

$$\left(-\frac{1}{2}\nabla^2 + \nu^{KS}(\mathbf{r})\right)\phi_a^{KS}(\mathbf{r}) = \varepsilon_a^{KS}\phi_a^{KS}(\mathbf{r}) \quad (1.8)$$

One approximation in the Kohn-Sham method is that the ground state density is for a non-interacting system. The electrostatic interactions are treated with an external potential, $\nu^{KS}(\mathbf{r})$, where the non-interacting particles can interact. The

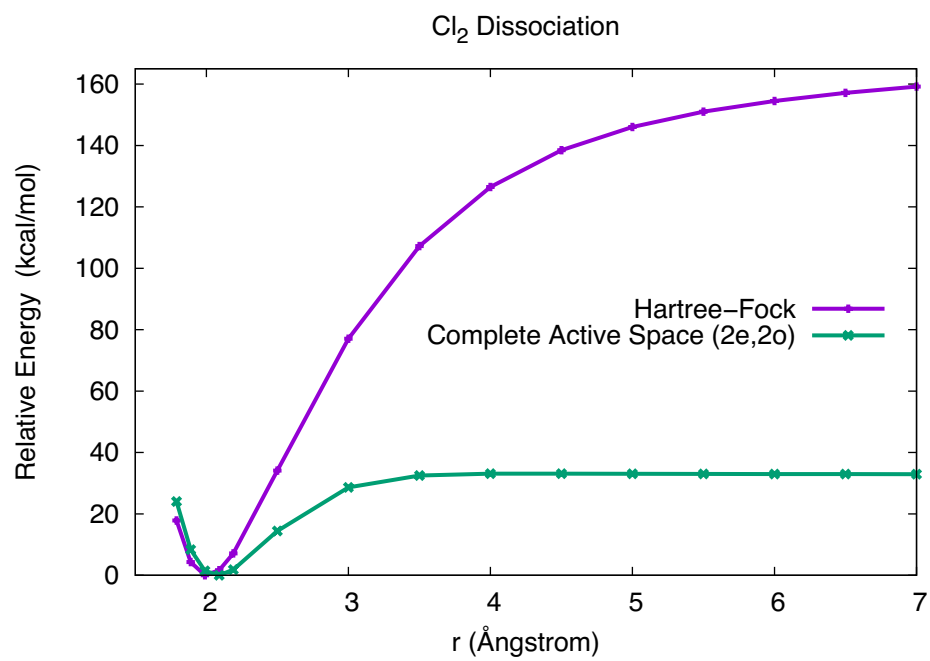


Figure 1.2: *The potential energy curve of Cl₂ as a function of the bond distance, r, calculated with two methods, Hartree-Fock and Complete Active Space Self-Consistent Field using a polarized triple-zeta valence basis set, TZVP.*

Kohn-Sham orbitals, ϕ^{KS} , represent the electron density:

$$\rho(\mathbf{r}) = 2 \sum_{i=1}^n |\phi_i^{KS}(\mathbf{r})|^2 \quad (1.9)$$

In order to calculate the total energy, we need a functional, F , as seen in Equation (1.10).

$$E = \mathbf{F}[\rho(\mathbf{r})] \quad (1.10)$$

The functional acts on the density to return the total energy of a system, much like the Hamiltonian described in the previous section. The total energy of a chemical system is made up of unique terms which can be represented as functionals of electron density:

$$E_{total}[\rho(\mathbf{r})] = \mathbf{T}[\rho(\mathbf{r})] + \mathbf{U}[\rho(\mathbf{r})] + \mathbf{V}[\rho(\mathbf{r})] \quad (1.11)$$

where $T[\rho(\mathbf{r})]$ is the electron kinetic energy term, $U[\rho(\mathbf{r})]$ is the electron interaction (Coulomb) term, and $V[\rho(\mathbf{r})]$ is the potential. We must simplify some terms for the sake of efficiency, and we can use a new total energy formula:

$$E_{total}[\rho(\mathbf{r})] = \mathbf{T}_s[\rho(\mathbf{r})] + \mathbf{U}_H[\rho(\mathbf{r})] + \mathbf{E}_{XC}[\rho(\mathbf{r})] + \mathbf{V}[\rho(\mathbf{r})] \quad (1.12)$$

The kinetic term will be approximated as the kinetic energy of non-interacting single-particles, $\mathbf{T}_s[\rho(\mathbf{r})]$, from the density. The second term is reduced to the classical Coulomb interaction, $\mathbf{U}_H[\rho(\mathbf{r})]$. With these approximations, a new term, $\mathbf{E}_{XC}[\rho(\mathbf{r})]$, arises to make up for the remaining energy. This term is the exchange-correlation energy term, which accounts for both electron-electron correlation and exchange effects. The exchange-correlation term presents the greatest difficulty in finding the exact ground-state energy since the exact exchange-correlation functional is not known.

Most density functional research focuses on accurately describing the $\mathbf{E}_{XC}[\rho(\mathbf{r})]$ term, first by splitting it to get separate exchange and correlation terms, and including parameters that are empirically derived to get results closer to experimental

values. The most popular functionals are of the hybrid type, mixing some Hartree-Fock exchange and the exchange-correlation functional.

1.4 Basis Functions

Both the wave function of the Hartree-Fock method and electron density of the DFT approach are represented by molecular orbitals:

$$\phi_a(\mathbf{r}) = \sum_{p=1}^K \chi_p(\mathbf{r}) C_{pa} \quad (1.13)$$

where χ_p are the basis functions and the unknown coefficients, C , are determined by the matrix Hartree-Fock equations or the Kohn-Sham equations. There are several types of functions that may be used to expand orbitals, ϕ_a , but Gaussian-type functions⁶ (GF) are usually used due to ease of integration.^b These basis functions have the form:

$$\chi^{GF}(x, y, z) \propto x^a y^b z^c e^{-\alpha r^2} \quad (1.14)$$

where $(a + b + c)$ is the atomic orbital angular momentum and α is an adjustable parameter.

A minimal basis set is one that uses one contracted GF per each atomic orbital occupied in the ground state of an atom. To get more accurate results, an extended basis set with a linear combination of many GFs is used. We generally use more basis functions to describe the valence space while using a minimal number of functions for the chemically inert core electrons.

Pseudopotential basis sets take the concept of an inert core further: instead of explicitly defining core electrons, they replace them by a suitable core potential. Generally, these basis sets are used for large systems with heavy atoms, and can implicitly include relativistic effects. Figure 1.3 shows the comparison between xenon 5s orbitals obtained with all-electron (AE) basis sets and pseudopotential basis sets.

^bThe popular program Amsterdam Density Functional⁷⁻⁹ (ADF) is an exception as it uses Slater-type orbitals.

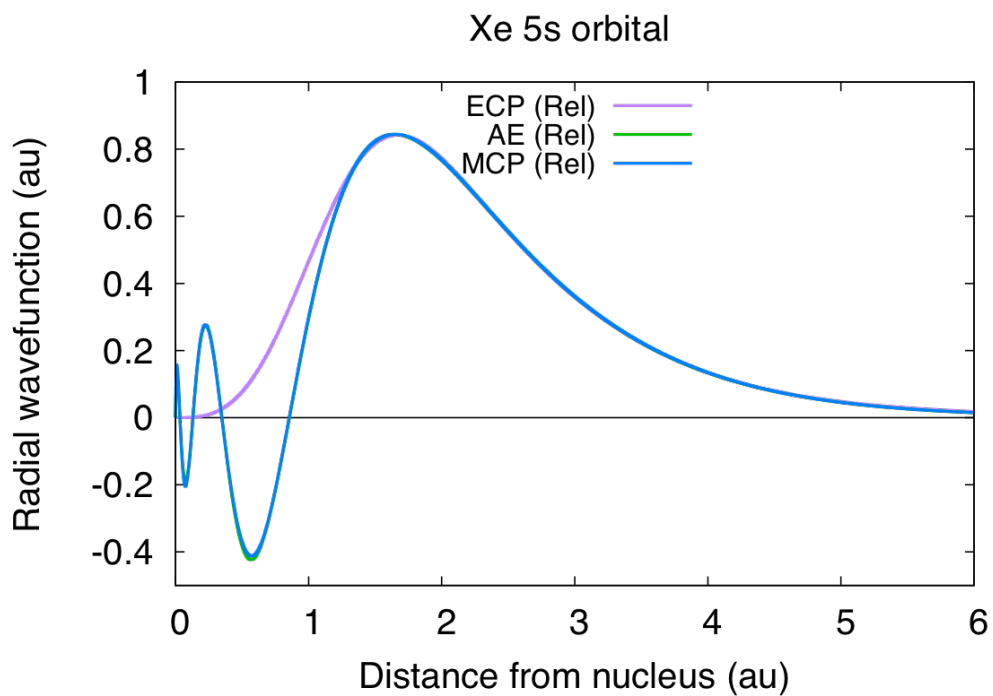


Figure 1.3: *The xenon 5s orbital as described by all-electron (AE), large-core model core potential (MCP), and large-core effective core potential (ECP) basis sets. The blue MCP orbital closely follows the structure of the green AE orbital, whereas the purple ECP orbital maintains the proper valence structure only.*

Some effective core potentials^{10,11} (ECP) afford only nodeless valence orbitals and give a good description of the valence region of the orbital only, leading to reduction of calculation time. Model core potentials¹² (MCP) give a correct description of both the valence and core region of the orbital, which allows for more accurate results when calculating core-based properties, e.g. spin-orbit coupling.

1.5 Some Advanced Computational Methods

Addressing the shortcomings of the Hartree-Fock method has long been of interest to theoreticians. Even today new methods are designed which indicates that no one recipe works satisfactorily for every chemical system. The Hartree-Fock method includes only Fermi electron correlation, which describes the interaction between electrons of same spin (as seen in the electron exchange term in the Hamiltonian). Coulomb correlation is the remaining difference between the Hartree-Fock energy and exact energy, and it can be split into two contributions: static and dynamical correlation. Static correlation can be accounted for by using more Slater determinants, usually generated through excitations from the ground-state determinant. Dynamical correlation can be corrected for by not using the mean-field approximation, but can also be overcome by using more determinants. However, including more and more determinants will increase the computational cost. One must thoughtfully consider the balance between computational efficiency and accuracy when choosing a quantum chemistry method for any chemical problem.

1.5.1 Configuration Interaction

The Hartree-Fock wave function is a good starting point to try to correct for the missing correlation energy. The Hartree-Fock method only considers occupied orbitals, but it also generates unoccupied (virtual) orbitals. In the configuration interaction method (CI),¹³ additional determinants are created by promoting electrons from oc-

cupied to unoccupied orbitals:

$$\Phi^{\text{CI}} = C_0^{\text{HF}} \Phi_0^{\text{HF}} + \sum_r \sum_a C_a^r \Phi_a^r + \sum_r \sum_a \sum_{s>r} \sum_{b>a} C_{ab}^{rs} \Phi_{ab}^{rs} \dots \quad (1.15)$$

where the first term is the ground-state Hartree-Fock wave function, the second term sums all single excitation configurations (over all occupied orbitals, a , to all unoccupied orbitals, r), the third term sums all unique double excitation configurations and so on. If we include all possible excitations, we call this method the full configuration interaction, and if paired with a complete basis set (infinite number of basis functions), this is the exact solution of the Schrödinger equation. Of course we cannot afford full CI calculations for large systems, so we must truncate CI to include just a few excitations, usually single and double excitations

1.5.2 Coupled Cluster

Another way to recover correlation energy is with the coupled cluster method.^{14,15} Using a cluster operator, \hat{T} , we can expand the Hartree-Fock wave function into a linear combination of excited determinants:

$$|\Phi^{\text{CC}}\rangle = e^{\hat{T}} \Phi^{\text{HF}} \quad (1.16)$$

The form of the cluster operator is:

$$\hat{T} = \hat{T}_1 + \hat{T}_2 + \hat{T}_3 + \dots + \hat{T}_N \quad (1.17)$$

where \hat{T}_1 is the operator which takes care of all single excitations, \hat{T}_2 takes care of double excitations, and so on. Much like CI, if we use N -tuple excitations up to the number of electrons in the system, N , we can get the exact wave function and exact energy, but we must trim the cluster operator for it to be computationally feasible in studies of large systems.

Additionally, choosing only up to double excitations generates a non-linear wave function and the method becomes non-variational. This means that the energy returned by a CC wave function can be either higher or lower than the exact energy.

A method proposed by Nakatsuji,¹⁶ Symmetry Adapted Cluster with Configuration Interaction (SAC-CI), implements both CC and CI formalisms, and will be used in Chapter 2 to better describe high-energy excitations.

1.5.3 Multiconfigurational Self-Consistent Field

In the above post-Hartree-Fock methods, using more than one determinant is important for including electron correlation and more accurate description of large systems overall, but in the expansion of the wave function we only vary the linear coefficients (C_0^{HF}, C_a^r, \dots) in Equation (1.15), to get better results while using the Hartree-Fock orbitals in the Slater determinants ($\Phi_0^{HF}, \Phi_a^r, \dots$). The next logical step would be to vary both the coefficients C and orbitals ϕ in a few select reference functions; this approach leads to the multiconfigurational self-consistent field^{17,18} (MCSCF) method. The form of the wave function is:

$$\Phi^{\text{MCSCF}} = \sum_{i=1}^N \Phi_i C_i \quad (1.18)$$

where Φ_i represents a Slater determinant that is based on an active space (allowed electron excitations within specified orbitals) that we define. Designing a good Φ^{MCSCF} requires chemical intuition to select an appropriate active space. If we selected all electrons and all orbitals to be within an active space, this would be analogous to full CI. For larger systems it is important to define an active space to include only important excitations to make computation feasible. Active space selection for tetrahedral P_4 will be studied in Chapter 3.

The active space can be partitioned to include only valence electrons, and if all excitations are allowed within the selected valence orbitals, we would generate a complete active space (CAS), which is defined in terms of the number of electrons in the number of molecular orbitals (e.g. six electrons in six orbitals). It can be partitioned further to include restricted active spaces¹⁹ (RAS) on either side of the complete active space, as shown in Figure 1.4. RAS1 is composed of occupied orbitals and is defined by the maximum number of holes allowed in this space. RAS3 can

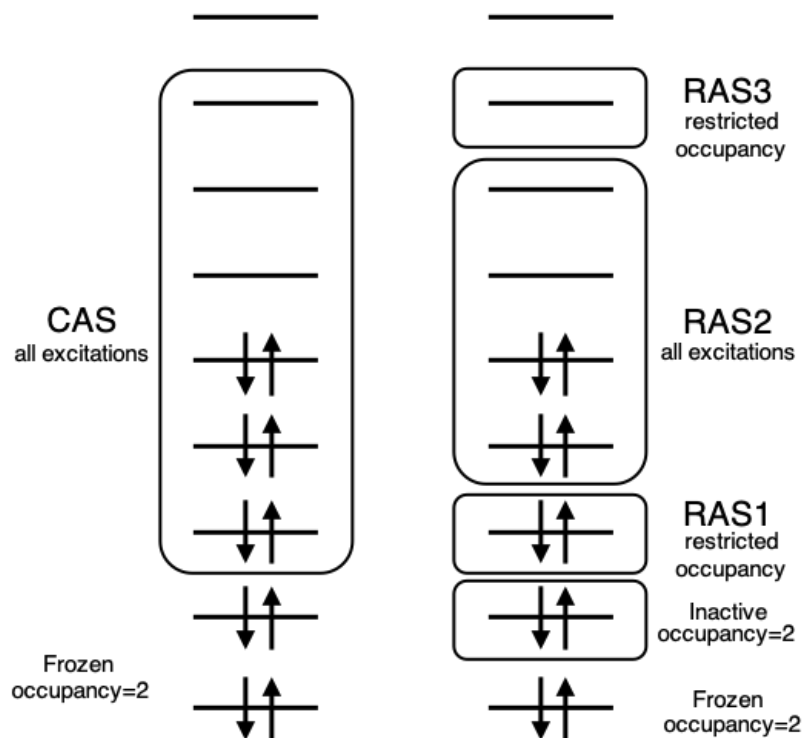


Figure 1.4: *Distribution of electrons in active space orbitals. On the left, the CASSCF wave function where the CAS allows all excitations within the orbitals circled. All other occupied molecular orbitals are frozen at the Hartree-Fock level. On the right is a representation of the RASSCF wave function, where the RAS2 space is equivalent to CAS, and all excitations are allowed within this space. The RAS1 space restricts the occupancy by specifying how many holes are allowed in that space at one time. Likewise, RAS3 occupancies are restricted by specifying how many electrons are allowed in that space at one time. The rest of the occupied orbitals below RAS1 must always have double occupancy, but can be partitioned into inactive (MC-SCF level) or frozen (Hartree-Fock level).*

allow excitations up to a predefined maximum number of electrons. Any orbitals below RAS1 can be specified as inactive or frozen, with the occupied inactive orbitals still varied in the SCF process, and frozen orbitals remaining at the Hartree-Fock level.

When studying the potential energy surface of an excited system, during the optimization process a state becomes lower in energy than another state, compared to what it was in a previous iteration, called the root-flipping problem. This makes keeping track of excited states complicated, and the state-average CASSCF^{20,21} (SA-CASSCF) method corrects for this by allowing optimization of energy and orbitals averaged over all states of interest.

While this method fixes the static correlation energy problem, the energy resulting from an MCSCF wave function does not include dynamical correlation. This can be included by adding a perturbative correction on top of this multiconfiguration method.

1.5.4 Møller-Plesset Perturbation Theory

By splitting the Hamiltonian into two parts, perturbation methods are used to get a better approximation to the total energy,

$$\hat{H} = \hat{H}^{(0)} + \hat{V}, \quad (1.19)$$

where $\hat{H}^{(0)}$ is the unperturbed, zeroth-order Hamiltonian defined in terms of the Hartree-Fock method and \hat{V} is the Møller-Plesset²² perturbation operator,

$$\hat{V} = \hat{H} - \hat{H}^{(0)}, \quad (1.20)$$

which is defined as the difference between the exact Hamiltonian and the Hartree-Fock Hamiltonian:

$$\hat{V} = \hat{V}(1, 2, \dots, N) = \sum_{l=1}^{N-1} \sum_{m>l}^N \frac{1}{r_{lm}} - \sum_{m=1}^N \sum_{a=1}^N [\hat{J}_a(m) - \hat{K}_a(m)] \quad (1.21)$$

The first term is the exact repulsion, the second is the mean-field repulsion from Hartree-Fock theory and the summation over l and m runs over N electrons while a

refers to the occupied spin orbitals. The most popular version of the Møller-Plesset approach, MP2, uses up to the second-order correction to add correlation energy, where the MP2 energy is:

$$E^{MP2} = E_{HF} + \sum_{k \neq 0} \frac{|\hat{V}_{k0}|^2}{E_0^{(0)} - E_k^{(0)}} \quad (1.22)$$

Since the Møller-Plesset method provides a correction for the Hartree-Fock wave function and energy, it will only be as good as the Hartree-Fock starting point. If the Hartree-Fock method cannot correctly describe a molecular system, chances are the Møller-Plesset approach will only be slightly better. Additionally, the Møller-Plesset method is not variational but will oscillate around the exact energy. Instead of using a Hartree-Fock reference wave function, we can use a CAS wave function, which can return some of the correlation energy that Hartree-Fock theory lacks. Some of the missing dynamical correlation is provided by adding second-order perturbation theory on top of the CAS wave function (CASPT2 method).^{23,24} State-specific CASPT2 (SS-CASPT2) is appropriate for energetically separated electronic states, but we need to take a different approach if there are any degeneracies. The Multi-state CASPT2 (MS-CASPT2) method couples all reference states after perturbation which gives a better description of potential energy surfaces near degenerate regions.²⁵ It is used in Chapter 3 to describe the excited state potential energy surface of P₄.

When there are low-lying excited states and the energies of the reference wave function and an intermediate state are almost equal, the denominator of Equation (1.23) becomes close to zero and can generate discontinuities along a potential energy surface, called intruder states. A shift parameter, Δ is added to the denominator to remedy this:²⁶

$$E^2 = \sum_{a < b} \sum_{r < s} \frac{\langle \Psi^{CAS} | \hat{V} | \Psi_{ab}^{rs} \rangle^2}{E^0 - E_{ab}^{rs} + \Delta}. \quad (1.23)$$

The CASPT2 method is extremely expensive to use, especially with a large basis set and active space, but the results are very accurate. If we have a large system, or the active space requires many electrons, it may be worth using a cheaper method

like time-dependent density functional theory to predict excitation energies.

1.5.5 Time-Dependent Density Functional Theory

Calculating excited states with quantum chemical methods is mostly outlined in the previous section. With wave function theory, instead of solving for the lowest energy solution, we can solve for whichever root is of interest. When using density functional theory, we must introduce a time-dependent external potential:

$$\left(-\frac{1}{2}\nabla^2 + \nu^{KS}(\mathbf{r}, t)\right) \Psi^{KS}(\mathbf{r}, t) = \varepsilon \Psi^{KS}(\mathbf{r}, t) \quad (1.24)$$

and the density is also time-dependent:

$$\rho(\mathbf{r}, t) = \sum_{i=1}^{N/2} |\phi^{KS}(\mathbf{r}, t)|^2 \quad (1.25)$$

The time-dependent density functional theory²⁷ creates an even more complicated exchange-correlation potential, but with an approximation we simplify the potential:

$$\nu_{XC}[\rho](\mathbf{r}, t) \approx \nu_{XC}[\rho(\mathbf{r}, t)] \quad (1.26)$$

so that only the density is time-dependent and the exchange correlation potential is the same as for the ground state.

1.5.6 Multiconfigurational Pair-Density Functional Theory

Combining multiconfigurational wave function theory with on-top pair density functional theory allows recovery of the dynamical correlation energy for multiconfigurational methods with little computational effort.

The pair density, Π , has the form:

$$\Pi(\mathbf{r}, \mathbf{r}) = \binom{N}{2} \int |\Phi^{CAS}(r_1, \sigma_1, \dots, r_N, \sigma_N)|^2 d\sigma_1 \dots d\sigma_N d\mathbf{r}_3 \dots d\mathbf{r}_N \quad (1.27)$$

which represents the probability of finding a pair of electrons near this point at the same time.

The multiconfigurational pair-density functional²⁸ (MC-PDFT) method evaluates the Coulomb and approximate kinetic energy from a multiconfigurational wave function, and all other energy terms are calculated with an on-top density functional, expressed in terms of the total density, $\rho(\mathbf{r})$, and on-top pair density, $\Pi(\mathbf{r})$. This is done to avoid double-counting the dynamic correlation energy, included with using many Slater determinants and with DFT. Along with accounting for both types of correlation energy, the cost of the calculation is reduced dramatically compared to similar methods like CASPT2. This method was used in Chapter 3 while studying the thermal decomposition of P_4 as a more computationally efficient alternative to the MS-CASPT2 approach.

1.6 Electronic Excited States

Electronic excited state chemistry involves the promotion of a ground-state chemical system to an excited state through the absorption of energy. There are many competing mechanisms that allow an excited state to return to a stable ground state, S_0 , the ground-state singlet.

Some de-excitation pathways release the extra energy in the form of luminescence. If the excited state is a singlet, the radiation is termed fluorescence (seen in the Jabłoński diagram, Figure 1.5). In some cases, the lowest singlet, S_1 and a triplet state, T_1 are close in energy and there is a possibility of intersystem crossing. This is a non-radiative pathway for an electron to move from the singlet to triplet state, and adopt the reverse spin. From the triplet state, the electron can fall back down to the ground state and emit light in the form of phosphorescence. This type of radiation is not likely to happen in systems with small spin-orbit coupling. Phosphorescence is often targeted by experimentalists because it involves a slow relaxation, making it easier to measure than fluorescence which is much quicker. Alternatively, internal conversion allows for a radiationless de-excitation process back down to the ground

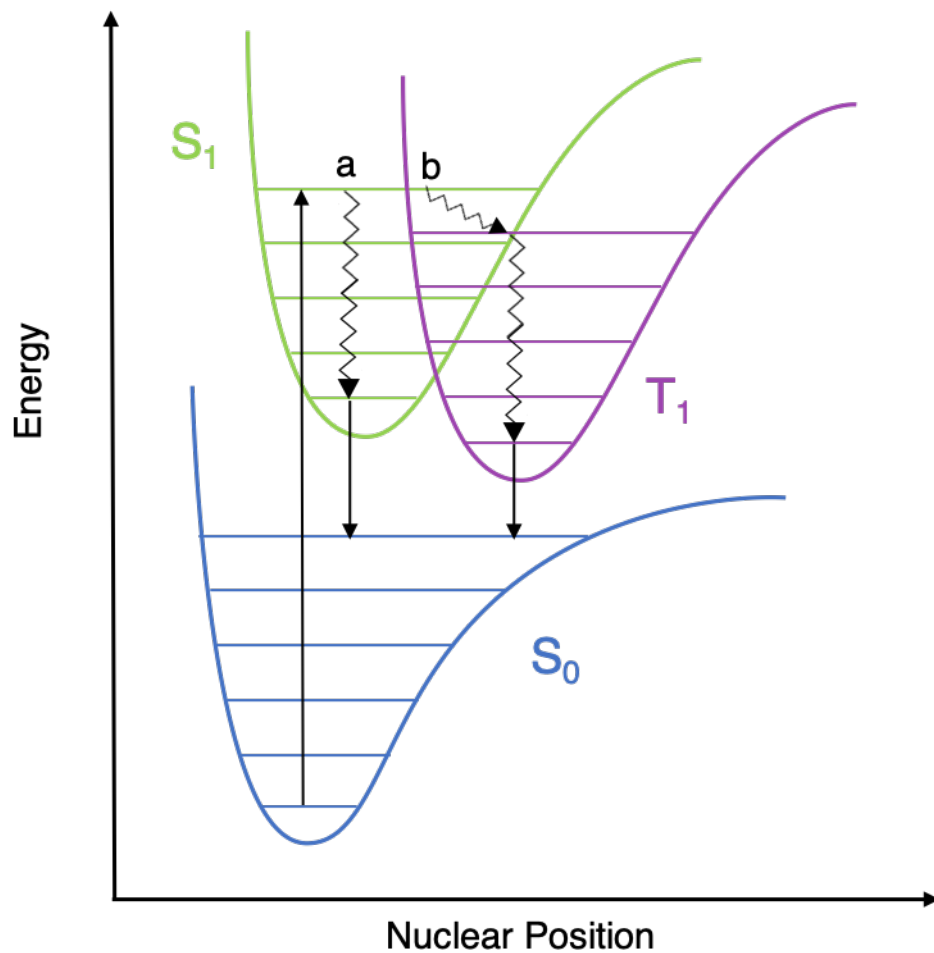


Figure 1.5: *The Jabłoński diagram depicts radiative and non-radiative pathways involved in excitations. Energy is absorbed in a vertical excitation by the ground-state molecule, S_0 , and ends up in an excited state, S_1 . De-excitation pathway a shows fluorescence, and pathway b shows phosphorescence through internal conversion. For both de-excitation pathways, the internal conversion to the lowest vibrational state is omitted for clarity.*

state.

The probability of an electronic transition taking place through the absorption of a single photon is measured by the oscillator strength, f , which related to the square of the transition dipole moment:

$$f_{if} = \frac{4m_e\pi\nu}{3e^2\hbar} |\langle \Phi_f | \mu | \Phi_i \rangle|^2 \quad (1.28)$$

where m_e is the mass of an electron, ν is the frequency of the transition, e is electron charge, and \hbar is the reduced Planck's constant. In the same equation, Φ_i is the initial and Φ_f is the final electronic state wave function.

If $f_{if} > 0$, the transition is called an allowed transition. The states must have the same spin for $f_{if} > 0$ (or we must include spin-orbit coupling). Selection rules dictate which transitions are allowed or forbidden and are different for different types of spectroscopy.

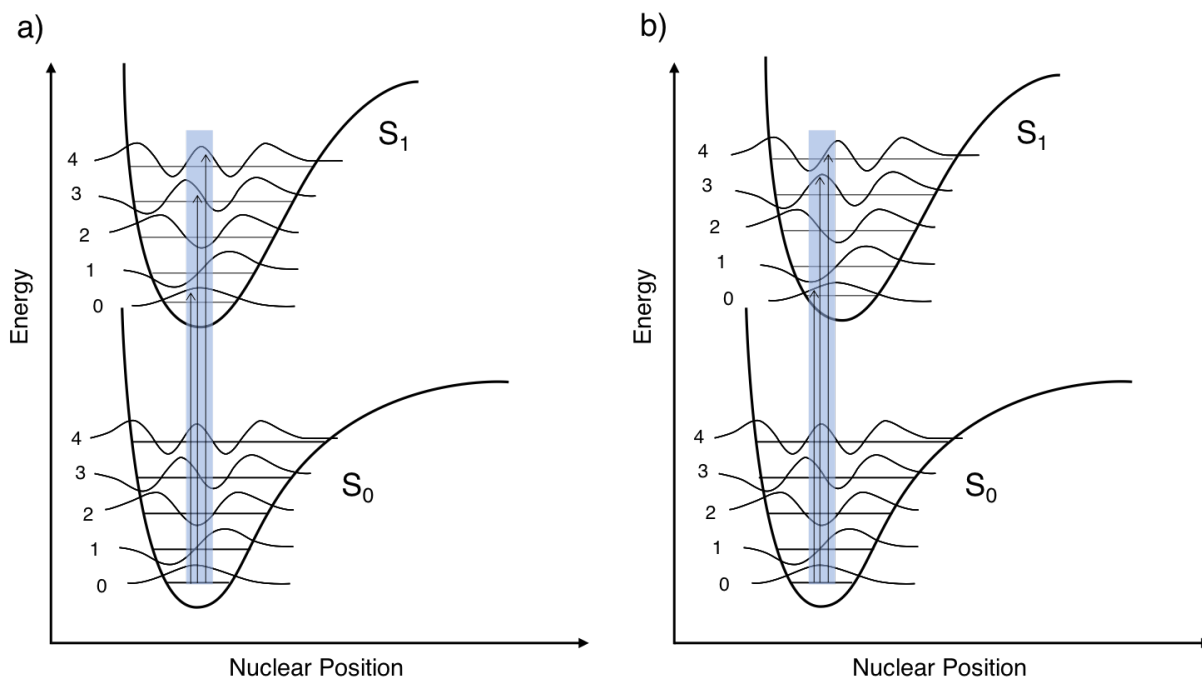


Figure 1.6: *The vibrational state wave function overlap predicts the intensity of the vertical transition: a) a good vibrational wave function overlap between ground state $v''=0$ and excited $v'=0, 2, \text{ and } 4$. b) a poor vibrational wave function overlap except for $v''=0$ and $v'=3$.*

Within each electronic level, there are many vibrational levels. Taking into account the Born-Oppenheimer approximation, with electrons moving much faster than nuclei, when the ground state system is excited the nuclear positions remain the same in the excited state for a brief time. After such vertical excitation, the system usually reaches a higher vibrational level than the lowest vibrational level, v'_0 , of the excited electronic state. The system then undergoes non-radiative vibrational rearrangement through the movement of nuclei and it finally arrives at the lowest energy vibrational level. The Franck-Condon Principle allows us to calculate the intensities of these vibronic transitions. The ground-state potential energy curve is shown lower in energy with the harmonic-oscillator wave functions overlaid on each of the vibrational levels. Each transition originates from the ground state electronic and vibrational level, and the overlap of the vibrational wave functions at initial and terminal points of a transition predicts the intensity of that transition. In Figure 1.6, the $v''=0$ to $v'=0$, 2 transitions shown on the left would have a larger intensities than the same two transitions shown on the right, while the $v''=0$ to $v'=4$ transition would have a larger intensity on the right.

1.7 Overview

Using the quantum chemistry methods introduced above, we aim to provide an understanding of experimental results, with a focus on electronic excited states. First, a study in modelling vacuum-ultraviolet visible spectra of small molecules is done to determine whether we can detect isomeric differences and capture high-energy transitions with efficient DFT and single-reference methods. Then, the thermal decomposition pathway of P_4 is calculated using multiconfigurational methods to provide insight into the stability of this molecule despite containing a high amount of ring strain. Afterwards, a new methodology was developed, with a balance of efficiency and accuracy in mind, to calculate high-energy excitations from core orbitals. Finally, the last chapter outlines the design of a selective and sensitive chemosensor for the detection of Hg^{2+} ions.

Chapter 2

Computing UV-Vis Spectra of 1-Bromo-1-Propene: A Comparison of Model Core Potential and All Electron Approaches^a

2.1 Introduction

Pseudopotentials have been used by chemists to increase computational efficiency by focusing on the chemically relevant valence electrons, with the effect of core electrons treated via a potential. This significantly reduced the number of basis functions and electrons explicitly defined, thus allowing for the study of large systems. The MCP method, developed by Huzinaga and coworkers,¹² is unique in that it retains the nodal structure of valence orbitals through a shift operator.

In the MCP approach, the one-electron operator $\hat{h}(\mathbf{r})$ is defined as:

$$\hat{h}(\mathbf{r}) = -\frac{1}{2}\nabla^2 - \frac{Z - N_c}{r} + V_{core}^{MCP}(\mathbf{r}) + \hat{\Omega}^{MCP}(\mathbf{r}) \quad (2.1)$$

where the first term defines the kinetic energy of electron i and the second term is the potential energy where the nucleus is screened by core electrons, N_c . The third term models the coulombic and exchange interaction between core and valence

^aThis chapter is adapted from the published paper *Can. J. Chem.*, **2017**, *95*, 627 - 631.

electrons. The fourth term is characteristic of the MCP method, as it maintains the orthogonality of the core and valence orbitals and prevents the valence orbitals from collapsing onto the core. The shift operator $\hat{\Omega}^{\text{MCP}}$ is defined as

$$\hat{\Omega}^{\text{MCP}}(\mathbf{r}) = \sum_{c=1}^{N_c} B_c |\bar{\phi}_c(\mathbf{r})\rangle \langle \bar{\phi}_c(\mathbf{r})|, \quad (2.2)$$

where $\bar{\phi}_c$ are the frozen core orbitals and B_c are constants. This operator shifts the core orbitals into virtual space while retaining their proper nodal features and ensures that the valence orbitals correspond to the lowest energy eigenvalues.

The MCP method reliably predicts many molecular properties;²⁹ however, its performance in predicting electronic excitations over a wide range of energies has not yet been thoroughly explored.^{30,31} In the present work we compare the results obtained using model core potentials to those calculated with all-electron basis sets in computing accurate vacuum UV-Vis (VUV) spectra. The molecule *trans*-1-bromo-1-propene (1B1P) was chosen for its small size and the inclusion of a heavy halogen, which will maximize the effect of the MCPs. Experimental spectra were provided by the Harynuk group at the University of Alberta, using a gas chromatograph with a vacuum ultra-violet (GC-VUV) detector attachment.³² This device can produce VUV spectra up to 12 eV, which poses challenges for current computational modelling of highly excited states.³³ While only the first few low-lying states may be accurately represented using current computational methods, we studied the extended spectral range in order to allow for comparison between different methods as well as the experimental GC-VUV spectra. Electronic excitations were computed using TD-DFT and compared to those obtained with our reference method, the Symmetry Adapted Cluster/Configuration Interaction method with single and double excitations³⁴ (SAC-CI SD-R). The density functionals chosen were compared to the best method to determine whether it is possible to generate satisfactory results using model core potential basis sets.

2.2 Computational Details

Gaussian 09 Revision E.01³⁵ was used to optimize the geometry of *trans*-1B1P at the MP2/6-311G++(d,p) level of theory and compute the electronic excitations with SAC-CI SD-R as the reference method. The singlet A' states and A'' states of the C_s symmetry were considered, and thirty states were calculated in each irreducible representation; these calculations were denoted as SAC-CI(30,30). Electric dipole excitations from the ground state $^1A'$ to both $^1A'$ and $^1A''$ states are allowed. The aug-cc-pVTZ (acct) basis set was used, with diffuse functions needed to capture the Rydberg and charge transfer states at high energies. Since SAC-CI SD-R is not yet available in any program that supports model core potentials, we are currently unable to directly investigate the effect of the MCPs when used with the SAC-CI approach. Instead, we relied on density functional theory as implemented in GAMESS-US³⁶ to carry out the comparison between the MCP and all-electron results. Two density functionals, CAM-B3LYP³⁷ and PBE0,³⁸ were selected based on previous benchmarking³⁹ as density functionals suitable for singlet excitations of small organic molecules. Although CAM-B3LYP was not selected as best overall,³⁹ it was important to include a long-range corrected functional designed to describe high energy transitions accurately. Electronic excitation energies were calculated using each functional and three basis sets. Results from all-electron calculations were compared to those obtained with the augmented triple- ζ basis set MCP-aTZP (amcp3), as well as a mixed basis set, where the MCP was used for the bromine atom only and all-electron basis sets were employed for carbon and hydrogen atoms (denoted as amcp3-Br).

2.3 Discussion

In order to compare the excitation energies obtained by the density functionals to our best method, first we defined six major peaks in the spectra of each functional and SAC-CI (see Figure 2.1). Each peak was analyzed in terms of excitation energies (ΔE), oscillator strength f , transitions and symmetry (see Tables 2.1-2.6).

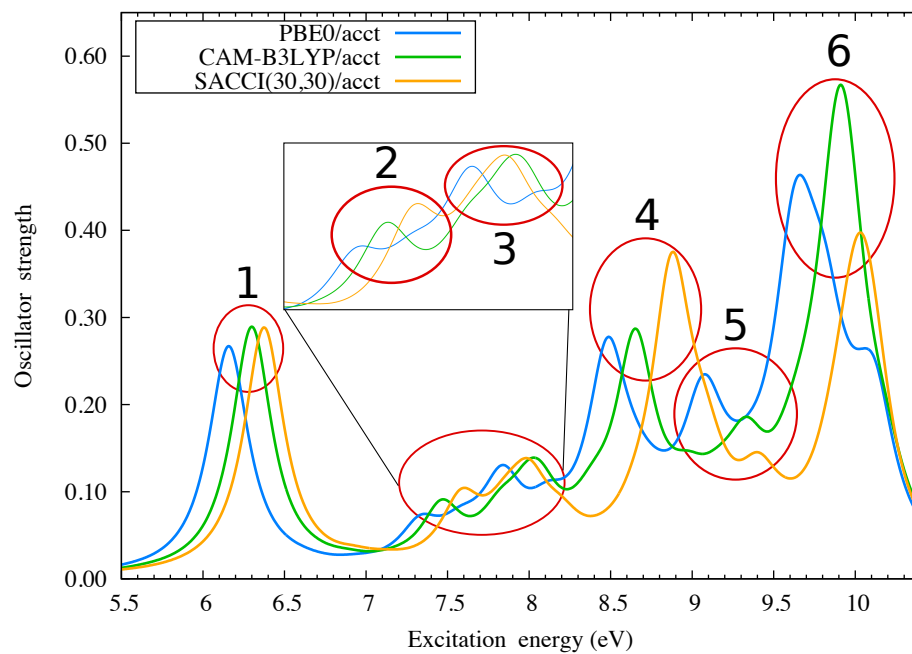


Figure 2.1: Labelling six major peaks on the electronic excitation spectra for CAM-B3LYP, PBE0 and SAC-CI with acct basis set. In simulating spectra from excitation energies and intensities we used Cauchy-Lorentz band shape with a 0.3 eV half-width.

Table 2.1: *trans-1B1P: Analysis of Major Peak #1*

Level of theory	$\Delta E^{(a)}$	$\Delta\Delta E^{(b)}$	$f^{(c)}$	Transition ^(d)	Symmetry ^(e)
SAC-CI(30,30)/acct	6.37	0.00	0.251	H → L+6	$a'' \rightarrow a''$
CAM-B3LYP/acct	6.30	-0.07	0.290	H → L+3	$a'' \rightarrow a''$
PBE0/acct	6.16	-0.21	0.258	H → L	$a'' \rightarrow a''$
CAM-B3LYP/amcp3	6.30	-0.07	0.284	H → L+4	$a'' \rightarrow a''$
PBE0/amcp3	6.19	-0.18	0.255	H → L+1	$a'' \rightarrow a''$
CAM-B3LYP/amcp3-Br	6.33	-0.04	0.276	H → L+4	$a'' \rightarrow a''$
PBE0/amcp3-Br	6.19	-0.18	0.255	H → L	$a'' \rightarrow a''$

^(a) excitation energy (in eV); ^(b) deviation from the reference SAC-CI(30,30)/acct value; ^(c) oscillator strength; ^(d) major contribution to the transition: H = HOMO, L = LUMO; ^(e) symmetry of the molecular orbitals involved

In the Tables, all excitation energies ΔE are in eV; the values in the following column are the deviations from the reference excitation energy, $\Delta\Delta E = \Delta E(M) - \Delta E[\text{SAC-CI}(30,30)]$, where the method M = CAM-B3LYP or PBE0.

2.3.1 Major Peaks #1 and #2

Both functionals produce satisfactory results with respect to SAC-CI. As seen in Tables 2.1 and 2.2, CAM-B3LYP produces excitation energies within at most 0.12 eV while PBE0 is within 0.26 eV, which are both good comparisons. The amcp3-Br basis set gives the most accurate excitation energy for the first peak. The oscillator strengths are similar for all states, with PBE0 results deviating the most with respect to SAC-CI. Since peaks #1 and #2 are the lowest lying transitions, it is expected that they would be the most accurately computed. Each method predicted a $\pi \rightarrow \pi^*$ transition (with $a'' \rightarrow a''$ symmetry) for the first peak, which produced a ${}^1A'$ final state. Regarding the second peak, each method predicted a $\sigma \rightarrow \sigma^*$ transition (with $a' \rightarrow a'$ symmetry) and the ${}^1A'$ final state.

Table 2.2: *trans-1B1P: Analysis of Major Peak #2^(a)*

Level of theory	ΔE	$\Delta\Delta E$	f	Transition	Symmetry
SAC-CI(30,30)/acct	7.58	0.00	0.070	H-1 \rightarrow L+2	$a' \rightarrow a'$
CAM-B3LYP/acct	7.46	-0.12	0.064	H-1 \rightarrow L+2	$a' \rightarrow a'$
PBE0/acct	7.33	-0.25	0.043	H-1 \rightarrow L+2	$a' \rightarrow a'$
CAM-B3LYP/amcp3	7.46	-0.12	0.066	H-1 \rightarrow L+1	$a' \rightarrow a'$
PBE0/amcp3	7.32	-0.26	0.044	H-1 \rightarrow L+2	$a' \rightarrow a'$
CAM-B3LYP/amcp3-Br	7.46	-0.12	0.064	H-1 \rightarrow L+1	$a' \rightarrow a'$
PBE0/amcp3-Br	7.32	-0.26	0.044	H-1 \rightarrow L+2	$a' \rightarrow a'$

^(a) see Table 2.1 for definition

2.3.2 Major Peak #3

This peak is made up of two major components: a main peak and a small shoulder peak at a higher energy. Each entry in Table 2.3 has two values to reflect this: the first is the main peak (a) and the second is the shoulder (b). Once again, CAM-B3LYP outperforms PBE0, with deviation ≤ 0.17 eV. In some cases, PBE0 produces excitation energies with a large error of almost 0.5 eV. Oscillator strength is generally underestimated for the main peak and overestimated for the shoulder peak. Interestingly, the amcp3-Br basis set brings about more accurate excitation energy than a full MCP basis, with respect to the reference method. In this case, the transition symmetries and final excited state differ for each method. The reference method gives a final state of ${}^1A'$ for the main peak (a) and a $\pi \rightarrow \pi^*$ transition, while other methods give $\pi \rightarrow \sigma^*$ or $\sigma \rightarrow \sigma^*$ transitions. For the shoulder peak (b), the reference method predicts a ${}^1A''$ final state and a $\pi \rightarrow \sigma^*$ transition, while other methods give $\pi \rightarrow \pi^*$ or $\sigma \rightarrow \sigma^*$ transitions. These discrepancies are most likely due to overlapping states and the complex nature of this peak.

Table 2.3: *trans-1B1P: Analysis of Major Peak #3^(a)*

Level of theory	ΔE	$\Delta\Delta E$	f	Transition	Symmetry
SAC-CI(30,30)/acct	a) 8.00	0.00	0.072	H \rightarrow L+8	$a'' \rightarrow a''$
	b) 8.20	0.00	0.030	H-1 \rightarrow L+1	$a'' \rightarrow a'$
CAM-B3LYP/acct	a) 7.99	-0.01	0.037	H \rightarrow L+9	$a'' \rightarrow a''$
	b) 8.06	-0.14	0.056	H-1 \rightarrow L+1	$a' \rightarrow a'$
PBE0/acct	a) 7.83	-0.17	0.053	H \rightarrow L+8	$a'' \rightarrow a''$
	b) 8.12	-0.08	0.041	H-2 \rightarrow L	$a'' \rightarrow a''$
CAM-B3LYP/amcp3	a) 7.83	-0.17	0.037	H \rightarrow L+7	$a'' \rightarrow a''$
	b) 8.07	-0.13	0.036	H-1 \rightarrow L+2	$a' \rightarrow a'$
PBE0/amcp3	a) 7.86	-0.14	0.026	H-1 \rightarrow L+4	$a' \rightarrow a'$
	b) 8.12	-0.08	0.029	H-2 \rightarrow L+1	$a'' \rightarrow a''$
CAM-B3LYP/amcp3-Br	a) 7.87	-0.13	0.042	H \rightarrow L+7	$a'' \rightarrow a''$
	b) 8.08	-0.12	0.037	H-1 \rightarrow L+2	$a' \rightarrow a'$
PBE0/amcp3-Br	a) 7.88	-0.12	0.024	H-1 \rightarrow L+4	$a' \rightarrow a'$
	b) 8.08	-0.12	0.014	H-3 \rightarrow L+11	$a'' \rightarrow a''$

^(a) see Table 2.1 for definition**Table 2.4:** *trans-1B1P: Analysis of Major Peak #4^(a)*

Level of theory	ΔE	$\Delta\Delta E$	f	Transition	Symmetry
SAC-CI(30,30)/acct	8.87	0.00	0.320	H-2 \rightarrow L+6	$a'' \rightarrow a''$
CAM-B3LYP/acct	8.65	-0.22	0.240	H \rightarrow L+11	$a'' \rightarrow a''$
PBE0/acct	8.48	-0.39	0.223	H \rightarrow L+11	$a'' \rightarrow a''$
CAM-B3LYP/amcp3	8.63	-0.24	0.286	H \rightarrow L+12	$a'' \rightarrow a''$
PBE0/amcp3	8.51	-0.36	0.256	H \rightarrow L+12	$a'' \rightarrow a''$
CAM-B3LYP/amcp3-Br	8.63	-0.24	0.275	H-2 \rightarrow L+3	$a'' \rightarrow a'^{(b)}$
PBE0/amcp3-Br	8.46	-0.41	0.261	H-2 \rightarrow L	$a'' \rightarrow a''$

^(a) see Table 2.1 for definition ^(b) final state has $^1A''$ symmetry

Table 2.5: *trans-1B1P: Analysis of Major Peak #5^(a)*

Level of theory	ΔE	$\Delta\Delta E$	f	Transition	Symmetry
SAC-CI(30,30)/acct	9.41	0.00	0.044	H-3 \rightarrow L	$a' \rightarrow a'$
CAM-B3LYP/acct	9.32	-0.10	0.053	H-1 \rightarrow L+8	$a' \rightarrow a'$
PBE0/acct	9.06	-0.35	0.102	H-3 \rightarrow L+1	$a' \rightarrow a'$
CAM-B3LYP/amcp3	9.27	-0.14	0.101	H-3 \rightarrow L	$a' \rightarrow a'$
PBE0/amcp3	9.01	-0.40	0.115	H-3 \rightarrow L	$a' \rightarrow a'$
CAM-B3LYP/amcp3-Br	9.33	-0.08	0.092	H-3 \rightarrow L	$a' \rightarrow a'$
PBE0/amcp3-Br	9.06	-0.35	0.124	H-3 \rightarrow L+1	$a' \rightarrow a'$

^(a) see Table 2.1 for definition

2.3.3 Major Peaks #4 and #5

The excitation energies for peak #4 and #5 predicted by CAM-B3LYP differ by, at most, 0.24 eV compared to SAC-CI reference calculations, as seen in Tables 2.4 and 2.5. For both density functionals, amcp3-Br gives more accurate results with respect to SAC-CI compared to all-electron basis sets. A much higher deviation is seen with PBE0, up to 0.41 eV, illustrating that the long-range corrected functional is more accurate when describing high energy transitions, especially when they have charge-transfer or Rydberg character.⁴⁰ The values of the lambda diagnostic in each calculation predict the spatial orbital overlap, with a small lambda diagnostic value representing a small overlap. Since Rydberg states are so diffuse they have a much smaller spatial overlap, and therefore small lambda values ($0.08 \leq \Lambda \leq 0.27$).⁴⁰ The charge transfer states cover a much broader range of lambda values, and it is difficult to determine these states from the lambda value only. The values for peak 4 are between 0.43 and 0.51 for each method and between 0.19 and 0.44 for peak 5, which suggests that these transitions may have some charge-transfer character, but are not Rydberg. The oscillator strength for these two peaks was severely overestimated by both functionals, with respect to the reference method. All excited states from each method represent $a' \rightarrow a'$ transitions, and produce a final excited state with $^1A'$

symmetry, except for CAM-B3LYP/amcp3-Br in peak 4 (see Table 2.4).

2.3.4 Major Peak #6

This peak is made up of two major states within 0.10 eV with approximately equal oscillator strength. CAM-B3LYP is able to reproduce this character, as determined by SAC-CI results, but overestimates oscillator strength compared to the reference method, as seen in Table 2.6. CAM-B3LYP underestimates excitation energy by up to 0.30 eV. PBE0 also overestimates oscillator strength, but significantly underestimates excitation energy by up to 0.45 eV, once again showing that long-range corrected functionals more accurately describe high excitation energies than non-corrected functionals. All methods predict an a' to a' transition to give a final excited state of $^1A'$ symmetry. The amcp3-Br basis set gives results comparable to the all-electron basis set, more so than the full amcp3 basis.

The GC-VUV absorption detector used by the Harynuk group is able to transmit wavelengths between 109 nm and 240 nm (between 5 eV and 12 eV).³² The computed spectral range between 10 and 12 eV is troublesome, as seen in Figure 2.2. Although the spectrum for both functionals are similar, neither results are close to what is produced with SAC-CI.

Rydberg states that occur at high energies are not well described by the present methods. To gain more insight into the nature of computed spectra in this range, Figure 2.3 shows contributions from individual excitations to the full spectrum obtained at the CAM-B3LYP/acct level of theory (similar results obtained with the PBE0 functional). A legend for the individual contributions can be seen in the appendix (Figure A1). At low energies, the number of states that contribute to each peak is much smaller. The lowest energy transition involves two major states with varying oscillator strengths. The next few peaks (#2 and #3) are made of a combination of 3 or 4 states. However, in the 9 – 12 eV range, the number of states under each peak drastically increases. It should also be noted that the oscillator strength of each transition is much smaller and they combine to produce large intensity peaks. Since TD-DFT is known to be accurate for only low-lying transitions, it is probable that

Table 2.6: *trans-1B1P: Analysis of Major Peak #6^(a)*

Level of theory	ΔE	$\Delta\Delta E$	f	Transition	Symmetry
SAC-CI(30,30)/acct	a) 10.01	0.00	0.141	H-3 \rightarrow L+2	$a' \rightarrow a'$
	b) 10.11	0.00	0.122	H-4 \rightarrow L	$a' \rightarrow a'$
CAM-B3LYP/acct	a) 9.89	-0.12	0.279	H-3 \rightarrow L+2	$a' \rightarrow a'$
	b) 9.93	-0.18	0.152	H-3 \rightarrow L+1	$a' \rightarrow a'$
PBE0/acct	a) 9.68	-0.33	0.104	H-3 \rightarrow L+3	$a' \rightarrow a'$
	b) 9.81	-0.30	0.094	H-3 \rightarrow L+4	$a' \rightarrow a'$
CAM-B3LYP/amcp3	a) 9.82	-0.29	0.295	H-3 \rightarrow L+1	$a' \rightarrow a'$
	b) 9.91	-0.20	0.128	H-1 \rightarrow L+11	$a' \rightarrow a'$
PBE0/amcp3	a) 9.58	-0.43	0.211	H-3 \rightarrow L+2	$a' \rightarrow a'$
	b) 9.66	-0.45	0.109	H-3 \rightarrow L+3	$a' \rightarrow a'$
CAM-B3LYP/amcp3-Br	a) 9.83	-0.18	0.306	H-3 \rightarrow L+1	$a' \rightarrow a'$
	b) 9.92	-0.19	0.141	H \rightarrow L+5	$a' \rightarrow a'$
PBE0/amcp3-Br	a) 9.59	-0.42	0.244	H-4 \rightarrow L+1	$a' \rightarrow a'$
	b) 9.68	-0.43	0.096	H-3 \rightarrow L+3	$a' \rightarrow a'$

^(a) see Table 2.1 for definition

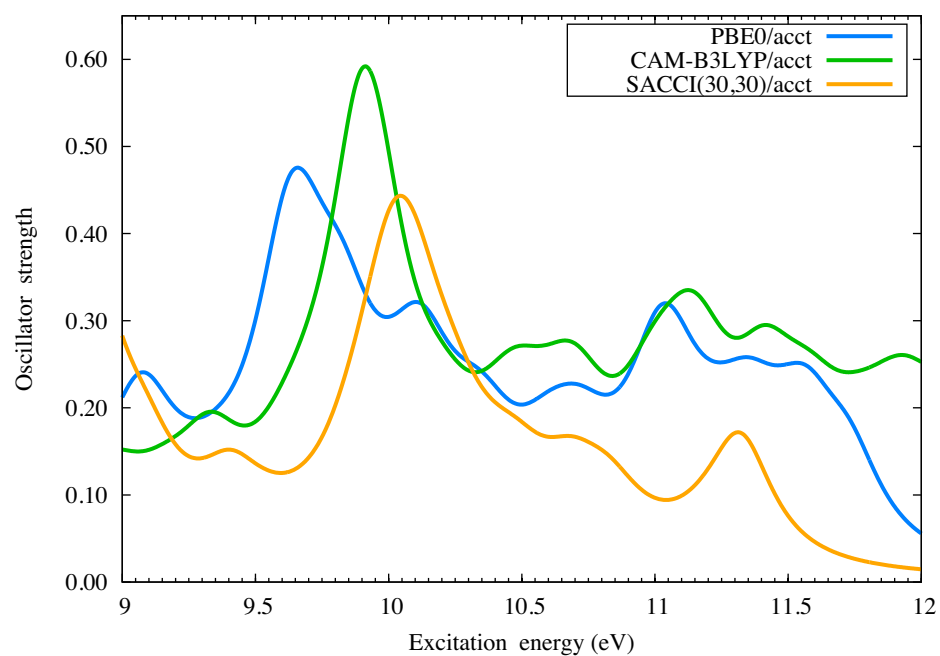


Figure 2.2: *Computed excitation energies for the 9 to 12 eV spectral range using the acct basis set.*

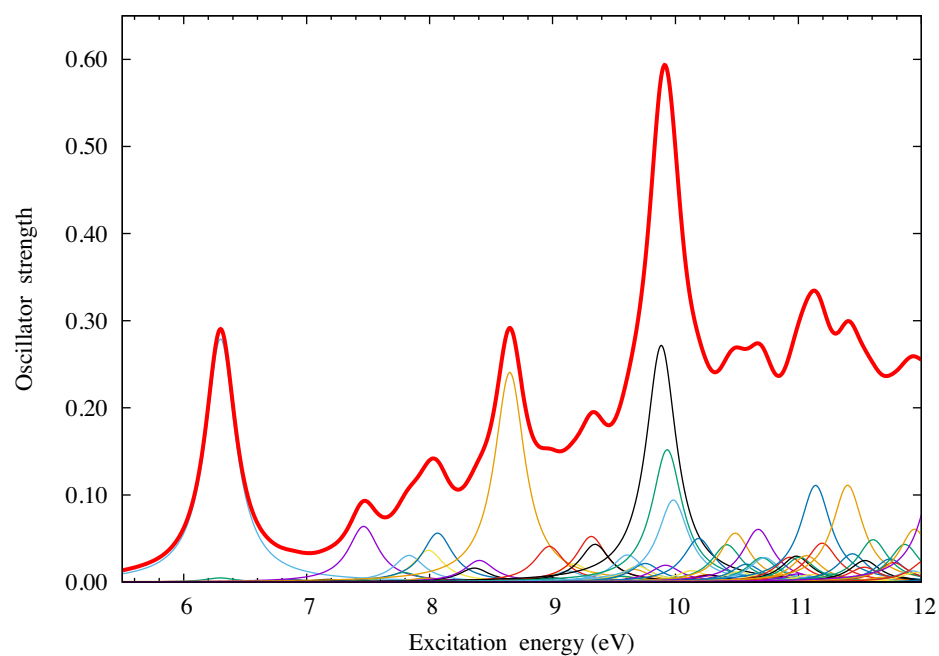


Figure 2.3: Contributions from individual states explicitly shown for results from CAM-B3LYP/acct.

many of these high excitation energies are underestimated and oscillator strengths are overestimated, as seen in the tables above. A small error in each of the transitions can build up and produce a much larger error, and the intense, high-energy peaks become unreliable.

2.3.5 Comparison with Experimental Spectra

The experimental spectrum was compared to the best methods, SAC-CI(30,30)/acct and CAM-B3LYP/amcp3 in Figure 2.4. The first computed peak is shifted slightly lower in energy than the experimental, but is still within 0.3 eV. The second experimental peak is not reproduced at all with either CAM-B3LYP or SAC-CI. This peak could possibly be multireference in character which neither of the computational methods employed here are capable of handling. The rest of the peaks slightly resemble the shape of the experimental spectrum, but with much lower intensities.

The *cis* isomer of 1B1P has similar energy and the experimental isomerization reaction barrier heights are fairly low: 0.23 kcal/mol for *cis* \rightleftharpoons *trans* and 2.21 kcal/mol for *trans* \rightleftharpoons *cis*.⁴¹ It is likely that over time, some of the *trans*-1-bromo-1-propene converted to *cis*-1-bromo-1-propene. The electronic excitation spectrum was calculated for the *cis* isomer, with all methods used previous, and compared to *trans*-1B1P. A similar analysis of the major peaks of *cis*-1B1P with SAC-CI and TD-DFT is included in Appendix A. The major peaks are identified in Figure A1, the decomposition of major peaks is in Tables A1 - A4, and comparison of calculated spectra to experiment is in Figure A2. The same conclusion was reached with *cis*-1B1P: CAMB3LYP/amcp3 produces the lowest $\Delta\Delta E$ with respect to SAC-CI.

The next logical step is to include the *cis*-1B1P spectra in the comparison to experiment. The overlap of spectra produces the second peak that every other method was missing, albeit shifted to a lower energy. The average of these plots was calculated for several weights and the best fit was 70% *trans*- and 30% *cis*-1-bromo-1-propene, with the oscillator strengths multiplied by a scaling factor of 1.5. Figures 2.5 and 2.6 show averaged spectra for SAC-CI/acct and CAM-B3LYP/amcp3-Br, respectively.

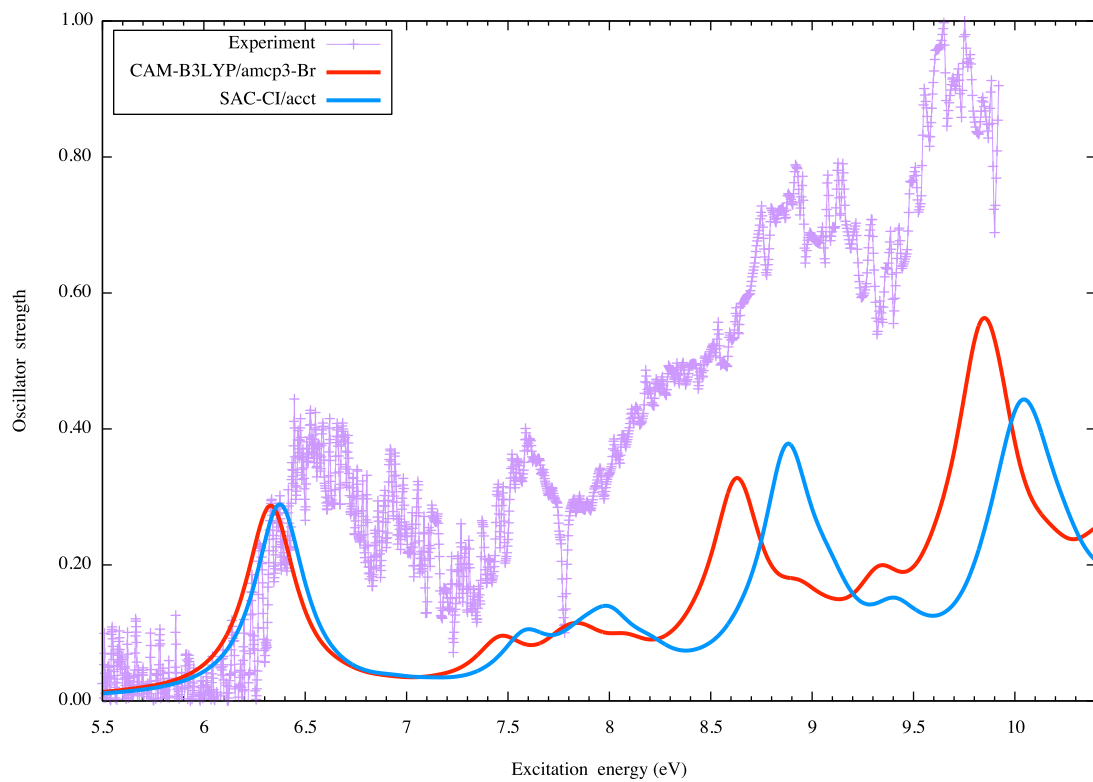


Figure 2.4: *Experimental spectrum compared to computed electronic excitations of trans-1B1P with SAC-CI(30,30)/acct and CAM-B3LYP/amcp3-Br.*

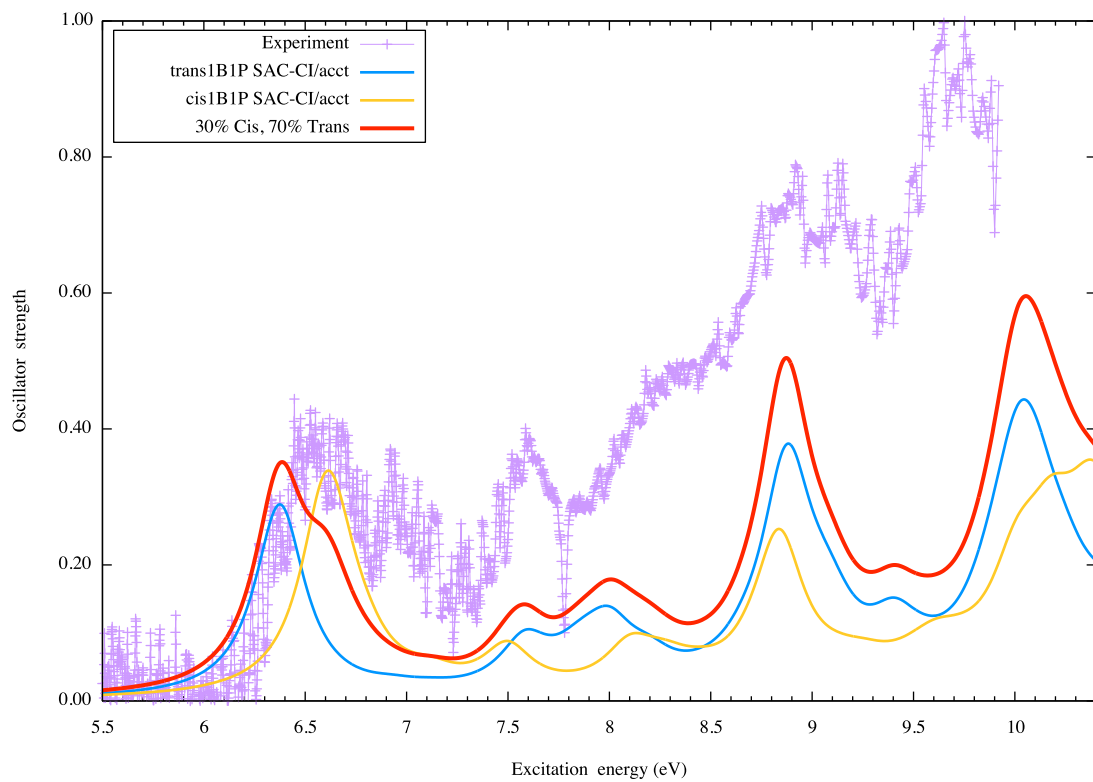


Figure 2.5: *Weighted calculated spectra of trans-1B1P and cis-1B1P with SAC-CI/acct compared to experimental spectrum.*

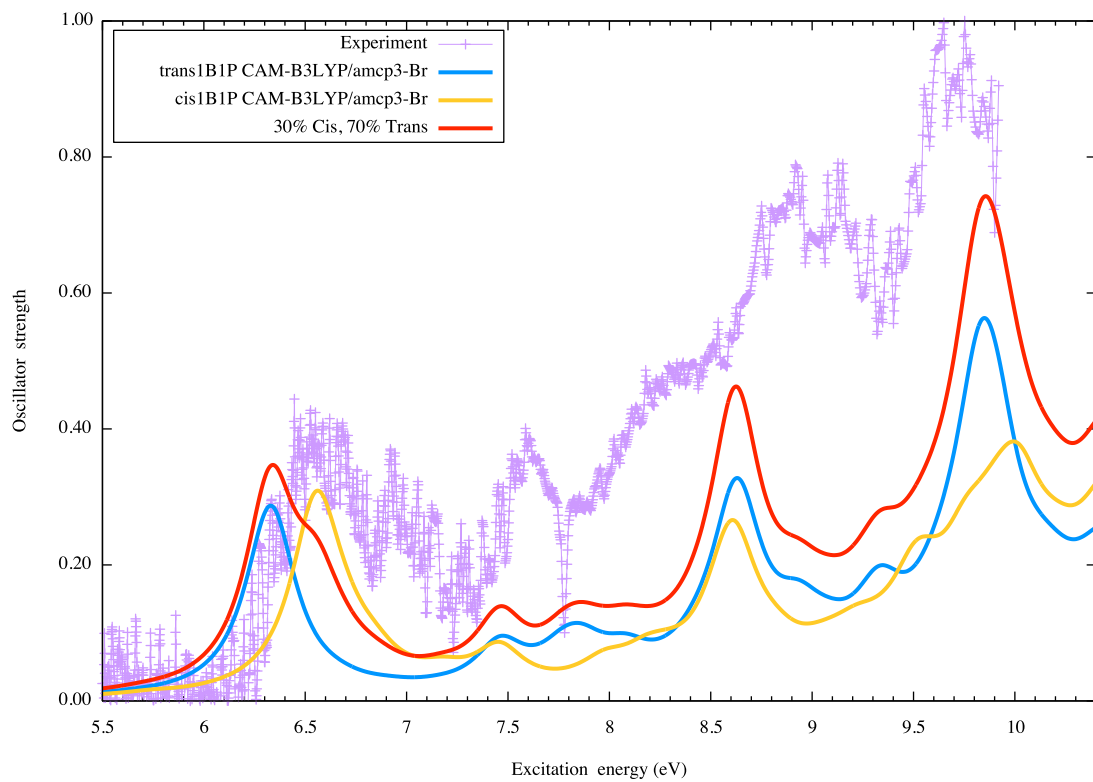


Figure 2.6: *Weighted calculated spectra of trans-1B1P and cis-1B1P with CAM-B3LYP/amcp3-Br compared to experimental spectrum.*

2.4 Conclusion

The CAM-B3LYP functional was found to be the most accurate one for all major peaks analyzed. Interestingly, the amcp3-Br basis set produces equally, or, in some cases, more accurate excitation energies than the all-electron basis set with respect to the SAC-CI results. Both density functionals produced unpredictable oscillator strengths with respect to experiment, although they were similar to the reference method at lower energies. The PBE0 functional was much less accurate compared to the reference method, sometimes underestimating excitation energies by 0.5 eV and significantly overestimating oscillator strengths. Symmetries and orbital excitations for each peak varied by method and were similar in most cases. Orbital excitation inconsistencies may be attributed to the nonuniform orbital ordering in the virtual space between density functionals and SAC-CI. This study shows it is important to consider long-range corrected functionals to accurately represent both low- and high-lying excited transitions, especially to capture Rydberg states, for computing VUV spectra. The 10-12 eV spectral range was considered problematic due to the amount of overlapping, small intensity peaks, and both density functionals were unreliable in this region. Most importantly, experimental spectra containing mixtures of isomers can be satisfactorily reproduced at lower excitation energies with both SAC-CI and CAM-B3LYP.

Chapter 3

Multireference Methods for Calculating the Dissociation Enthalpy of Tetrahedral P_4 to Two P_2 ^a

3.1 Introduction

Although elements within a group of the periodic table have similar valence electron configurations, the elements of Group 15 have drastically different lowest-energy structures. The most common form of nitrogen is N_2 , whereas P_2 is the least stable form of phosphorus.⁴² Tetrahedral P_4 is well known⁴³ and has been extensively studied theoretically to learn about the structure and stability of this allotrope. Tetranitrogen, N_4 , has been experimentally detected with neutralization-reionization mass spectrometry in a structure that is not a dimer or van der Waals molecule, but the actual structure was not experimentally determined.⁴⁴

Theoretical work has shown tetrahedral P_4 (white phosphorus) is a stable allotrope, although high in energy,⁴⁵ probably due to the significant amount of ring strain expected within a tetrahedral structure. Kutzelnigg⁴⁶ hypothesized that the reason for the contrasting structures of nitrogen and phosphorus is the difference in the valence orbital radii. The 2s and 2p valence orbitals of nitrogen occupy similar

^aThis chapter is adapted from the published paper *J. Phys. Chem. A*, **2018**, *122*, 5742-5749.

space, but in heavier atoms, the p orbitals are significantly more diffuse than the s orbitals. This difference is apparently large enough to stabilize the tetrahedral structure of P_4 . Since the valence orbitals in N_4 have a similar radius, the repulsion between atomic orbitals on each nitrogen atom in a possible tetrahedral N_4 molecule would be much larger than what would be expected in P_4 .

Bock and Müller⁴⁷ used semiempirical methods to calculate the potential energy hypersurface of the $P_4 \rightarrow 2P_2$ reaction, and Schmidt and Gordon⁴⁸ have used similar methods to calculate the stability of P_2 , tetrahedral P_4 , and cubic P_8 structures. Harworth and Bacskay⁴⁹ calculated heats of formation of various phosphorus compounds with more advanced computational methods, but concluded that their methods cannot describe the P-P bonding within P_2 and P_4 . Jerabek and Frenking⁵⁰ explored the unusual bonding in P_4 by energy decomposition analysis and compared it with analogous nitrogen-based compounds to explain the stability of the tetrahedral structure. Karton and Martin⁵¹ calculated accurate thermochemical data for P_2 and P_4 with the high-accuracy W4 thermochemistry protocol.⁵² Recently, the photolytic decomposition pathway has been reported by Wang et al.,⁵³ however, the thermal decomposition mechanism has not yet been widely investigated with advanced computational methods.

At high temperatures (above 1100 K)⁵⁴ tetrahedral P_4 decomposes to two diphosphorus molecules. In this chapter we calculate the enthalpy of reaction for the $P_4 \rightarrow 2P_2$ dissociation in order to evaluate computational performance of two multireference methods for thermochemical modelling and to assess the reliability of the model core potential methodology.

3.2 Computational Details

The equilibrium distances of P_2 and P_4 were calculated by quadratically fitting the lowest three points in a series of geometries with various bond lengths. Symmetry constraints are used so that the energy only depends on the bond length, where P_4 was optimized in T_d symmetry (note that the symmetry constraint to optimize

the bond length is different from the symmetry used in computing the energies), and P_2 was optimized in C_{2v} symmetry. Both CASPT2 and MC-PDFT calculations were performed to find the equilibrium distances, and both of them used the ground state wave function from a CASSCF calculation as the reference. For the MC-PDFT calculations, we used the translated PBE (tPBE) on-top density functional.

A potential energy curve for the thermal decomposition of tetrahedral P_4 was calculated by pulling the two P_2 subunits apart while maintaining C_{2v} symmetry. Two different potential energy curves were calculated. The first was done by increasing the distance $R(P_2-P_2)$ between the centres of the bonds in the P1-P2 and P3-P4 fragments, as shown in Figure 3.1, where the P atoms are designated as P_n , with $n = 1-4$. The second one was less rigid, and for each $R(P_2-P_2)$ value, the P1-P2 and P3-P4 distances are optimized.

A key issue in treating bond-breaking processes is whether one can employ a single-reference method or whether a multireference treatment is required. In exploratory work, calculations of dissociation potential curves were performed using single-reference methods, specifically CISD, several variants of coupled cluster (CC) methodology,^{55,56} and Kohn-Sham density functional theory (KS-DFT); however, these methods did not provide a good description of the reaction barrier (see Figure B1 in Appendix B). We conclude from these calculations that single-reference methods, with up to quasiperturbative quadruple excitations, are not appropriate for describing the $P_4 \rightarrow 2P_2$ bond-breaking processes, and therefore we will consider only multireference calculations.⁵⁷

All complete active space calculations were carried out by Molcas 8.0, and the MC-PDFT calculations were carried out with Molcas 8.2.⁵⁸ The dissociation curve was computed with SA-CASSCF and MS-CASPT2, and was carried out for the ground and first excited state. The SA-CASSCF wave function was used as a reference state because this yields a smoother potential curve than is obtained by state-specific CASSCF. To obtain good convergence of the state-averaged calculation, the first root was weighted 0.8 and the second was weighted 0.2. The MC-PDFT method was also used to calculate the potential energy surface, with the tPBE on-top density

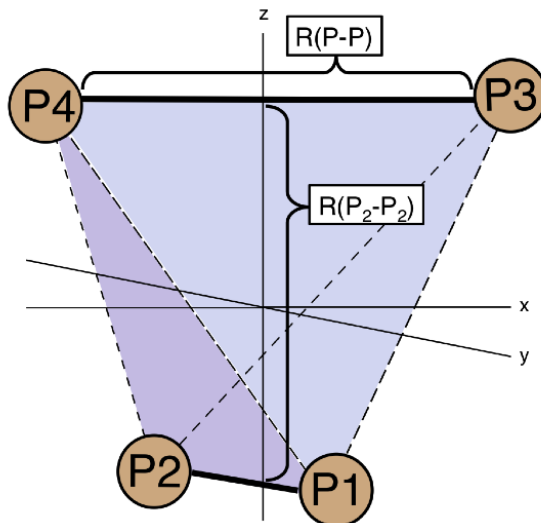


Figure 3.1: Tetrahedral P_4 structure and coordinate system for calculating the potential energy hypersurface of the dissociation of P_4 .

functional.

Two active spaces⁵⁹ were used in finding the equilibrium geometries and the reaction enthalpy. We used C_{2v} symmetry, and the active space labels refer to the number of each orbitals belonging to a specific irreducible representation in the order (a_1, b_1, b_2, a_2) . The first active space, (4332), distributes 12 electrons into the twelve 3p-like molecular orbitals. The hybridization of the σ P-P bonds in P_4 is $s^{0.05}p^{0.93}$, but the hybridization of the σ P-P bonds in P_2 has substantially more s character, $s^{0.21}p^{0.78}$.⁴⁹ To improve the description of the changing bond character, a second active space, denoted (6442), was used, distributing 20 electrons in 16 molecular orbitals. To find how the ionization-potential-electron-affinity (IPEA) shift⁶⁰ affects the equilibrium distance in MS-CASPT2 calculations, both IPEA equal to 0.25 hartrees and IPEA equal to 0 hartrees were tested for P_2 . For calculating reaction enthalpies, the MS-CASPT2 calculations were done with a non-default IPEA shift of zero because this reduced problems due to intruder states. Twenty orbitals are frozen for all MS-CASPT2 calculations, distributed as (8552).

The equilibrium geometries are calculated using all-electron basis sets, from cc-

pVTZ to cc-pV5Z⁶¹ and from cc-pV(T+d)Z to cc-pV(5+d)Z,⁶² and for the potential energy curve calculations we also tried the cc-pVDZ basis set. Basis set with diffuse functions (aug-cc-pV5Z) was used to study how diffuse functions affect the equilibrium distance of P₂. The cc-pV(X+d)Z basis sets were tested to see if the addition of tight d polarization functions will better describe the valence electrons and speed up convergence with larger basis sets.

To reduce computational cost by describing core electrons with a potential, we also performed calculations with two basis sets designed for use with model core potentials, non-relativistic MCP-DZP and MCP-TZP.⁶³ These basis sets differ in their polarization/correlating spaces: MCP-DZP employs a single contracted set of three primitive d subshells; and MCP-TZP uses two d subshells (one a three-term contracted one and the other uncontracted) and one contracted f subshell, and their polarization and correlating functions were designed to mimic those of the corresponding all-electron-consistent basis sets.

The optimized geometry of P₄ in T_d symmetry was first obtained using the KS-DFT approach with the B3LYP^{64,65} density functional and the 6-31G(d)⁶⁶ basis set. This yields a $R(\text{P-P})$ distance of 2.218 Å, which was used as the starting geometry in the potential energy surface calculations. We also performed geometry optimizations with the multireference methods outlined above to verify that these methods provide a good description of the process. Along with measured equilibrium geometries, we compared our potential energy surface results with experimental enthalpy values, where the dissociation energy was calculated as the difference between the energies of the tetraphosphorus structure $R(\text{P}_2\text{-P}_2) = 1.852$ Å and the dissociated complex (2 P₂) at $R(\text{P}_2\text{-P}_2) = 3.968$ Å.

After calculating energies for partially optimized geometries along the dissociation path, we converted to enthalpy of reaction by adding zero-point energies (ZPEs) and thermal energies to the reactants and products. This was done using Gaussian 09.⁶⁷ The ZPEs and thermal contributions to the reaction enthalpy were calculated with KS-DFT using the M06^{68,69} exchange-correlation functional and the aug-cc-pVTZ basis set. The quasiharmonic oscillator approximation (i.e., harmonic oscillator

formulas with scaled frequencies to account for anharmonicity and remove systematic errors) was used, and frequencies were scaled by a factor of 0.984.⁷⁰ All thermal contributions and reaction enthalpies were calculated at 298 K. The sum of the ZPE and thermal corrections is 0.9 kcal/mol higher for the reactant than for the product, so 0.9 kcal/mol was subtracted from all energies of the dissociation reaction to convert them to enthalpies of reaction.

3.3 Discussion

3.3.1 Equilibrium Geometry of P₂

The geometry of P₂ was calculated with two types of multireference methods (CASPT2 and MC-PDFT) with various basis sets and active spaces, and the results are reported in Table 3.1, including the calculated bond length, $R(\text{P-P})$, and the difference between calculated and experimental values (signed error, SE). The active spaces we used for P₂ are analogous to the (4332) and (6442) active spaces used for P₄, where the smaller is called (2220) and the larger space is (4220). Table 3.1 also compares our calculations to some results⁷¹⁻⁷⁵ in the literature. The CASPT2 results calculated with different active spaces at the cc-pVTZ level give very similar results, although they are slightly more accurate for the larger active space. However, the results are very sensitive to the basis set, where increasing the basis set from cc-pVTZ to cc-pV5Z and adding diffuse functions both decrease the SE. The cc-pV(*X*+d)Z basis sets, which contain an extra tight d function on P, converge faster than the original cc-pVXZ basis sets, but they seem to be converging to about the same values. Removing the IPEA shift deteriorates the results. The smallest error obtained in any of the calculations is obtained with CASPT2/cc-pV5Z with a default IPEA shift, and results in a SE of 0.009 Å. This may be compared to 0.009-0.024 Å from the previous multireference calculations in Table 3.1.

A similar basis set study with the MC-PDFT method on P₂ again shows that increasing the basis set from cc-pVTZ to cc-pV5Z systematically decreases the error. For cc-pVTZ and cc-pVQZ basis sets, MC-PDFT is just as accurate as CASPT2. For

Table 3.1: *Equilibrium P_2 Bond Lengths, $R(P-P)$, (\AA) and Signed Errors of Multireference Methods Compared to Experimental Bond Lengths*

Ref	Method	Active Space	Basis Set	IPEA Shift ^a	$R(P-P)$	Signed Error
present	CASPT2	(2220)	cc-pVTZ	0.25	1.9198	0.026
		(4220)	cc-pVTZ	0.25	1.9184	0.025
			cc-pVQZ	0.25	1.9083	0.015
			cc-pV5Z	0.25	1.9024	0.009
			cc-pV5Z	0.00	1.9086	0.015
			aug-cc-pV5Z	0.25	1.9050	0.012
			cc-pV(T+d)Z	0.25	1.9126	0.019
			cc-pV(Q+d)Z	0.25	1.9065	0.013
			cc-pV(5+d)Z	0.25	1.9041	0.011
present	MC-PDFT	(4220)	cc-pVTZ	-	1.9127	0.019
			cc-pVQZ	-	1.9063	0.013
			cc-pV5Z	-	1.9034	0.010
			aug-cc-pV5Z	-	1.9054	0.012
			cc-pV(T+d)Z	-	1.9057	0.012
			cc-pV(Q+d)Z	-	1.9043	0.011
			cc-pV(5+d)Z	-	1.9047	0.011
71	MRCI+Q	3s3p ^b	aug-cc-pVQZ	-	1.9174	0.024
72	MRCI	3s3p ^b	aug-cc-pV6Z	-	1.9028	0.009
73	MRCI+Q	3s3p ^b	aug-cc-pVQZ	-	1.9042	0.011
74	MRCI+Q	3s3p ^b	aug-cc-pVQZ	-	1.906	0.013
75	Experiment	-	-	-	1.8934	-

^(a) in hartrees.

^(b)This active space is equivalent to the (4220) active space used here.

the cc-pV5Z basis set, which is very expensive for CASPT2 but not as expensive with MC-PDFT, the error of CASPT2 is 0.009 Å, and the error of MC-PDFT is 0.010 Å. It is very encouraging that MC-PDFT shows less dependence on the basis set than CASPT2 does; the change of the SE in proceeding from cc-pVTZ to cc-pV5Z is 0.016 Å for CASPT2, but only 0.009 Å for MC-PDFT.

3.3.2 Equilibrium Geometry of P₄

The results for P₄ are in Table 3.2. For P₄, MC-PDFT gives a less accurate bond distance than does CASPT2 for both sizes of active space. The best result of MC-PDFT is given by the (4220) active space using the cc-pVTZ basis set. Using larger basis sets increased the error, with a difference of 0.011 Å between cc-pVTZ to cc-pV5Z.

Table 3.2: *Equilibrium Bond Length [$R(P-P)(\text{Å})$] of P₄ and Signed Errors of Multireference Methods Compared to Experiment*

Ref	Method	Active Space	Basis Set	$R(P-P)$	Signed Error
present	CASPT2 ^a	(2220)	cc-pVTZ	2.2181	-0.005
		(4220)	cc-pVTZ	2.2170	-0.006
present	MC-PDFT	(2220)	cc-pVTZ	2.1962	-0.027
		(4220)	cc-pVTZ	2.2103	-0.013
			cc-pVQZ	2.2013	-0.022
			cc-pV5Z	2.1995	-0.023
Brassington ⁴³	Experiment	-	-	2.2228	

^(a)The value used for the IPEA shift is 0.25 hartrees.

3.3.3 Reaction Enthalpies

We next compare the calculated reaction enthalpies to the experimental enthalpy of the P₄ → 2P₂ reaction, which is 54.8 kcal/mol.⁷⁵ The calculated reaction enthalpies are listed in Table 3.3. For MS-CASPT2, with a given basis set, the two active

spaces yield similar enthalpies with both all-electron and MCP basis sets; but the results with triple zeta basis sets are much more accurate than those with double zeta basis sets. The two calculations with triple zeta basis sets differ from experiment by at most 2.7 kcal/mol, but with double zeta basis sets the errors are 14.2 kcal/mol. The best MS-CASPT2 results are calculated with the larger active space and the MCP-TZP basis set; this calculation yields 54.3 kcal/mol, which agrees with the experimental results within 1 kcal/mol. The MC-PDFT results are more accurate than MS-CASPT2 for double zeta basis sets but less accurate for triple zeta basis sets. They also allow calculations with even larger basis sets. With the larger active space and the largest basis set, the error in the MC-PDFT reaction enthalpy is 6.5 kcal/mol. While MS-CASPT2 has a significant dependence on the basis set size, and the dissociation enthalpy varies by about 15 kcal/mol in going from a double zeta to triple zeta basis set for both all-electron and MCP types of basis, this is not the case for MC-PDFT, for which the largest change is about 5 kcal/mol.

Table 3.3: *Reaction Enthalpy (kcal/mol) at 298 K Calculated with Multireference Methods^a*

Basis Set	MS-CASPT2		MC-PDFT	
	(4332) Space	(6442) Space	(4332) Space	(6442) Space
cc-pVDZ	36.0	37.2	56.7	55.9
cc-pVTZ	52.7	52.1	61.7	60.5
cc-pVQZ	-	-	62.7	61.8
cc-pV5Z	-	-	61.8	61.3
MCP-DZP	40.4	40.7	62.3	61.8
MCP-TZP	53.6	54.3	63.6	62.9

^(a) The experimental reaction enthalpy is 54.8 kcal/mol. The results in this table were calculated from calculations like those in Figure 3.2.

3.3.4 Potential Energy Curves

The results from the MS-CASPT2 potential curve calculations are shown in Figure 3.2, which shows results from with both MCP-TZP and cc-pVTZ basis sets (results

with MCP-DZP and cc-pVDZ basis sets are shown in Figure B2 in Appendix B). The two active spaces give very similar results along the reaction pathway, except for a small difference at the top of the barrier. The calculations with the model core potential basis sets agree reasonably well with the all-electron calculations.

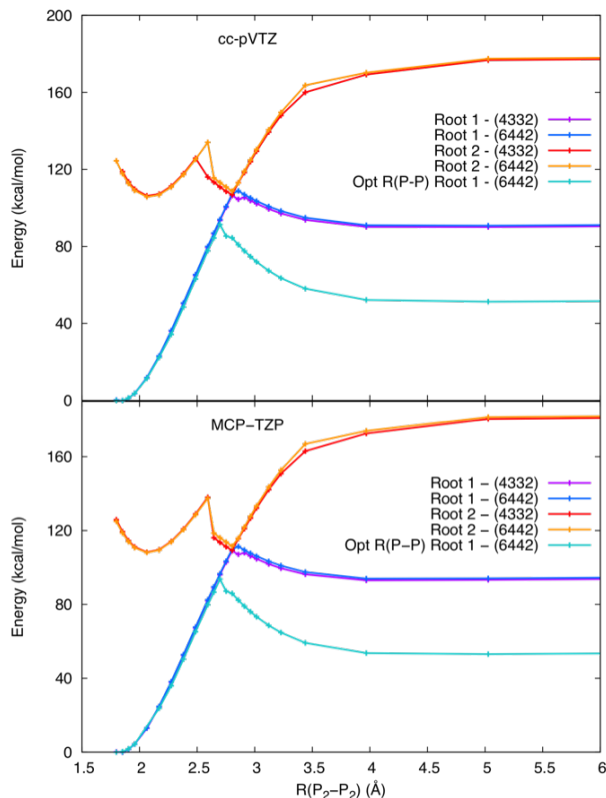


Figure 3.2: *MS-CASPT2 potential energy curves of the decomposition pathway of P_4 to $2 P_2$ with varying distances between the P_2 subunits, $R(P_2-P_2)$. The Opt $R(P-P)$ pathway allows the distance within the subunits, $R(P-P)$ to relax. The equilibrium geometry of P_4 was calculated with B3LYP/6-31G(d). The curves were calculated with two active spaces, (4332) and (6442), and two basis sets. Top: Curve calculated with the all-electron, cc-pVTZ basis set. Bottom: Curve calculated with the model potential MCP-TZP basis set. Both the ground state (Root 1) and the first excited state (Root 2) are shown in each case.*

The dissociation potential was also calculated with MC-PDFT, and since this method is much more computationally affordable, the work was extended to include

larger all-electron basis sets, cc-pVQZ and cc-pV5Z, where the valence electron space is expanded to quadruple zeta and quintuple zeta, respectively. The results are in Figures 3.3 and 3.4 with the smaller basis sets in Figure B3 in Appendix B. The potential energy curves calculated with MCP-TZP and cc-pVTZ are shown in Figure 3.3, which shows that the surfaces have similar shapes to the MS-CASPT2 results. The surfaces generated with cc-pVQZ and cc-pV5Z have a similar shape, which can be seen in Figure 3.4.

3.3.5 Computational Considerations

A key point in favor of the MC-PDFT method is that this approach does not suffer from the problem of intruder states. Another key point is computational efficiency. Balancing accuracy and computational efficiency is a necessary process for practical work. A large portion of the MS-CASPT2 calculations took almost two days to complete, sometimes longer for geometries far from the equilibrium structures. Since this procedure is not computationally feasible for larger systems, the newer MC-PDFT method was used, and the results were compared with results from MS-CASPT2. Since the SA-CASSCF calculation is the same for both methods, Table 3.4 shows the average CPU time for the post-SCF portion of the MS-CASPT2 and MC-PDFT calculations performed with all-electron basis sets (cc-pVDZ and cc-pVTZ) and MCP basis sets (MCP-DZP and MCP-TZP). All calculations were run on the WestGrid Grex SGI Altix XE 1300 cluster on one core. The MCP basis sets, on average, reduced the CPU time of the PT2 step by almost 25%, but did not make a large change in the timing for the MC-PDFT step. The overall calculation time for the post-SCF step for the (6442) active space is remarkably reduced when using MC-PDFT, where the MC-PDFT calculation is 900 times faster on average than PT2 for all-electron basis sets, and almost 800 times faster for MCP basis sets.

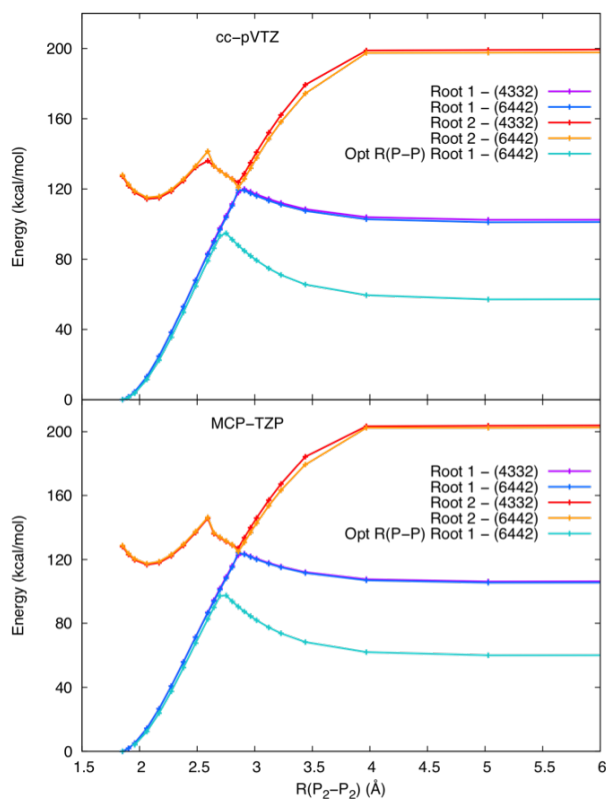


Figure 3.3: MC-PDFT potential energy curves of the decomposition pathway of P_4 to $2 P_2$ with varying distances between the P_2 subunits, $R(P_2-P_2)$. The Opt $R(P-P)$ pathway allows the distance within the subunits, $R(P-P)$ to relax. The equilibrium geometry of P_4 was calculated with B3LYP/6-31G(d). The curves were calculated with two active spaces, (4332) and (6442), and two basis sets. Top: Curve calculated with the all-electron, cc-pVTZ basis set. Bottom: Curve calculated with the model potential MCP-TZP basis set. Both the ground state (Root 1) and the first excited state (Root 2) are shown in each case.

3.3.6 Change of Valence Orbital Shape Along the Dissociation Path

The ground state natural orbitals in the valence space have been calculated from the SA-CASSCF calculations using the (6442) active space at each distance along the dissociation path and are shown in Figures 3.5 and 3.6. The smaller active space, (4332), generates a very similar set of ground state natural orbitals, so the orbitals

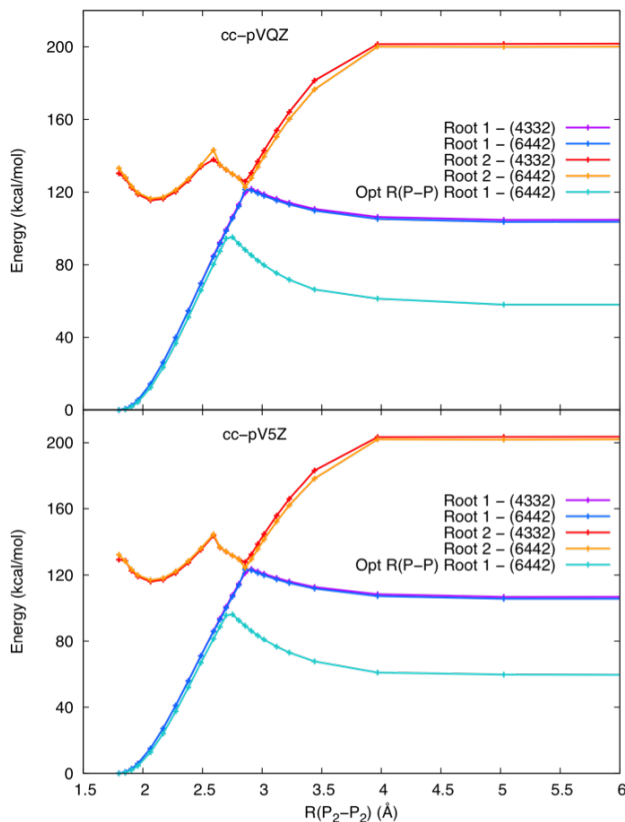


Figure 3.4: MC-PDFT potential energy curves of the decomposition pathway of P_4 to 2 P_2 with varying distances between the P_2 subunits, $R(P_2-P_2)$. The Opt R(P-P) pathway allows the distance within the subunits, $R(P-P)$ to relax. The equilibrium geometry of P_4 was calculated with B3LYP/6-31G(d). The curves were calculated with two active spaces, (4332) and (6442), and two basis sets. Top: Curve calculated with the all-electron, cc-pVQZ basis set. Bottom: Curve calculated with the all-electron cc-pV5Z basis set. Both the ground state (Root 1) and the first excited state (Root 2) are shown in each case.

Table 3.4: Average Computer Time Using the (6442) Active Space (in Minutes)^a

Basis Set	MS-CASPT2 ^a	MC-PDFT ^b
All-electron	235.61	0.26
MCP	185.40	0.24

^(a) Time for the PT2 step, excluding the SA-CASSCF step. ^(b) Time for the PDFT step, excluding the SA-CASSCF step.

from the smaller active space are not illustrated. As the P_2 - P_2 distance is extended to 2.49 Å and further to 3.71 Å, the orbitals remain similar to the ones at 1.59 Å, but there are two distinct changes in the orbitals. The first is elongation followed by two-unit localization. For example, for the $11a_1$ orbital in Figure 3.5, one can clearly see how the center red portion of the orbital is elongated from 1.59 Å to 2.49 Å, and then localized at 3.71 Å. Similar behaviour is observed for the $3a_2$ orbital. The second type of orbital change is localization to a single subunit, which is observed in orbitals of b_1 and b_2 symmetries. As the P_2 - P_2 distance becomes large, orbitals tend not to spread evenly on the entire P_4 molecule; they localize to a single P_2 unit. The latter behaviour can be avoided by calculating the molecule in a higher symmetry, but here we allow the variational procedure to lower the symmetry if that lowers the energy.

When P_4 is near the ground state equilibrium geometry, it can be seen from the natural orbital occupation numbers (NOONs) that the dominant configuration is $(9a_1)^2(10a_1)^2(11a_1)^2(12a_1)^2(13a_1)^2(6b_1)^2(7b_1)^2(6b_2)^2(7b_2)^2(3a_2)^2$. When the distance between the P_2 subunits is increased, electrons are redistributed mainly within $13a_1$, $14a_1$, $3a_2$, $4a_2$, $7b_1$, $8b_1$, $7b_2$ and $8b_2$ orbitals, which suggests that these orbitals should be included in the active space when the dissociation of P_4 is studied. Although the $11a_1$ and $12a_1$ orbitals are not involved in redistribution as significantly as the eight orbitals listed above, their NOONs range from 1.95 up to 2.00, which means they also should also be considered in the active space. In contrast, the NOONs of the $9a_1$, $10a_1$, $6b_1$ and $7b_1$ orbitals stay nearly constant at 1.99, suggesting they are not as active as the other orbitals, thus it is reasonable to consider them as inactive when one studies the dissociation.

When following how the NOONs of $14a_1$ orbital and $3a_2$ orbital change, one sees that when P_4 is completely dissociated to 2 P_2 the dominant ground state configuration has the $14a_1$ orbital occupied such that the order of the orbital energies for $14a_1$ and $3a_2$ orbitals is swapped.

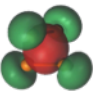
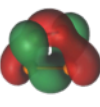
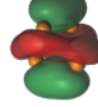
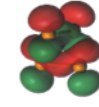
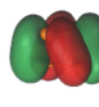
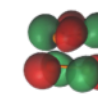
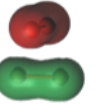
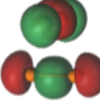
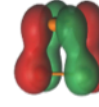
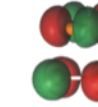
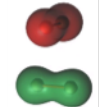
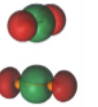
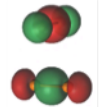
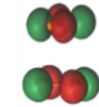
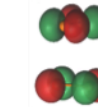
$R_{P_2-P_2}$ (Å)	$9a_1$	$10a_1$	$11a_1$	$12a_1$	$13a_1$	$14a_1$	$3a_2$	$4a_2$
1.59	 2.00	 1.99	 1.96	 1.95	 1.95	 0.04	 1.95	 0.07
2.49	 1.99	 1.99	 1.96	 1.95	 1.86	 0.11	 1.80	 0.23
3.71	 1.99	 1.99	 1.95	 1.95	 1.84	 1.79	 0.19	 0.18

Figure 3.5: Ground state P_4 natural valence orbitals of symmetry a_1 and a_2 for P_2 - P_2 distances of 1.59, 2.49, and 3.71 Å. The natural orbital occupation number is shown below the orbital.

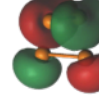
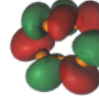
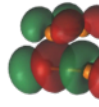
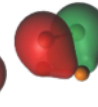
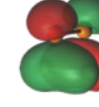
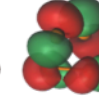
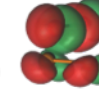
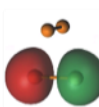
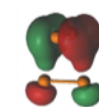
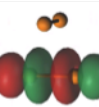
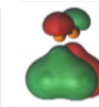
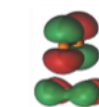
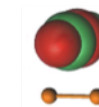
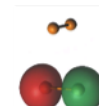
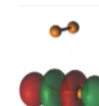
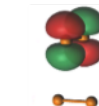
$R_{P_2-P_2}$ (Å)	$6b_1$	$7b_1$	$8b_1$	$9b_1$	$6b_2$	$7b_2$	$8b_2$	$9b_2$
1.59	 1.99	 1.95	 0.07	 0.04	 1.99	 1.95	 0.07	 0.04
2.49	 1.99	 1.88	 0.13	 0.05	 1.99	 1.88	 0.13	 0.05
3.71	 1.99	 1.82	 0.19	 0.06	 1.99	 1.82	 0.19	 0.06

Figure 3.6: Ground state P_4 natural valence orbitals of symmetry b_1 and b_2 for P_2 - P_2 distances of 1.59, 2.49, and 3.71 Å. The natural orbital occupation number is shown below the orbital.

3.4 Conclusion

The calculated equilibrium geometry of P_2 is within 0.01 Å of the experimental value when using CASPT2 and MC-PDFT with a sufficiently large basis sets, such as cc-pV5Z. The most accurate computed P_4 geometry has an error of only 0.005 Å, whereas the most accurate MC-PDFT geometry for P_4 has an error of 0.013 Å. The MS-CASPT2 method correctly describes the qualitative character of the energy along the dissociation pathway; most importantly the reaction barrier is represented as a smooth curve. MC-PDFT also predicts reasonable energies along the dissociation pathway. The computed reaction enthalpy is especially accurate with MS-CASPT2/MCP-TZP, where the results were within one kcal/mol of experiment. The two active spaces used, (4332) and (6442), gave similar results in all cases. However, a triple-zeta basis set is absolutely required to get reasonable results with MS-CASPT2. The MC-PDFT results avoid the intruder-state problems of the MS-CASPT2 calculations, and MC-PDFT can obtain reasonable results even with double zeta basis sets, but with triple zeta basis sets the results are less accurate than those obtained by MS-CASPT2. Computational efficiency was greatly increased by introducing MC-PDFT, as some post-SCF calculations finished within seconds, even as some post-SCF steps by MS-CASPT2 may take up to 24 hours, depending on how far a structure is from the equilibrium geometry. Most of the valence orbitals of P_4 have nearly constant character along the dissociation path studied in this thesis. We found that electrons prefer to be in the $3a_2$ orbital at equilibrium, but $14a_1$ at dissociation.

Chapter 4

Δ DFT/MIX: A reliable and efficient method for calculating core electron binding energies of large molecules^a

4.1 Introduction

Evaluating core electron binding energies (CEBEs) for molecules has long been a topic of interest for computational chemists, first studied theoretically by Bagus and Schaefer.^{76,77} The Δ SCF method,⁷⁸ frequently used to predict the 1s electron ionization potential, is limited in that it does not describe electron correlation and may not localize the core hole.⁷⁹ More computer-intensive excited state methods may be used to remedy these limitations, but inhibit the calculation of CEBEs for larger molecules due to high demand for computing resources. Gilbert et al.,⁸⁰ introduced the maximum overlap method (MOM), which provides solutions for excited states using self-consistent field (SCF) equations, and prevents orbitals in the high-energy core hole states from collapsing onto the orbitals in a high-energy configuration, typically corresponding to a valence-ionized molecule.

Previously the Δ MP2/MIX method⁸¹ was developed where electron correlation is accounted for using the second-order Møller-Plesset perturbation theory²²(MP2)

^aThis chapter is adapted from the published paper *J. Electron. Spectrosc. Relat. Phenom.*, **2018**, *227*, 44-50.

and the atom on which the core hole is placed is described with an all-electron basis set. All other atoms (except H) are described with model core potential basis sets (MCPs). This approach eliminates any confusion as to where the core hole will be located, especially important if there are equivalent centres within the molecule. Although the Δ MMP2/MIX method resulted in a mean absolute deviation (MAD) of 0.09 eV for a custom molecule test set,⁸¹ the MAD increased significantly to 0.3 eV when applied to nucleic acid bases (NAB).

The recent focus of the Chong group has been calibrating methods for predicting photoelectron spectra of small molecules. They developed a density functional theory (DFT) based method of evaluating CEBEs using a combination of density functionals (B88/P86) and the unrestricted generalized transition-state (uGTS) model, and calibrated using a set of small molecules containing C, N, O, and F atoms and 23 CEBEs.⁸² With the addition of relativistic corrections, they produced excellent results with a MAD of 0.23 eV for the Chong test set. Upon further analysis of this model, Chong was able to break down the deviation from experiment into possible errors, and found that the model was producing positive errors, while the functional was underestimating energies, resulting in a cancellation of errors. To avoid the model error, an energy difference approach, ΔE_{KS} , was used with DFT (PW86x-PW91c), and an overall MAD of 0.15 eV was achieved with a core-valence correlated basis set.^{83,84} Chong showed it is important to localize the core hole when using DFT, with delocalized results deviating from experiment on average by 9.6 eV.⁸⁵ Plekan et al. also computed CEBEs, but used the fourth-order algebraic-diagrammatic construction method, ADC(4).⁸⁶ This method has already been tested in calculations for nucleic acid bases.⁸⁷⁻⁸⁹

Methods for calculating CEBEs of nucleic acid bases have often been calibrated using the Chong test set; however, using this test set for calibration may not be adequate when applying the results to larger systems. Here, we also use this set, but with the addition of four new molecules. Our main goal is to develop a sensitive computational method that can compute CEBEs of large molecules, specifically the small characteristic differences between nucleic acid base tautomers, which may be

important for comparing with experimental X-ray photoelectron spectroscopy results in detecting mutations within the structure of DNA. The new method, Δ DFT/MIX, is similar to the ΔE_{KS} method suggested by Chong, but is using model core potentials, as was done in Δ MP2/MIX.

4.2 Computational Details

In the Δ DFT/MIX method, we replace the MP2 method with the DFT approach, while keeping the mixed (all-electron and model core potential) basis sets to force core hole localization. The CEBEs were calculated by taking the energy difference between the neutral molecule and its respective ion,

$$\Delta\text{DFT} = E_{\text{ion}} - E_{\text{neutral}}.$$

A unique localized core hole was created by using MCP basis sets on all atoms except the atom of interest. The MIX method⁸¹ describes all hydrogen atoms with the cc-pVDZ basis set⁹⁰ and the atom on which the 1s core hole was created is described with the cc-pCVTZ basis set,⁹¹ which has tight correlating functions for a good description of electron correlation within the K-shell. All other atoms were treated using the pseudopotential MCP-DZP basis set.⁶³ Relativistic corrections, using the values calculated by Chong,⁹² were added to the Δ DFT value to give better results; their values for C, N, O, F are 0.05, 0.11, 0.20, and 0.34 eV, respectively. A benchmarking analysis was undertaken to evaluate CEBEs from the Chong test set,⁹³ along with four new molecules containing nitrogen-carbon bonds. The 17 molecules and 29 CEBEs are listed in Table 4.1. 70 density functionals, included in GAMESS (Aug 18, 2016 R1),⁹⁴ were used to compare results to experimental values. Geometry optimization of all molecules was performed using MP2 with the 6-311G(d,p)³ basis set. The density functionals that gave the most accurate results compared to experiment in the benchmarking study were then used to calculate CEBEs of NAB tautomers adenine A, uracil, thymine, cytosine A, C, D, and guanine A, B, and C.

4.3 Discussion

4.3.1 Calibration of Δ DFT/MIX method

It is important to benchmark methods using a test set that is chemically similar to the future application. The Chong test set was of particular interest since it contains fragments similar to those present within the NABs, such as single bonds to N, C, O, and F, double bonds to N, C, and O, and triple bonds to N and C. Four new molecules (see Figure 4.1) were added to further match the NAB environments, as double and single bonds from C to multiple N atoms were lacking in the original test set. If the Δ DFT/MIX method provides accurate results for the test set, it would be expected that the results will also be accurate for NABs. The list of molecules in this test set, as well as deviation from the experimental results for each functional can be seen in Table 4.1. Out of the 70 density functionals benchmarked, the three most accurate functionals were B3LYP,^{64,65} BLYP,^{64,95} and TPSSm,⁹⁶ resulting in MADs of 0.28, 0.37 and 0.29 eV, respectively. The results generated with the other functionals are shown in Tables C1–C66 in Appendix C. Addition of the relativistic corrections (B3LYP_r, BLYP_r, TPSSm_r), reduced the MAD and the best results were produced by TPSSm_r and B3LYP_r (MAD of 0.21 eV). The MAD values were computed using differences with respect to experimental data, and shown as $\delta(X) = \text{CEBE}_{\text{calc}}(X) - \text{CEBE}_{\text{exp}}$, where X stands for the method used.

4.3.2 Application to Nucleic Acid Bases

The three most accurate density functionals in the test set were used to calculate the CEBEs of NAB adenine A, uracil, and thymine. The experimental CEBEs of the 1s electron from atoms within each nucleic acid base are reported in the following tables, along with difference between experimental and theoretical values and overall MADs for the functional per each NAB.

In Table 4.2, the calculated CEBE results for adenine A are compared with the experimental values. Overall, B3LYP gives the the smallest MAD compared to the other functionals and the Δ MP2/MIX and ADC(4) methods.

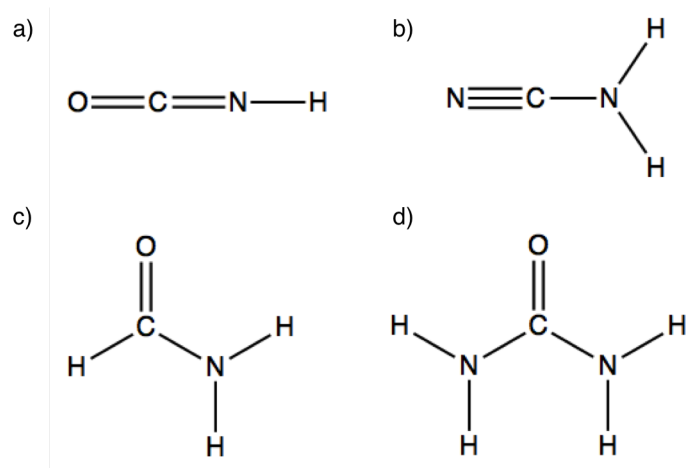


Figure 4.1: Structural formulas of the four new additions to the Chong test set, a) OCNH b) NCNH_2 c) NH_2CHO d) $\text{OC}(\text{NH}_2)_2$.

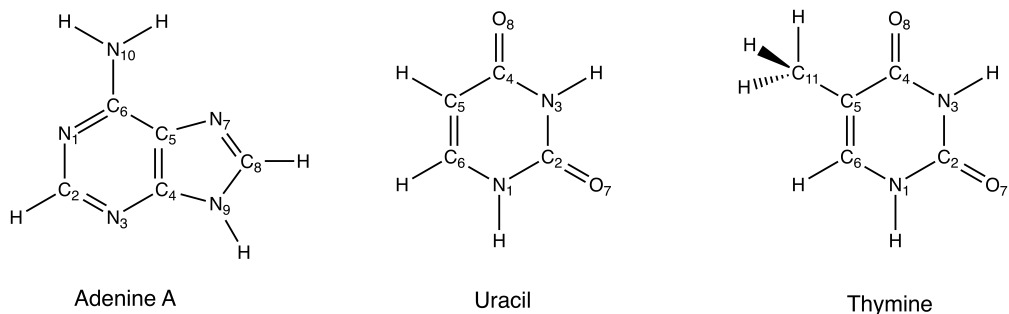


Figure 4.2: Structural formulas of nucleic acid bases used to compare calculated core electron binding energies to experimentally measured values.

Table 4.1: The Chong test set used to benchmark density functionals for evaluating core electron binding energy (eV); the ionized atom is in bold font.

Molecule	Exp ⁹⁷	$\delta(\text{B3LYP})$	$\delta(\text{B3LYP}_r)$	$\delta(\text{BLYP})$	$\delta(\text{BLYP}_r)$	$\delta(\text{TPSSm})$	$\delta(\text{TPSSm}_r)$
C₂H₂	290.82	0.57	0.62	0.41	0.46	0.48	0.53
CH₄	290.91	-0.05	0.00	-0.15	-0.10	-0.07	-0.02
CH₃OH	292.42	-0.06	-0.01	-0.24	-0.19	-0.10	-0.04
CH₃CN	292.45	0.30	0.35	0.06	0.11	0.11	0.16
CH₃CN	292.98	-0.18	-0.13	-0.41	-0.36	-0.33	-0.28
HCN	293.40	0.23	0.28	0.01	0.06	0.05	0.10
H₂CO	294.47	0.08	0.13	-0.17	-0.12	-0.06	-0.01
CO	296.21	0.42	0.47	0.06	0.11	0.06	0.11
CO₂	297.69	0.09	0.14	-0.54	-0.49	-0.55	-0.50
NH₃	405.56	-0.19	-0.09	-0.24	-0.14	-0.16	-0.06
CH₃CN	405.64	-0.34	-0.24	-0.49	-0.39	-0.34	-0.24
HCN	406.78	-0.07	0.03	-0.17	-0.07	-0.07	0.03
NNO	408.71	-0.02	0.08	-0.35	-0.25	-0.27	-0.17
N₂	409.98	-0.07	0.03	-0.30	-0.20	-0.17	-0.07
NNO	412.59	-0.04	0.06	-0.60	-0.50	-0.41	-0.31
CH₃OH	539.11	-0.66	-0.49	-0.63	-0.46	-0.49	-0.32
H₂CO	539.48	-0.67	-0.50	-0.58	-0.41	-0.46	-0.29
H₂O	539.90	-0.55	-0.38	-0.53	-0.36	-0.45	-0.28
CO₂	541.28	-0.33	-0.16	-0.36	-0.20	-0.27	-0.10
NNO	541.42	-0.19	-0.02	-0.15	0.02	0.00	0.17
CO	542.55	-0.48	-0.31	-0.46	-0.29	-0.35	-0.18
HF	694.23	-0.85	-0.51	-0.75	-0.41	-0.69	-0.35
F₂	696.69	-0.97	-0.63	-0.93	-0.59	-0.63	-0.29
NCNH₂	293.46	-0.03	0.02	-0.38	-0.33	-0.34	-0.29
NH₂CHO	294.45	-0.12	-0.03	-0.53	-0.48	-0.48	-0.43
OC(NH₂)₂	294.84	-0.15	0.00	-0.64	-0.59	-0.59	-0.54
OC(NH₂)₂	406.09	-0.23	-0.12	-0.37	-0.22	-0.29	-0.19
NH₂CHO	406.30	0.00	0.12	-0.09	0.06	-0.01	0.11
OCNH	406.44	-0.13	-0.04	-0.22	-0.04	-0.14	-0.04
MAD	-	0.28	0.21	0.37	0.28	0.29	0.21

Table 4.2: *Experimental and theoretical values of 1s core electron binding energy (eV) in adenine A.*

	Exp ⁸⁸	$\delta(\text{B3LYP}_r)$	$\delta(\text{BLYP}_r)$	$\delta(\text{TPSSm}_r)$	$\delta(\Delta\text{MP2/MIX})^{81}$	$\delta(\text{ADC}(4))^{86}$
N ₁	404.4	-0.21	-0.36	-0.24	0.03	-0.13
N ₃	404.4	-0.02	-0.17	-0.06	0.20	1.22
N ₇	404.4	-0.11	0.15	0.27	0.58	0.59
N ₉	406.7	-0.11	-0.19	-0.02	0.26	-0.07
N ₁₀	405.7	-0.04	-0.15	-0.03	0.00	-0.08
C ₂	292.5	-0.81	-1.17	-0.96	-0.70	-0.56
C ₄	292.5	-0.41	-0.74	-0.54	0.18	-0.03
C ₅	291.0	-0.17	-0.39	-0.23	0.25	0.19
C ₆	292.5	-0.01	-0.37	-0.16	0.21	0.46
C ₈	292.5	-0.41	-0.74	-0.50	-0.02	0.16
MAD	-	0.23	0.34	0.30	0.24	0.35

Table 4.3 presents CEBEs within uracil. Once again, the carbon 1s values are generally underestimated, but those for oxygen and nitrogen are not as predictable. B3LYP is the most accurate functional with respect to experiment, with a MAD of 0.15 eV, compared to $\Delta\text{MP2/MIX}$ and $\text{ADC}(4)$ methods which both reach a low MAD of 0.13 eV.

Table 4.3: *Experimental and theoretical values of 1s core electron binding energy (eV) in uracil.*

	Exp ⁸⁸	$\delta(\text{B3LYP}_r)$	$\delta(\text{BLYP}_r)$	$\delta(\text{TPSSm}_r)$	$\delta(\Delta\text{MP2/MIX})^{81}$	$\delta(\text{ADC}(4))^{88}$
O ₇	537.6	0.01	0.00	0.07	0.04	-0.19
O ₈	537.6	-0.43	-0.43	-0.36	-0.30	0.10
N ₁	406.8	0.27	0.10	0.24	0.30	0.12
N ₃	406.8	-0.17	-0.37	-0.26	-0.13	-0.30
C ₂	295.4	-0.06	-0.62	-0.53	0.02	0.14
C ₄	294.4	-0.09	-0.61	-0.53	0.04	0.01
C ₅	291.0	0.04	-0.18	-0.12	0.02	-0.14
C ₆	292.8	0.13	-0.23	-0.13	0.21	-0.02
MAD	-	0.15	0.32	0.28	0.13	0.13

The CEBEs in thymine are shown in Table 4.4. Much like uracil, the calculated nitrogen and oxygen binding energies are unpredictable in terms of over- or underestimating experimental results, where carbon is generally underestimated. The lowest

Table 4.4: *Experimental and theoretical values of 1s core electron binding energy (eV) in thymine.*

	Exp ⁸⁸	$\delta(\text{B3LYP}_r)$	$\delta(\text{BLYP}_r)$	$\delta(\text{TPSSm}_r)$	$\delta(\Delta\text{MP2/MIX})^{81}$	$\delta(\text{ADC}(4))^{86}$
O ₇	537.3	0.10	-0.39	-0.32	0.15	0.16
O ₈	537.3	-0.24	-0.81	-0.74	-0.10	0.04
N ₁	406.7	0.13	-0.11	0.03	0.21	0.01
N ₃	406.7	-0.19	-0.58	-0.47	-0.12	-0.18
C ₂	295.2	-0.13	-0.72	-0.63	-0.01	-0.16
C ₄	294.2	-0.17	-0.71	-0.63	-0.04	0.01
C ₅	291.0	-0.06	-0.28	-0.22	0.00	-0.33
C ₆	292.3	0.03	-0.33	-0.21	0.29	-0.01
C ₁₁	291.0	0.22	0.04	-0.20	0.24	-0.05
MAD	-	0.14	0.44	0.39	0.13	0.12

MAD value is obtained with B3LYP_r, while BLYP_r and TPSSm_r MADs are almost twice as large.

Considering the results of all three NABs above, B3LYP_r gives the most accurate results with respect to experiment, even though the calibration study (Table 4.1) favoured both B3LYP_r and TPSSm_r results with a MAD of 0.21 eV.

4.3.3 Sensitivity of the $\Delta\text{B3LYP}/\text{MIX}$ Method to Nucleic Acid Base Tautomers

Once the density functionals were tested on the select NABs above, the method was used to detect CEBE differences between NAB tautomers, specifically the three tautomers of cytosine (A, C, and D) and guanine (A, B, and C). The results in Tables 4.5 and 4.6 were obtained with B3LYP_r since it gave the lowest MAD in the NAB study above.

Three cytosine tautomers (A, B, and C) are shown in Figure 4.3. The atoms with unique chemical environments are highlighted for greater visibility and numbered for core-hole specificity. Even though C₅ and C₆ are not in different local chemical environments, the corresponding experimental 1s electron binding energies differ slightly, so it is necessary to include them in the results, shown in Table 4.5. The second column collects results from $\Delta\text{B3LYP}/\text{MIX}$ and the third column is the difference

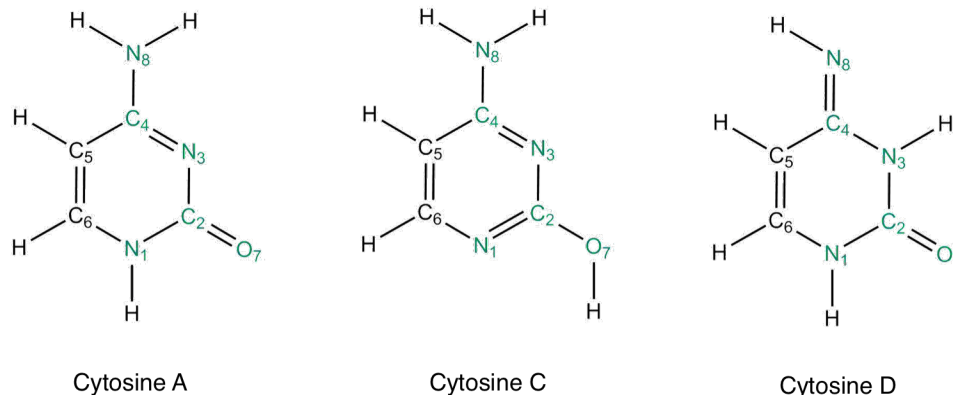


Figure 4.3: Structures of cytosine A, C, and D, with unique atomic environments highlighted.

between the calculated and experimental values, δ . The results from B3LYP_r give fairly accurate results overall for carbon and oxygen, but this method has large deviations from experiment when evaluating nitrogen CEBEs, as large as 0.79 eV. Even with these outliers, the overall MAD is still fairly low at 0.21 eV, 0.11 eV and 0.27 eV for cytosine A, C and D respectively.

Sensitivity has been tested through comparison of CEBEs of atoms within unique chemical environments. For example, N₃ is doubly bound to C₄ and singly bound to C₂ in cytosine A and C, but within cytosine D, N₃ is singly bound to both C₄ and C₂. The theoretical CEBEs of N₃ in cytosine A, C, and D are 404.11, 404.51 and 406.34 eV, respectively. Only cytosine D CEBEs should be shifted since both A and C tautomers are in equivalent environments, but the calculated results are still able to distinguish that A and C are in similar environments, whereas D is not. C₅ is chemically indistinct between all tautomers and the CEBE results from B3LYP are 290.73, 290.66, and 290.76 eV for cytosine A, C, and D, respectively, but once again there is a small error between the same chemical environments. The experimental CEBE of O₇ is distinct between all cytosine tautomers, and it is apparent in Table 4.5 that the Δ B3LYP/MIX method is sensitive enough to differentiate between them.

The structures of guanine tautomers A, B, and, C are shown in Figure 4.4 where the chemically unique atoms are coloured green. CEBEs within guanine are collected in Table 4.6. As with cytosine, B3LYP results deviate from experiment by up to

Table 4.5: *Experimental and theoretical values of core electron binding energies show method sensitivity for detecting small energetic differences within cytosine tautomers.*

	Cytosine A			Cytosine C			Cytosine D		
	Exp ⁸⁸	B3LYP _r	$\delta(\text{B3LYP}_r)$	Exp ⁸⁸	B3LYP _r	$\delta(\text{B3LYP}_r)$	Exp ⁸⁸	B3LYP _r	$\delta(\text{B3LYP}_r)$
O ₇	536.50	537.01	0.51	539.40	539.37	-0.03	537.30	537.30	0.00
N ₁	406.10	406.32	0.22	404.50	404.41	-0.09	406.10	406.69	0.59
N ₃	404.50	404.11	-0.39	404.50	404.51	0.01	406.10	406.34	0.24
N ₈	406.10	405.99	-0.11	406.10	405.93	-0.17	404.50	403.71	-0.79
C ₂	293.90	294.04	0.14	293.90	293.78	-0.12	295.10	295.05	-0.05
C ₄	293.20	293.22	0.02	293.20	292.99	-0.21	293.20	293.22	0.02
C ₅	290.60	290.73	0.13	290.60	290.66	0.06	290.60	290.76	0.16
C ₆	292.40	292.57	0.17	291.70	291.52	-0.22	292.40	292.72	0.32
MAD			0.21			0.11			0.27

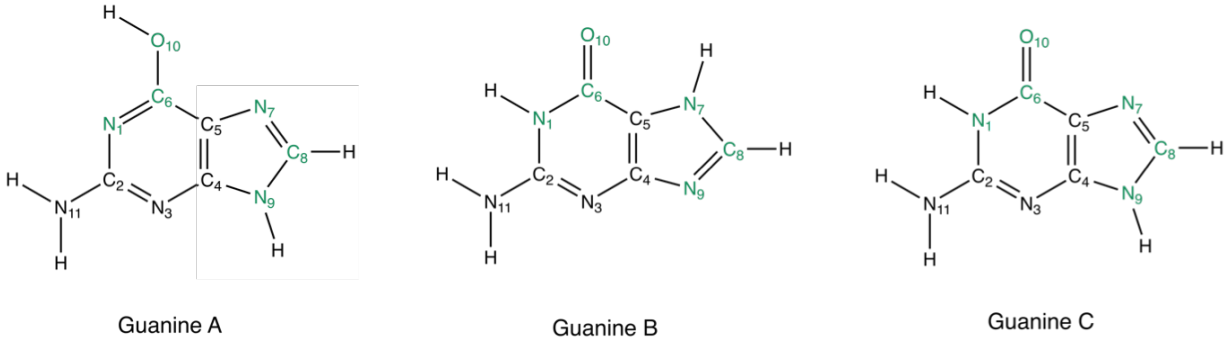


Figure 4.4: Structures of guanine A, B, and C, with unique atomic environments highlighted.

0.79 eV for nitrogen 1s electron binding energies. The MADs of the Δ B3LYP/MIX results for guanine A, B and C are 0.15, 0.19, and 0.17 eV, respectively.

The nitrogen atoms in guanine, N_1 and N_3 , are great cases to probe sensitivity for distinct chemical environments of atoms. N_1 in guanine A is double-bonded to C_6 and its 1s CEBE is 404.34 eV, whereas in guanine B and C, it is attached to C_6 and H with single bonds, with CEBEs at 406.26 and 406.36 eV. The N_3 atom is not chemically unique between the three tautomers and no chemical shifts are seen experimentally; our calculated values were 404.34 eV ($\delta=-0.18$ eV), 404.24 eV ($\delta=-0.26$ eV), and 404.74 eV ($\delta=0.24$ eV) for guanine A, B, and C, respectively, but all results are within 0.25 eV of the experimental value. The case of guanine supports the view that it is easy to distinguish NAB tautomers using the Δ B3LYP/MIX method.

It is important to note the wide range of deviations from experiment that DFT results can produce. All calculated values from the test set and NABs using Δ B3LYP/MIX, our best method, are included in the data in Figure 4.5. Overall, there is no trend that could predict whether the calculated results will be over- or underestimated, thus the deviations cannot be easily rectified with uniformly shifting the binding energies. Noticeably, the CEBE results from the test set are within a much smaller range than the results from NABs. Also, nitrogen has a much smaller range of deviations from experimental CEBEs than oxygen and carbon in the test set, but this set is much smaller than with the NABs. In extreme cases, calculated carbon and nitrogen CEBEs are within ± 0.8 eV of experimental results. However, while some

Table 4.6: *Experimental and theoretical values of core electron binding energies show method sensitivity for detecting small energetic differences within guanine tautomers.*

	Guanine A			Guanine B			Guanine C		
	Exp ⁸⁹	B3LYP _r	$\delta(\text{B3LYP}_r)$	Exp ⁸⁹	B3LYP _r	$\delta(\text{B3LYP}_r)$	Exp ⁸⁹	B3LYP _r	$\delta(\text{B3LYP}_r)$
O ₁₀	539.40	539.47	0.07	536.70	536.34	-0.36	536.70	536.61	-0.09
N ₁	404.50	404.34	-0.16	406.30	406.26	-0.04	406.30	406.36	0.06
N ₃	404.50	404.34	-0.18	404.50	404.24	-0.26	404.50	404.74	0.24
N ₇	404.50	404.52	0.02	406.30	406.52	0.22	404.50	404.49	-0.01
N ₉	406.30	406.53	0.23	404.50	404.23	-0.27	406.30	406.63	0.33
N ₁₁	405.10	405.52	0.42	406.30	406.01	-0.29	406.30	406.39	0.09
C ₂	293.15	293.06	-0.09	293.80	293.60	-0.20	293.80	293.82	0.02
C ₄	292.10	292.23	0.13	292.10	291.81	-0.29	292.10	292.24	0.14
C ₅	290.90	290.79	-0.11	290.90	291.03	0.13	290.90	290.74	-0.16
C ₆	293.15	293.15	0.00	293.80	293.66	-0.14	293.80	293.53	-0.27
C ₈	292.10	291.92	-0.18	292.10	292.07	-0.03	292.10	291.85	-0.25
MAD			0.15			0.19			0.17

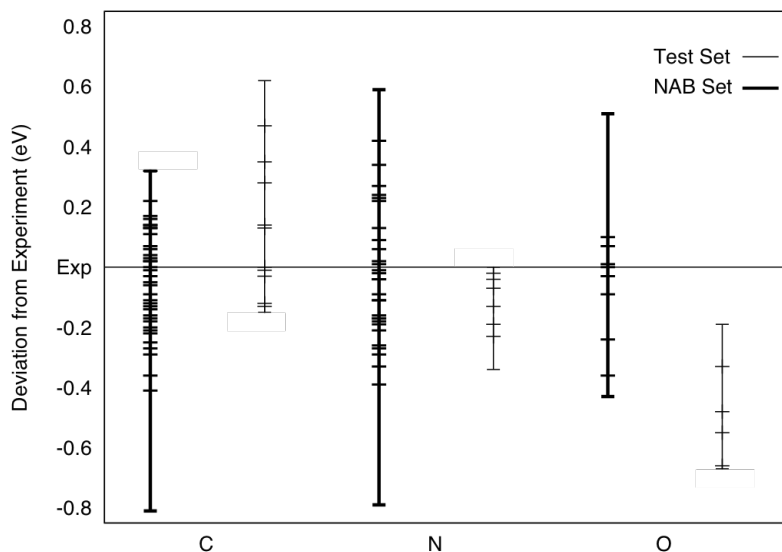


Figure 4.5: Deviation of $\Delta B3LYP/MIX$ core electron binding energies (eV) from experiment, per carbon, nitrogen, and oxygen atom. The results are split into the Chong test set results and NAB results.

deviations may be larger than others, the percent error is still less than 0.3%, and the results can be considered reliable. In Figure 4.6, the correlation between the theoretical and experimental CEBEs from C, N, O, and F for both the test set and NAB results are shown. The calculated CEBEs for C and N have excellent agreement with experiment, while O and F CEBEs have a wider range of theoretical values and are slightly underestimated overall. Even so, we believe the present method is capable of helping experimentalists to assign X-ray photoelectron spectroscopy peaks not only of different NABs, but also of different tautomers of the same NAB.

4.3.4 Timing

With the prospect of applying the $\Delta DFT/MIX$ method to larger molecules, calculation timing should be considered. A study on analogues of pyridine was undertaken to compare timing of the two methods underlying the MIX approach, B3LYP and

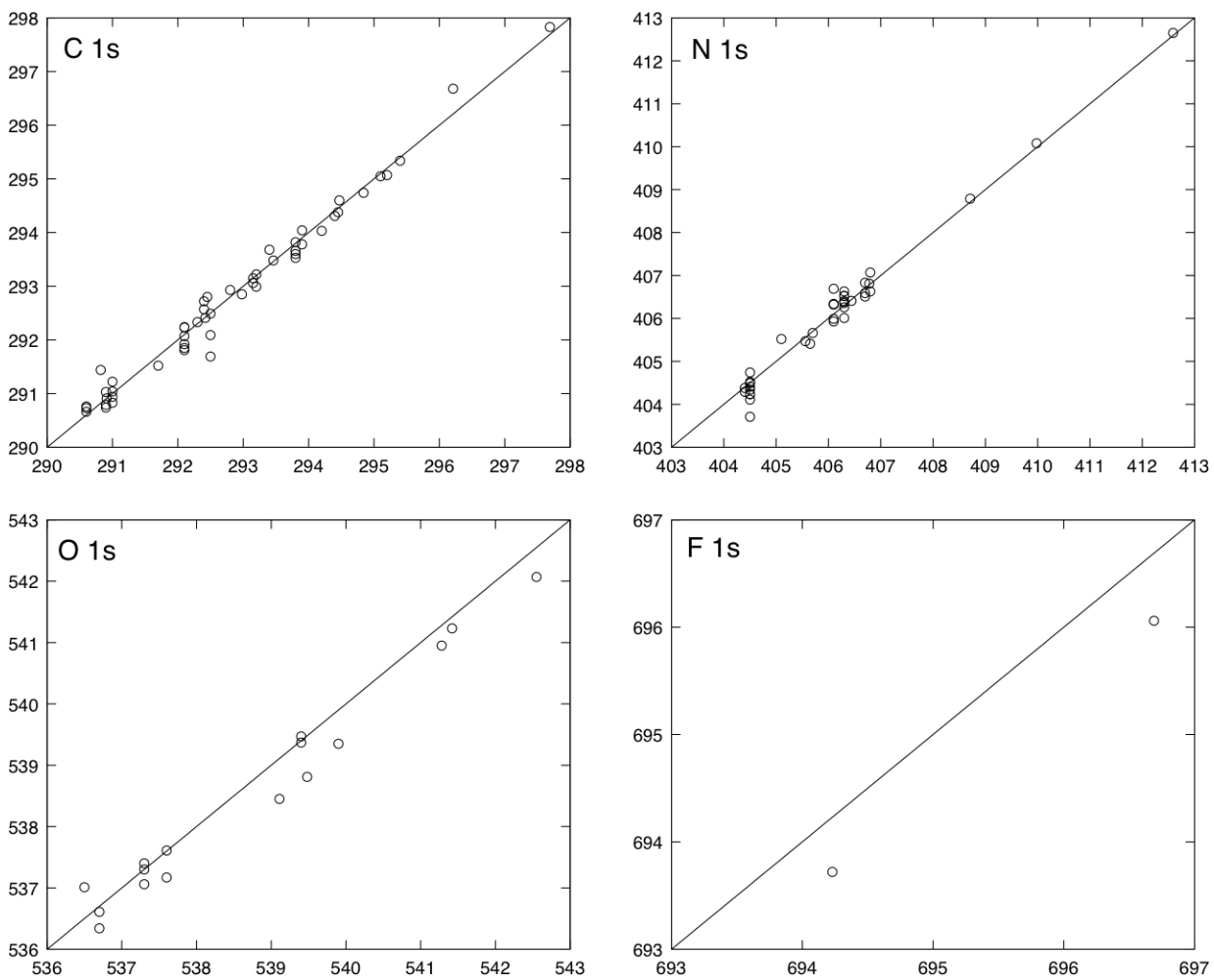


Figure 4.6: Correlation between calculated (*x*-axis) and experimental (*y*-axis) 1s core electron binding energies (in eV)

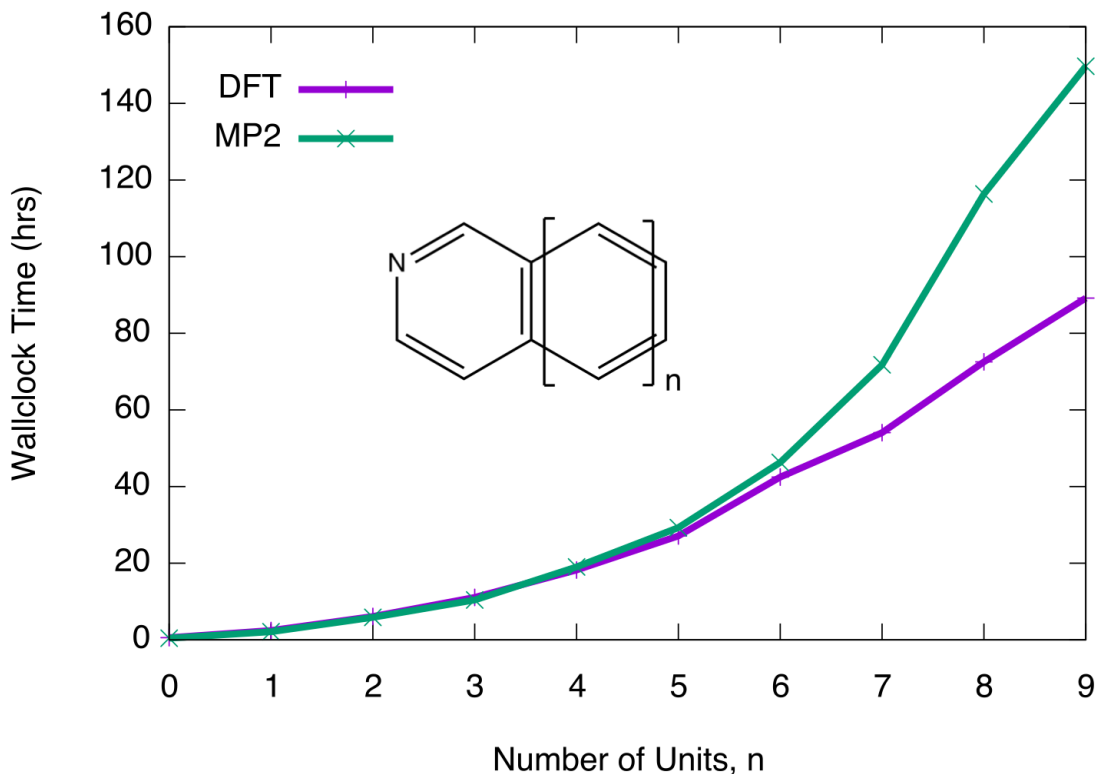


Figure 4.7: *Timing study of B3LYP and MP2 calculations by increasing molecular size by number of units, n, on one core on the WestGrid Altix XE 1300 cluster.*

MP2. A series of B3LYP/cc-pVTZ and MP2/cc-pVTZ calculations were run on the WestGrid Grex SGI Altix XE 1300 cluster on one core. The timing results are shown in Figure 4.7. For small molecules, B3LYP and MP2 timings are identical, but this rapidly changes once the number of units begin to increase. When $n=9$, DFT is faster by 60 hours.

4.4 Conclusion

A set of small organic molecules was used to assess the most accurate density functionals for calculating the 1s core electron binding energies of nitrogen, carbon, oxygen, and fluorine atoms. Previous work has been done to calibrate DFT methods for calculating core electron binding energies; recommended in that work, relativistic corrections per atom,⁸² were applied in the present study. When a density functional

underestimates the experimental result, these corrections gave more accurate results. Sometimes, however, the relativistic correction introduces larger error. Often, the density functionals will both under- and overestimate the CEBE of the same type of atom within a molecule. Overall, both B3LYP_r and TPSSm_r were equally accurate for the test set, but when the method was applied to nucleic acid bases the most accurate functional was B3LYP_r, based on the mean absolute deviations with respect to experimental results (MAD=0.18 eV); the error for TPSSm_r was almost doubled (MAD=0.32 eV). Typically, the Δ B3LYP/MIX method has a similar or smaller MAD than previous Δ MP2/MIX and ADC(4) results.

An interplay between computational efficiency and accuracy is always a factor, especially when calculating properties of large molecules. The MAD of the Δ B3LYP/MIX method is at most 0.08 eV larger than the resulting MADs from Δ MP2/MIX and ADC(4), without the need of shifting computed CEBEs, as done with the ADC(4) (shifted by 2-3 eV) to match experimental spectra. The Δ B3LYP/MIX method is an accurate and fast method to calculate core electron binding energies of both small and large molecules. The Δ DFT approach is sensitive enough, in most cases, to detect whether an atom is within a different chemical environment in different nucleic acid base tautomers, and the calculated results reflect the energetic shift seen experimentally. As long as the experimental CEBEs differ by at least the MAD of 0.19 eV, we believe that this approach will be able to assign experimental XPS of different NAB tautomers.

The Δ DFT/MIX method is a reliable method for calculating the core electron binding energies of large molecules. Using this approach, instead of the previously benchmarked Δ MP2/MIX method, reduces calculation time for large chemical systems.

Chapter 5

Designing Fluorescent Chemosensors with Metal-Complexed Crown Ethers

5.1 Introduction

The presence of heavy metals in the environment is an ever-growing concern due to their bioaccumulation and biomagnification.⁹⁸ Currently, a number of methods are utilized for the determination and detection of heavy metal ions, including inductively coupled plasma spectroscopy,⁹⁹ atomic absorption spectroscopy,¹⁰⁰ molecular absorption spectroscopy,¹⁰¹ and electro-analytical techniques.^{102,103}

Although these methods are effective and well established, their utility is hindered because they often require extensive sample preparation along with specialized and costly laboratory equipment. Advancements in fluorescence spectroscopy present remarkably sensitive and selective alternatives that offer the added advantage of simplicity and low-cost instrumentation.^{104,105} However, improvement of fluorescence based sensors for the detection of heavy metals remains a challenge for several reasons. Firstly, heavy metals often behave as fluorescence quenchers,^{106,107} which not only proves to be disadvantageous for signal output, but also interferes with the use of time-resolved fluorometry techniques. Further, many fluoroionophores non-specifically recognize analytes and show simultaneous response to numerous cations.^{108,109} Finally, given their high hydration enthalpy, heavy metals are rather difficult to detect in

aqueous environments.¹¹⁰ These limitations must be considered and addressed when designing and investigating heavy metal sensors, particularly for biological and environmental applications.^{111,112}

The detection of Hg^{2+} has attracted attention,^{113–117} since mercury and its derivatives, commonly used in industry, have high toxicity and are implicated in the cause of prenatal brain damage¹¹⁸ and numerous other diseases including acrodynia,¹¹⁹ Hunter-Russell syndrome,¹²⁰ and Minamata disease.¹²¹ While fluorescent Hg^{2+} chemosensors exist, the vast majority operate based on fluorescence quenching mechanisms^{112–115,122} and very few undergo fluorescence enhancement^{112,123–125} – the superior technique that reduces the likelihood of false positive signals.¹¹² Moreover, the d^{10} electronic configuration of Hg^{2+} prohibits the use of other detection techniques, e.g. UV-Vis spectroscopy.¹²⁶

Fluorescent chemosensors designed for metal ion detection are most commonly made up of an ionophore receptor bound to a fluorophore signalling unit via a spacer.^{127–134} The ionophore refers to the receptor group responsible for ion recognition, while the role of the fluorophore is to quantify and relay this detection by emitting fluorescence. The purpose of the spacer unit is to join the fluorophore to the receptor whilst keeping the ground state electronic systems of the receptor and the fluorophore disconnected.¹³⁵ In designing sensors, the ionophore receptor is of utmost importance for it is responsible for the metal binding efficiency and overall selectivity of the chemosensor.¹³⁶ Most fluoroionophores for Hg^{2+} make use of macrocycle receptors;^{112–114,122,137,138} in particular, several research groups have documented fluorescent Hg^{2+} sensors which utilize a crown ether based moiety as the receptor unit.^{108–110} Ever since their discovery in 1967,¹³⁹ crown ethers have been relied on for their cation-capturing ability and are commonly used for the extraction of various metal cations from different media.^{140–142} Their ability to bind metal cations stems from the interaction between the metal cation and the lone electron pairs from the oxygen atoms.¹⁴³ Through incorporation of sulfides, crown ether binding preferences can be shifted toward soft heavy metal cations,¹⁴⁴ like the mercury (II) ion of interest. In 2009, Kim et al. reported the synthesis of a 4,4-difluoro-4-bora-3a,4a-

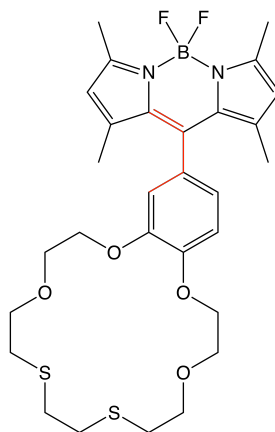


Figure 5.1: *Free BODIPY-benzothiacycrown chemosensor proposed by Kim et al.*

diaza-s-indacene (BODIPY) appended thiacycrown ether that displayed highly selective chelation enhanced fluorescence (CHEF) in response to mercury (II).¹³⁶

In this chapter, we have studied the BODIPY-benzothiacycrown chemosensor (Figure 5.1) proposed by Kim et al. which showed highly selective CHEF in response to the Hg^{2+} metal ion. The absorption peak for the Hg^{2+} complex is red-shifted compared to the free-ligand and other metal ions tested in the paper. This led us to investigate the selectivity of the chemosensor as a positive fluorescent sensor for the Hg^{2+} metal, as well as considering other sulfur substituted crown ethers and other metal ions in order to understand what drives the selectiveness of the crown. We also studied the effect complexation has on excitation energies by varying the position of the fluorophore with respect to the rest of the chemosensor.

5.2 Computational Details

Since the systems of interest are large and contain transition metals, each structure was optimized at the PBE0/6-31G(d) level, using an initial geometry optimized with the PM6 semiempirical method.¹⁴⁵ All calculations were done with a mixed basis set, combining all-electron and ECP (or in some cases MCP) in the interest of computational efficiency. The light atoms were described with a polarized double- ζ basis set, 6-31G(d), and transition metals were modelled with the polarized double- ζ effec-

tive core potential LANL2DZ, augmented with *d*- and *f*-type basis functions for main group and transition metals. The *f*-type polarization functions, extracted from the cc-pVDZ-PP basis set, were used for Cd and Hg atoms, while the triple- ζ model core potentials (MCP) provided *d*-type polarization functions for all other metals. Vertical excitations were calculated using TD-DFT methodology with the PBE0 functional for the first ten lowest singlet excited states. All MCP calculations were completed with GAMESS (Dec 5, 2014 R1),³⁶ all other calculations were done with Gaussian 09.³⁵

5.3 Discussion

To design the chemosensor, first we consider just the ionophore, focusing on the stabilities of 13 different structures shown in Figure 5.2. Second, we introduce the metals to the ionophore and calculate the binding affinities of metal ions with respect to each other. Following this, we optimize position of the ionophore with respect to the fluorophore. The full system (ionophore, linker, fluorophore, and metal ion) is then used to calculate vertical excitations to compare with those of the free ligand.

5.3.1 Selectivity of the Ionophores

Kim et al. state that the ionophore is the most important part of the entire chemosensor for both selectivity and binding efficiency.¹³⁶ We started with the six-membered crown ether and replaced oxygen atoms until all positions contained sulfur, leaving us with thirteen structural combinations of the crowns, labelled in Figure 5.2.

Extensive preliminary research was done to understand all structural differences of the crown ethers. In some cases, the minimum energy structures were flat and some were bent, as shown in Figure 5.3. The relative energies of the flat and bent structures are reported in Table D1. There is only a slight difference in energy, at most 25 kJ/mol, between the two structures. For most of the crown ether structures, the flat structure is lower in energy than the bent analogue, but some cases the bent is slightly favoured, as in the case of 18C-O₆S₀. One advantage of a bent structure

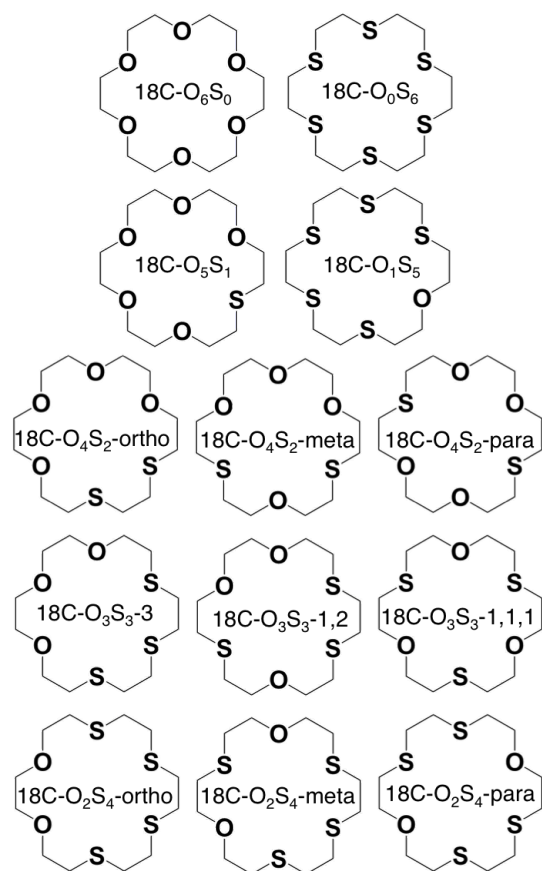


Figure 5.2: *The naming of all possible combinations of the positions of oxygen and sulfur atoms in the ionophore considered in this chapter.*

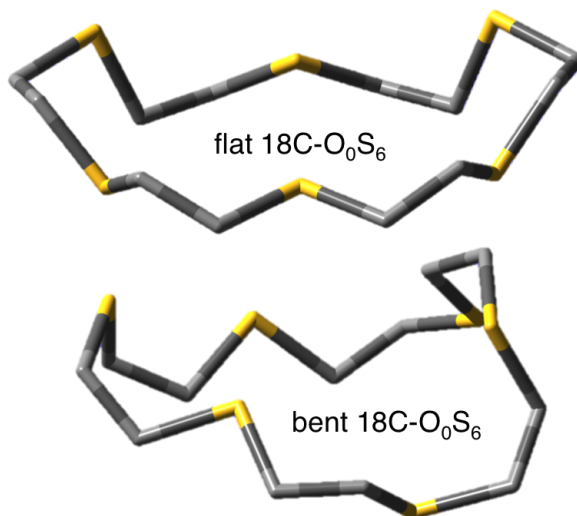


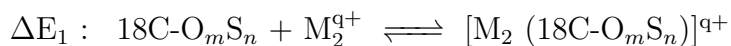
Figure 5.3: An example of the two minimum energy structures of the ionophores. Top: flat 18C-O₀S₆. Bottom: bent 18C-O₀S₆.

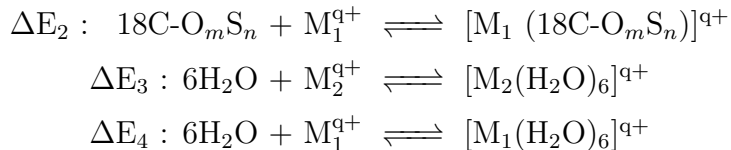
could be tighter binding of the metal to the crown through closer interactions. The free crown geometry is not a factor in the exchange reaction equations reported in Section 5.3.2, and we would expect it to bend to incorporate the metal ion.

The relative energies of the ionophores with isomers are reported in Table D2. The total energies of isomers are all within at most 17 kJ/mol, which is not enough of an energy difference to eliminate unstable isomers of the free crown. Further studies will focus on binding affinity to the metal ion and difference in excitation energies between the free ligand and the metal ion in order to tailor the chemosensor towards incorporation and detection of Hg²⁺.

5.3.2 Binding Affinity of Crown Ethers

The crown structures differ in the number of sulfur and oxygen atoms, so we cannot explicitly compare energies of all compounds. Instead, a reaction-based energetics method was used to calculate binding energies ($\Delta\Delta E_{\text{rxn}}$), where there is an exchange of metals between a M^{q+} complex and a metal hydrate. The binding energies are calculated in four parts:

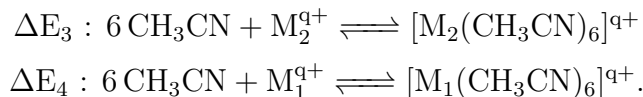




with the overall reaction energy computed as:

$$\Delta\Delta E_{rxn} = (\Delta E_1 + \Delta E_3) - (\Delta E_2 + \Delta E_4)$$

Explicit solvent surrounds the metal ion to recover explicit microsolvation effects.^{146,147} Energy changes were computed similarly with acetonitrile solvent:



Two sets of binding affinity results were generated. The first is a small set of metal ions with all 13 combinations of crowns. Figures D1 - D3 in Appendix D show the values of binding energies of the metal ion exchange reactions calculated for three ions Zn^{2+} , Cd^{2+} , and Hg^{2+} , and three types of solvation: gas phase, water, and acetonitrile. Overall, Cd^{2+} has a higher affinity compared to Zn^{2+} , but some structures are much more likely to bind to Zn^{2+} . The greatest binding affinity with any solvent is between Cd^{2+} and with 18C-O₂S₄-ortho at about -130 kJ/mol. The 18C-O₂S₄-meta and 18C-O₄S₂-para structures have the next greatest binding affinities with Cd^{2+} . Comparison of results for Hg^{2+} and Zn^{2+} shows that all crowns preferentially bind to Hg^{2+} . The crown with the greatest binding affinity for Hg^{2+} , in relation to Zn^{2+} , is 18C-O₂S₄-ortho at almost -200 kJ/mol. The energetics of the ion exchange reaction between Hg^{2+} and Cd^{2+} show that all crowns are selective for Hg^{2+} . The crown with the highest binding affinity for Hg^{2+} with respect to Cd^{2+} is 18C-O₄S₂-para at about -95 kJ/mol. This introductory exploration into binding affinities allows us to narrow down our search for the best candidate for mercury detection before introducing more metal ions. The trend for binding affinity across metal ions is $\text{Hg}^{2+} > \text{Cd}^{2+} > \text{Zn}^{2+}$. The crown with the highest affinity for the mercury ion is 18C-O₄S₂-para, but we will also consider the O₆ crown, S₆ crown as well as the 18C-O₄S₂-ortho crown included in the experimental paper, and extend the work to include more metal ions for the second set of binding affinity results.

Focusing on the metal ions (M_1) that are more negative (green) than Hg^{2+} (M_2),

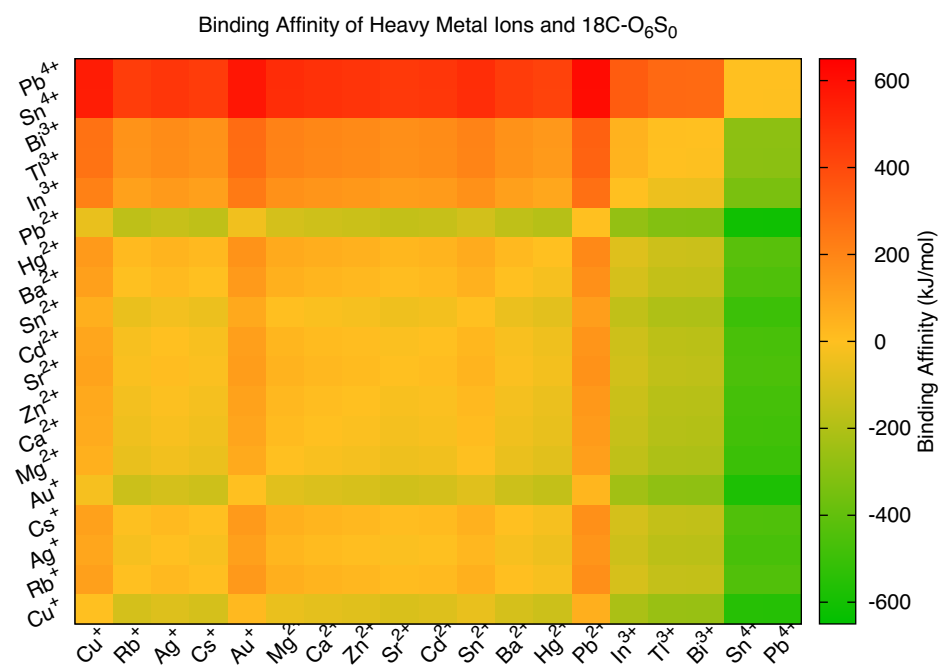


Figure 5.4: Heat map of binding affinity (in kJ/mol) of metal ions of varying size and charge with the 18C-O₆S₀ crown. Negative values (yellow to green) indicate that M_1 binds with greater affinity to the crown than M_2 .

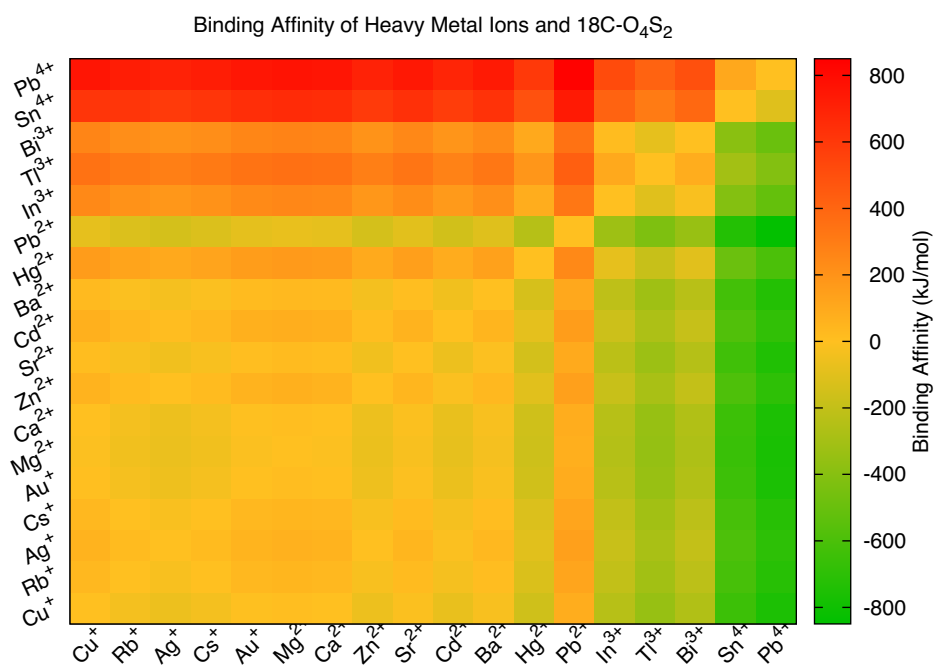


Figure 5.5: Heat map of binding affinity (in kJ/mol) of metal ions of varying size and charge with the 18C-O₄S₂-para crown. Negative values (yellow to green) indicate that M_1 binds with greater affinity to the crown than M_2 .

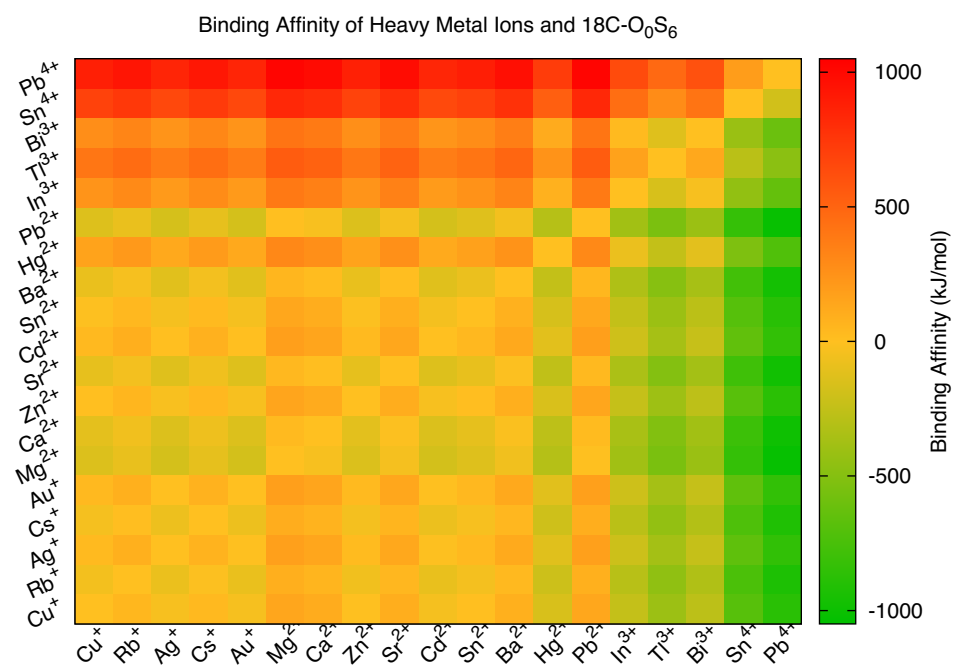


Figure 5.6: A heat map of binding affinity (in kJ/mol) of metal ions of varying size and charge with the 18C-O₀S₆ crown. Negative values (yellow to green) indicate that M_1 binds with greater affinity to the crown than M_2 .

each crown in Figures 5.4 - 5.6, is more likely to bind to In^{3+} , Sn^{4+} , Tl^{3+} , Bi^{3+} , and Pb^{4+} . The trend predicts that the crowns are more likely to bind to metal ions with greater positive charge. However, we must also consider the full system including the fluorophore since experimentally concentration of Hg^{2+} was measured on the basis of fluorescence of the chemosensor.

5.3.3 Introducing the Fluorophore

The full ligand of interest consists of a crown, a benzene linker, and the BODIPY fluorophore, which complicates the structure. Considering all linker and fluorophore positions on each of the 13 crown structures gives us 64 new combinations, which are named with the core crown structure and an alphabetic isomer label. The naming scheme is shown for each crown in Figure 5.7.

Preliminary research was done to identify the most stable chemosensors. Relative energies with respect to linker position are plotted in Figures D4-D7, separated by each isomer.

The most stable $18\text{C-O}_5\text{S}_1$ isomers are **B** and **E**, which have only 1 kJ/mol difference in energy. The lowest energy $18\text{C-O}_1\text{S}_5$ isomer is **F**, which is the lowest energy isomer (by 17 kJ/mol). Figure D5 shows three structural isomers of the parent crown $18\text{C-O}_2\text{S}_4$, where the lowest energy linker position for ortho, meta, and para are **F**, **A**, and **A**, respectively, by at least 3 kJ/mol. Figure D6 has the three structural isomers of $18\text{C-O}_3\text{S}_3$, **-(3)**, **-(2,1)**, and **-(1,1,1)**. For the $18\text{C-O}_3\text{S}_3$ -**3** isomers the most stable linker position is **E** by 6 kJ/mol, the $18\text{C-O}_3\text{S}_3$ -**1,1,1** isomer has two positions, **A** and **B**, which are the lowest energy conformations, and are within 1 kJ/mol of each other. The $18\text{C-O}_3\text{S}_3$ -**2,1** isomer has **L** as the most stable linker position by 5 kJ/mol. Figure D7 shows the three structural isomers of $18\text{C-O}_4\text{S}_2$, ortho, meta, and para, for which the lowest energy linker positions are **B** (**F** within 2 kJ/mol), **E** (**F** within 2 kJ/mol), and **B**, respectively.

The metal ions were reintroduced to coordinate to the crown ether. A similar exchange reaction approach was used to calculate the binding affinity of the full chemosensor (with crown, linker and fluorophore) and a different hydrated metal.

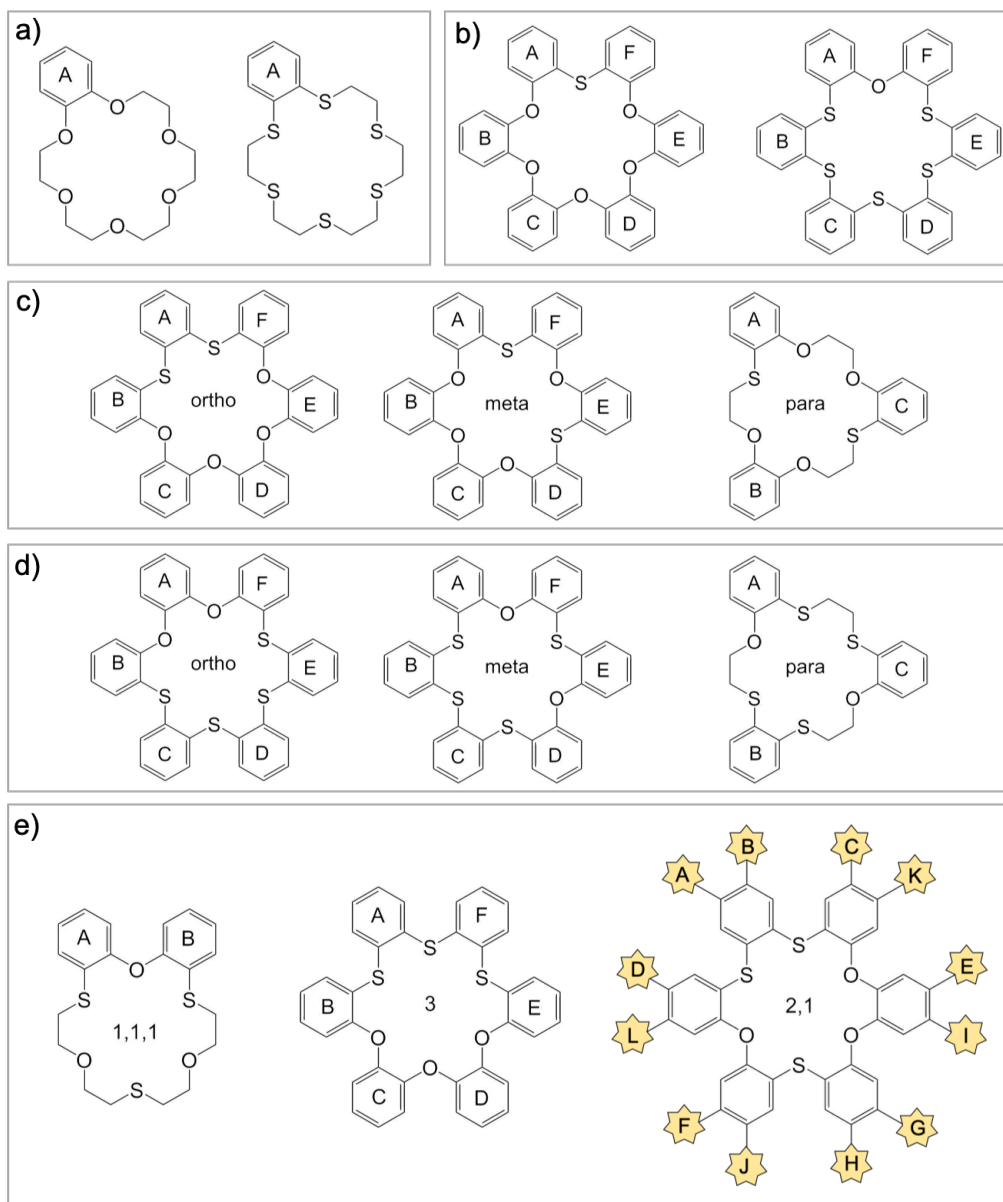


Figure 5.7: 64 structural combinations of the crowns from Figure 5.2, with varying positions of fluorophore. a) $18C-O_6S_0$ and $18C-O_0S_6$ have just one isomer each. b) $18C-O_5S_1$ and $18C-O_1S_5$ have six isomers. c) $18C-O_4S_2$ -ortho and -meta have six isomers and -para has three possible isomers, similar to $18C-O_2S_4$ in d). e) $18C-O_3S_3$ -1,1,1 has two possible isomers, and $18C-O_3S_3$ -3 has six, while with $18C-O_3S_3$ -2,1 all 12 linker positions and fluorophore binding sites are considered.

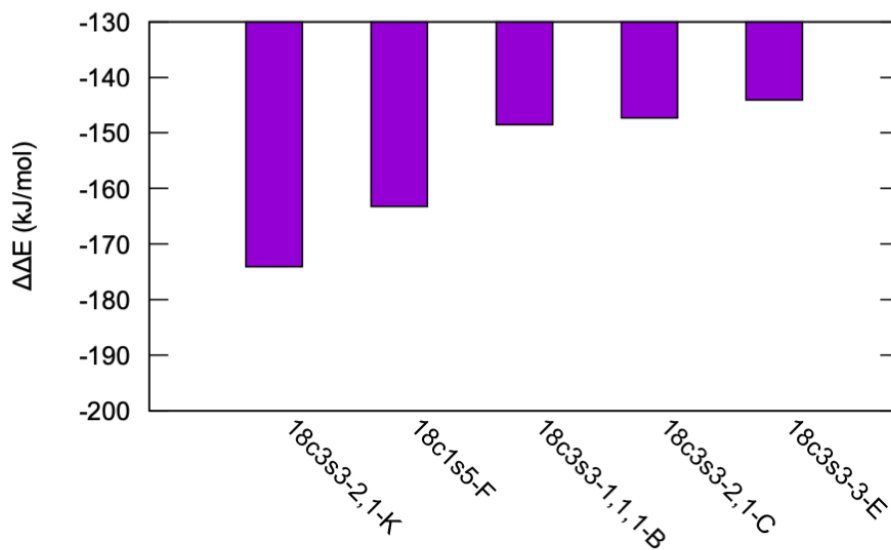


Figure 5.8: Binding affinity for Hg^{2+} versus Zn^{2+} . A negative value ($\Delta\Delta E$) indicates that Hg^{2+} has a higher affinity for the chemosensor than Zn^{2+} .

The five best results (most negative binding affinities) are shown in Figures 5.8 and 5.9. All chemosensors have a preferred binding affinity for Hg^{2+} , with respect to both Cd^{2+} and Zn^{2+} . Both Figures show similarities in that the chemosensors with the most negative binding affinities have three sulfur and three oxygen atoms in the crown ionophore. In the ionophore-only binding affinity studies, the O_3S_3 structures prefer Hg^{2+} , but not to the same extent as other ionophores (namely the O_2S_4 and O_4S_2 analogues). This shows that the binding affinity can be dependent on the entire chemosensor, and not just the ionophore.

5.3.4 Excitation Energies of Chemosensors

As an exercise in the study of structural importance, we calculated excitation energies as the fluorophore was rotated with respect to the linker and crown, and in this section we assess the best dihedral angles for the brightest and most shifted excitation energy with respect to the parent, and each of the three metal complexes (Zn^{2+} , Cd^{2+} , Hg^{2+}). Experimentalists rely heavily on spectra to determine molecular properties, and being able to detect a significant shift in absorption spectra between different compounds is

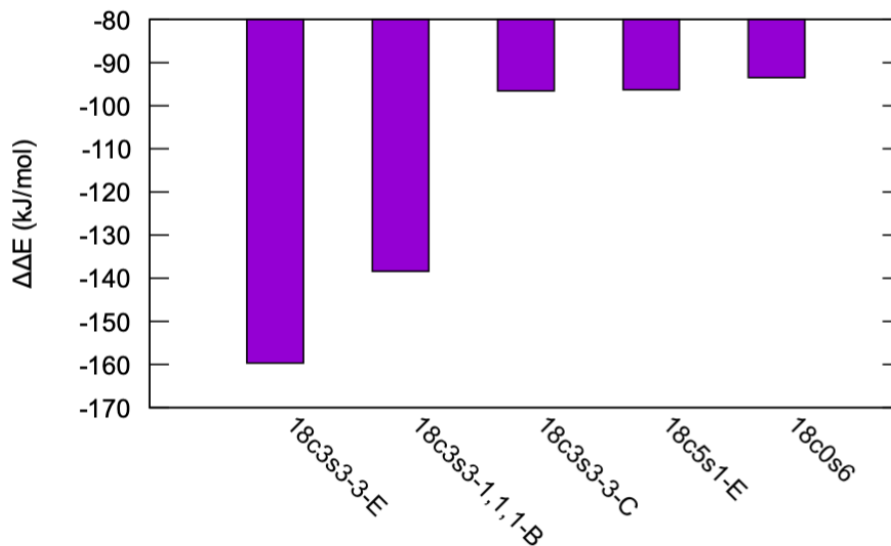


Figure 5.9: Binding affinity for Hg^{2+} versus Cd^{2+} . A negative value ($\Delta\Delta E$) indicates that Hg^{2+} has a higher affinity for the crown than Cd^{2+} .

paramount. We calculated the ten lowest singlet transitions for the parent and metal complex to find the largest difference in excitation energy.

Effect of Fluorophore Rotation on Excitation Energy

The bond attaching the fluorophore to the rest of the chemosensor can freely rotate, so it is possible to examine the excitation energies at different angles. If a specific angle provides a greater difference in wavelength and intensity in the presence of a metal ion with respect to the free ligand, it may be easier to detect the metal ion. An unrelaxed scan of the rotation of the fluorophore in 2° increments about the dihedral angle shown in red in Figure 5.1. The ligand used here is from the experimental paper, 18C-O₄S₂-para. At each point, the lowest three singlet excitation energies were calculated TD-DFT (with the PBE0 functional) and an all-electron 6-31G(d) basis set for lighter atoms and LANL2DZ for the metal. This level of theory will be denoted as TD-DFT(PBE0)/6-31G(d). Results calculated with TD-DFT(CAMB3LYP) and CIS are reported in Appendix D.^a

^aThere may be differences in the level of theory used in the Appendices, and in such cases explanation will be given in the figure captions.

First, an energy profile of the unrelaxed rotation was obtained with the RHF method to determine the highest and lowest energy compounds, as seen in Figure 5.10. The value of 0° is defined as the deviation from the dihedral at the optimized geometry. As expected, the lowest energy compound positions BODIPY almost perpendicular to the plane of the benzene linker, whereas the highest energy compounds (at a difference of +225 kJ/mol) are planar and have repulsive interactions between the hydrogens on the benzene and hydrogens on the fluorophore. The molecule is not likely to rotate 360° experimentally due to steric interactions, but there may be other low energy structures with a higher absorption intensity and shifted excitation energy. These structures may possibly be locked into place with bulkier substituents on BODIPY, therefore designing a brighter chemosensor.

In Figure 5.11, the excitation energy as a function of fluorophore-linker dihedral angle is reported for the brightest three singlet states for the free ligand, and three metal complexes calculated at the TD-DFT(PBE0)/6-31G(d) level of theory. The free ligand results (top left) oscillate by 0.2 eV during rotation for all three states reported. States S_2 and S_3 stop oscillating in the $100\text{-}180^\circ$ range. The Hg^{2+} complex (top right) oscillates by about 0.2 eV, similarly to the parent ligand, but there are no excitations that would warrant an in-depth search of structure. The Zn^{2+} (bottom left) and Cd^{2+} (bottom right) complexes have very similar excitation profiles, where the S_1 state oscillates smoothly within 0.5 eV, and the two higher excited states are similar in energy and shape.

However, it is not enough to look only at excitation energies, but the oscillator strengths should also be analyzed. While there may be a large separation in the excited state energies between the free ligand and the complex, if the states are dark, nothing would be seen experimentally.

The oscillator strengths for the brightest three singlet excited states (the same excitations that are in Figure 5.11) are shown in Figure 5.12. The free ligand compound (top left) shows that there is a large dependence on rotation for all oscillator strengths from the excitations, particularly S_1 and S_2 . The relationship between these two states seem to be inverse: when one state is bright the other is dark, except for at

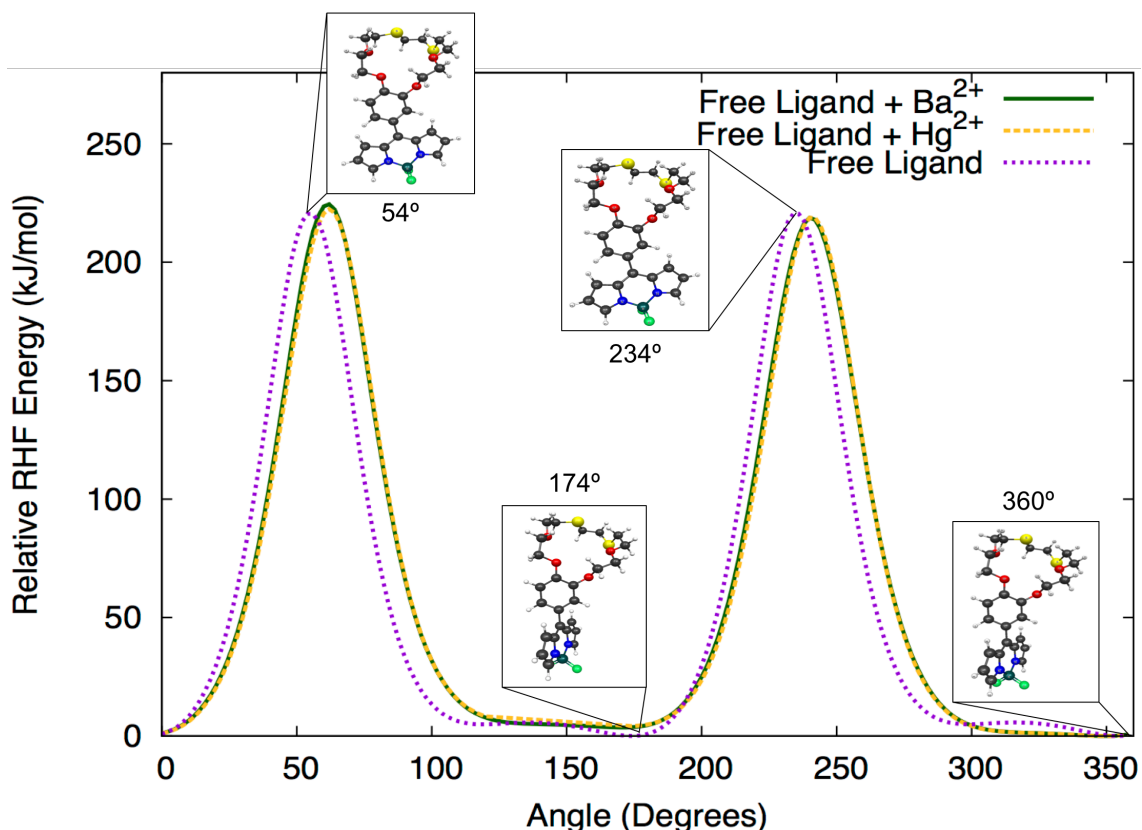


Figure 5.10: A relative RHF energy profile as a function of dihedral angle rotating BODIPY in relation to the benzene linker. At 54° and 234° , the highest energy structures have steric interactions between the hydrogens on BODIPY and on the linker. At 174° and 0° (or 360° , the initial optimized geometry), the most stable structures are highlighted, with the position of the linker slightly rotated to avoid the unfavorable hydrogen interactions.

140° . The S_3 excitation is less dependent on rotation and is always bright. The Hg^{2+} complex (top right) shows that the oscillator strengths for S_3 and S_4 are also related, at 20° and 110° one state becomes bright and the other goes dark, whereas S_{10} is fairly dark except for the 40 - 80° range. There are similarities for Zn^{2+} and Cd^{2+} just as they were for the excitation energies. The oscillator strength for S_1 in both cases is always large, whereas the oscillator strengths from the higher excitations turn on and off with respect to each other, notably at about 35° and 75° for the Zn^{2+} complex, and at 25° and 90° for the Cd^{2+} complex. If we wanted to target higher excitation energies, so they would be more removed from the parent ligands' excitations, we

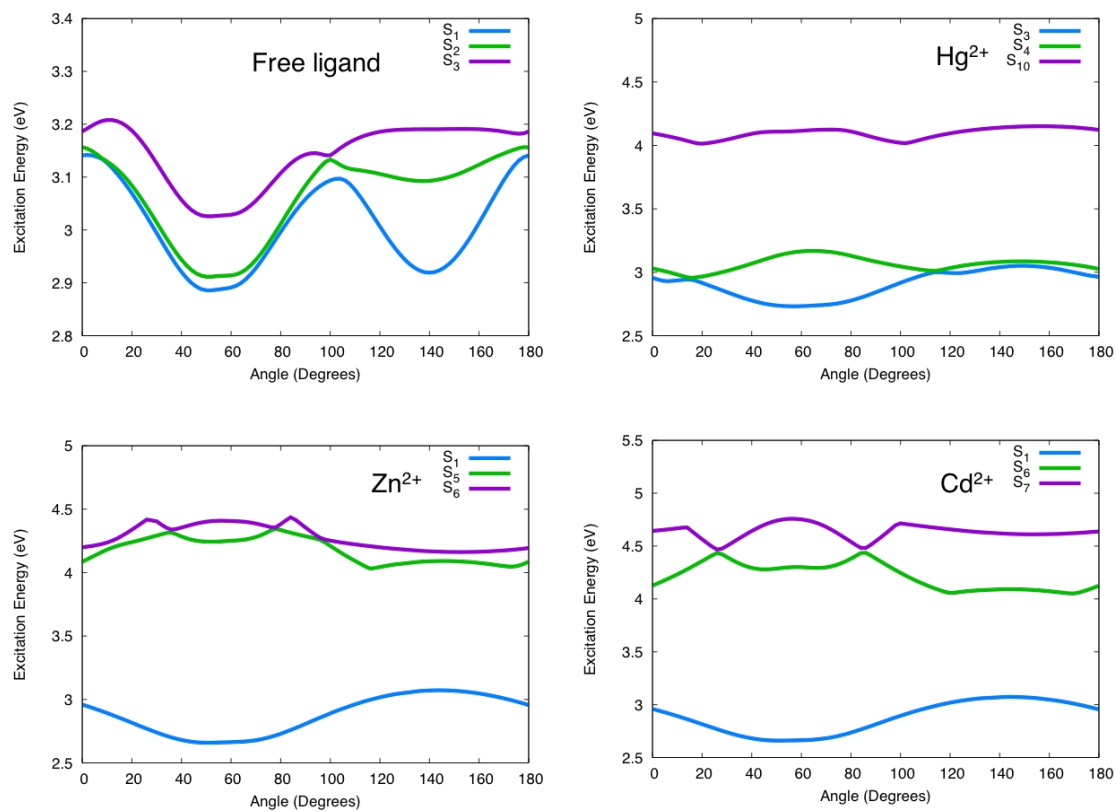


Figure 5.11: A plot of excitation energy as a function of BODIPY-linker dihedral angle. The energies of the brightest three singlet excited states, calculated with TD-DFT(PBE0)/6-31G(d), for the free ligand (top left), ligand with Hg^{2+} (top right), ligand with Zn^{2+} (bottom right), and ligand with Cd^{2+} (bottom left).

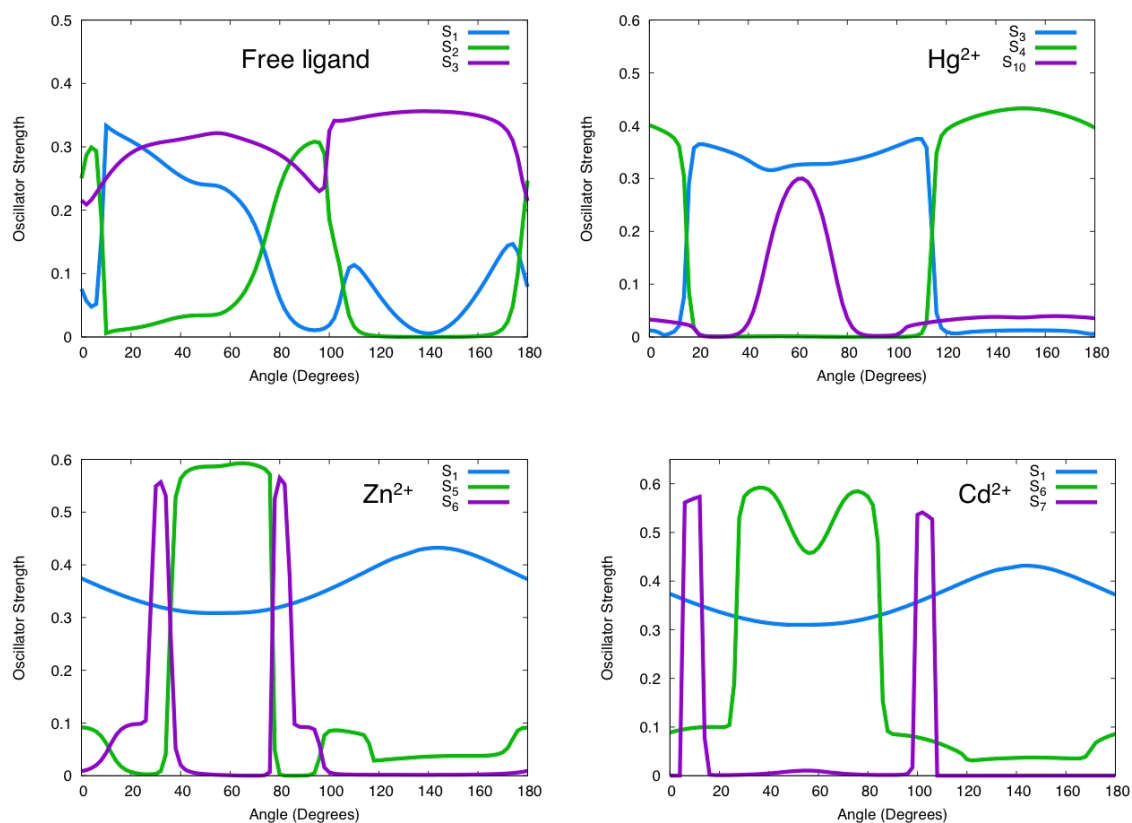


Figure 5.12: A plot of oscillator strength as a function of BODIPY-linker dihedral angle. The oscillator strengths of the brightest three singlet excited states, calculated with TD-DFT(PBE0)/6-31G(d), for the free ligand (top left), ligand with Hg²⁺ (top right), ligand with Zn²⁺ (bottom right), and ligand with Cd²⁺ (bottom left).

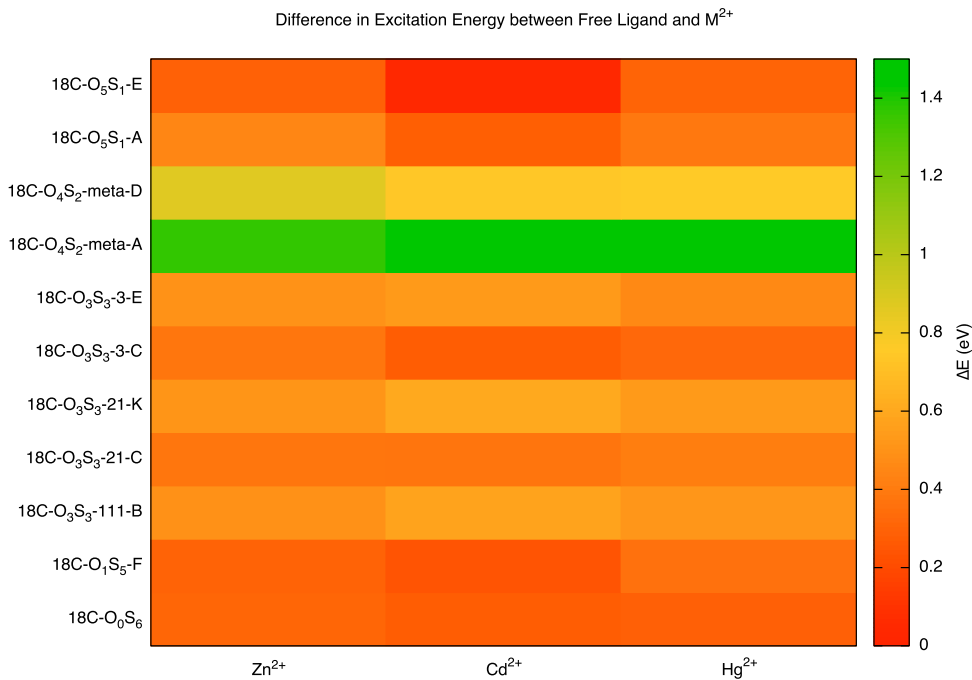


Figure 5.13: Heat map of the difference in excitation energies, ΔE (in eV), of the free ligand and the metal complex. Red squares represent little to no difference with respect to the excitation energy of the parent ligand, and green squares indicate a difference of at least 1 eV.

could do so through trying to lock the dihedral angle at one of those values where the oscillator strength was at a maximum.

Excited States of Chemosensors with M^{2+} Included

To easily detect heavy metal ions, we first selected the chemosensors which preferentially bind to Hg^{2+} . Additionally, the free ligand and metal ion must have a distinct shift in spectra. We computed only the ten lowest singlet vertical excitation energies for the sake of computational time and data set size. Only the states with an oscillator strength greater than 0.1 were considered. Figure 5.13 shows a heat map of the excitation energy difference between the free chemosensor and the metal complex, where red represents little to no difference and green represents a difference of 1.5 eV. Only the compounds that differ the most are shown in this figure.

The 18C-O₄S₂-meta-A structure is very clearly the best candidate to maximize

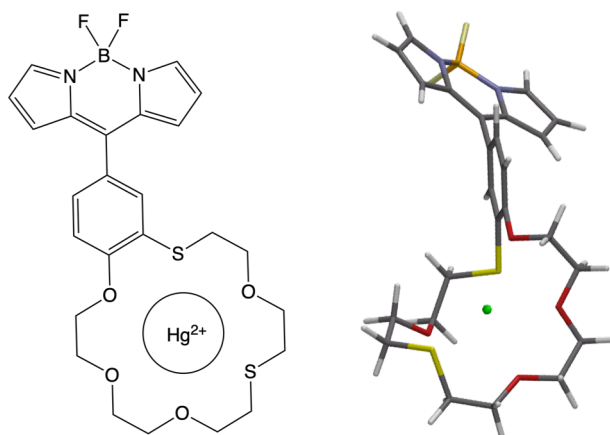


Figure 5.14: *The 18C-O₄S₂-meta-A chemosensor for Hg²⁺. Left: Two-dimensional structure. Right: Three-dimensional structure optimized at the PBE0/6-31G(d)/LANL2DZ level of theory.*

the shift between free chemosensor and any metal complex ($\Delta E=1.4$ eV). Pairing this data with the binding affinity data, Hg²⁺ will be more likely bind to this crown by -56 kJ/mol than Cd²⁺ and by -67 kJ/mol than Zn²⁺. This structure is shown in Figure 5.14, revealing in the three-dimensional structure on the right that the crown ionophore is bent to maximize interactions to the incorporated metal.

5.4 Conclusion

We found that we were not able to gain much information from the energetics of the free crowns and isomers: all structures were within a small energy range. However, when we incorporated the metals, we were able to establish the best chemosensors for Hg²⁺. Binding affinity trends with the ionophore predicted that the crowns are more likely to bind to metal ions with greater positive charge, which is not what was found in the fluorescence experiments. When studying the many structures and isomers of the chemosensor, the selection of metals was narrowed down to include only Group 13. Binding affinities were calculated with each of the three metals, and it was found that almost all of the structures tested preferred to bind with Hg²⁺. The rotation of

the fluorophore with respect to the rest of the chemosensor provided insight into how the oscillator strengths are related with respect to the rotation, but the excitations did not fluctuate much along the profile. The excited state studies brought insight into those structures with the maximum excitation energy gap between the parent ligand and the metal complex. The structure which brought about the largest gap was the 18C-O₄S₂-meta-A structure, and while this structure did not have the largest binding affinity for Hg²⁺, it was still preferred over both Cd²⁺ and Zn²⁺ ions.

Chapter 6

Conclusions

6.1 Summary of Thesis Research

While exploring methodologies to better represent high-lying excitation energies in Chapter 2, results from each of the density functionals with MCP basis sets gave closer values to the SAC-CI reference than all-electron basis sets. Comparison of the results of these methods to experimental GC-VUV spectra showed that oscillator strengths are reliable at lower energies. At higher excitation energies the calculated oscillator strengths are underestimated, but very likely there are many transitions with small intensities adding together to generate an overall high intensity. The worst results came from the PBE0 functional, up to 0.5 eV different than SAC-CI values. The best results along the energy range were calculated with CAM-B3LYP, a long-range corrected functional which improves the description of Rydberg states, although high energy excitations are hard to accurately predict with any method, DFT or SAC-CI, compared to experiment. We are able to predict the shape of the GC-VUV spectra with individual molecules or mixtures of isomers with both DFT and SAC-CI.

The importance of correlated methods for the decomposition of P_4 was clear when preliminary calculations with single-reference and uncorrelated methods were performed; these methods over or underestimated reaction barriers and generated jagged potential energy surfaces around the transition state. Using correlated methods in Chapter 3 generated smooth curves and accurate reaction barriers. Values calculated using the MS-CASPT2 method with the MCP-TZP basis sets are very accurate com-

pared to experiment. The reaction barrier calculated with MC-PDFT/cc-pVDZ is within 1 kcal/mol, but as we increase the basis set the reaction barrier becomes about 10 kcal/mol larger. This good result is probably due to cancellation of errors. MC-PDFT is about two-three orders of magnitude faster in the post-CAS PDFT step than the PT2 step, making the method applicable for larger systems. The (6442) active space includes extra electrons and molecular orbitals to improve on the (4332) valence active space, but brings about only a small difference in reaction enthalpy.

Chapter 4 models high-energy ionized states using DFT where we directly calculated differences in energies. Out of the many density functionals used in this work, the top functionals (TPSSm, B3LYP, BLYP) were used to calculate core electron binding energies of nucleic acid bases. A relativistic correction was applied, but since some functionals can over and underestimate CEBEs for the same atom, only cases where functionals underestimate are corrected. Even so, the mean average deviation with respect to experimental results is only 0.18 eV on average for B3LYP (with relativistic corrections). Computational efficiency is increased with the Δ DFT method compared to the previously suggested Δ MP2 method, while the accuracy remains the same. The Δ DFT method is sensitive enough to determine differences between nucleic acid base tautomers and calculations reflect small experimental shifts.

To detect heavy metals, we need a ligand that is both selective towards a specific metal and has a distinct shift in excitation energy when the metal is coordinated. Comparing the energetics of different isomers of the ionophores and chemosensors studied in Chapter 5 did not allow us to eliminate those less stable. A reaction-based method of calculating binding energies separated the energies as well as including explicit solvation effects. This data, paired with excitation energies of the parent and metal complex provided insight to designing a Hg^{2+} specific thiacyclopentadiene-based chemosensor with a vertical excitation shift of 1.5 eV, namely the 18C-O₄S₂-meta-a chemosensor.

6.2 Future Work

The single-reference methods used in Chapter 2 were not successful in capturing the high-energy region of the experimental spectra. Expanding the methods to include multireference symmetry adapted cluster¹⁴⁸ (MR-SAC), or any multireference method would allow for better description of excited states. The SAC-CI SD-R method only allows for single and double-excitations, and increasing the number of excited electrons could better describe the high-energy excitation range. In addition, using a basis set with more diffuse functions might better describe any Rydberg states that had not been captured previously.

In Chapter 3, the thermal decomposition of P_4 was carried out in C_{2v} symmetry; however, it is possible that the dissociation occurs in a lower symmetry. It would be worthwhile to investigate less symmetric geometries and also to investigate the thermal decomposition of As_4 and Sb_4 . In the latter regard, it is expected that as the inclusion of relativistic effects is more important for heavier elements,¹⁴⁹ the ANO-RCC basis set (or MCPs) could be used to account for this. New active spaces must be designed to account for d-orbitals and we expect these active spaces to be more sensitive to the electrons and orbitals included.

With the many different types of density functionals used in Chapter 4, only some are parameterized with experimental valence ionization potentials, not even core ionization potentials. It was of interest to parameterize a functional to fix this problem. We have altered the GAMESS source code to include adjustable parameters for B3LYP since it was the most accurate functional for CEBEs. We plan to generate altered parameters for this functional to better represent CEBEs for nucleic acid bases. We are interested in improving this method in order to apply it to larger systems (e.g. base pairs) since it is accurate and extremely efficient.

The best chemosensor in Chapter 5 was the best only out of the structures studied, and while the data set was large, it could still be extended to include larger crowns to see if that would affect the binding affinity. Additionally, other fluorophores could be used to compute excitation energies to see if the shifts between parent and metal

complex widen. A more comprehensive test of metals could be done, including those M^{3+} and M^{4+} ions that had a more negative binding affinity for some crowns compared to Hg^{2+} .

Bibliography

- [1] Radhakrishnan, M. L. *Thinking, Periodically: Poetic Life Notions in Brownian Motion*; CreateSpace Independent Publishing Platform, 2018.
- [2] Levine, I. N. *Quantum Chemistry*; Pearson Higher Ed., 2013.
- [3] McLean, A.; Chandler, G. *The Journal of Chemical Physics* **1980**, *72*, 5639–5648.
- [4] Hohenberg, P.; Kohn, W. *Phys. Rev. B* **1964**, *136*, 864–871.
- [5] Kohn, W.; Sham, L. J. *Phys. Rev.* **1965**, *140*, A1133–A1138.
- [6] Boys, S. F. *Proc. R. Soc. Lond. A* **1950**, *200*, 542–554.
- [7] te Velde, G.; Bickelhaupt, F. M.; Baerends, E. J.; Fonseca Guerra, C.; van Gisbergen, S. J. A.; Snijders, J. G.; Ziegler, T. *J. Comput. Chem.* **2001**, *22*, 931–967.
- [8] Guerra, C. F.; Snijders, J.; te Velde, G. t.; Baerends, E. J. *Theor. Chem. Acc.* **1998**, *99*, 391–403.
- [9] Baerends, E. J. et al. ADF2017, SCM, Theoretical Chemistry, Vrije Universiteit, Amsterdam, The Netherlands, <https://www.scm.com>.
- [10] Stevens, W. J.; Basch, H.; Krauss, M. *J. Chem. Phys.* **1984**, *81*, 6026–6033.
- [11] Stevens, W. J.; Krauss, M.; Basch, H.; Jasien, P. G. *Can. J. Chem.* **1992**, *70*, 612–630.

- [12] Bonifacic, V.; Huzinaga, S. *J. Chem. Phys.* **1974**, *60*, 2779–2786.
- [13] Löwdin, P. *Adv. Chem. Phys.* **1959**, *2*, 207–322.
- [14] Coester, F.; Kümmel, H. *Nucl. Phys.* **1960**, *17*, 477–485.
- [15] Čížek, J. *J. Chem. Phys.* **1966**, *45*, 4256–4266.
- [16] Nakatsuji, H.; Hirao, K. *J. Chem. Phys.* **1978**, *68*, 2053–2065.
- [17] Hegarty, D.; Robb, M. A. *Mol. Phys.* **1979**, *38*, 1795–1812.
- [18] Eade, R. H.; Robb, M. A. *Chem. Phys. Lett.* **1981**, *83*, 362–368.
- [19] Malmqvist, P.-Å.; Rendell, A.; Roos, B. O. *J. Phys. Chem.* **1990**, *94*, 5477–5482.
- [20] Szalay, P. G.; Muller, T.; Gidofalvi, G.; Lischka, H.; Shepard, R. *Chem. Rev.* **2011**, *112*, 108–181.
- [21] Werner, H.-J.; Meyer, W. *J. Chem. Phys.* **1981**, *74*, 5794–5801.
- [22] Møller, C.; Plesset, M. S. *Phys. Rev.* **1934**, *46*, 618–622.
- [23] Andersson, K.; Malmqvist, P. A.; Roos, B. O.; Sadlej, A. J.; Wolinski, K. *J. Phys. Chem.* **1990**, *94*, 5483–5488.
- [24] Andersson, K.; Malmqvist, P.-Å.; Roos, B. O. *J. Chem. Phys.* **1992**, *96*, 1218–1226.
- [25] Finley, J.; Malmqvist, P.-Å.; Roos, B. O.; Serrano-Andrés, L. *Chem. Phys. Lett.* **1998**, *288*, 299–306.
- [26] Forsberg, N.; Malmqvist, P.-Å. *Chem. Phys. Lett.* **1997**, *274*, 196–204.
- [27] Bauernschmitt, R.; Ahlrichs, R. *Chem. Phys. Lett.* **1996**, *256*, 454–464.
- [28] Li Manni, G.; Carlson, R. K.; Luo, S.; Ma, D.; Olsen, J.; Truhlar, D. G.; Gagliardi, L. *J. Chem. Theory Comput.* **2014**, *10*, 3669–3680.

- [29] Klobukowski, M.; Huzinaga, S.; Sakai, Y. *Model core potentials: Theory and applications*; World Scientific: Singapore, 1999; Vol. 3.
- [30] San Mon, M.; Mori, H.; Miyoshi, E. *Chem. Phys. Lett.* **2008**, *462*, 23–26.
- [31] Mori, H.; Yamagishi, A.; Sato, H. *J. Chem. Phys.* **2011**, *135*, 084506/1–7.
- [32] Schug, K. A.; Sawicki, I.; Carlton Jr, D. D.; Fan, H.; McNair, H. M.; Nimmo, J. P.; Kroll, P.; Smuts, J.; Walsh, P.; Harrison, D. *Anal. Chem.* **2014**, *86*, 8329–8335.
- [33] Dreuw, A.; Head-Gordon, M. *Chemical reviews* **2005**, *105*, 4009–4037.
- [34] Nakatsuji, H. *J. Chem. Phys.* **1991**, *94*, 6716–6727.
- [35] Frisch, M.; Trucks, G.; Schlegel, H.; Scuseria, G.; Robb, M.; Cheeseman, J.; Scalmani, G.; Barone, V.; Mennucci, B.; Petersson, G. *Inc., Wallingford CT*
- [36] Schmidt, M.; Baldridge, K.; Boatz, J.; Elbert, S.; Gordon, M.; Jensen, J.; Koseki, S.; Matsunaga, N.; Nguyen, K.; Su, S.; Windus, T.; Dupuis, M.; Montgomery, J. *J. Comput. Chem.* **1993**, *14*, 1347–1363.
- [37] Yanai, T.; Tew, D. P.; Handy, N. C. *Chem. Phys. Lett.* **2004**, *393*, 51–57.
- [38] Adamo, C.; Barone, V. *J. Chem. Phys.* **1999**, *110*, 6158–6170.
- [39] Jacquemin, D.; Wathelet, V.; Perpète, E. A.; Adamo, C. *J. Chem. Theory Comput.* **2009**, *5*, 2420–2435.
- [40] Peach, M. J.; Benfield, P.; Helgaker, T.; Tozer, D. J. *J. Chem. Phys.* **2008**, *128*, 044118/1–8.
- [41] Huh, D.-S.; Jung, K.-H. *Bull. Korean Chem. Soc.* **1992**, *13*, 65–70.
- [42] Haeser, M.; Schneider, U.; Ahlrichs, R. *J. Am. Chem. Soc.* **1992**, *114*, 9551–9559.

- [43] Brassington, N.; Edwards, H.; Long, D. *J. Raman Spectrosc.* **1981**, *11*, 346–348.
- [44] Rennie, E. E.; Mayer, P. M. *J. Chem. Phys.* **2004**, *120*, 10561–10578.
- [45] Ahlrichs, R.; Brode, S.; Ehrhardt, C. *J. Am. Chem. Soc.* **1985**, *107*, 7260–7264.
- [46] Kutzelnigg, W. *Angew. Chem. Int. Ed.* **1984**, *23*, 272–295.
- [47] Bock, H.; Müller, H. *Inorg. Chem.* **1984**, *23*, 4365–4368.
- [48] Schmidt, M. W.; Gordon, M. S. *Inorg. Chem.* **1985**, *24*, 4503–4506.
- [49] Haworth, N. L.; Bacskay, G. B. *J. Chem. Phys.* **2002**, *117*, 11175–11187.
- [50] Jerabek, P.; Frenking, G. *Theor. Chem. Acc.* **2014**, *133*, 1447/1–9.
- [51] Karton, A.; Martin, J. M. *Mol. Phys.* **2007**, *105*, 2499–2505.
- [52] Karton, A.; Rabinovich, E.; Martin, J. M.; Ruscic, B. *J. Chem. Phys.* **2006**, *125*, 144108/1–17.
- [53] Wang, L.-P.; Tofan, D.; Chen, J.; Van Voorhis, T.; Cummins, C. C. *RSC Adv.* **2013**, *3*, 23166–23171.
- [54] Corbridge, D. E. C. *Structural chemistry of phosphorus*; Elsevier Scientific Pub. Co.: Amsterdam, NL, 1974.
- [55] Bartlett, R. J. *Annu. Rev. Phys. Chem.* **1981**, *32*, 359–401.
- [56] Kowalski, K.; Piecuch, P. *J. Chem. Phys.* **2000**, *113*, 18–35.
- [57] Sherrill, C. D. *Annu Rep Comput Chem* **2005**, *1*, 45–56.
- [58] Aquilante, F.; Autschbach, J.; Carlson, R. K.; Chibotaru, L. F.; Delcey, M. G.; De Vico, L.; Ferré, N.; Frutos, L. M.; Gagliardi, L.; Garavelli, M. *J. Comput. Chem.* **2016**, *37*, 506–541.
- [59] Veryazov, V.; Malmqvist, P. Å.; Roos, B. O. *Int. J. Quantum Chem.* **2011**, *111*, 3329–3338.

- [60] Ghigo, G.; Roos, B. O.; Malmqvist, P.-Å. *Chem. Phys. Lett.* **2004**, *396*, 142–149.
- [61] Woon, D. E.; Dunning Jr., T. H. *J. Chem. Phys.* **1993**, *98*, 1358–1371.
- [62] Dunning Jr, T. H.; Peterson, K. A.; Wilson, A. K. *J. Chem. Phys.* **2001**, *114*, 9244–9253.
- [63] Miyoshi, E.; Mori, H.; Hirayama, R.; Osanai, Y.; Noro, T.; Honda, H.; Klobukowski, M. *J. Chem. Phys.* **2005**, *122*, 074104/1–8.
- [64] Lee, C.; Yang, W.; Parr, R. G. *Phys. Rev. B: Condens. Matter* **1988**, *37*, 785–789.
- [65] Becke, A. D. *J. Chem. Phys.* **1993**, *98*, 5648–5652.
- [66] Rassolov, V. A.; Ratner, M. A.; Pople, J. A.; Redfern, P. C.; Curtiss, L. A. *J. Comput. Chem.* **2001**, *22*, 976–984.
- [67] Frisch, M. J.; Trucks, G. W.; Schlegel, H. B.; Scuseria, G. E.; Robb, M. A.; Cheeseman, J. R.; Scalmani, G.; Barone, V.; Petersson, G. A. Gaussian09 Revision B.01. 2009; Gaussian Inc. Wallingford CT.
- [68] Zhao, Y.; Truhlar, D. G. *Acc. Chem. Res.* **2008**, *41*, 157–167.
- [69] Zhao, Y.; Truhlar, D. G. *Theor. Chem. Acc.* **2008**, *120*, 215–241.
- [70] Alecu, I.; Zheng, J.; Zhao, Y.; Truhlar, D. G. *J. Chem. Theory Comput.* **2010**, *6*, 2872–2887.
- [71] de Brouckere, G.; Feller, D. *J. Phys. B: At. Mol. Opt. Phys.* **1995**, *28*, 1393–1410.
- [72] Wang, J.-M.; Feng, H.-Q.; Sun, J.-F. *Int. J. Quantum Chem.* **2013**, *113*, 902–907.

- [73] Jie-Min, W.; Heng-Qiang, F.; Jin-Feng, S.; De-Heng, S. *Chin. Phys. B* **2012**, *21*, 023102/1–8.
- [74] Xu, L. T.; Dunning Jr, T. H. *J. Chem. Theory Comput.* **2015**, *11*, 2496–2507.
- [75] Haynes, W. M. In *CRC Handbook of Chemistry and Physics*, 97th ed.; Press, C., Ed.; Taylor & Francis: Boca Raton, FL, 2016.
- [76] Bagus, P. S.; Schaefer III, H. F. *J. Chem. Phys.* **1971**, *55*, 1474–1475.
- [77] Bagus, P. S.; Schaefer III, H. F. *J. Chem. Phys.* **1972**, *56*, 224–226.
- [78] Ziegler, T.; Rauk, A.; Baerends, E. J. *Theor. Chim. Acta* **1977**, *43*, 261–271.
- [79] Snyder, L. C. *J. Chem. Phys.* **1971**, *55*, 95–99.
- [80] Gilbert, A. T.; Besley, N. A.; Gill, P. M. *J. Phys. Chem. A* **2008**, *112*, 13164–13171.
- [81] Shim, J.; Klobukowski, M.; Barysz, M.; Leszczynski, J. *Phys. Chem. Chem. Phys.* **2011**, *13*, 5703–5711.
- [82] Chong, D. P. *J. Chem. Phys.* **1995**, *103*, 1842–1845.
- [83] Cavigliasso, G.; Chong, D. P. *J. Chem. Phys.* **1999**, *111*, 9485–9492.
- [84] Chong, D. P.; Aplincourt, P.; Bureau, C. *J. Phys. Chem. A* **2002**, *106*, 356–362.
- [85] Chong, D. P. *J. Electron. Spectrosc. Relat. Phenom.* **2007**, *159*, 94–96.
- [86] Plekan, O.; Feyer, V.; Richter, R.; Coreno, M.; De Simone, M.; Prince, K.; Trofimov, A.; Gromov, E.; Zaytseva, I.; Schirmer, J. *Chem. Phys.* **2008**, *347*, 360–375.
- [87] Schirmer, J. *Phys. Rev. A* **1982**, *26*, 2395–2416.
- [88] Feyer, V.; Plekan, O.; Richter, R.; Coreno, M.; Vall-Llosera, G.; Prince, K. C.; Trofimov, A. B.; Zaytseva, I. L.; Moskovskaya, T. E.; Gromov, E. V. *J. Phys. Chem. A* **2009**, *113*, 5736–5742.

- [89] Plekan, O.; Feyer, V.; Richter, R.; Coreno, M.; Vall-llosera, G.; Prince, K. C.; Trofimov, A. B.; Zaytseva, I. L.; Moskovskaya, T. E.; Gromov, E. V. *J. Phys. Chem. A* **2009**, *113*, 9376–9385.
- [90] Dunning Jr., T. H. *J. Chem. Phys.* **1989**, *90*, 1007–1023.
- [91] Woon, D. E.; Dunning Jr, T. H. *J. Chem. Phys.* **1995**, *103*, 4572–4585.
- [92] Mukherjee, P.; Chong, D. *Chem. Phys. Lett.* **1985**, *120*, 163–166.
- [93] Chong, D. P. *Chem. Phys. Lett.* **1995**, *232*, 486–490.
- [94] Schmidt, M. W.; Baldrige, K. K.; Boatz, J. A.; Elbert, S. T.; Gordon, M. S.; Jensen, J. H.; Koseki, S.; Matsunaga, N.; Nguyen, K. A.; Su, S. *J. Comput. Chem.* **1993**, *14*, 1347–1363.
- [95] Becke, A. D. *Phys. Rev. A* **1988**, *38*, 3098–3100.
- [96] Perdew, J. P.; Ruzsinszky, A.; Tao, J.; Csonka, G. I.; Scuseria, G. E. *Phys. Rev. A* **2007**, *76*, 042506/1–6.
- [97] Jolly, W.; Bomben, K.; Eyermann, C. *At. Data Nucl. Data Tables* **1984**, *31*, 433–493.
- [98] Lee, S.-H.; Helal, A.; Kim, H.-S. *Bull. Korean Chem. Soc.* **2010**, *31*, 615–619.
- [99] Passariello, B.; Barbaro, M.; Quaresima, S.; Casciello, A.; Marabini, A. *Microchem. J.* **1996**, *54*, 348–354.
- [100] Martinis, E. M.; Bertón, P.; Olsina, R. A.; Altamirano, J. C.; Wuilloud, R. G. *J. Hazard. Mater.* **2009**, *167*, 475–481.
- [101] Yang, F.; Liu, R.; Tan, Z.; Wen, X.; Zheng, C.; Lv, Y. *J. Hazard. Mater.* **2010**, *183*, 549–553.
- [102] Abu-Shawish, H. M. *J. Hazard. Mater.* **2009**, *167*, 602–608.

- [103] Khani, H.; Rofouei, M. K.; Arab, P.; Gupta, V. K.; Vafaei, Z. *J. Hazard. Mater.* **2010**, *183*, 402–409.
- [104] Kondo, S.; Takahashi, T.; Takiguchi, Y.; Unno, M. *Tetrahedron Lett.* **2011**, *52*, 453–457.
- [105] Móczár, I.; Huszthy, P.; Mezei, A.; Kádár, M.; Nyitrai, J.; Tóth, K. *Tetrahedron* **2010**, *66*, 350–358.
- [106] McClure, D. S. *J. Chem. Phys.* **1952**, *20*, 682–686.
- [107] Varnes, A. W.; Dodson, R. B.; Wehry, E. *J. Am. Chem. Soc.* **1972**, *94*, 946–950.
- [108] Lee, D.-N.; Kim, G.-J.; Kim, H.-J. *Tetrahedron Lett.* **2009**, *50*, 4766–4768.
- [109] Kiwan, A.; El-Shahawi, M.; Aldhaheri, S.; Saleh, M. *Talanta* **1997**, *45*, 203–211.
- [110] Guo, X.; Qian, X.; Jia, L. *J. Am. Chem. Soc.* **2004**, *126*, 2272–2273.
- [111] Klein, G.; Kaufmann, D.; Schürch, S.; Reymond, J.-L. *Chem. Commun.* **2001**, 561–562.
- [112] Prodi, L.; Bargossi, C.; Montalti, M.; Zaccheroni, N.; Su, N.; Bradshaw, J. S.; Izatt, R. M.; Savage, P. B. *J. Am. Chem. Soc.* **2000**, *122*, 6769–6770.
- [113] Descalzo, A. B.; Martínez-Máñez, R.; Radeaglia, R.; Rurack, K.; Soto, J. *J. Am. Chem. Soc.* **2003**, *125*, 3418–3419.
- [114] Zhang, X.-B.; Guo, C.-C.; Li, Z.-Z.; Shen, G.-L.; Yu, R.-Q. *Anal. Chem.* **2002**, *74*, 821–825.
- [115] Aragoni, M. C.; Arca, M.; Demartin, F.; Devillanova, F. A.; Isaia, F.; Garau, A.; Lippolis, V.; Jalali, F.; Papke, U.; Shamsipur, M. *Inorg. Chem.* **2002**, *41*, 6623–6632.
- [116] Chen, C.-T.; Huang, W.-P. *J. Am. Chem. Soc.* **2002**, *124*, 6246–6247.

- [117] Mayr, T.; Liebsch, G.; Klimant, I.; Wolfbeis, O. S. *Analyst* **2002**, *127*, 201–203.
- [118] Davidson, P. W.; Myers, G. J.; Cox, C.; Shamlaye, C. F.; Marsh, D. O.; Tanner, M. A.; Berlin, M.; Sloane-Reeves, J.; Cernichiari, E.; Choisy, O. *Neurotoxicology* **1995**, *16*, 677–688.
- [119] Mutter, J.; Yeter, D. *Curr. Med. Chem.* **2008**, *15*, 3000–3010.
- [120] Harada, M. *Crit. Rev. Toxicol.* **1995**, *25*, 1–24.
- [121] Fujiki, M.; Tajima, S. *Water Sci. Technol.* **1992**, *25*, 133–140.
- [122] Yoon, J.; Ohler, N. E.; Vance, D. H.; Aumiller, W. D.; Czarnik, A. W. *Tetrahedron Lett.* **1997**, *38*, 3845–3848.
- [123] Sakamoto, H.; Ishikawa, J.; Nakao, S.; Wada, H. *Chem. Commun.* **2000**, 2395–2396.
- [124] Sasaki, D.; Padilla, B. *Chem. Commun.* **1998**, 1581–1582.
- [125] Nolan, E. M.; Lippard, S. J. *J. Am. Chem. Soc.* **2003**, *125*, 14270–14271.
- [126] Zalewski, P. D.; Forbes, I. J.; Betts, W. *Biochem. J* **1993**, *296*, 403–408.
- [127] Chen, X.; Jou, M. J.; Lee, H.; Kou, S.; Lim, J.; Nam, S.-W.; Park, S.; Kim, K.-M.; Yoon, J. *Sens. Actuators, B* **2009**, *137*, 597–602.
- [128] Fakhari, A. R.; Ganjali, M. R.; Shamsipur, M. *Anal. Chem.* **1997**, *69*, 3693–3696.
- [129] Hsieh, Y.-C.; Chir, J.-L.; Wu, H.-H.; Chang, P.-S.; Wu, A.-T. *Carbohydr. Res.* **2009**, *344*, 2236–2239.
- [130] Kubo, K.; Sakurai, T. *Heterocycles* **2000**, *52*, 945–976.
- [131] Callan, J. F.; de Silva, A. P.; Magri, D. C. *Tetrahedron* **2005**, *61*, 8551–8588.
- [132] Bren, V. A. *Russ. Chem. Rev.* **2001**, *70*, 1017–1036.

- [133] Kimura, K.; Sakamoto, H.; Nakamura, M. *Bull. Chem. Soc. Jpn.* **2003**, *76*, 225–245.
- [134] Alfimov, M. V.; Fedorova, O. A.; Gromov, S. P. *J. Photochem. Photobiol., A* **2003**, *158*, 183–198.
- [135] Killoran, J.; O’Shea, D. F. *Chem. Commun.* **2006**, 1503–1505.
- [136] Kim, H.-J.; Kim, S.-H.; Kim, J.-H.; Lee, E.-H.; Kim, K.-W.; Kim, J. S. *Bull. Korean Chem. Soc.* **2008**, *29*, 1831–1834.
- [137] Cha, N. R.; Kim, M. Y.; Kim, Y. H.; Choe, J.-I.; Chang, S.-K. *J. Chem. Soc., Perkin Trans. 2* **2002**, *0*, 1193–1196.
- [138] Rurack, K.; Resch-Genger, U.; Bricks, J. L.; Spieles, M. *Chem. Commun.* **2000**, 2103–2104.
- [139] Pedersen, C. J. *J. Am. Chem. Soc.* **1967**, *89*, 7017–7036.
- [140] Humphry-Baker, R.; Grätzel, M.; Tundo, P.; Pelizzetti, E. *Angew. Chem. Int. Ed.* **1979**, *18*, 630–631.
- [141] Gubelmann, M.; Harriman, A.; Lehn, J.-M.; Sessler, J. L. *J. Chem. Soc., Chem. Commun.* **1988**, 77–79.
- [142] Lehn, J.-M. *Angew. Chem. Int. Ed.* **1990**, *29*, 1304–1319.
- [143] Gajewski, M.; Tuszynski, J.; Mori, H.; Miyoshi, E.; Klobukowski, M. *Inorg. Chim. Acta* **2008**, *361*, 2166–2171.
- [144] Chartres, J. D.; Davies, M. S.; Lindoy, L. F.; Meehan, G. V.; Wei, G. *Inorg. Chem. Commun.* **2006**, *9*, 751–754.
- [145] Stewart, J. J. *J. Mol. Model.* **2007**, *13*, 1173–1213.
- [146] Thompson, M. A.; Glendening, E. D.; Feller, D. *J. Phys. Chem.* **1994**, *98*, 10465–10476.

- [147] Glendening, E. D.; Feller, D.; Thompson, M. A. *J. Am. Chem. Soc.* **1994**, *116*, 10657–10669.
- [148] Nakatsuji, H. *The Journal of chemical physics* **1985**, *83*, 713–722.
- [149] Xu, X.; Truhlar, D. G. *J. Chem. Theory Comput.* **2011**, *8*, 80–90.

Appendix A

Appendix to Chapter 2

A1 Legend of Individual Contributions

5.644 A" 0.0011	9.073 A' 0.0158	10.398 A" 0.0014	11.268 A" 0.0310
6.266 A" 0.0041	9.092 A" 0.0043	10.426 A" 0.0159	11.340 A" 0.0053
6.330 A' 0.2761	9.109 A" 0.0045	10.479 A' 0.0561	11.399 A' 0.0939
6.670 A' 0.0042	9.174 A" 0.0012	10.495 A' 0.0190	11.426 A" 0.0093
6.681 A" 0.0005	9.294 A' 0.0104	10.550 A' 0.0035	11.463 A" 0.0015
6.893 A" 0.0029	9.334 A' 0.0919	10.617 A' 0.0047	11.487 A' 0.0187
6.956 A" 0.0013	9.360 A" 0.0006	10.641 A" 0.0330	11.520 A' 0.0143
7.157 A' 0.0027	9.579 A' 0.0104	10.661 A' 0.0221	11.573 A' 0.0485
7.462 A' 0.0640	9.610 A" 0.0255	10.664 A" 0.0342	11.616 A' 0.0121
7.766 A' 0.0069	9.657 A' 0.0065	10.739 A' 0.0112	11.639 A" 0.0001
7.773 A' 0.0303	9.690 A" 0.0220	10.754 A" 0.0137	11.688 A" 0.0182
7.866 A' 0.0420	9.739 A' 0.0102	10.829 A" 0.0122	11.693 A' 0.0322
7.930 A" 0.0014	9.827 A' 0.3060	10.930 A' 0.0751	11.710 A" 0.0048
8.074 A" 0.0001	9.843 A' 0.0309	10.943 A" 0.0263	11.737 A' 0.0086
8.081 A' 0.0368	9.882 A' 0.0340	10.947 A' 0.0467	11.756 A" 0.0006
8.325 A' 0.0031	9.889 A" 0.0007	10.975 A' 0.0127	11.802 A' 0.0116
8.417 A" 0.0016	9.923 A' 0.1413	10.988 A" 0.0198	11.839 A' 0.0114
8.431 A' 0.0156	10.082 A" 0.0101	10.998 A' 0.0338	11.863 A" 0.0227
8.534 A" 0.0047	10.125 A' 0.0149	11.035 A' 0.0454	11.909 A" 0.0093
8.629 A' 0.2751	10.148 A' 0.0260	11.067 A" 0.0004	11.939 A' 0.0580
8.932 A" 0.0557	10.202 A' 0.0332	11.117 A" 0.0357	11.962 A' 0.0813
8.938 A' 0.0102	10.287 A" 0.0105	11.142 A" 0.0001	12.015 A" 0.1345
8.987 A' 0.0032	10.354 A" 0.0064	11.158 A' 0.0117	12.020 A' 0.0335
9.007 A' 0.0001	10.382 A' 0.0380	11.186 A' 0.0275	

Figure A1: Legend of individual contributions from CAM-B3LYP/amcp3-Br. Labels represent excitation energy, symmetry of the state and oscillator strength, respectively.

A2 Experimental and Calculated Spectra with a Triple-zeta Basis Set

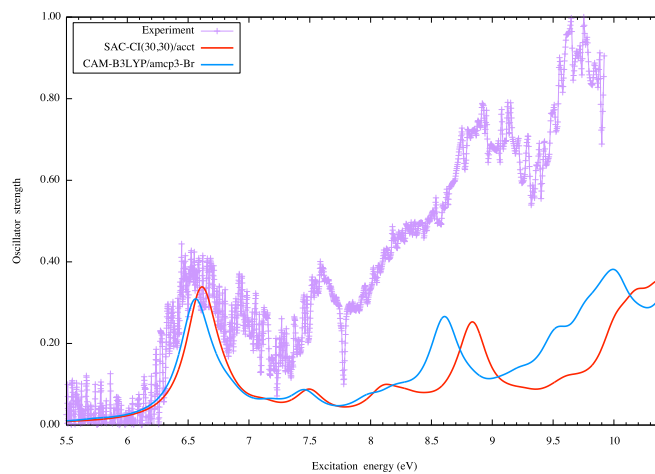


Figure A2: *Experimental spectra compared to computed electronic excitations of cis-1B1P with SAC-CI(30,30)/acct and CAM-B3LYP/amcp3.*

A3 Analysis of Major Peaks for *cis*-1-bromo-1-propene

Table A1: *cis*-1B1P: Analysis of Major Peak #1

Level of theory	$\Delta E^{(a)}$	$\Delta\Delta E^{(b)}$	$f^{(c)}$	Transition ^(d)	Symmetry ^(e)
SAC-CI(30,30)/acct	6.60	0.00	0.259	H \rightarrow L+9	$a'' \rightarrow a''$
CAM-B3LYP/acct	6.53	-0.07	0.294	H \rightarrow L+4	$a'' \rightarrow a''$
PBE0/acct	6.37	-0.23	0.260	H \rightarrow L	$a'' \rightarrow a''$
CAM-B3LYP/amcp3	6.52	-0.08	0.287	H \rightarrow L+5	$a'' \rightarrow a''$
PBE0/amcp3	6.39	-0.21	0.254	H \rightarrow L+1	$a'' \rightarrow a''$
CAM-B3LYP/amcp3-Br	6.56	-0.04	0.277	H \rightarrow L+5	$a'' \rightarrow a''$
PBE0/amcp3-Br	6.40	-0.20	0.256	H \rightarrow L+1	$a'' \rightarrow a''$

^(a) excitation energy (in eV); ^(b) deviation from the reference SAC-CI(30,30)/acct value; ^(c) oscillator strength; ^(d) major contribution to the transition: H = HOMO, L = LUMO; ^(e) symmetry of the molecular orbitals involved

Table A2: *cis*-1B1P: Analysis of Major Peak #2^(a)

Level of theory	ΔE	$\Delta\Delta E$	f	Transition	Symmetry
SAC-CI(30,30)/acct	7.50	0.00	0.064	H-1 \rightarrow L	$a' \rightarrow a'$
CAM-B3LYP/acct	7.43	-0.07	0.060	H-1 \rightarrow L	$a' \rightarrow a'$
PBE0/acct	7.23	-0.27	0.041	H-1 \rightarrow L+1	$a' \rightarrow a'$
CAM-B3LYP/amcp3	7.43	-0.07	0.061	H-1 \rightarrow L	$a' \rightarrow a'$
PBE0/amcp3	7.24	-0.26	0.041	H-1 \rightarrow L	$a' \rightarrow a'$
CAM-B3LYP/amcp3-Br	7.46	-0.04	0.058	H-1 \rightarrow L	$a' \rightarrow a'$
PBE0/amcp3-Br	7.27	-0.23	0.039	H-1 \rightarrow L	$a' \rightarrow a'$

^(a) excitation energy (in eV); ^(b) deviation from the reference SAC-CI(30,30)/acct value; ^(c) oscillator strength; ^(d) major contribution to the transition: H = HOMO, L = LUMO; ^(e) symmetry of the molecular orbitals involved

Table A3: *cis-1B1P*: Analysis of Major Peak #3^(a)

Level of theory	ΔE	$\Delta\Delta E$	f	Transition	Symmetry
SAC-CI(30,30)/acct	a) 8.09	0.00	0.029	H \rightarrow L+5	$a'' \rightarrow a'$
	b) 8.12	0.00	0.031	H \rightarrow L+7	$a'' \rightarrow a''$
CAM-B3LYP/acct	a) 8.10	0.01	0.022	H \rightarrow L+9	$a'' \rightarrow a'$
	b) 8.15	0.03	0.041	H-1 \rightarrow L+1	$a' \rightarrow a'$
PBE0/acct	a) 7.81	-0.28	0.018	H-1 \rightarrow L+4	$a' \rightarrow a'$
	b) 7.95	-0.17	0.027	H \rightarrow L+8	$a'' \rightarrow a''$
CAM-B3LYP/amcp3	a) 7.93	-0.16	0.014	H \rightarrow L+7	$a'' \rightarrow a''$
	b) 8.17	0.05	0.028	H-1 \rightarrow L+1	$a' \rightarrow a'$
PBE0/amcp3	a) 7.84	-0.25	0.022	H-1 \rightarrow L+4	$a' \rightarrow a'$
	b) 7.88	-0.24	0.012	H-1 \rightarrow L+3	$a' \rightarrow a'$
CAM-B3LYP/amcp3-Br	a) 7.98	-0.11	0.016	H \rightarrow L+9	$a'' \rightarrow a'$
	b) 8.18	0.06	0.029	H-1 \rightarrow L+1	$a' \rightarrow a'$
PBE0/amcp3-Br	a) 7.77	-0.32	0.011	H \rightarrow L+8	$a'' \rightarrow a''$
	b) 7.85	-0.27	0.024	H-1 \rightarrow L+4	$a' \rightarrow a'$

^(a) excitation energy (in eV); ^(b) deviation from the reference SAC-CI(30,30)/acct value; ^(c) oscillator strength; ^(d) major contribution to the transition: H = HOMO, L = LUMO; ^(e) symmetry of the molecular orbitals involved

Table A4: *cis-1B1P*: Analysis of Major Peak #4^(a)

Level of theory	ΔE	$\Delta\Delta E$	f	Transition	Symmetry
SAC-CI(30,30)/acct	8.84	0.00	0.230	H-2 \rightarrow L+9	$a'' \rightarrow a''$
CAM-B3LYP/acct	8.59	-0.25	0.208	H-2 \rightarrow L+4	$a'' \rightarrow a''$
PBE0/acct	8.36	-0.48	0.211	H-2 \rightarrow L	$a'' \rightarrow a''$
CAM-B3LYP/amcp3	8.59	-0.25	0.200	H-2 \rightarrow L+5	$a'' \rightarrow a''$
PBE0/amcp3	8.36	-0.48	0.212	H-2 \rightarrow L+1	$a'' \rightarrow a''$
CAM-B3LYP/amcp3-Br	8.61	-0.23	0.209	H-2 \rightarrow L+5	$a'' \rightarrow a''$
PBE0/amcp3-Br	8.37	-0.47	0.212	H-2 \rightarrow L+1	$a'' \rightarrow a''$

^(a) excitation energy (in eV); ^(b) deviation from the reference SAC-CI(30,30)/acct value; ^(c) oscillator strength; ^(d) major contribution to the transition: H = HOMO, L = LUMO; ^(e) symmetry of the molecular orbitals involved

Appendix B

Appendix to Chapter 3

B1 Decomposition Pathways Calculated with Single-Reference Methods

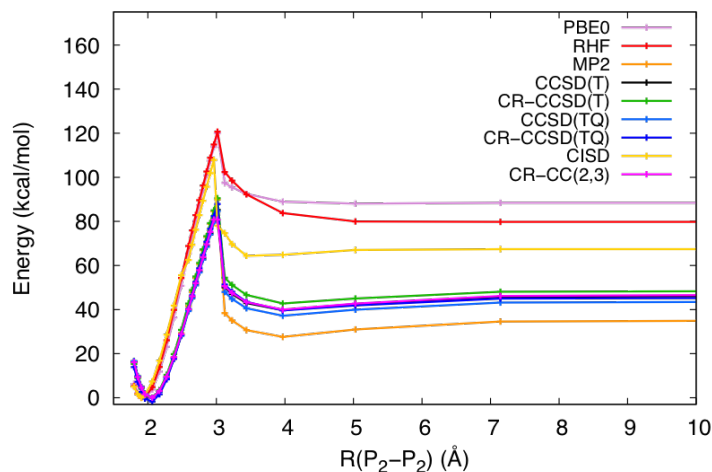


Figure B1: Single-reference thermal decomposition pathway of P_4 to $2 P_2$ calculated with the Z3PolP basis set. Hartree-Fock, density functional theory, Møller-Plesset perturbation theory, coupled cluster theory, and configuration interaction were all used to describe the reaction barrier.

B2 Z3PolP Basis Set for Phosphorus

```
s 11
 1 77492.43 0.00032889
 2 11605.79 0.00255399
 3 2645.960 0.01311021
 4 754.9800 0.05184352
 5 248.7500 0.15807518
 6 91.15700 0.34063549
 7 36.22600 0.40493752
 8 15.21100 0.17135916
 9 4.713800 0.01041557
10 1.782700 -0.00098215
11 0.342500 0.00038196
  s 11
 1 77492.43 0.00008960
 2 11605.79 0.00069149
 3 2645.960 0.00361519
 4 754.9800 0.01437330
 5 248.7500 0.04755313
 6 91.15700 0.11461912
 7 36.22600 0.20429350
 8 15.21100 0.07715679
 9 4.713800 -0.53624613
10 1.782700 -0.58051158
11 0.342500 -0.03822857
  s 11
 1 77492.43 0.00002460
 2 11605.79 0.00019028
 3 2645.960 0.00099246
 4 754.9800 0.00396939
 5 248.7500 0.01312635
 6 91.15700 0.03232476
 7 36.22600 0.05861673
 8 15.21100 0.02476100
 9 4.713800 -0.20148307
10 1.782700 -0.36726465
11 0.342500 0.62278077
  s 1
 1 0.124600 1.0
  s 1
 1 0.045300 1.0
  p 8
 1 384.84 0.00371277
 2 90.552 0.02858598
 3 28.806 0.12114498
 4 10.688 0.30146979
 5 4.2521 0.43395368
 6 1.7405 0.29131714
 7 0.5979 0.03949569
 8 0.2292 -0.00477062
```

```
p 8
1 384.84 0.00088854
2 90.552 0.00682869
3 28.806 0.02992373
4 10.688 0.07547624
5 4.2521 0.11792099
6 1.7405 0.06429591
7 0.5979 -0.26544390
8 0.2292 -0.56647570
p 1
1 0.0838 1.00
p 1
1 0.0306 1.00
d 3
1 0.2292 -0.40029656
2 0.0838 -1.0000000
3 0.0306 -0.12013748
```

B3 Reaction Enthalpies

Table B1: *MS-CASPT2 Reaction Enthalpy with Frozen P-P distance (kcal/mol)^a*

Basis Set	(4332) Space	(6442) Space
cc-pVDZ	91.8	105.6
cc-pVTZ	94.2	106.4
MCP-DZP	69.0	70.6
MCP-TZP	92.0	93.0

^(a) The experimental reaction enthalpy is 54.7 kcal/mol.

B4 Frozen Decomposition Pathways

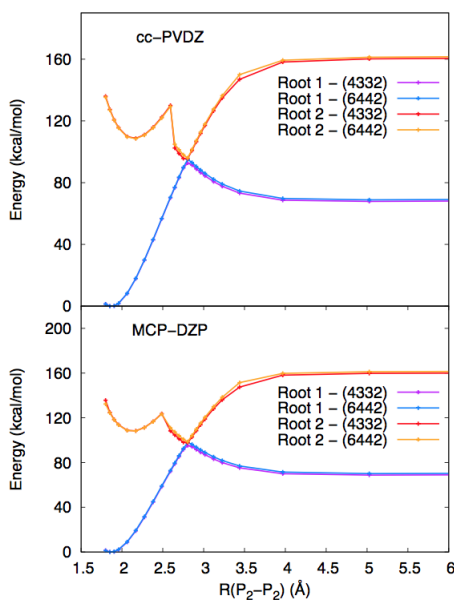


Figure B2: *MS-CASPT2 potential energy curves of the decomposition of P_4 to $2 P_2$ by varying the distance between P_2 subunits, $R(P_2-P_2)$ and keeping the distance within the P_2 subunits, $R(P-P)$, frozen. The optimized geometry from B3LYP/6-31G(d) was used as the equilibrium geometry of P_4 . The top plot was calculated with the double zeta cc-pVDZ basis set, and the bottom plot was calculated with MCP-DZP. Both show results with two different active spaces: (4332) and (6442) and two roots: the ground state (Root 1) and first excited state (Root 2).*

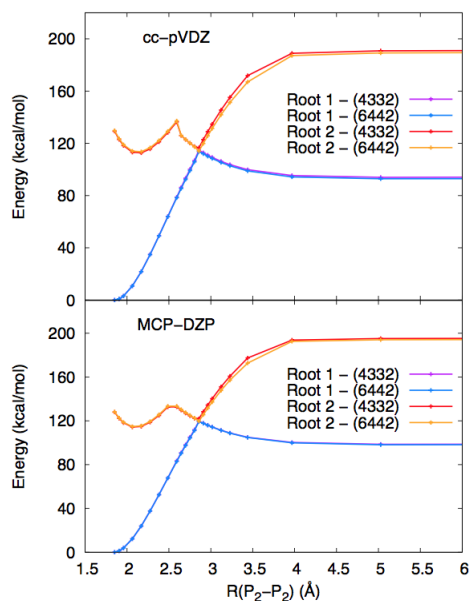


Figure B3: MC-PDFT potential energy curves of the decomposition of P_4 to $2 P_2$ by varying the distance between P_2 subunits, $R(P_2-P_2)$ and keeping the distance within the P_2 subunits, $R(P-P)$, frozen. The optimized geometry from B3LYP/6-31G(d) was used as the equilibrium geometry of P_4 . The top plot was calculated with the double zeta cc-PVDZ basis set, and the bottom plot was calculated with MCP-DZP. Both plots show results with two different active spaces: (4332) and (6442) and two roots: the ground state (Root 1) and first excited state (Root 2).

B5 Coordinates Along the Decomposition Pathway

+00.00, +00.05			
P1	2.1457081030	0.0000000000	-1.5000000000
P2	0.0000000000	2.1457081030	1.5000000000
+00.00, +00.10			
P1	2.1957081030	0.0000000000	-1.5000000000
P2	0.0000000000	2.1957081030	1.5000000000
+00.00, +00.15			
P1	2.2457081030	0.0000000000	-1.5000000000
P2	0.0000000000	2.2457081030	1.5000000000
+00.00, +00.20			
P1	2.2957081030	0.0000000000	-1.5000000000
P2	0.0000000000	2.2957081030	1.5000000000

+00.00,+00.25			
P1	2.3457081030	0.0000000000	-1.5000000000
P2	0.0000000000	2.3457081030	1.5000000000
+00.00,+00.30			
P1	2.3957081030	0.0000000000	-1.5000000000
P2	0.0000000000	2.3957081030	1.5000000000
+00.00,-00.05			
P1	2.0457081030	0.0000000000	-1.5000000000
P2	0.0000000000	2.0457081030	1.5000000000
+00.00,-00.10			
P1	1.9957081030	0.0000000000	-1.5000000000
P2	0.0000000000	1.9957081030	1.5000000000
+00.00,-00.15			
P1	1.9457081030	0.0000000000	-1.5000000000
P2	0.0000000000	1.9457081030	1.5000000000
+00.00,-00.20			
P1	1.8957081030	0.0000000000	-1.5000000000
P2	0.0000000000	1.8957081030	1.5000000000
+00.00,-00.25			
P1	1.8457081030	0.0000000000	-1.5000000000
P2	0.0000000000	1.8457081030	1.5000000000
+00.00,-00.30			
P1	1.7957081030	0.0000000000	-1.5000000000
P2	0.0000000000	1.7957081030	1.5000000000
+00.00,-00.35			
P1	1.7457081030	0.0000000000	-1.5000000000
P2	0.0000000000	1.7457081030	1.5000000000
+00.00,-00.40			
P1	1.6957081030	0.0000000000	-1.5000000000
P2	0.0000000000	1.6957081030	1.5000000000
+00.00,-00.45			
P1	1.6457081030	0.0000000000	-1.5000000000
P2	0.0000000000	1.6457081030	1.5000000000
+00.00,-00.50			
P1	1.5957081030	0.0000000000	-1.5000000000
P2	0.0000000000	1.5957081030	1.5000000000
+00.00,+00.00			
P1	2.0957081030	0.0000000000	-1.5000000000
P2	0.0000000000	2.0957081030	1.5000000000

+00.05,+00.05			
P1	2.1457081030	0.0000000000	-1.5500000000
P2	0.0000000000	2.1457081030	1.5500000000
+00.05,+00.10			
P1	2.1957081030	0.0000000000	-1.5500000000
P2	0.0000000000	2.1957081030	1.5500000000
+00.05,+00.15			
P1	2.2457081030	0.0000000000	-1.5500000000
P2	0.0000000000	2.2457081030	1.5500000000
+00.05,+00.20			
P1	2.2957081030	0.0000000000	-1.5500000000
P2	0.0000000000	2.2957081030	1.5500000000
+00.05,+00.25			
P1	2.3457081030	0.0000000000	-1.5500000000
P2	0.0000000000	2.3457081030	1.5500000000
+00.05,+00.30			
P1	2.3957081030	0.0000000000	-1.5500000000
P2	0.0000000000	2.3957081030	1.5500000000
+00.05,-00.05			
P1	2.0457081030	0.0000000000	-1.5500000000
P2	0.0000000000	2.0457081030	1.5500000000
+00.05,-00.10			
P1	1.9957081030	0.0000000000	-1.5500000000
P2	0.0000000000	1.9957081030	1.5500000000
+00.05,-00.15			
P1	1.9457081030	0.0000000000	-1.5500000000
P2	0.0000000000	1.9457081030	1.5500000000
+00.05,-00.20			
P1	1.8957081030	0.0000000000	-1.5500000000
P2	0.0000000000	1.8957081030	1.5500000000
+00.05,-00.25			
P1	1.8457081030	0.0000000000	-1.5500000000
P2	0.0000000000	1.8457081030	1.5500000000
+00.05,-00.30			
P1	1.7957081030	0.0000000000	-1.5500000000
P2	0.0000000000	1.7957081030	1.5500000000
+00.05,-00.35			
P1	1.7457081030	0.0000000000	-1.5500000000

P2	0.0000000000	1.7457081030	1.5500000000
+00.05,-00.40			
P1	1.6957081030	0.0000000000	-1.5500000000
P2	0.0000000000	1.6957081030	1.5500000000
+00.05,-00.45			
P1	1.6457081030	0.0000000000	-1.5500000000
P2	0.0000000000	1.6457081030	1.5500000000
+00.05,-00.50			
P1	1.5957081030	0.0000000000	-1.5500000000
P2	0.0000000000	1.5957081030	1.5500000000
+00.05,+00.00			
P1	2.0957081030	0.0000000000	-1.5500000000
P2	0.0000000000	2.0957081030	1.5500000000
+00.10,+00.05			
P1	2.1457081030	0.0000000000	-1.6000000000
P2	0.0000000000	2.1457081030	1.6000000000
+00.10,+00.10			
P1	2.1957081030	0.0000000000	-1.6000000000
P2	0.0000000000	2.1957081030	1.6000000000
+00.10,+00.15			
P1	2.2457081030	0.0000000000	-1.6000000000
P2	0.0000000000	2.2457081030	1.6000000000
+00.10,+00.20			
P1	2.2957081030	0.0000000000	-1.6000000000
P2	0.0000000000	2.2957081030	1.6000000000
+00.10,+00.25			
P1	2.3457081030	0.0000000000	-1.6000000000
P2	0.0000000000	2.3457081030	1.6000000000
+00.10,-00.05			
P1	2.0457081030	0.0000000000	-1.6000000000
P2	0.0000000000	2.0457081030	1.6000000000
+00.10,-00.10			
P1	1.9957081030	0.0000000000	-1.6000000000
P2	0.0000000000	1.9957081030	1.6000000000
+00.10,-00.15			
P1	1.9457081030	0.0000000000	-1.6000000000
P2	0.0000000000	1.9457081030	1.6000000000
+00.10,-00.20			

P1	1.8957081030	0.0000000000	-1.6000000000
P2	0.0000000000	1.8957081030	1.6000000000
+00.10,-00.25			
P1	1.8457081030	0.0000000000	-1.6000000000
P2	0.0000000000	1.8457081030	1.6000000000
+00.10,-00.30			
P1	1.7957081030	0.0000000000	-1.6000000000
P2	0.0000000000	1.7957081030	1.6000000000
+00.10,-00.35			
P1	1.7457081030	0.0000000000	-1.6000000000
P2	0.0000000000	1.7457081030	1.6000000000
+00.10,-00.40			
P1	1.6957081030	0.0000000000	-1.6000000000
P2	0.0000000000	1.6957081030	1.6000000000
+00.10,-00.45			
P1	1.6457081030	0.0000000000	-1.6000000000
P2	0.0000000000	1.6457081030	1.6000000000
+00.10,-00.50			
P1	1.5957081030	0.0000000000	-1.6000000000
P2	0.0000000000	1.5957081030	1.6000000000
+00.10,+00.00			
P1	2.0957081030	0.0000000000	-1.6000000000
P2	0.0000000000	2.0957081030	1.6000000000
+00.20,+00.05			
P1	2.1457081030	0.0000000000	-1.7000000000
P2	0.0000000000	2.1457081030	1.7000000000
+00.20,+00.10			
P1	2.1957081030	0.0000000000	-1.7000000000
P2	0.0000000000	2.1957081030	1.7000000000
+00.20,+00.15			
P1	2.2457081030	0.0000000000	-1.7000000000
P2	0.0000000000	2.2457081030	1.7000000000
+00.20,+00.20			
P1	2.2957081030	0.0000000000	-1.7000000000
P2	0.0000000000	2.2957081030	1.7000000000
+00.20,-00.05			
P1	2.0457081030	0.0000000000	-1.7000000000
P2	0.0000000000	2.0457081030	1.7000000000

+00.20,-00.10			
P1	1.9957081030	0.0000000000	-1.7000000000
P2	0.0000000000	1.9957081030	1.7000000000
+00.20,-00.15			
P1	1.9457081030	0.0000000000	-1.7000000000
P2	0.0000000000	1.9457081030	1.7000000000
+00.20,-00.20			
P1	1.8957081030	0.0000000000	-1.7000000000
P2	0.0000000000	1.8957081030	1.7000000000
+00.20,-00.25			
P1	1.8457081030	0.0000000000	-1.7000000000
P2	0.0000000000	1.8457081030	1.7000000000
+00.20,-00.30			
P1	1.7957081030	0.0000000000	-1.7000000000
P2	0.0000000000	1.7957081030	1.7000000000
+00.20,-00.35			
P1	1.7457081030	0.0000000000	-1.7000000000
P2	0.0000000000	1.7457081030	1.7000000000
+00.20,-00.40			
P1	1.6957081030	0.0000000000	-1.7000000000
P2	0.0000000000	1.6957081030	1.7000000000
+00.20,-00.45			
P1	1.6457081030	0.0000000000	-1.7000000000
P2	0.0000000000	1.6457081030	1.7000000000
+00.20,-00.50			
P1	1.5957081030	0.0000000000	-1.7000000000
P2	0.0000000000	1.5957081030	1.7000000000
+00.20,+00.00			
P1	2.0957081030	0.0000000000	-1.7000000000
P2	0.0000000000	2.0957081030	1.7000000000
+00.30,+00.05			
P1	2.1457081030	0.0000000000	-1.8000000000
P2	0.0000000000	2.1457081030	1.8000000000
+00.30,+00.10			
P1	2.1957081030	0.0000000000	-1.8000000000
P2	0.0000000000	2.1957081030	1.8000000000
+00.30,+00.15			
P1	2.2457081030	0.0000000000	-1.8000000000
P2	0.0000000000	2.2457081030	1.8000000000

+00.30,+00.20			
P1	2.2957081030	0.0000000000	-1.8000000000
P2	0.0000000000	2.2957081030	1.8000000000
+00.30,-00.05			
P1	2.0457081030	0.0000000000	-1.8000000000
P2	0.0000000000	2.0457081030	1.8000000000
+00.30,-00.10			
P1	1.9957081030	0.0000000000	-1.8000000000
P2	0.0000000000	1.9957081030	1.8000000000
+00.30,-00.15			
P1	1.9457081030	0.0000000000	-1.8000000000
P2	0.0000000000	1.9457081030	1.8000000000
+00.30,-00.20			
P1	1.8957081030	0.0000000000	-1.8000000000
P2	0.0000000000	1.8957081030	1.8000000000
+00.30,-00.25			
P1	1.8457081030	0.0000000000	-1.8000000000
P2	0.0000000000	1.8457081030	1.8000000000
+00.30,-00.30			
P1	1.7957081030	0.0000000000	-1.8000000000
P2	0.0000000000	1.7957081030	1.8000000000
+00.30,-00.35			
P1	1.7457081030	0.0000000000	-1.8000000000
P2	0.0000000000	1.7457081030	1.8000000000
+00.30,-00.40			
P1	1.6957081030	0.0000000000	-1.8000000000
P2	0.0000000000	1.6957081030	1.8000000000
+00.30,-00.45			
P1	1.6457081030	0.0000000000	-1.8000000000
P2	0.0000000000	1.6457081030	1.8000000000
+00.30,-00.50			
P1	1.5957081030	0.0000000000	-1.8000000000
P2	0.0000000000	1.5957081030	1.8000000000
+00.30,+00.00			
P1	2.0957081030	0.0000000000	-1.8000000000
P2	0.0000000000	2.0957081030	1.8000000000
+00.40,+00.05			
P1	2.1457081030	0.0000000000	-1.9000000000

P2	0.0000000000	2.1457081030	1.9000000000
+00.40,+00.10			
P1	2.1957081030	0.0000000000	-1.9000000000
P2	0.0000000000	2.1957081030	1.9000000000
+00.40,+00.15			
P1	2.2457081030	0.0000000000	-1.9000000000
P2	0.0000000000	2.2457081030	1.9000000000
+00.40,+00.20			
P1	2.2957081030	0.0000000000	-1.9000000000
P2	0.0000000000	2.2957081030	1.9000000000
+00.40,-00.05			
P1	2.0457081030	0.0000000000	-1.9000000000
P2	0.0000000000	2.0457081030	1.9000000000
+00.40,-00.10			
P1	1.9957081030	0.0000000000	-1.9000000000
P2	0.0000000000	1.9957081030	1.9000000000
+00.40,-00.15			
P1	1.9457081030	0.0000000000	-1.9000000000
P2	0.0000000000	1.9457081030	1.9000000000
+00.40,-00.20			
P1	1.8957081030	0.0000000000	-1.9000000000
P2	0.0000000000	1.8957081030	1.9000000000
+00.40,-00.25			
P1	1.8457081030	0.0000000000	-1.9000000000
P2	0.0000000000	1.8457081030	1.9000000000
+00.40,-00.30			
P1	1.7957081030	0.0000000000	-1.9000000000
P2	0.0000000000	1.7957081030	1.9000000000
+00.40,-00.35			
P1	1.7457081030	0.0000000000	-1.9000000000
P2	0.0000000000	1.7457081030	1.9000000000
+00.40,-00.40			
P1	1.6957081030	0.0000000000	-1.9000000000
P2	0.0000000000	1.6957081030	1.9000000000
+00.40,-00.45			
P1	1.6457081030	0.0000000000	-1.9000000000
P2	0.0000000000	1.6457081030	1.9000000000
+00.40,-00.50			

P1	1.5957081030	0.0000000000	-1.9000000000
P2	0.0000000000	1.5957081030	1.9000000000
+00.40,+00.00			
P1	2.0957081030	0.0000000000	-1.9000000000
P2	0.0000000000	2.0957081030	1.9000000000
+00.50,+00.05			
P1	2.1457081030	0.0000000000	-2.0000000000
P2	0.0000000000	2.1457081030	2.0000000000
+00.50,+00.10			
P1	2.1957081030	0.0000000000	-2.0000000000
P2	0.0000000000	2.1957081030	2.0000000000
+00.50,+00.15			
P1	2.2457081030	0.0000000000	-2.0000000000
P2	0.0000000000	2.2457081030	2.0000000000
+00.50,+00.20			
P1	2.2957081030	0.0000000000	-2.0000000000
P2	0.0000000000	2.2957081030	2.0000000000
+00.50,-00.05			
P1	2.0457081030	0.0000000000	-2.0000000000
P2	0.0000000000	2.0457081030	2.0000000000
+00.50,-00.10			
P1	1.9957081030	0.0000000000	-2.0000000000
P2	0.0000000000	1.9957081030	2.0000000000
+00.50,-00.15			
P1	1.9457081030	0.0000000000	-2.0000000000
P2	0.0000000000	1.9457081030	2.0000000000
+00.50,-00.20			
P1	1.8957081030	0.0000000000	-2.0000000000
P2	0.0000000000	1.8957081030	2.0000000000
+00.50,-00.25			
P1	1.8457081030	0.0000000000	-2.0000000000
P2	0.0000000000	1.8457081030	2.0000000000
+00.50,-00.30			
P1	1.7957081030	0.0000000000	-2.0000000000
P2	0.0000000000	1.7957081030	2.0000000000
+00.50,-00.35			
P1	1.7457081030	0.0000000000	-2.0000000000
P2	0.0000000000	1.7457081030	2.0000000000

+00.50,-00.40			
P1	1.6957081030	0.0000000000	-2.0000000000
P2	0.0000000000	1.6957081030	2.0000000000
+00.50,-00.45			
P1	1.6457081030	0.0000000000	-2.0000000000
P2	0.0000000000	1.6457081030	2.0000000000
+00.50,-00.50			
P1	1.5957081030	0.0000000000	-2.0000000000
P2	0.0000000000	1.5957081030	2.0000000000
+00.50,+00.00			
P1	2.0957081030	0.0000000000	-2.0000000000
P2	0.0000000000	2.0957081030	2.0000000000
+00.60,+00.05			
P1	2.1457081030	0.0000000000	-2.1000000000
P2	0.0000000000	2.1457081030	2.1000000000
+00.60,+00.10			
P1	2.1957081030	0.0000000000	-2.1000000000
P2	0.0000000000	2.1957081030	2.1000000000
+00.60,+00.15			
P1	2.2457081030	0.0000000000	-2.1000000000
P2	0.0000000000	2.2457081030	2.1000000000
+00.60,+00.20			
P1	2.2957081030	0.0000000000	-2.1000000000
P2	0.0000000000	2.2957081030	2.1000000000
+00.60,-00.05			
P1	2.0457081030	0.0000000000	-2.1000000000
P2	0.0000000000	2.0457081030	2.1000000000
+00.60,-00.10			
P1	1.9957081030	0.0000000000	-2.1000000000
P2	0.0000000000	1.9957081030	2.1000000000
+00.60,-00.15			
P1	1.9457081030	0.0000000000	-2.1000000000
P2	0.0000000000	1.9457081030	2.1000000000
+00.60,-00.20			
P1	1.8957081030	0.0000000000	-2.1000000000
P2	0.0000000000	1.8957081030	2.1000000000
+00.60,-00.25			
P1	1.8457081030	0.0000000000	-2.1000000000
P2	0.0000000000	1.8457081030	2.1000000000

+00.60,-00.30			
P1	1.7957081030	0.0000000000	-2.1000000000
P2	0.0000000000	1.7957081030	2.1000000000
+00.60,-00.35			
P1	1.7457081030	0.0000000000	-2.1000000000
P2	0.0000000000	1.7457081030	2.1000000000
+00.60,-00.40			
P1	1.6957081030	0.0000000000	-2.1000000000
P2	0.0000000000	1.6957081030	2.1000000000
+00.60,-00.45			
P1	1.6457081030	0.0000000000	-2.1000000000
P2	0.0000000000	1.6457081030	2.1000000000
+00.60,-00.50			
P1	1.5957081030	0.0000000000	-2.1000000000
P2	0.0000000000	1.5957081030	2.1000000000
+00.60,+00.00			
P1	2.0957081030	0.0000000000	-2.1000000000
P2	0.0000000000	2.0957081030	2.1000000000
+00.70,+00.05			
P1	2.1457081030	0.0000000000	-2.2000000000
P2	0.0000000000	2.1457081030	2.2000000000
+00.70,+00.10			
P1	2.1957081030	0.0000000000	-2.2000000000
P2	0.0000000000	2.1957081030	2.2000000000
+00.70,+00.15			
P1	2.2457081030	0.0000000000	-2.2000000000
P2	0.0000000000	2.2457081030	2.2000000000
+00.70,+00.20			
P1	2.2957081030	0.0000000000	-2.2000000000
P2	0.0000000000	2.2957081030	2.2000000000
+00.70-00.05			
P1	2.0457081030	0.0000000000	-2.2000000000
P2	0.0000000000	2.0457081030	2.2000000000
+00.70-00.10			
P1	1.9957081030	0.0000000000	-2.2000000000
P2	0.0000000000	1.9957081030	2.2000000000
+00.70-00.15			
P1	1.9457081030	0.0000000000	-2.2000000000

P2	0.0000000000	1.9457081030	2.2000000000
+00.70-00.20			
P1	1.8957081030	0.0000000000	-2.2000000000
P2	0.0000000000	1.8957081030	2.2000000000
+00.70-00.25			
P1	1.8457081030	0.0000000000	-2.2000000000
P2	0.0000000000	1.8457081030	2.2000000000
+00.70-00.30			
P1	1.7957081030	0.0000000000	-2.2000000000
P2	0.0000000000	1.7957081030	2.2000000000
+00.70-00.35			
P1	1.7457081030	0.0000000000	-2.2000000000
P2	0.0000000000	1.7457081030	2.2000000000
+00.70-00.40			
P1	1.6957081030	0.0000000000	-2.2000000000
P2	0.0000000000	1.6957081030	2.2000000000
+00.70-00.45			
P1	1.6457081030	0.0000000000	-2.2000000000
P2	0.0000000000	1.6457081030	2.2000000000
+00.70-00.50			
P1	1.5957081030	0.0000000000	-2.2000000000
P2	0.0000000000	1.5957081030	2.2000000000
+00.70,+00.00			
P1	2.0957081030	0.0000000000	-2.2000000000
P2	0.0000000000	2.0957081030	2.2000000000
+00.75+00.05			
P1	2.1457081030	0.0000000000	-2.2500000000
P2	0.0000000000	2.1457081030	2.2500000000
+00.75+00.10			
P1	2.1957081030	0.0000000000	-2.2500000000
P2	0.0000000000	2.1957081030	2.2500000000
+00.75+00.15			
P1	2.2457081030	0.0000000000	-2.2500000000
P2	0.0000000000	2.2457081030	2.2500000000
+00.75+00.20			
P1	2.2957081030	0.0000000000	-2.2500000000
P2	0.0000000000	2.2957081030	2.2500000000
+00.75-00.05			

P1	2.0457081030	0.0000000000	-2.2500000000
P2	0.0000000000	2.0457081030	2.2500000000
+00.75-00.10			
P1	1.9957081030	0.0000000000	-2.2500000000
P2	0.0000000000	1.9957081030	2.2500000000
+00.75-00.15			
P1	1.9457081030	0.0000000000	-2.2500000000
P2	0.0000000000	1.9457081030	2.2500000000
+00.75-00.20			
P1	1.8957081030	0.0000000000	-2.2500000000
P2	0.0000000000	1.8957081030	2.2500000000
+00.75-00.25			
P1	1.8457081030	0.0000000000	-2.2500000000
P2	0.0000000000	1.8457081030	2.2500000000
+00.75-00.30			
P1	1.7957081030	0.0000000000	-2.2500000000
P2	0.0000000000	1.7957081030	2.2500000000
+00.75-00.35			
P1	1.7457081030	0.0000000000	-2.2500000000
P2	0.0000000000	1.7457081030	2.2500000000
+00.75-00.40			
P1	1.6957081030	0.0000000000	-2.2500000000
P2	0.0000000000	1.6957081030	2.2500000000
+00.75-00.45			
P1	1.6457081030	0.0000000000	-2.2500000000
P2	0.0000000000	1.6457081030	2.2500000000
+00.75-00.50			
P1	1.5957081030	0.0000000000	-2.2500000000
P2	0.0000000000	1.5957081030	2.2500000000
+00.75,+00.00			
P1	2.0957081030	0.0000000000	-2.2500000000
P2	0.0000000000	2.0957081030	2.2500000000
+00.80,+00.10			
P1	2.1957081030	0.0000000000	-2.3000000000
P2	0.0000000000	2.1957081030	2.3000000000
+00.80,+00.15			
P1	2.2457081030	0.0000000000	-2.3000000000
P2	0.0000000000	2.2457081030	2.3000000000

+00.80,-00.05			
P1	2.0457081030	0.0000000000	-2.3000000000
P2	0.0000000000	2.0457081030	2.3000000000
+00.80,-00.10			
P1	1.9957081030	0.0000000000	-2.3000000000
P2	0.0000000000	1.9957081030	2.3000000000
+00.80,-00.15			
P1	1.9457081030	0.0000000000	-2.3000000000
P2	0.0000000000	1.9457081030	2.3000000000
+00.80,-00.20			
P1	1.8957081030	0.0000000000	-2.3000000000
P2	0.0000000000	1.8957081030	2.3000000000
+00.80,-00.25			
P1	1.8457081030	0.0000000000	-2.3000000000
P2	0.0000000000	1.8457081030	2.3000000000
+00.80,-00.30			
P1	1.7957081030	0.0000000000	-2.3000000000
P2	0.0000000000	1.7957081030	2.3000000000
+00.80,-00.35			
P1	1.7457081030	0.0000000000	-2.3000000000
P2	0.0000000000	1.7457081030	2.3000000000
+00.80,-00.40			
P1	1.6957081030	0.0000000000	-2.3000000000
P2	0.0000000000	1.6957081030	2.3000000000
+00.80,-00.45			
P1	1.6457081030	0.0000000000	-2.3000000000
P2	0.0000000000	1.6457081030	2.3000000000
+00.80,-00.50			
P1	1.5957081030	0.0000000000	-2.3000000000
P2	0.0000000000	1.5957081030	2.3000000000
+00.80,+00.00			
P1	2.0957081030	0.0000000000	-2.3000000000
P2	0.0000000000	2.0957081030	2.3000000000
+00.85,+00.05			
P1	2.1457081030	0.0000000000	-2.3500000000
P2	0.0000000000	2.1457081030	2.3500000000
+00.85,+00.10			
P1	2.1957081030	0.0000000000	-2.3500000000
P2	0.0000000000	2.1957081030	2.3500000000

+00.85,+00.15			
P1	2.2457081030	0.0000000000	-2.3500000000
P2	0.0000000000	2.2457081030	2.3500000000
+00.85,+00.20			
P1	2.2957081030	0.0000000000	-2.3500000000
P2	0.0000000000	2.2957081030	2.3500000000
+00.85,-00.05			
P1	2.0457081030	0.0000000000	-2.3500000000
P2	0.0000000000	2.0457081030	2.3500000000
+00.85,-00.10			
P1	1.9957081030	0.0000000000	-2.3500000000
P2	0.0000000000	1.9957081030	2.3500000000
+00.85,-00.15			
P1	1.9457081030	0.0000000000	-2.3500000000
P2	0.0000000000	1.9457081030	2.3500000000
+00.85,-00.20			
P1	1.8957081030	0.0000000000	-2.3500000000
P2	0.0000000000	1.8957081030	2.3500000000
+00.85,-00.25			
P1	1.8457081030	0.0000000000	-2.3500000000
P2	0.0000000000	1.8457081030	2.3500000000
+00.85,-00.30			
P1	1.7957081030	0.0000000000	-2.3500000000
P2	0.0000000000	1.7957081030	2.3500000000
+00.85,-00.35			
P1	1.7457081030	0.0000000000	-2.3500000000
P2	0.0000000000	1.7457081030	2.3500000000
+00.85,-00.40			
P1	1.6957081030	0.0000000000	-2.3500000000
P2	0.0000000000	1.6957081030	2.3500000000
+00.85,-00.45			
P1	1.6457081030	0.0000000000	-2.3500000000
P2	0.0000000000	1.6457081030	2.3500000000
+00.85,-00.50			
P1	1.5957081030	0.0000000000	-2.3500000000
P2	0.0000000000	1.5957081030	2.3500000000
+00.85,+00.00			
P1	2.0957081030	0.0000000000	-2.3500000000

P2	0.0000000000	2.0957081030	2.3500000000
+00.90,+00.05			
P1	2.1457081030	0.0000000000	-2.4000000000
P2	0.0000000000	2.1457081030	2.4000000000
+00.90,-00.05			
P1	2.0457081030	0.0000000000	-2.4000000000
P2	0.0000000000	2.0457081030	2.4000000000
+00.90,-00.10			
P1	1.9957081030	0.0000000000	-2.4000000000
P2	0.0000000000	1.9957081030	2.4000000000
+00.90,-00.15			
P1	1.9457081030	0.0000000000	-2.4000000000
P2	0.0000000000	1.9457081030	2.4000000000
+00.90,-00.20			
P1	1.8957081030	0.0000000000	-2.4000000000
P2	0.0000000000	1.8957081030	2.4000000000
+00.90,-00.25			
P1	1.8457081030	0.0000000000	-2.4000000000
P2	0.0000000000	1.8457081030	2.4000000000
+00.90,-00.30			
P1	1.7957081030	0.0000000000	-2.4000000000
P2	0.0000000000	1.7957081030	2.4000000000
+00.90,-00.35			
P1	1.7457081030	0.0000000000	-2.4000000000
P2	0.0000000000	1.7457081030	2.4000000000
+00.90,-00.40			
P1	1.6957081030	0.0000000000	-2.4000000000
P2	0.0000000000	1.6957081030	2.4000000000
+00.90,-00.45			
P1	1.6457081030	0.0000000000	-2.4000000000
P2	0.0000000000	1.6457081030	2.4000000000
+00.90,-00.50			
P1	1.5957081030	0.0000000000	-2.4000000000
P2	0.0000000000	1.5957081030	2.4000000000
+00.90,+00.00			
P1	2.0957081030	0.0000000000	-2.4000000000
P2	0.0000000000	2.0957081030	2.4000000000
+00.95,+00.05			

P1	2.1457081030	0.0000000000	-2.4500000000
P2	0.0000000000	2.1457081030	2.4500000000
+00.95,-00.05			
P1	2.0457081030	0.0000000000	-2.4500000000
P2	0.0000000000	2.0457081030	2.4500000000
+00.95,-00.10			
P1	1.9957081030	0.0000000000	-2.4500000000
P2	0.0000000000	1.9957081030	2.4500000000
+00.95,-00.15			
P1	1.9457081030	0.0000000000	-2.4500000000
P2	0.0000000000	1.9457081030	2.4500000000
+00.95,-00.20			
P1	1.8957081030	0.0000000000	-2.4500000000
P2	0.0000000000	1.8957081030	2.4500000000
+00.95,-00.25			
P1	1.8457081030	0.0000000000	-2.4500000000
P2	0.0000000000	1.8457081030	2.4500000000
+00.95,-00.30			
P1	1.7957081030	0.0000000000	-2.4500000000
P2	0.0000000000	1.7957081030	2.4500000000
+00.95,-00.35			
P1	1.7457081030	0.0000000000	-2.4500000000
P2	0.0000000000	1.7457081030	2.4500000000
+00.95,-00.40			
P1	1.6957081030	0.0000000000	-2.4500000000
P2	0.0000000000	1.6957081030	2.4500000000
+00.95,-00.45			
P1	1.6457081030	0.0000000000	-2.4500000000
P2	0.0000000000	1.6457081030	2.4500000000
+00.95,-00.50			
P1	1.5957081030	0.0000000000	-2.4500000000
P2	0.0000000000	1.5957081030	2.4500000000
+00.95,+00.00			
P1	2.0957081030	0.0000000000	-2.4500000000
P2	0.0000000000	2.0957081030	2.4500000000
+01.00,+00.05			
P1	2.1457081030	0.0000000000	-2.5000000000
P2	0.0000000000	2.1457081030	2.5000000000

+01.00,-00.05			
P1	2.0457081030	0.0000000000	-2.5000000000
P2	0.0000000000	2.0457081030	2.5000000000
+01.00,-00.10			
P1	1.9957081030	0.0000000000	-2.5000000000
P2	0.0000000000	1.9957081030	2.5000000000
+01.00,-00.15			
P1	1.9457081030	0.0000000000	-2.5000000000
P2	0.0000000000	1.9457081030	2.5000000000
+01.00,-00.20			
P1	1.8957081030	0.0000000000	-2.5000000000
P2	0.0000000000	1.8957081030	2.5000000000
+01.00,-00.25			
P1	1.8457081030	0.0000000000	-2.5000000000
P2	0.0000000000	1.8457081030	2.5000000000
+01.00,-00.30			
P1	1.7957081030	0.0000000000	-2.5000000000
P2	0.0000000000	1.7957081030	2.5000000000
+01.00,-00.35			
P1	1.7457081030	0.0000000000	-2.5000000000
P2	0.0000000000	1.7457081030	2.5000000000
+01.00,-00.40			
P1	1.6957081030	0.0000000000	-2.5000000000
P2	0.0000000000	1.6957081030	2.5000000000
+01.00,-00.45			
P1	1.6457081030	0.0000000000	-2.5000000000
P2	0.0000000000	1.6457081030	2.5000000000
+01.00,-00.50			
P1	1.5957081030	0.0000000000	-2.5000000000
P2	0.0000000000	1.5957081030	2.5000000000
+01.00,+00.00			
P1	2.0957081030	0.0000000000	-2.5000000000
P2	0.0000000000	2.0957081030	2.5000000000
+01.05,+00.05			
P1	2.1457081030	0.0000000000	-2.5500000000
P2	0.0000000000	2.1457081030	2.5500000000
+01.05,-00.05			
P1	2.0457081030	0.0000000000	-2.5500000000
P2	0.0000000000	2.0457081030	2.5500000000

+01.05,-00.10			
P1	1.9957081030	0.0000000000	-2.5500000000
P2	0.0000000000	1.9957081030	2.5500000000
+01.05,-00.15			
P1	1.9457081030	0.0000000000	-2.5500000000
P2	0.0000000000	1.9457081030	2.5500000000
+01.05,-00.20			
P1	1.8957081030	0.0000000000	-2.5500000000
P2	0.0000000000	1.8957081030	2.5500000000
+01.05,-00.25			
P1	1.8457081030	0.0000000000	-2.5500000000
P2	0.0000000000	1.8457081030	2.5500000000
+01.05,-00.30			
P1	1.7957081030	0.0000000000	-2.5500000000
P2	0.0000000000	1.7957081030	2.5500000000
+01.05,-00.35			
P1	1.7457081030	0.0000000000	-2.5500000000
P2	0.0000000000	1.7457081030	2.5500000000
+01.05,-00.40			
P1	1.6957081030	0.0000000000	-2.5500000000
P2	0.0000000000	1.6957081030	2.5500000000
+01.05,-00.45			
P1	1.6457081030	0.0000000000	-2.5500000000
P2	0.0000000000	1.6457081030	2.5500000000
+01.05,-00.50			
P1	1.5957081030	0.0000000000	-2.5500000000
P2	0.0000000000	1.5957081030	2.5500000000
+01.05,+00.00			
P1	2.0957081030	0.0000000000	-2.5500000000
P2	0.0000000000	2.0957081030	2.5500000000
+01.10,+00.05			
P1	2.1457081030	0.0000000000	-2.6000000000
P2	0.0000000000	2.1457081030	2.6000000000
+01.10,-00.05			
P1	2.0457081030	0.0000000000	-2.6000000000
P2	0.0000000000	2.0457081030	2.6000000000
+01.10,-00.10			
P1	1.9957081030	0.0000000000	-2.6000000000

P2	0.0000000000	1.9957081030	2.6000000000
+01.10,-00.15			
P1	1.9457081030	0.0000000000	-2.6000000000
P2	0.0000000000	1.9457081030	2.6000000000
+01.10,-00.20			
P1	1.8957081030	0.0000000000	-2.6000000000
P2	0.0000000000	1.8957081030	2.6000000000
+01.10,-00.25			
P1	1.8457081030	0.0000000000	-2.6000000000
P2	0.0000000000	1.8457081030	2.6000000000
+01.10,-00.30			
P1	1.7957081030	0.0000000000	-2.6000000000
P2	0.0000000000	1.7957081030	2.6000000000
+01.10,-00.35			
P1	1.7457081030	0.0000000000	-2.6000000000
P2	0.0000000000	1.7457081030	2.6000000000
+01.10,-00.40			
P1	1.6957081030	0.0000000000	-2.6000000000
P2	0.0000000000	1.6957081030	2.6000000000
+01.10,-00.45			
P1	1.6457081030	0.0000000000	-2.6000000000
P2	0.0000000000	1.6457081030	2.6000000000
+01.10,-00.50			
P1	1.5957081030	0.0000000000	-2.6000000000
P2	0.0000000000	1.5957081030	2.6000000000
+01.10,+00.00			
P1	2.0957081030	0.0000000000	-2.6000000000
P2	0.0000000000	2.0957081030	2.6000000000
+01.20,+00.05			
P1	2.1457081030	0.0000000000	-2.7000000000
P2	0.0000000000	2.1457081030	2.7000000000
+01.20,-00.05			
P1	2.0457081030	0.0000000000	-2.7000000000
P2	0.0000000000	2.0457081030	2.7000000000
+01.20,-00.10			
P1	1.9957081030	0.0000000000	-2.7000000000
P2	0.0000000000	1.9957081030	2.7000000000
+01.20,-00.15			

P1	1.9457081030	0.0000000000	-2.7000000000
P2	0.0000000000	1.9457081030	2.7000000000
+01.20,-00.20			
P1	1.8957081030	0.0000000000	-2.7000000000
P2	0.0000000000	1.8957081030	2.7000000000
+01.20,-00.25			
P1	1.8457081030	0.0000000000	-2.7000000000
P2	0.0000000000	1.8457081030	2.7000000000
+01.20,-00.30			
P1	1.7957081030	0.0000000000	-2.7000000000
P2	0.0000000000	1.7957081030	2.7000000000
+01.20,-00.35			
P1	1.7457081030	0.0000000000	-2.7000000000
P2	0.0000000000	1.7457081030	2.7000000000
+01.20,-00.40			
P1	1.6957081030	0.0000000000	-2.7000000000
P2	0.0000000000	1.6957081030	2.7000000000
+01.20,-00.45			
P1	1.6457081030	0.0000000000	-2.7000000000
P2	0.0000000000	1.6457081030	2.7000000000
+01.20,-00.50			
P1	1.5957081030	0.0000000000	-2.7000000000
P2	0.0000000000	1.5957081030	2.7000000000
+01.20,+00.00			
P1	2.0957081030	0.0000000000	-2.7000000000
P2	0.0000000000	2.0957081030	2.7000000000
+01.30,+00.05			
P1	2.1457081030	0.0000000000	-2.8000000000
P2	0.0000000000	2.1457081030	2.8000000000
+01.30,-00.05			
P1	2.0457081030	0.0000000000	-2.8000000000
P2	0.0000000000	2.0457081030	2.8000000000
+01.30,-00.10			
P1	1.9957081030	0.0000000000	-2.8000000000
P2	0.0000000000	1.9957081030	2.8000000000
+01.30,-00.15			
P1	1.9457081030	0.0000000000	-2.8000000000
P2	0.0000000000	1.9457081030	2.8000000000

+01.30,-00.20			
P1	1.8957081030	0.0000000000	-2.8000000000
P2	0.0000000000	1.8957081030	2.8000000000
+01.30,-00.25			
P1	1.8457081030	0.0000000000	-2.8000000000
P2	0.0000000000	1.8457081030	2.8000000000
+01.30,-00.30			
P1	1.7957081030	0.0000000000	-2.8000000000
P2	0.0000000000	1.7957081030	2.8000000000
+01.30,-00.35			
P1	1.7457081030	0.0000000000	-2.8000000000
P2	0.0000000000	1.7457081030	2.8000000000
+01.30,-00.40			
P1	1.6957081030	0.0000000000	-2.8000000000
P2	0.0000000000	1.6957081030	2.8000000000
+01.30,-00.45			
P1	1.6457081030	0.0000000000	-2.8000000000
P2	0.0000000000	1.6457081030	2.8000000000
+01.30,-00.50			
P1	1.5957081030	0.0000000000	-2.8000000000
P2	0.0000000000	1.5957081030	2.8000000000
+01.30,+00.00			
P1	2.0957081030	0.0000000000	-2.8000000000
P2	0.0000000000	2.0957081030	2.8000000000
+01.50,+00.05			
P1	2.1457081030	0.0000000000	-3.0000000000
P2	0.0000000000	2.1457081030	3.0000000000
+01.50,-00.05			
P1	2.0457081030	0.0000000000	-3.0000000000
P2	0.0000000000	2.0457081030	3.0000000000
+01.50,-00.10			
P1	1.9957081030	0.0000000000	-3.0000000000
P2	0.0000000000	1.9957081030	3.0000000000
+01.50,-00.15			
P1	1.9457081030	0.0000000000	-3.0000000000
P2	0.0000000000	1.9457081030	3.0000000000
+01.50,-00.20			
P1	1.8957081030	0.0000000000	-3.0000000000
P2	0.0000000000	1.8957081030	3.0000000000

+01.50,-00.25			
P1	1.8457081030	0.0000000000	-3.0000000000
P2	0.0000000000	1.8457081030	3.0000000000
+01.50,-00.30			
P1	1.7957081030	0.0000000000	-3.0000000000
P2	0.0000000000	1.7957081030	3.0000000000
+01.50,-00.35			
P1	1.7457081030	0.0000000000	-3.0000000000
P2	0.0000000000	1.7457081030	3.0000000000
+01.50,-00.40			
P1	1.6957081030	0.0000000000	-3.0000000000
P2	0.0000000000	1.6957081030	3.0000000000
+01.50,-00.45			
P1	1.6457081030	0.0000000000	-3.0000000000
P2	0.0000000000	1.6457081030	3.0000000000
+01.50,-00.50			
P1	1.5957081030	0.0000000000	-3.0000000000
P2	0.0000000000	1.5957081030	3.0000000000
+01.50,+00.00			
P1	2.0957081030	0.0000000000	-3.0000000000
P2	0.0000000000	2.0957081030	3.0000000000
+02.00,+00.05			
P1	2.1457081030	0.0000000000	-3.5000000000
P2	0.0000000000	2.1457081030	3.5000000000
+02.00,-00.05			
P1	2.0457081030	0.0000000000	-3.5000000000
P2	0.0000000000	2.0457081030	3.5000000000
+02.00,-00.10			
P1	1.9957081030	0.0000000000	-3.5000000000
P2	0.0000000000	1.9957081030	3.5000000000
+02.00,-00.15			
P1	1.9457081030	0.0000000000	-3.5000000000
P2	0.0000000000	1.9457081030	3.5000000000
+02.00,-00.20			
P1	1.8957081030	0.0000000000	-3.5000000000
P2	0.0000000000	1.8957081030	3.5000000000
+02.00,-00.25			
P1	1.8457081030	0.0000000000	-3.5000000000

P2	0.0000000000	1.8457081030	3.5000000000
+02.00,-00.30			
P1	1.7957081030	0.0000000000	-3.5000000000
P2	0.0000000000	1.7957081030	3.5000000000
+02.00,-00.35			
P1	1.7457081030	0.0000000000	-3.5000000000
P2	0.0000000000	1.7457081030	3.5000000000
+02.00,-00.40			
P1	1.6957081030	0.0000000000	-3.5000000000
P2	0.0000000000	1.6957081030	3.5000000000
+02.00,-00.45			
P1	1.6457081030	0.0000000000	-3.5000000000
P2	0.0000000000	1.6457081030	3.5000000000
+02.00,-00.50			
P1	1.5957081030	0.0000000000	-3.5000000000
P2	0.0000000000	1.5957081030	3.5000000000
+02.00,+00.00			
P1	2.0957081030	0.0000000000	-3.5000000000
P2	0.0000000000	2.0957081030	3.5000000000
+03.00,+00.05			
P1	2.1457081030	0.0000000000	-4.5000000000
P2	0.0000000000	2.1457081030	4.5000000000
+03.00,-00.05			
P1	2.0457081030	0.0000000000	-4.5000000000
P2	0.0000000000	2.0457081030	4.5000000000
+03.00,-00.10			
P1	1.9957081030	0.0000000000	-4.5000000000
P2	0.0000000000	1.9957081030	4.5000000000
+03.00,-00.15			
P1	1.9457081030	0.0000000000	-4.5000000000
P2	0.0000000000	1.9457081030	4.5000000000
+03.00,-00.20			
P1	1.8957081030	0.0000000000	-4.5000000000
P2	0.0000000000	1.8957081030	4.5000000000
+03.00,-00.25			
P1	1.8457081030	0.0000000000	-4.5000000000
P2	0.0000000000	1.8457081030	4.5000000000
+03.00,-00.30			

P1	1.7957081030	0.0000000000	-4.5000000000
P2	0.0000000000	1.7957081030	4.5000000000
+03.00,-00.35			
P1	1.7457081030	0.0000000000	-4.5000000000
P2	0.0000000000	1.7457081030	4.5000000000
+03.00,-00.40			
P1	1.6957081030	0.0000000000	-4.5000000000
P2	0.0000000000	1.6957081030	4.5000000000
+03.00,-00.45			
P1	1.6457081030	0.0000000000	-4.5000000000
P2	0.0000000000	1.6457081030	4.5000000000
+03.00,-00.50			
P1	1.5957081030	0.0000000000	-4.5000000000
P2	0.0000000000	1.5957081030	4.5000000000
+03.00,+00.00			
P1	2.0957081030	0.0000000000	-4.5000000000
P2	0.0000000000	2.0957081030	4.5000000000
+05.00,+00.05			
P1	2.1457081030	0.0000000000	-6.5000000000
P2	0.0000000000	2.1457081030	6.5000000000
+05.00,-00.05			
P1	2.0457081030	0.0000000000	-6.5000000000
P2	0.0000000000	2.0457081030	6.5000000000
+05.00,-00.10			
P1	1.9957081030	0.0000000000	-6.5000000000
P2	0.0000000000	1.9957081030	6.5000000000
+05.00,-00.15			
P1	1.9457081030	0.0000000000	-6.5000000000
P2	0.0000000000	1.9457081030	6.5000000000
+05.00,-00.20			
P1	1.8957081030	0.0000000000	-6.5000000000
P2	0.0000000000	1.8957081030	6.5000000000
+05.00,-00.25			
P1	1.8457081030	0.0000000000	-6.5000000000
P2	0.0000000000	1.8457081030	6.5000000000
+05.00,-00.30			
P1	1.7957081030	0.0000000000	-6.5000000000
P2	0.0000000000	1.7957081030	6.5000000000

+05.00,-00.35			
P1	1.7457081030	0.0000000000	-6.5000000000
P2	0.0000000000	1.7457081030	6.5000000000
+05.00,-00.40			
P1	1.6957081030	0.0000000000	-6.5000000000
P2	0.0000000000	1.6957081030	6.5000000000
+05.00,-00.45			
P1	1.6457081030	0.0000000000	-6.5000000000
P2	0.0000000000	1.6457081030	6.5000000000
+05.00,-00.50			
P1	1.5957081030	0.0000000000	-6.5000000000
P2	0.0000000000	1.5957081030	6.5000000000
+05.00,+00.00			
P1	2.0957081030	0.0000000000	-6.5000000000
P2	0.0000000000	2.0957081030	6.5000000000
+10.00,+00.05			
P1	2.1457081030	0.0000000000	-11.5000000000
P2	0.0000000000	2.1457081030	11.5000000000
+10.00,-00.05			
P1	2.0457081030	0.0000000000	-11.5000000000
P2	0.0000000000	2.0457081030	11.5000000000
+10.00,-00.10			
P1	1.9957081030	0.0000000000	-11.5000000000
P2	0.0000000000	1.9957081030	11.5000000000
+10.00,-00.15			
P1	1.9457081030	0.0000000000	-11.5000000000
P2	0.0000000000	1.9457081030	11.5000000000
+10.00,-00.20			
P1	1.8957081030	0.0000000000	-11.5000000000
P2	0.0000000000	1.8957081030	11.5000000000
+10.00,-00.25			
P1	1.8457081030	0.0000000000	-11.5000000000
P2	0.0000000000	1.8457081030	11.5000000000
+10.00,-00.30			
P1	1.7957081030	0.0000000000	-11.5000000000
P2	0.0000000000	1.7957081030	11.5000000000
+10.00,-00.35			
P1	1.7457081030	0.0000000000	-11.5000000000
P2	0.0000000000	1.7457081030	11.5000000000

+10.00,-00.40			
P1	1.6957081030	0.0000000000	-11.5000000000
P2	0.0000000000	1.6957081030	11.5000000000
+10.00,-00.45			
P1	1.6457081030	0.0000000000	-11.5000000000
P2	0.0000000000	1.6457081030	11.5000000000
+10.00,-00.50			
P1	1.5957081030	0.0000000000	-11.5000000000
P2	0.0000000000	1.5957081030	11.5000000000
+10.00,+00.00			
P1	2.0957081030	0.0000000000	-11.5000000000
P2	0.0000000000	2.0957081030	11.5000000000
+25.00,+00.05			
P1	2.1457081030	0.0000000000	-26.5000000000
P2	0.0000000000	2.1457081030	26.5000000000
+25.00,-00.05			
P1	2.0457081030	0.0000000000	-26.5000000000
P2	0.0000000000	2.0457081030	26.5000000000
+25.00,-00.10			
P1	1.9957081030	0.0000000000	-26.5000000000
P2	0.0000000000	1.9957081030	26.5000000000
+25.00,-00.15			
P1	1.9457081030	0.0000000000	-26.5000000000
P2	0.0000000000	1.9457081030	26.5000000000
+25.00,-00.20			
P1	1.8957081030	0.0000000000	-26.5000000000
P2	0.0000000000	1.8957081030	26.5000000000
+25.00,-00.25			
P1	1.8457081030	0.0000000000	-26.5000000000
P2	0.0000000000	1.8457081030	26.5000000000
+25.00,-00.30			
P1	1.7957081030	0.0000000000	-26.5000000000
P2	0.0000000000	1.7957081030	26.5000000000
+25.00,-00.35			
P1	1.7457081030	0.0000000000	-26.5000000000
P2	0.0000000000	1.7457081030	26.5000000000
+25.00,-00.40			
P1	1.6957081030	0.0000000000	-26.5000000000

P2	0.0000000000	1.6957081030	26.5000000000
+25.00,-00.45			
P1	1.6457081030	0.0000000000	-26.5000000000
P2	0.0000000000	1.6457081030	26.5000000000
+25.00,-00.50			
P1	1.5957081030	0.0000000000	-26.5000000000
P2	0.0000000000	1.5957081030	26.5000000000
+25.00,+00.00			
P1	2.0957081030	0.0000000000	-26.5000000000
P2	0.0000000000	2.0957081030	26.5000000000
-00.05,+00.05			
P1	2.1457081030	0.0000000000	-1.4500000000
P2	0.0000000000	2.1457081030	1.4500000000
-00.05,+00.10			
P1	2.1957081030	0.0000000000	-1.4500000000
P2	0.0000000000	2.1957081030	1.4500000000
-00.05,+00.15			
P1	2.2457081030	0.0000000000	-1.4500000000
P2	0.0000000000	2.2457081030	1.4500000000
-00.05,+00.20			
P1	2.2957081030	0.0000000000	-1.4500000000
P2	0.0000000000	2.2957081030	1.4500000000
-00.05,+00.25			
P1	2.3457081030	0.0000000000	-1.4500000000
P2	0.0000000000	2.3457081030	1.4500000000
-00.05,+00.30			
P1	2.3957081030	0.0000000000	-1.4500000000
P2	0.0000000000	2.3957081030	1.4500000000
-00.05,-00.05			
P1	2.0457081030	0.0000000000	-1.4500000000
P2	0.0000000000	2.0457081030	1.4500000000
-00.05,-00.10			
P1	1.9957081030	0.0000000000	-1.4500000000
P2	0.0000000000	1.9957081030	1.4500000000
-00.05,-00.15			
P1	1.9457081030	0.0000000000	-1.4500000000
P2	0.0000000000	1.9457081030	1.4500000000
-00.05,-00.20			

P1	1.8957081030	0.0000000000	-1.4500000000
P2	0.0000000000	1.8957081030	1.4500000000
-00.05,-00.25			
P1	1.8457081030	0.0000000000	-1.4500000000
P2	0.0000000000	1.8457081030	1.4500000000
-00.05,-00.30			
P1	1.7957081030	0.0000000000	-1.4500000000
P2	0.0000000000	1.7957081030	1.4500000000
-00.05,-00.35			
P1	1.7457081030	0.0000000000	-1.4500000000
P2	0.0000000000	1.7457081030	1.4500000000
-00.05,-00.40			
P1	1.6957081030	0.0000000000	-1.4500000000
P2	0.0000000000	1.6957081030	1.4500000000
-00.05,-00.45			
P1	1.6457081030	0.0000000000	-1.4500000000
P2	0.0000000000	1.6457081030	1.4500000000
-00.05,-00.50			
P1	1.5957081030	0.0000000000	-1.4500000000
P2	0.0000000000	1.5957081030	1.4500000000

Appendix C

Appendix to Chapter 4

C1 Core Electron Binding Energies of the Test Set Calculated with Other Density Functionals

Table C1: *CEBE results (eV) from density functional SVWN; the Chong test set is used and the ionized atom is in bold font.*

Molecule	Exp ⁹⁷	$\delta(\text{SVWN})$	$\delta(\text{SVWN}_r)$
C ₂ H ₂	290.82	-3.03	-2.98
C H ₄	290.91	-3.85	-3.80
C H ₃ OH	292.42	-3.85	-3.80
C H ₃ CN	292.45	-3.50	-3.45
C H ₃ CN	292.98	-3.83	-3.78
C HN	293.40	-3.43	-3.38
C H ₂ CO	294.47	-3.69	-3.64
C O	296.21	-3.32	-3.27
C O ₂	297.69	-4.07	-4.02
N H ₃	405.56	-4.47	-4.38
C H ₃ CN	405.64	-4.51	-4.52
C HN	406.78	-4.19	-4.10
N NO	408.71	-4.40	-4.31
N ₂	409.98	-4.30	-4.21
N NO	412.59	-4.57	-4.48
C H ₃ OH	539.11	-5.26	-5.09
C H ₂ CO	539.48	-5.16	-4.99
C H ₂ O	539.90	-5.35	-5.18
C O ₂	541.28	-5.02	-4.85
N NO	541.42	-4.74	-4.57
C O	542.55	-5.03	-4.86
H F	694.23	-6.20	-5.86
F ₂	696.69	-6.00	-5.66
MAD	–	4.42	4.31

Table C2: *CEBE results (eV) from density functional SVWN1RPA; the Chong test set is used and the ionized atom is in bold font.*

Molecule	Exp ⁹⁷	$\delta(\text{SVWN1RPA})$	$\delta(\text{SVWN1RPA}_r)$
C ₂ H ₂	290.82	-2.46	-2.41
C H ₄	290.91	-3.28	-3.23
C H ₃ OH	292.42	-3.27	-3.22
C H ₃ CN	292.45	-2.92	-2.87
C H ₃ CN	292.98	-3.25	-3.20
C HN	293.40	-2.85	-2.80
C H ₂ CO	294.47	-3.11	-3.06
C O	296.21	-2.73	-2.68
C O ₂	297.69	-3.48	-3.43
N H ₃	405.56	-3.89	-3.80
C H ₃ CN	405.64	-3.93	-3.84
C HN	406.78	-3.61	-3.52
N NO	408.71	-3.80	-3.71
N ₂	409.98	-3.70	-3.61
N NO	412.59	-3.97	-3.88
C H ₃ OH	539.11	-4.67	-4.50
C H ₂ CO	539.48	-4.57	-4.40
C H ₂ O	539.90	-4.76	-4.59
C O ₂	541.28	-4.42	-4.25
N NO	541.42	-4.14	-3.97
C O	542.55	-4.43	-4.26
H F	694.23	-5.59	-5.25
F ₂	696.69	-5.38	-5.04
MAD	–	3.83	3.72

Table C3: *CEBE results (eV) from density functional BOP; the Chong test set is used and the ionized atom is in bold font.*

Molecule	Exp ⁹⁷	$\delta(\text{BOP})$	$\delta(\text{BOP}_r)$
C ₂ H ₂	290.82	0.26	0.31
C H ₄	290.91	-0.28	-0.23
C H ₃ OH	292.42	-0.36	-0.31
C H ₃ CN	292.45	-0.09	-0.04
C H ₃ CN	292.98	-0.54	-0.49
C HN	293.40	-0.15	-0.10
C H ₂ CO	294.47	-0.30	-0.25
C O	296.21	-0.07	-0.02
C O ₂	297.69	-0.73	-0.68
N H ₃	405.56	-0.41	-0.32
C H ₃ CN	405.64	-0.67	-0.58
C HN	406.78	-0.35	-0.26
N NO	408.71	-0.54	-0.45
N ₂	409.98	-0.48	-0.39
N NO	412.59	-0.80	-0.71
C H ₃ OH	539.11	-0.84	-0.67
C H ₂ CO	539.48	-0.81	-0.64
C H ₂ O	539.90	-0.73	-0.56
C O ₂	541.28	-0.59	-0.42
N NO	541.42	-0.38	-0.21
C O	542.55	-0.71	-0.54
H F	694.23	-1.01	-0.67
F ₂	696.69	-1.19	-0.85
MAD	-	0.54	0.42

Table C4: *CEBE results (eV) from density functional BP86; the Chong test set is used and the ionized atom is in bold font.*

Molecule	Exp ⁹⁷	$\delta(\text{BP86})$	$\delta(\text{BP86}_r)$
C ₂ H ₂	290.82	0.34	0.39
C H ₄	290.91	-0.31	-0.26
C H ₃ O H	292.42	-0.36	-0.31
C H ₃ C N	292.45	-0.01	0.04
C H ₃ C N	292.98	-0.53	-0.48
C H C N	293.40	-0.11	-0.06
H ₂ C O	294.47	-0.29	-0.24
C O	296.21	-0.10	-0.05
C O ₂	297.69	-0.73	-0.68
N H ₃	405.56	-0.30	-0.21
C H ₃ C N	405.64	-0.49	-0.40
H C N	406.78	-0.19	-0.10
N N O	408.71	-0.40	-0.31
N ₂	409.98	-0.34	-0.26
N N O	412.59	-0.61	-0.52
C H ₃ O H	539.11	-0.57	-0.40
H ₂ C O	539.48	-0.53	-0.36
H ₂ O	539.90	-0.55	0.00
C O ₂	541.28	-0.35	-0.18
N N O	541.42	-0.12	0.05
C O	542.55	-0.45	-0.28
H F	694.23	-0.80	-0.46
F ₂	696.69	-0.85	-0.51
MAD	–	0.41	0.28

Table C5: *CEBE results (eV) from density functional GLYP; the Chong test set is used and the ionized atom is in bold font.*

Molecule	Exp ⁹⁷	$\delta(\text{GLYP})$	$\delta(\text{GLYP}_r)$
C ₂ H ₂	290.82	0.21	0.26
C H ₄	290.91	-0.36	-0.31
C H ₃ OH	292.42	-0.45	-0.40
C H ₃ CN	292.45	-0.13	-0.08
C H ₃ CN	292.98	-0.60	-0.55
C HN	293.40	-0.19	-0.14
C H ₂ CO	294.47	-0.37	-0.32
C O	296.21	-0.13	-0.08
C O ₂	297.69	-0.73	-0.68
N H ₃	405.56	-0.47	-0.38
C H ₃ CN	405.64	-0.71	-0.62
C HN	406.78	-0.40	-0.31
N NO	408.71	-0.55	-0.46
N ₂	409.98	-0.51	-0.42
N NO	412.59	-0.82	-0.73
C H ₃ OH	539.11	-0.87	-0.70
C H ₂ CO	539.48	-0.83	-0.66
C H ₂ O	539.90	-0.76	-0.59
C O ₂	541.28	-0.60	-0.43
N NO	541.42	-0.39	-0.22
C O	542.55	-0.71	-0.54
H F	694.23	-0.99	-0.65
F ₂	696.69	-1.17	-0.83
MAD	-	0.56	0.45

Table C6: *CEBE results (eV) from density functional GP86; the Chong test set is used and the ionized atom is in bold font.*

Molecule	Exp ⁹⁷	$\delta(\text{GP86})$	$\delta(\text{GP86}_r)$
C ₂ H ₂	290.82	0.13	0.18
C H ₄	290.91	-0.52	-0.47
C H ₃ OH	292.42	-0.57	-0.52
C H ₃ CN	292.45	-0.21	-0.16
C H ₃ CN	292.98	-0.72	-0.67
C HN	293.40	-0.31	-0.26
C H ₂ CO	294.47	-0.50	-0.45
C O	296.21	-0.29	-0.24
C O ₂	297.69	-0.92	-0.87
N H ₃	405.56	-0.52	-0.43
C H ₃ CN	405.64	-0.71	-0.62
C HN	406.78	-0.42	-0.33
N NO	408.71	-0.60	-0.51
N ₂	409.98	-0.56	-0.47
N NO	412.59	-0.84	-0.75
C H ₃ OH	539.11	-0.81	-0.64
C H ₂ CO	539.48	-0.79	-0.62
C H ₂ O	539.90	-0.78	-0.61
C O ₂	541.28	-0.58	-0.41
N NO	541.42	-0.36	-0.19
C O	542.55	-0.70	-0.53
F H	694.23	-1.04	-0.70
F ₂	696.69	-1.10	-0.76
MAD	-	0.61	0.50

Table C7: *CEBE results (eV) from density functional GVWN; the Chong test set is used and the ionized atom is in bold font.*

Molecule	Exp ⁹⁷	$\delta(\text{GVWN})$	$\delta(\text{GVWN}_r)$
C ₂ H ₂	290.82	1.56	1.61
C H ₄	290.91	1.07	1.12
C H ₃ OH	292.42	0.98	1.03
C H ₃ C N	292.45	1.21	1.25
C H ₃ C N	292.98	0.82	0.88
C HN	293.40	1.17	1.22
H ₂ C O	294.47	1.03	1.09
C O	296.21	1.24	1.28
C O ₂	297.69	0.67	0.72
N H ₃	405.56	0.94	1.03
C H ₃ C N	405.64	0.63	0.72
C HN	406.78	0.93	1.02
N NO	408.71	0.82	0.91
N ₂	409.98	0.85	0.94
N NO	412.59	0.54	0.63
C H ₃ O H	539.11	0.48	0.65
H ₂ C O	539.48	0.48	0.65
H ₂ O	539.90	0.65	0.82
C O ₂	541.28	0.77	0.93
N NO	541.42	0.95	1.12
C O	542.55	0.60	0.77
H F	694.23	0.43	0.77
F ₂	696.69	0.19	0.53
MAD	–	0.83	0.94

Table C8: *CEBE results (eV) from density functional GPW91; the Chong test set is used and the ionized atom is in bold font.*

Molecule	Exp ⁹⁷	$\delta(\text{GPW91})$	$\delta(\text{GPW91}_r)$
C ₂ H ₂	290.82	-0.12	-0.07
C H ₄	290.91	-0.75	-0.70
C H ₃ OH	292.42	-0.80	-0.75
C H ₃ CN	292.45	-0.46	-0.41
C H ₃ CN	292.98	-0.95	-0.90
C HN	293.40	-0.56	-0.51
C H ₂ CO	294.47	-0.74	-0.69
C O	296.21	-0.56	-0.53
C O ₂	297.69	-1.19	-1.14
N H ₃	405.56	-0.80	-0.71
C H ₃ CN	405.64	-1.01	-0.92
C HN	406.78	-0.71	-0.63
N NO	408.71	-0.91	-0.82
N ₂	409.98	-0.86	-0.77
N NO	412.59	-1.12	-1.04
C H ₃ OH	539.11	-1.15	-0.98
C H ₂ CO	539.48	-1.14	-0.97
C H ₂ O	539.90	-1.13	-0.96
C O ₂	541.28	-0.93	-0.76
N NO	541.42	-0.72	-0.55
C O	542.55	-1.04	-0.87
H F	694.23	-1.43	-1.09
F ₂	696.69	-1.50	-1.16
MAD	-	0.90	0.78

Table C9: *CEBE results (eV) from density functional PBEVWN; the Chong test set is used and the ionized atom is in bold font.*

Molecule	Exp ⁹⁷	$\delta(\text{PBEVWN})$	$\delta(\text{PBEVWN}_r)$
C ₂ H ₂	290.82	1.61	1.66
C H ₄	290.91	1.10	1.15
C H ₃ OH	292.42	1.02	1.07
C H ₃ CN	292.45	1.27	1.32
C H ₃ CN	292.98	0.84	0.89
C HN	293.40	1.22	1.27
C H ₂ CO	294.47	1.08	1.13
C O	296.21	1.27	1.32
C O ₂	297.69	0.69	0.75
N H ₃	405.56	0.97	1.06
C H ₃ CN	405.64	0.69	0.78
C HN	406.78	1.00	1.09
N NO	408.71	0.84	0.93
N ₂	409.98	0.90	0.99
N NO	412.59	0.61	0.70
C H ₃ OH	539.11	0.51	0.68
C H ₂ CO	539.48	0.55	0.72
C H ₂ O	539.90	0.65	0.82
C O ₂	541.28	0.80	0.97
N NO	541.42	1.01	1.18
C O	542.55	0.67	0.84
H F	694.23	0.40	0.74
F ₂	696.69	0.20	0.54
MAD	–	0.87	0.98

Table C10: *CEBE results (eV) from density functional PBEOP; the Chong test set is used and the ionized atom is in bold font.*

Molecule	Exp ⁹⁷	$\delta(\text{PBEOP})$	$\delta(\text{PBEOP}_r)$
C ₂ H ₂	290.82	0.12	0.17
C H ₄	290.91	-0.45	-0.40
C H ₃ OH	292.42	-0.53	-0.48
C H ₃ CN	292.45	-0.23	-0.18
C H ₃ CN	292.98	-0.71	-0.66
C HN	293.40	-0.30	-0.25
C H ₂ CO	294.47	-0.46	-0.41
C O	296.21	-0.23	-0.18
C O ₂	297.69	-0.89	-0.84
N H ₃	405.56	-0.60	-0.51
C H ₃ CN	405.64	-0.83	-0.74
C HN	406.78	-0.51	-0.42
N NO	408.71	-0.72	-0.63
N ₂	409.98	-0.65	-0.56
N NO	412.59	-0.96	-0.87
C H ₃ OH	539.11	-1.04	-0.87
C H ₂ CO	539.48	-0.99	-0.82
C H ₂ O	539.90	-0.96	-0.79
C O ₂	541.28	-0.80	-0.62
N NO	541.42	-0.56	-0.39
C O	542.55	-0.89	-0.72
H F	694.23	-1.27	-0.93
F ₂	696.69	-1.42	-1.08
MAD	–	0.70	0.59

Table C11: *CEBE results (eV) from density functional OLYP; the Chong test set is used and the ionized atom is in bold font.*

Molecule	Exp ⁹⁷	$\delta(\text{OLYP})$	$\delta(\text{OLYP}_r)$
C ₂ H ₂	290.82	-0.10	-0.05
C H ₄	290.91	-0.74	-0.69
C H ₃ OH	292.42	-0.77	-0.72
C H ₃ CN	292.45	-0.45	-0.40
C H ₃ CN	292.98	-0.96	-0.91
C HN	293.40	-0.56	-0.51
C H ₂ CO	294.47	-0.69	-0.64
C O	296.21	-0.51	-0.46
C O ₂	297.69	-1.21	-1.16
N H ₃	405.56	-0.99	-0.90
C H ₃ CN	405.64	-1.16	-1.07
C HN	406.78	-0.82	-0.73
N NO	408.71	-1.08	-0.99
N ₂	409.98	-0.99	-0.90
N NO	412.59	-1.26	-1.17
C H ₃ OH	539.11	-1.58	-1.41
C H ₂ CO	539.48	-1.51	-1.34
C H ₂ O	539.90	-1.58	-1.41
C O ₂	541.28	-1.34	-1.17
C NO	541.42	-1.09	-0.92
C O	542.55	-1.43	-1.26
H F	694.23	-2.19	-1.85
F ₂	696.69	-2.16	-1.82
MAD	-	1.09	0.98

Table C12: *CEBE results (eV) from density functional PW91; the Chong test set is used and the ionized atom is in bold font.*

Molecule	Exp ⁹⁷	$\delta(\text{PW91})$	$\delta(\text{PW91}_r)$
C ₂ H ₂	290.82	0.07	0.12
C H ₄	290.91	-0.58	-0.53
C H ₃ OH	292.42	-0.63	-0.58
C H ₃ CN	292.45	-0.28	-0.23
C H ₃ CN	292.98	-0.80	-0.75
C HN	293.40	-0.38	-0.33
C H ₂ CO	294.47	-0.56	-0.51
C O	296.21	-0.39	-0.34
C O ₂	297.69	-1.01	-0.96
N H ₃	405.56	-0.63	-0.54
C H ₃ CN	405.64	-0.81	-0.72
C HN	406.78	-0.49	-0.40
N NO	408.71	-0.74	-0.65
N ₂	409.98	-0.66	-0.57
N NO	412.59	-0.92	-0.82
C H ₃ OH	539.11	-0.95	-0.78
C H ₂ CO	539.48	-0.89	-0.72
C H ₂ O	539.90	-0.95	-0.78
C O ₂	541.28	-0.72	-0.55
N NO	541.42	-0.49	-0.33
C O	542.55	-0.78	-0.61
H F	694.23	-1.24	-0.90
F ₂	696.69	-1.28	-0.94
MAD	-	0.71	0.59

Table C13: *CEBE results (eV) from density functional PBE; the Chong test set is used and the ionized atom is in bold font.*

Molecule	Exp ⁹⁷	$\delta(\text{PBE})$	$\delta(\text{PBE}_r)$
C ₂ H ₂	290.82	-0.24	-0.19
C H ₄	290.91	-0.91	-0.86
C H ₃ OH	292.42	-0.95	-0.90
C H ₃ C N	292.45	-0.59	-0.54
C H ₃ C N	292.98	-1.12	-1.07
C HN	293.40	-0.70	-0.65
C H ₂ C O	294.47	-0.88	-0.83
C O	296.21	-0.72	-0.67
C O ₂	297.69	-1.36	-1.31
N H ₃	405.56	-0.97	-0.88
C H ₃ C N	405.64	-1.14	-1.05
C HN	406.78	-0.83	-0.74
N NO	408.71	-1.09	-1.00
N ₂	409.98	-1.01	-0.92
N NO	412.59	-1.25	-1.16
C H ₃ O H	539.11	-1.32	-1.15
C H ₂ O	539.48	-1.26	-1.09
C H ₂ O	539.90	-1.33	-1.16
C O ₂	541.28	-1.11	-0.94
N NO	541.42	-0.87	-0.70
C O	542.55	-1.17	-1.00
H F	694.23	-1.69	-1.35
F ₂	696.69	-1.71	-1.36
MAD	–	1.05	0.94

Table C14: *CEBE* results (*eV*) from density functional *EDF1*; the Chong test set is used and the ionized atom is in bold font.

Molecule	Exp ⁹⁷	$\delta(\text{EDF1})$	$\delta(\text{EDF1}_r)$
C ₂ H ₂	290.82	0.01	0.06
CH ₄	290.91	-0.61	-0.56
CH ₃ OH	292.42	-0.64	-0.59
CH ₃ CN	292.45	-0.33	-0.28
CH ₃ CN	292.98	-0.83	-0.78
H CN	293.40	-0.42	-0.37
H ₂ CO	294.47	-0.56	-0.51
CO	296.21	-0.36	-0.31
CO ₂	297.69	-1.01	-0.96
NH ₃	405.56	-0.79	-0.70
CH ₃ CN	405.64	-0.99	-0.90
H CN	406.78	-0.67	-0.58
NNO	408.71	-0.87	-0.78
N ₂	409.98	-0.80	-0.71
NNO	412.59	-1.08	-0.99
CH ₃ OH	539.11	-1.29	-1.12
H ₂ CO	539.48	-1.25	-1.08
H ₂ O	539.90	-1.25	-1.08
CO ₂	541.28	-1.04	-0.87
NNO	541.42	-0.80	-0.63
CO	542.55	-1.15	-0.98
HF	694.23	-1.70	-1.36
F ₂	696.69	-1.73	-1.39
MAD	-	0.88	0.76

Table C15: *CEBE results (eV) from density functional revPBE; the Chong test set is used and the ionized atom is in bold font.*

Molecule	Exp ⁹⁷	$\delta(\text{revPBE})$	$\delta(\text{revPBE}_r)$
C ₂ H ₂	290.82	0.10	0.15
C H ₄	290.91	-0.51	-0.46
C H ₃ O H	292.42	-0.57	-0.52
C H ₃ C N	292.45	-0.28	-0.23
C H ₃ N	292.98	-0.75	-0.70
H CN	293.40	-0.38	-0.33
H ₂ C O	294.47	-0.53	-0.48
C O	296.21	-0.43	-0.38
C O ₂	297.69	-1.06	-1.01
N H ₃	405.56	-0.57	-0.48
C H ₃ C N	405.64	-0.78	-0.69
H CN	406.78	-0.47	-0.41
N N O	408.71	-0.75	-0.66
N ₂	409.98	-0.67	-0.58
N N O	412.59	-0.92	-0.83
C H ₃ O H	539.11	-0.94	-0.77
H ₂ C O	539.48	-0.90	-0.73
H ₂ O	539.90	-0.93	-0.76
C O ₂	541.28	-0.75	-0.58
N N O	541.42	-0.52	-0.35
C O	542.55	-0.83	-0.66
H F	694.23	-1.31	-0.97
F ₂	696.69	-1.38	-1.04
MAD	-	0.71	0.60

Table C16: *CEBE results (eV) from density functional RPBE; the Chong test set is used and the ionized atom is in bold font.*

Molecule	Exp ⁹⁷	$\delta(\text{RPBE})$	$\delta(\text{RPBE}_r)$
C ₂ H ₂	290.82	0.27	0.32
C H ₄	290.91	-0.34	-0.29
C H ₃ OH	292.42	-0.41	-0.36
C H ₃ C N	292.45	-0.11	-0.06
C H ₃ C N	292.98	-0.58	-0.53
C HN	293.40	-0.22	-0.17
C H ₂ C O	294.47	-0.37	-0.32
C O	296.21	-0.27	-0.22
C O ₂	297.69	-0.91	-0.86
N H ₃	405.56	-0.39	-0.30
C H ₃ C N	405.64	-0.60	-0.51
C HN	406.78	-0.29	-0.20
N NO	408.71	-0.58	-0.49
N ₂	409.98	-0.49	-0.40
N NO	412.59	-0.74	-0.65
C H ₃ O H	539.11	-0.76	-0.59
C H ₂ C O	539.48	-0.71	-0.54
C H ₂ O	539.90	-0.75	-0.58
C O ₂	541.28	-0.57	-0.40
N NO	541.42	-0.33	-0.16
C O	542.55	-0.64	-0.47
H F	694.23	-1.13	-0.79
F ₂	696.69	-1.20	-0.86
MAD	-	0.55	0.44

Table C17: *CEBE results (eV) from density functional PBEsol; the Chong test set is used and the ionized atom is in bold font.*

Molecule	Exp ⁹⁷	$\delta(\text{PBEsol})$	$\delta(\text{PBEsol}_r)$
C ₂ H ₂	290.82	-1.78	-1.73
C H ₄	290.91	-2.52	-2.47
C H ₃ OH	292.42	-2.54	-2.49
C H ₃ CN	292.45	-2.19	-2.14
C H ₃ CN	292.98	-2.63	-2.58
C HN	293.40	-2.23	-2.18
C H ₂ CO	294.47	-2.45	-2.40
C O	296.21	-2.22	-2.17
C O ₂	297.69	-2.92	-2.87
N H ₃	405.56	-2.82	-2.73
C H ₃ CN	405.64	-2.93	-2.84
C HN	406.78	-2.62	-2.52
N NO	408.71	-2.88	-2.79
N ₂	409.98	-2.78	-2.69
N NO	412.59	-3.04	-2.95
C H ₃ OH	539.11	-3.35	-3.18
C H ₂ CO	539.48	-3.28	-3.11
C H ₂ O	539.90	-3.42	-3.25
C O ₂	541.28	-3.15	-2.98
N NO	541.42	-2.89	-2.72
C O	542.55	-3.18	-3.01
F H	694.23	-4.03	-3.69
F ₂	696.69	-3.93	-3.59
MAD	-	2.86	2.74

Table C18: *CEBE results (eV) from density functional HCTH93; the Chong test set is used and the ionized atom is in bold font.*

Molecule	Exp ⁹⁷	$\delta(\text{HCTH93})$	$\delta(\text{HCTH93}_r)$
C ₂ H ₂	290.82	-0.30	-0.25
C H ₄	290.91	-0.95	-0.90
C H ₃ OH	292.42	-0.92	-0.87
C H ₃ CN	292.45	-0.62	-0.57
C H ₃ CN	292.98	-1.15	-1.10
C HN	293.40	-0.73	-0.68
C H ₂ CO	294.47	-0.83	-0.78
C O	296.21	-0.59	-0.54
C O ₂	297.69	-1.34	-1.29
N H ₃	405.56	-1.35	-1.26
C H ₃ CN	405.64	-1.52	-1.43
C HN	406.78	-1.20	-1.11
N NO	408.71	-1.39	-1.30
N ₂	409.98	-1.32	-1.23
N NO	412.59	-1.58	-1.49
C H ₃ OH	539.11	-2.13	-1.96
C H ₂ CO	539.48	-2.09	-1.92
C H ₂ O	539.90	-2.12	-1.95
C O ₂	541.28	-1.88	-1.71
N NO	541.42	-1.61	-1.44
C O	542.55	-2.02	-1.85
H F	694.23	-2.92	-2.58
F ₂	696.69	-2.78	-2.44
MAD	–	1.45	1.33

Table C19: *CEBE results (eV) from density functional HCTH120; the Chong test set is used and the ionized atom is in bold font.*

Molecule	Exp ⁹⁷	$\delta(\text{HCTH120})$	$\delta(\text{HCTH120}_r)$
C ₂ H ₂	290.82	-0.19	-0.14
C H ₄	290.91	-0.86	-0.81
C H ₃ OH	292.42	-0.83	-0.78
C H ₃ C N	292.45	-0.54	-0.49
C H ₃ C N	292.98	-1.03	-0.98
H CN	293.40	-0.61	-0.56
H ₂ C O	294.47	-0.72	-0.67
C O	296.21	-0.43	-0.38
C O ₂	297.69	-1.20	-1.14
N H ₃	405.56	-1.30	-1.21
C H ₃ C N	405.64	-1.43	-1.34
H CN	406.78	-1.10	-1.01
N NO	408.71	-1.28	-1.19
N ₂	409.98	-1.21	-1.12
N NO	412.59	-1.48	-1.39
C H ₃ O H	539.11	-2.08	-1.91
H ₂ C O	539.48	-2.02	-1.85
H ₂ O	539.90	-2.07	-1.90
C O ₂	541.28	-1.80	-1.63
N NO	541.42	-1.52	-1.35
C O	542.55	-1.93	-1.76
H F	694.23	-2.86	-2.52
F ₂	696.69	-2.71	-2.37
MAD	–	1.36	1.24

Table C20: *CEBE results (eV) from density functional HCTH147; the Chong test set is used and the ionized atom is in bold font.*

Molecule	Exp ⁹⁷	$\delta(\text{HCTH147})$	$\delta(\text{HCTH147}_r)$
C ₂ H ₂	290.82	-0.30	-0.25
C H ₄	290.91	-0.98	-0.93
C H ₃ OH	292.42	-0.94	-0.89
C H ₃ C N	292.45	-0.65	-0.60
C H ₃ CN	292.98	-1.15	-1.10
H CN	293.40	-0.73	-0.68
H ₂ C O	294.47	-0.83	-0.73
C O	296.21	-0.55	-0.50
C O ₂	297.69	-1.32	-1.27
N H ₃	405.56	-1.43	-1.34
C H ₃ C N	405.64	-1.55	-1.46
H CN	406.78	-1.23	-1.14
N NO	408.71	-1.42	-1.33
N ₂	409.98	-1.34	-1.25
N NO	412.59	-1.61	-1.52
C H ₃ O H	539.11	-2.23	-2.06
H ₂ C O	539.48	-2.17	-2.00
H ₂ O	539.90	-2.22	-2.05
C O ₂	541.28	-1.95	-1.78
N NO	541.42	-1.67	-1.50
C O	542.55	-2.09	-1.92
H F	694.23	-3.04	-2.70
F ₂	696.69	-2.87	-2.53
MAD	–	1.49	1.37

Table C21: *CEBE results (eV) from density functional HCTH407; the Chong test set is used and the ionized atom is in bold font.*

Molecule	Exp ⁹⁷	$\delta(\text{HCTH407})$	$\delta(\text{HCTH407}_r)$
C ₂ H ₂	290.82	-0.43	-0.39
C H ₄	290.91	-1.13	-1.08
C H ₃ OH	292.42	-1.07	-1.02
C H ₃ C N	292.45	-0.80	-0.75
C H ₃ C N	292.98	-1.28	-1.23
C HN	293.40	-0.88	-0.83
C H ₂ C O	294.47	-0.96	-0.91
C O	296.21	-0.74	-0.70
C O ₂	297.69	-1.51	-1.46
N H ₃	405.56	-1.62	-1.53
C H ₃ C N	405.64	-1.73	-1.64
C HN	406.78	-1.41	-1.32
N NO	408.71	-1.63	-1.54
N ₂	409.98	-1.53	-1.44
N NO	412.59	-1.76	-1.67
C H ₃ O H	539.11	-2.44	-2.27
C H ₂ O	539.48	-2.38	-2.21
C H ₂ O	539.90	-2.47	-2.30
C O ₂	541.28	-2.19	-2.02
N NO	541.42	-1.87	-1.70
C O	542.55	-2.33	-2.16
H F	694.23	-3.32	-2.98
F ₂	696.69	-3.10	-2.76
MAD	–	1.68	1.56

Table C22: *CEBE results (eV) from density functional SOGGA; the Chong test set is used and the ionized atom is in bold font.*

Molecule	Exp ⁹⁷	$\delta(\text{SOGGA})$	$\delta(\text{SOGGA}_r)$
C ₂ H ₂	290.82	-2.05	-2.00
C H ₄	290.91	-2.82	-2.77
C H ₃ OH	292.42	-2.84	-2.79
C H ₃ CN	292.45	-2.48	-2.43
C H ₃ CN	292.98	-2.92	-2.87
C HN	293.40	-2.53	-2.48
C H ₂ CO	294.47	-2.75	-2.70
C O	296.21	-2.54	-2.49
C O ₂	297.69	-3.25	-3.20
N H ₃	405.56	-3.10	-3.01
C H ₃ CN	405.64	-3.19	-3.10
C HN	406.78	-2.88	-2.79
N NO	408.71	-3.17	-3.08
N ₂	409.98	-3.07	-2.98
N NO	412.59	-3.31	-3.22
C H ₃ OH	539.11	-3.61	-3.44
C H ₂ CO	539.48	-3.53	-3.36
C H ₂ O	539.90	-3.71	-3.54
C O ₂	541.28	-3.43	-3.26
N NO	541.42	-3.16	-2.99
C O	542.55	-3.44	-3.27
H F	694.23	-4.34	-4.00
F ₂	696.69	-4.21	-3.87
MAD	–	3.15	3.03

Table C23: *CEBE results (eV) from density functional MOHLYP; the Chong test set is used and the ionized atom is in bold font.*

Molecule	Exp ⁹⁷	$\delta(\text{MOHLYP})$	$\delta(\text{MOHLYP}_r)$
C ₂ H ₂	290.82	-1.23	-1.18
C H ₄	290.91	-1.84	-1.79
C H ₃ OH	292.42	-1.91	-1.85
C H ₃ C N	292.45	-1.64	-1.59
C H ₃ C N	292.98	-2.10	-2.05
C HN	293.40	-1.74	-1.69
C H ₂ C O	294.47	-1.88	-1.83
C O	296.21	-1.76	-1.71
C O ₂	297.69	-2.50	-2.45
N H ₃	405.56	-2.30	-2.21
C H ₃ C N	405.64	-2.52	-2.43
C HN	406.78	-2.19	-2.10
N NO	408.71	-2.54	-2.45
N ₂	409.98	-2.43	-2.34
N NO	412.59	-2.73	-2.64
C H ₃ O H	539.11	-3.12	-2.95
C H ₂ O	539.48	-3.06	-2.89
C H ₂ O	539.90	-3.12	-2.95
C O ₂	541.28	-2.96	-2.79
N NO	541.42	-2.71	-2.54
C O	542.55	-3.02	-2.85
H F	694.23	-4.00	-3.66
F ₂	696.69	-4.04	-3.70
MAD	–	2.49	2.38

Table C24: *CEBE results (eV) from density functional B97-D; the Chong test set is used and the ionized atom is in bold font.*

Molecule	Exp ⁹⁷	$\delta(\text{B97-D})$	$\delta(\text{B97-D}_r)$
C ₂ H ₂	290.82	-0.06	-0.01
C H ₄	290.91	-0.68	-0.63
C H ₃ OH	292.42	-0.65	-0.60
C H ₃ CN	292.45	-0.39	-0.34
C H ₃ CN	292.98	-0.91	-0.86
C HN	293.40	-0.48	-0.43
C H ₂ CO	294.47	-0.55	-0.50
C O	296.21	-0.28	-0.23
C O ₂	297.69	-1.03	-0.98
N H ₃	405.56	-1.14	-1.05
C H ₃ CN	405.64	-1.31	-1.22
C HN	406.78	-1.00	-1.07
N NO	408.71	-1.17	-1.07
N ₂	409.98	-1.10	-1.01
N NO	412.59	-1.39	-1.30
C H ₃ OH	539.11	-1.92	-1.75
C H ₂ CO	539.48	-1.89	-1.72
C H ₂ O	539.90	-1.89	-1.71
C O ₂	541.28	-1.67	-1.50
N NO	541.42	-1.41	-1.24
C O	542.55	-1.84	-1.67
F H	694.23	-2.64	-2.30
F ₂	696.69	-2.55	-2.21
MAD	-	1.21	1.10

Table C25: *CEBE results (eV) from density functional BHHLYP; the Chong test set is used and the ionized atom is in bold font.*

Molecule	Exp ⁹⁷	$\delta(\text{BHHLYP})$	$\delta(\text{BHHLYP}_r)$
C ₂ H ₂	290.82	1.12	1.17
C H ₄	290.91	0.46	0.51
C H ₃ OH	292.42	0.54	0.59
C H ₃ C N	292.45	0.91	0.96
C H ₃ C N	292.98	0.54	0.59
C HCN	293.40	0.88	0.93
C H ₂ C O	294.47	0.76	0.81
C O	296.21	1.26	1.31
C O ₂	297.69	1.36	1.41
N H ₃	405.56	0.36	0.45
C H ₃ C N	405.64	0.30	0.39
C HCN	406.78	0.52	0.61
N NO	408.71	0.90	0.99
N ₂	409.98	0.69	0.78
N NO	412.59	1.20	1.29
C H ₃ O H	539.11	0.13	0.04
H ₂ C O	539.48	0.25	-0.08
H ₂ O	539.90	0.00	0.17
C O ₂	541.28	0.28	0.45
N NO	541.42	0.29	0.46
C O	542.55	0.04	0.21
H F	694.23	0.28	0.06
F ₂	696.69	0.41	-0.07
MAD	—	0.58	0.62

Table C26: *CEBE results (eV) from density functional B3PW91; the Chong test set is used and the ionized atom is in bold font.*

Molecule	Exp ⁹⁷	$\delta(\text{B3PW91})$	$\delta(\text{B3PW91}_r)$
C ₂ H ₂	290.82	0.30	0.36
C H ₄	290.91	-0.37	-0.32
C H ₃ OH	292.42	-0.34	-0.29
C H ₃ CN	292.45	0.02	0.07
C H ₃ CN	292.98	-0.44	-0.39
C HN	293.40	-0.07	-0.02
C H ₂ CO	294.47	-0.22	-0.17
C O	296.21	0.06	0.11
C O ₂	297.69	-0.27	-0.22
N H ₃	405.56	-0.46	-0.37
C H ₃ CN	405.64	-0.58	-0.49
C HN	406.78	-0.32	-0.23
N NO	408.71	-0.31	-0.22
N ₂	409.98	-0.35	-0.26
N NO	412.59	-0.28	-0.19
C H ₃ OH	539.11	-0.89	-0.72
C H ₂ CO	539.48	-0.92	-0.75
C H ₂ O	539.90	-0.85	-0.68
C O ₂	541.28	-0.60	-0.43
N NO	541.42	-0.45	-0.28
C O	542.55	-0.75	-0.58
H F	694.23	-1.21	-0.87
F ₂	696.69	-1.23	-0.89
MAD	-	0.49	0.39

Table C27: *CEBE results (eV) from density functional B3LYP1; the Chong test set is used and the ionized atom is in bold font.*

Molecule	Exp ⁹⁷	$\delta(\text{B3LYP1})$	$\delta(\text{B3LYP1}_r)$
C ₂ H ₂	290.82	0.68	0.73
CH ₄	290.91	0.06	0.11
CH ₃ OH	292.42	0.05	0.10
CH ₃ CN	292.45	0.41	0.46
C H ₃ CN	292.98	-0.07	-0.02
HCN	293.40	0.34	0.39
H ₂ CO	294.47	0.19	0.24
CO	296.21	0.53	0.58
CO ₂	297.69	0.21	0.26
NH ₃	405.56	-0.08	0.01
CH ₃ CN	405.64	-0.23	-0.14
HCN	406.78	0.04	0.13
NNO	408.71	0.09	0.18
N ₂	409.98	0.04	0.13
NNO	412.59	0.07	0.16
CH ₃ OH	539.11	-0.55	-0.38
H ₂ CO	539.48	-0.56	-0.39
H ₂ O	539.90	-0.44	-0.27
CO ₂	541.28	-0.22	-0.05
NNO	541.42	-0.08	0.09
CO	542.55	-0.37	-0.20
HF	694.23	-0.73	-0.39
F ₂	696.69	-0.85	-0.51
MAD	-	0.30	0.26

Table C28: *CEBE results (eV) from density functional B97; the Chong test set is used and the ionized atom is in bold font.*

Molecule	Exp ⁹⁷	$\delta(\text{B97})$	$\delta(\text{B97}_r)$
C ₂ H ₂	290.82	0.72	0.77
C H ₄	290.91	0.09	0.14
C H ₃ OH	292.42	0.04	0.09
C H ₃ CN	292.45	0.48	0.53
C H ₃ CN	292.98	-0.05	0.00
C HN	293.40	0.36	0.41
C H ₂ CO	294.47	0.16	0.21
C O	296.21	0.52	0.57
C O ₂	297.69	0.15	0.20
N H ₃	405.56	-0.02	0.07
C H ₃ CN	405.64	-0.17	-0.08
C HN	406.78	0.10	0.19
N NO	408.71	0.13	0.22
N ₂	409.98	0.06	0.15
N NO	412.59	0.05	0.14
C H ₃ OH	539.11	-0.50	-0.33
C H ₂ CO	539.48	-0.52	-0.35
C H ₂ O	539.90	-0.41	-0.24
C O ₂	541.28	-0.19	-0.02
N NO	541.42	-0.08	0.09
C O	542.55	-0.32	-0.15
H F	694.23	-0.79	-0.45
F ₂	696.69	-0.95	-0.61
MAD	-	0.30	0.26

Table C29: *CEBE results (eV) from density functional B97-1; the Chong test set is used and the ionized atom is in bold font.*

Molecule	Exp ⁹⁷	$\delta(\text{B97-1})$	$\delta(\text{B97-1}_r)$
C ₂ H ₂	290.82	0.84	0.89
C H ₄	290.91	0.21	0.26
C H ₃ OH	292.42	0.15	0.20
C H ₃ CN	292.45	0.60	0.65
C H ₃ CN	292.98	0.08	0.13
C HN	293.40	0.49	0.54
C H ₂ CO	294.47	0.28	0.33
C O	296.21	0.66	0.71
C O ₂	297.69	0.32	0.37
N H ₃	405.56	0.14	0.23
C H ₃ CN	405.64	0.00	0.09
C HN	406.78	0.26	0.35
N NO	408.71	0.32	0.41
N ₂	409.98	0.23	0.32
N NO	412.59	0.24	0.33
C H ₃ OH	539.11	-0.30	-0.13
C H ₂ CO	539.48	-0.32	-0.15
C H ₂ O	539.90	-0.20	-0.03
C O ₂	541.28	0.03	0.10
N NO	541.42	0.12	0.29
C O	542.55	-0.11	0.06
H F	694.23	-0.54	-0.20
F ₂	696.69	-0.71	-0.37
MAD	-	0.31	0.31

Table C30: *CEBE results (eV) from density functional B97-2; the Chong test set is used and the ionized atom is in bold font.*

Molecule	Exp ⁹⁷	$\delta(\text{B97-2})$	$\delta(\text{B97-2}_r)$
C ₂ H ₂	290.82	0.48	0.53
C H ₄	290.91	-0.20	-0.15
C H ₃ OH	292.42	-0.13	-0.08
C H ₃ CN	292.45	0.19	0.24
C H ₃ CN	292.98	-0.25	-0.10
C HN	293.40	0.11	0.16
C H ₂ CO	294.47	0.02	0.07
C O	296.21	0.37	0.42
C O ₂	297.69	-0.06	-0.01
N H ₃	405.56	-0.42	-0.33
C H ₃ CN	405.64	-0.50	-0.41
C HN	406.78	-0.23	-0.15
N NO	408.71	-0.20	-0.11
N ₂	409.98	-0.25	-0.16
N NO	412.59	-0.18	-0.09
C H ₃ OH	539.11	-1.01	-0.84
C H ₂ CO	539.48	-1.04	-0.87
C H ₂ O	539.90	-0.98	-0.81
C O ₂	541.28	-0.71	-0.54
C NO	541.42	-0.54	-0.37
C O	542.55	-0.90	-0.73
F H	694.23	-1.54	-1.20
F ₂	696.69	-1.48	-1.14
MAD	-	0.51	0.41

Table C31: *CEBE results (eV) from density functional B97-3; the Chong test set is used and the ionized atom is in bold font.*

Molecule	Exp ⁹⁷	$\delta(\text{B97-3})$	$\delta(\text{B97-3}_r)$
C ₂ H ₂	290.82	0.82	0.87
C H ₄	290.91	0.18	0.22
C H ₃ OH	292.42	0.22	0.27
C H ₃ CN	292.45	0.61	0.66
C H ₃ CN	292.98	0.12	0.17
C HN	293.40	0.49	0.54
C H ₂ CO	294.47	0.36	0.41
C O	296.21	0.68	0.73
C O ₂	297.69	0.49	0.54
N H ₃	405.56	0.12	0.21
C H ₃ CN	405.64	-0.03	0.06
C HN	406.78	0.20	0.29
N NO	408.71	0.34	0.35
N ₂	409.98	0.22	0.31
N NO	412.59	0.41	0.05
C H ₃ OH	539.11	-0.35	-0.18
C H ₂ CO	539.48	-0.45	-0.28
C H ₂ O	539.90	-0.27	-0.10
C O ₂	541.28	-0.04	0.13
N NO	541.42	0.07	0.24
C O	542.55	-0.28	-0.11
H F	694.23	-0.67	-0.33
F ₂	696.69	-0.75	-0.41
MAD	-	0.35	0.32

Table C32: *CEBE results (eV) from density functional B97-K; the Chong test set is used and the ionized atom is in bold font.*

Molecule	Exp ⁹⁷	$\delta(\text{B97-K})$	$\delta(\text{B97-K}_f)$
C ₂ H ₂	290.82	1.82	1.87
C H ₄	290.91	1.22	1.27
C H ₃ OH	292.42	1.17	1.21
C H ₃ CN	292.45	1.63	1.68
C H ₃ CN	292.98	1.12	1.17
C HN	293.40	1.49	1.54
C H ₂ CO	294.47	1.29	1.34
C O	296.21	1.68	1.72
C O ₂	297.69	1.67	1.72
N H ₃	405.56	1.42	1.51
C H ₃ CN	405.64	1.29	1.38
C HN	406.78	1.51	1.60
N NO	408.71	1.72	1.81
N ₂	409.98	1.53	1.62
N NO	412.59	1.88	1.97
C H ₃ OH	539.11	1.20	1.37
C H ₂ CO	539.48	1.11	1.28
C H ₂ O	539.90	1.34	1.51
C O ₂	541.28	1.54	1.71
N NO	541.42	1.54	1.71
C O	542.55	1.39	1.56
H F	694.23	1.29	1.63
F ₂	696.69	0.96	1.30
MAD	–	1.43	1.54

Table C33: *CEBE results (eV) from density functional B98; the Chong test set is used and the ionized atom is in bold font.*

Molecule	Exp ⁹⁷	$\delta(\text{B98})$	$\delta(\text{B98}_r)$
C ₂ H ₂	290.82	0.74	0.79
C H ₄	290.91	0.11	0.16
C H ₃ OH	292.42	0.06	0.11
C H ₃ CN	292.45	0.52	0.56
C H ₃ CN	292.98	-0.01	0.04
C HN	293.40	0.41	0.46
C H ₂ CO	294.47	0.19	0.24
C O	296.21	0.60	0.65
C O ₂	297.69	0.29	0.34
N H ₃	405.56	-0.02	0.07
C H ₃ CN	405.64	-0.17	-0.08
C HN	406.78	0.10	0.19
N NO	408.71	0.19	0.28
N ₂	409.98	0.09	0.18
N NO	412.59	0.10	0.20
C H ₃ OH	539.11	-0.52	-0.35
C H ₂ CO	539.48	-0.55	-0.38
C H ₂ O	539.90	-0.41	-0.24
C O ₂	541.28	-0.18	-0.01
N NO	541.42	-0.09	0.08
C O	542.55	-0.32	-0.15
H F	694.23	-0.78	-0.44
F ₂	696.69	-0.96	-0.62
MAD	-	0.32	0.29

Table C34: *CEBE* results (*eV*) from density functional *PBE0*; the Chong test set is used and the ionized atom is in bold font.

Molecule	Exp ⁹⁷	$\delta(\text{PBE0})$	$\delta(\text{PBE0}_r)$
C ₂ H ₂	290.82	0.15	0.20
C H ₄	290.91	-0.56	-0.51
C H ₃ OH	292.42	-0.52	-0.47
C H ₃ CN	292.45	-0.16	-0.11
C H ₃ CN	292.98	-0.57	-0.52
C HN	293.40	-0.23	-0.18
C H ₂ CO	294.47	-0.38	-0.33
C O	296.21	-0.08	-0.03
C O ₂	297.69	-0.36	-0.31
N H ₃	405.56	-0.62	-0.53
C H ₃ CN	405.64	-0.69	-0.60
C HN	406.78	-0.44	-0.35
N NO	408.71	-0.41	-0.32
N ₂	409.98	-0.47	-0.38
N NO	412.59	-0.30	-0.21
C H ₃ OH	539.11	-1.02	-0.85
C H ₂ CO	539.48	-1.05	-0.88
C H ₂ O	539.90	-1.01	-0.84
C O ₂	541.28	-0.73	-0.56
N NO	541.42	-0.59	-0.42
C O	542.55	-0.87	-0.70
H F	694.23	-1.39	-1.05
F ₂	696.69	-1.36	-1.02
MAD	–	0.61	0.49

Table C35: *CEBE results (eV) from density functional X3LYP; the Chong test set is used and the ionized atom is in bold font.*

Molecule	Exp ⁹⁷	$\delta(\text{X3LYP})$	$\delta(\text{X3LYP}_r)$
C ₂ H ₂	290.82	0.61	0.66
C H ₄	290.91	-0.01	0.04
C H ₃ OH	292.42	-0.02	0.03
C H ₃ CN	292.45	0.34	0.45
C H ₃ CN	292.98	-0.12	-0.07
C HN	293.40	0.28	0.33
C H ₂ CO	294.47	0.13	0.18
C O	296.21	0.48	0.53
C O ₂	297.69	0.18	0.23
N H ₃	405.56	-0.15	-0.06
C H ₃ CN	405.64	-0.29	-0.20
C HN	406.78	-0.02	0.07
N NO	408.71	0.05	0.14
N ₂	409.98	-0.01	0.08
N NO	412.59	0.05	0.07
C H ₃ OH	539.11	-0.61	-0.44
C H ₂ CO	539.48	-0.62	-0.45
C H ₂ O	539.90	-0.51	-0.34
C O ₂	541.28	-0.28	-0.10
N NO	541.42	-0.14	0.02
C O	542.55	-0.43	-0.26
H F	694.23	-0.80	-0.46
F ₂	696.69	-0.91	-0.57
MAD	-	0.31	0.25

Table C36: *CEBE results (eV) from density functional VS98; the Chong test set is used and the ionized atom is in bold font.*

Molecule	Exp ⁹⁷	$\delta(\text{VS98})$	$\delta(\text{VS98}_r)$
C ₂ H ₂	290.82	0.67	0.72
CH ₄	290.91	-0.19	-0.14
CH ₃ OH	292.42	0.09	0.14
CH ₃ CN	292.45	0.16	0.21
CH ₃ CN	292.98	-0.00	0.05
H CN	293.40	0.35	0.40
H ₂ CO	294.47	0.34	0.39
CO	296.21	0.60	0.65
CO ₂	297.69	-0.24	-0.19
NH ₃	405.56	-0.12	-0.03
CH ₃ CN	405.64	-0.02	0.07
H CN	406.78	0.38	0.47
NNO	408.71	-0.06	0.03
N ₂	409.98	0.38	0.47
NNO	412.59	0.09	0.18
CH ₃ OH	539.11	-0.13	0.04
H ₂ CO	539.48	0.19	0.36
H ₂ O	539.90	-0.38	-0.21
CO ₂	541.28	-0.18	-0.01
NNO	541.42	0.37	0.54
CO	542.55	0.14	0.31
HF	694.23	-0.61	-0.27
F ₂	696.69	0.21	0.55
MAD	-	0.26	0.28

Table C37: *CEBE results (eV) from density functional PKZB; the Chong test set is used and the ionized atom is in bold font.*

Molecule	Exp ⁹⁷	$\delta(\text{PKZB})$	$\delta(\text{PKZB}_r)$
C ₂ H ₂	290.82	-0.42	-0.37
C H ₄	290.91	-1.05	-1.00
C H ₃ OH	292.42	-1.04	-0.99
C H ₃ CN	292.45	-0.79	-0.74
C H ₃ CN	292.98	-1.28	-1.23
C HN	293.40	-0.91	-0.86
C H ₂ CO	294.47	-1.01	-0.96
C O	296.21	-0.91	-0.86
C O ₂	297.69	-1.66	-1.61
N H ₃	405.56	-1.40	-1.31
C H ₃ CN	405.64	-1.54	-1.45
C HN	406.78	-1.22	-1.13
N NO	408.71	-1.59	-1.50
N ₂	409.98	-1.41	-1.32
N NO	412.59	-1.69	-1.60
C H ₃ OH	539.11	-2.04	-1.87
C H ₂ CO	539.48	-1.93	-1.76
C H ₂ O	539.90	-2.12	-1.95
C O ₂	541.28	-1.94	-1.76
N NO	541.42	-1.63	-1.46
C O	542.55	-1.81	-1.61
H F	694.23	-2.89	-2.55
F ₂	696.69	-2.69	-2.35
MAD	-	1.52	1.40

Table C38: *CEBE results (eV) from density functional tHCTH; the Chong test set is used and the ionized atom is in bold font.*

Molecule	Exp ⁹⁷	$\delta(\text{tHCTH})$	$\delta(\text{tHCTH}_r)$
C ₂ H ₂	290.82	-0.38	-0.33
C H ₄	290.91	-1.03	-0.98
C H ₃ OH	292.42	-0.98	-0.93
C H ₃ C N	292.45	-0.73	-0.68
C H ₃ C N	292.98	-1.23	-1.18
C HN	293.40	-0.81	-0.76
H ₂ C O	294.47	-0.87	-0.82
C O	296.21	-0.57	-0.52
C O ₂	297.69	-1.40	-1.35
N H ₃	405.56	-1.63	-1.54
C H ₃ C N	405.64	-1.74	-1.65
C HN	406.78	-1.43	-1.34
N NO	408.71	-1.60	-1.52
N ₂	409.98	-1.53	-1.44
N NO	412.59	-1.85	-1.76
C H ₃ O H	539.11	-2.52	-2.35
H ₂ C O	539.48	-2.48	-2.31
H ₂ O	539.90	-2.52	-2.36
C O ₂	541.28	-2.26	-2.09
N NO	541.42	-1.98	-1.81
C O	542.55	-2.45	-2.28
H F	694.23	-3.40	-3.06
F ₂	696.69	-3.22	-2.88
MAD	-	1.68	1.56

Table C39: *CEBE results (eV) from density functional tHCTHhyb; the Chong test set is used and the ionized atom is in bold font.*

Molecule	Exp ⁹⁷	$\delta(\text{tHCTHhyb})$	$\delta(\text{tHCTHhyb}_r)$
C ₂ H ₂	290.82	0.44	0.49
C H ₄	290.91	-0.19	-0.14
C H ₃ OH	292.42	-0.25	-0.20
C H ₃ C N	292.45	0.18	0.23
C H ₃ C N	292.98	-0.35	-0.30
H CN	293.40	0.08	0.13
H ₂ C O	294.47	-0.13	-0.08
C O	296.21	0.27	0.32
C O ₂	297.69	-0.23	-0.18
N H ₃	405.56	-0.43	-0.34
C H ₃ C N	405.64	-0.56	-0.47
H C N	406.78	-0.28	-0.19
N NO	408.71	-0.28	-0.19
N ₂	409.98	-0.34	-0.25
N NO	412.59	-0.45	-0.36
C H ₃ O H	539.11	-1.01	-0.85
H ₂ C O	539.48	-1.00	-0.83
H ₂ O	539.90	-0.93	-0.76
C O ₂	541.28	-0.68	-0.51
N NO	541.42	-0.56	-0.39
C O	542.55	-0.80	-0.63
H F	694.23	-1.38	-1.04
F ₂	696.69	-1.50	-1.17
MAD	-	0.54	0.44

Table C40: *CEBE results (eV) from density functional BMK; the Chong test set is used and the ionized atom is in bold font.*

Molecule	Exp ⁹⁷	$\delta(\text{BMK})$	$\delta(\text{BMK}_r)$
C ₂ H ₂	290.82	1.63	1.68
C H ₄	290.91	1.18	1.23
C H ₃ O H	292.42	0.94	0.99
C H ₃ C N	292.45	1.54	1.59
C H ₃ C N	292.98	1.11	1.16
H CN	293.40	1.54	1.59
H ₂ C O	294.47	1.09	1.14
C O	296.21	1.58	1.63
C O ₂	297.69	1.48	1.53
N H ₃	405.56	1.42	1.51
C H ₃ C N	405.64	1.21	1.30
H CN	406.78	1.42	1.51
N N O	408.71	1.89	1.98
N ₂	409.98	1.46	1.55
N N O	412.59	1.75	1.84
C H ₃ O H	539.11	1.27	1.44
H ₂ C O	539.48	1.25	1.42
H ₂ O	539.90	1.51	1.68
C O ₂	541.28	1.83	2.00
N N O	541.42	1.67	1.81
C O	542.55	1.80	1.97
H F	694.23	1.79	2.13
F ₂	696.69	1.31	1.65
MAD	–	1.46	1.58

Table C41: *CEBE results (eV) from density functional TPSS; the Chong test set is used and the ionized atom is in bold font.*

Molecule	Exp ⁹⁷	$\delta(\text{TPSS})$	$\delta(\text{TPSS}_r)$
C ₂ H ₂	290.82	0.50	0.55
C H ₄	290.91	-0.05	0.00
C H ₃ OH	292.42	-0.07	-0.02
CH ₃ C N	292.45	0.14	0.19
C H ₃ CN	292.98	-0.30	-0.25
HCN	293.40	0.09	0.14
H ₂ C O	294.47	-0.02	0.03
C O	296.21	0.10	0.15
C O ₂	297.69	-0.50	-0.45
N H ₃	405.56	-0.13	-0.04
CH ₃ C N	405.64	-0.30	-0.21
HCN	406.78	-0.04	0.05
N NO	408.71	-0.22	-0.13
N ₂	409.98	-0.12	-0.03
N NO	412.59	-0.36	-0.27
CH ₃ O H	539.11	-0.43	-0.26
H ₂ C O	539.48	-0.41	-0.23
H ₂ O	539.90	-0.39	-0.22
C O ₂	541.28	-0.20	-0.03
N NO	541.42	0.06	0.23
C O	542.55	-0.29	-0.12
H F	694.23	-0.59	-0.25
F ₂	696.69	-0.52	-0.18
MAD	-	0.25	0.18

Table C42: *CEBE results (eV) from density functional revTPSS; the Chong test set is used and the ionized atom is in bold font.*

Molecule	Exp ⁹⁷	$\delta(\text{revTPSS})$	$\delta(\text{revTPSS}_r)$
C ₂ H ₂	290.82	0.65	0.70
C H ₄	290.91	0.11	0.16
C H ₃ OH	292.42	0.10	0.15
C H ₃ CN	292.45	0.32	0.37
C H ₃ CN	292.98	-0.15	-0.10
C HN	293.40	0.28	0.33
C H ₂ CO	294.47	0.17	0.22
C O	296.21	0.34	0.39
C O ₂	297.69	-0.24	-0.19
N H ₃	405.56	0.05	0.14
C H ₃ CN	405.64	-0.11	-0.02
C HN	406.78	0.15	0.24
N NO	408.71	0.02	0.11
N ₂	409.98	0.12	0.21
N NO	412.59	-0.13	-0.04
C H ₃ OH	539.11	-0.18	-0.01
C H ₂ CO	539.48	-0.16	0.01
C H ₂ O	539.90	-0.12	0.05
C O ₂	541.28	0.08	0.25
N NO	541.42	0.34	0.51
C O	542.55	-0.02	0.15
H F	694.23	-0.18	0.16
F ₂	696.69	-0.10	0.24
MAD	-	0.18	0.21

Table C43: *CEBE results (eV) from density functional M05; the Chong test set is used and the ionized atom is in bold font.*

Molecule	Exp ⁹⁷	$\delta(\text{M05})$	$\delta(\text{M05}_r)$
C ₂ H ₂	290.82	0.32	0.37
C H ₄	290.91	-0.23	-0.18
C H ₃ OH	292.42	-0.06	-0.01
C H ₃ CN	292.45	0.09	0.14
C H ₃ CN	292.98	-0.32	-0.27
C HN	293.40	0.04	0.09
C H ₂ CO	294.47	0.10	0.15
C O	296.21	0.32	0.37
C O ₂	297.69	-0.20	-0.15
N H ₃	405.56	-0.55	-0.46
C H ₃ CN	405.64	-0.67	-0.58
C HN	406.78	-0.45	-0.36
N NO	408.71	-0.46	-0.37
N ₂	409.98	-0.42	-0.33
N NO	412.59	-0.33	-0.24
C H ₃ OH	539.11	-1.09	-0.92
C H ₂ CO	539.48	-1.11	-0.94
C H ₂ O	539.90	-1.16	-0.99
C O ₂	541.28	-0.87	-0.70
N NO	541.42	-0.57	-0.40
C O	542.55	-1.04	-0.87
H F	694.23	-1.61	-1.27
F ₂	696.69	-1.35	-1.01
MAD	-	0.58	0.49

Table C44: *CEBE results (eV) from density functional M05-2X; the Chong test set is used and the ionized atom is in bold font.*

Molecule	Exp ⁹⁷	$\delta(\text{M05-2X})$	$\delta(\text{M05-2X}_r)$
C ₂ H ₂	290.82	1.10	1.15
C H ₄	290.91	0.32	0.37
C H ₃ OH	292.42	0.46	0.51
C H ₃ CN	292.45	0.80	0.85
C H ₃ CN	292.98	0.47	0.52
C HN	293.40	0.81	0.86
C H ₂ CO	294.47	0.69	0.74
C O	296.21	1.17	1.22
C O ₂	297.69	1.17	1.22
N H ₃	405.56	0.25	0.34
C H ₃ CN	405.64	0.34	0.43
C HN	406.78	0.55	0.64
N NO	408.71	0.90	0.99
N ₂	409.98	0.65	0.74
N NO	412.59	1.09	1.18
C H ₃ OH	539.11	-0.23	-0.06
C H ₂ CO	539.48	-0.29	-0.12
C H ₂ O	539.90	-0.15	0.02
C O ₂	541.28	0.24	0.41
N NO	541.42	0.24	0.41
C O	542.55	0.07	0.24
H F	694.23	-0.51	-0.17
F ₂	696.69	-0.38	-0.04
MAD	-	0.56	0.57

Table C45: *CEBE results (eV) from density functional BPBE; the Chong test set is used and the ionized atom is in bold font.*

Molecule	Exp ⁹⁷	$\delta(\text{BPBE})$	$\delta(\text{BPBE}_r)$
C ₂ H ₂	290.82	-0.09	-0.04
C H ₄	290.91	-0.73	-0.68
C H ₃ OH	292.42	-0.78	-0.73
C H ₃ CN	292.45	-0.45	-0.40
C H ₃ CN	292.98	-0.95	-0.90
C HN	293.40	-0.55	-0.50
C H ₂ CO	294.47	-0.72	-0.67
C O	296.21	-0.57	-0.52
C O ₂	297.69	-1.20	-1.15
N H ₃	405.56	-0.78	-0.69
C H ₃ CN	405.64	-0.98	-0.89
C HN	406.78	-0.68	-0.59
N NO	408.71	-0.91	-0.82
N ₂	409.98	-0.84	-0.75
N NO	412.59	-1.09	-1.01
C H ₃ OH	539.11	-1.12	-0.95
C H ₂ CO	539.48	-1.08	-0.91
C H ₂ O	539.90	-1.10	-0.93
C O ₂	541.28	-0.91	-0.74
N NO	541.42	-0.68	-0.51
C O	542.55	-0.99	-0.82
H F	694.23	-1.42	-1.08
F ₂	696.69	-1.48	-1.14
MAD	-	0.87	0.76

Table C46: *CEBE results (eV) from density functional M06; the Chong test set is used and the ionized atom is in bold font.*

Molecule	Exp ⁹⁷	$\delta(\text{M06})$	$\delta(\text{M06}_r)$
C ₂ H ₂	290.82	-0.35	-0.30
C H ₄	290.91	-0.69	-0.63
C H ₃ OH	292.42	-0.70	-0.65
C H ₃ CN	292.45	-0.54	-0.49
C H ₃ CN	292.98	-0.85	-0.80
C HN	293.40	-0.63	-0.58
C H ₂ CO	294.47	-0.66	-0.61
C O	296.21	-0.30	-0.25
C O ₂	297.69	-0.59	-0.54
N H ₃	405.56	-0.79	-0.70
C H ₃ CN	405.64	-1.30	-1.21
C HN	406.78	-1.05	-0.96
N NO	408.71	-0.73	-0.64
N ₂	409.98	-1.02	-0.93
N NO	412.59	-0.80	-0.71
C H ₃ OH	539.11	-1.20	-1.02
C H ₂ CO	539.48	-1.28	-1.11
C H ₂ O	539.90	-1.05	-0.69
C O ₂	541.28	-0.82	-0.66
N NO	541.42	-0.80	-0.63
C O	542.55	-1.15	-0.98
H F	694.23	-1.22	-0.88
F ₂	696.69	-1.61	-1.27
MAD	-	0.88	0.75

Table C47: *CEBE results (eV) from density functional M06-L; the Chong test set is used and the ionized atom is in bold font.*

Molecule	Exp ⁹⁷	$\delta(\text{M06-L})$	$\delta(\text{M06-L}_r)$
C ₂ H ₂	290.82	0.17	0.22
C H ₄	290.91	-0.27	-0.22
C H ₃ OH	292.42	-0.25	-0.20
CH ₃ C N	292.45	-0.08	-0.03
C H ₃ CN	292.98	-0.43	-0.39
HCN	293.40	-0.19	-0.14
H ₂ C O	294.47	-0.21	-0.17
C O	296.21	-0.28	-0.23
C O ₂	297.69	-0.50	-0.45
N H ₃	405.56	-0.18	-0.09
CH ₃ C N	405.64	-0.66	-0.57
HCN	406.78	-0.41	-0.32
NNO	408.71	-0.37	-0.28
N ₂	409.98	-0.47	-0.39
NNO	412.59	-0.39	-0.29
CH ₃ O H	539.11	-0.49	-0.32
H ₂ C O	539.48	-0.52	-0.35
H ₂ O	539.90	-0.39	-0.22
C O ₂	541.28	-0.21	-0.05
N NO	541.42	-0.01	0.16
C O	542.55	-0.50	-0.33
H F	694.23	-0.57	-0.23
F ₂	696.69	-0.79	-0.45
MAD	—	0.36	0.27

Table C48: *CEBE results (eV) from density functional M06-2X; the Chong test set is used and the ionized atom is in bold font.*

Molecule	Exp ⁹⁷	$\delta(\text{M06-2X})$	$\delta(\text{M06-2X}_r)$
C ₂ H ₂	290.82	0.44	0.49
C H ₄	290.91	-0.37	-0.32
C H ₃ OH	292.42	-0.20	-0.15
C H ₃ CN	292.45	0.04	0.09
C H ₃ CN	292.98	-0.16	-0.11
C HN	293.40	0.18	0.23
C H ₂ CO	294.47	0.07	0.12
C O	296.21	0.58	0.63
C O ₂	297.69	0.49	0.54
N H ₃	405.56	-0.54	-0.45
C H ₃ CN	405.64	-0.34	-0.25
C HN	406.78	-0.15	-0.06
N NO	408.71	0.17	0.26
N ₂	409.98	-0.01	0.08
N NO	412.59	0.40	0.48
C H ₃ OH	539.11	-0.96	-0.79
C H ₂ CO	539.48	-0.99	-0.82
C H ₂ O	539.90	-0.97	-0.80
C O ₂	541.28	-0.60	-0.43
N NO	541.42	-0.53	-0.36
C O	542.55	-0.74	-0.57
H F	694.23	-1.40	-1.06
F ₂	696.69	-1.08	-0.74
MAD	-	0.49	0.43

Table C49: *CEBE results (eV) from density functional M06–HF; the Chong test set is used and the ionized atom is in bold font.*

Molecule	Exp ⁹⁷	$\delta(\text{M06–HF})$	$\delta(\text{M06–HF}_r)$
C ₂ H ₂	290.82	0.62	0.67
C H ₄	290.91	–0.35	–0.30
C H ₃ OH	292.42	–0.24	–0.19
C H ₃ CN	292.45	–0.03	0.02
C H ₃ CN	292.98	–0.04	0.01
C HN	293.40	0.40	0.45
C H ₂ CO	294.47	0.09	0.13
C O	296.21	0.90	0.95
C O ₂	297.69	1.07	1.12
N H ₃	405.56	–0.58	–0.49
C H ₃ CN	405.64	0.00	0.09
C HN	406.78	0.17	0.26
N NO	408.71	0.73	0.82
N ₂	409.98	0.37	0.46
N NO	412.59	1.01	1.10
C H ₃ OH	539.11	–1.00	–0.83
C H ₂ CO	539.48	–1.02	–0.85
C H ₂ O	539.90	–0.92	–0.75
C O ₂	541.28	–0.49	–0.32
N NO	541.42	–0.77	–0.60
C O	542.55	–0.44	–0.27
H F	694.23	–1.28	–0.94
F ₂	696.69	–1.08	–0.74
MAD	–	0.59	0.54

Table C50: *CEBE results (eV) from density functional M08–HX; the Chong test set is used and the ionized atom is in bold font.*

Molecule	Exp ⁹⁷	$\delta(\text{M08–HX})$	$\delta(\text{M08–HX}_r)$
C ₂ H ₂	290.82	1.52	1.57
C H ₄	290.91	0.72	0.77
C H ₃ OH	292.42	0.80	0.85
C H ₃ CN	292.45	1.09	1.14
C H ₃ CN	292.98	0.86	0.91
C HN	293.40	1.16	1.21
C H ₂ CO	294.47	0.99	1.04
C O	296.21	1.30	1.35
C O ₂	297.69	1.30	1.35
N H ₃	405.56	0.80	0.89
C H ₃ CN	405.64	0.98	1.07
C HN	406.78	1.19	1.28
N NO	408.71	1.32	1.41
N ₂	409.98	1.17	1.26
N NO	412.59	1.58	1.67
C H ₃ OH	539.11	0.72	0.89
C H ₂ CO	539.48	0.69	0.86
C H ₂ O	539.90	0.65	0.82
C O ₂	541.28	0.91	1.08
N NO	541.42	0.91	1.08
C O	542.55	0.85	1.02
H F	694.23	0.51	0.85
F ₂	696.69	0.69	1.03
MAD	–	0.99	1.10

Table C51: *CEBE results (eV) from density functional M08-SO; the Chong test set is used and the ionized atom is in bold font.*

Molecule	Exp ⁹⁷	$\delta(\text{M08-SO})$	$\delta(\text{M08-SO}_r)$
C ₂ H ₂	290.82	1.52	1.57
C H ₄	290.91	0.72	0.77
C H ₃ OH	292.42	0.80	0.85
C H ₃ CN	292.45	1.09	1.14
C H ₃ CN	292.98	0.86	0.91
C HN	293.40	1.16	1.21
C H ₂ CO	294.47	0.99	1.04
C O	296.21	1.30	1.35
C O ₂	297.69	1.30	1.35
N H ₃	405.56	0.80	0.89
C H ₃ CN	405.64	0.98	1.07
C HN	406.78	1.19	1.28
N NO	408.71	1.32	1.41
N ₂	409.98	1.17	1.26
N NO	412.59	1.58	1.67
C H ₃ OH	539.11	0.72	0.89
C H ₂ CO	539.48	0.69	0.86
C H ₂ O	539.90	0.65	0.82
C O ₂	541.28	0.91	1.08
N NO	541.42	0.91	1.08
C O	542.55	0.85	1.02
H F	694.23	0.51	0.85
F ₂	696.69	0.69	1.03
MAD	–	0.99	1.10

Table C52: *CEBE results (eV) from density functional CAMB3LYP; the Chong test set is used and the ionized atom is in bold font.*

Molecule	Exp ⁹⁷	$\delta(\text{CAMB3LYP})$	$\delta(\text{CAMB3LYP}_r)$
C ₂ H ₂	290.82	0.60	0.65
C H ₄	290.91	-0.04	0.01
C H ₃ OH	292.42	-0.02	0.03
C H ₃ CN	292.45	0.34	0.39
C H ₃ CN	292.98	-0.05	0.00
H CN	293.40	0.30	0.35
H ₂ C O	294.47	0.14	0.19
C O	296.21	0.55	0.60
C O ₂	297.69	0.37	0.42
N H ₃	405.56	-0.11	-0.02
C H ₃ C N	405.64	-0.20	-0.11
H CN	406.78	0.04	0.13
N NO	408.71	0.16	0.25
N ₂	409.98	0.08	0.17
N NO	412.59	0.31	0.40
C H ₃ O H	539.11	-0.50	-0.33
H ₂ C O	539.48	-0.52	-0.35
H ₂ O	539.90	-0.39	-0.22
C O ₂	541.28	-0.15	0.02
N NO	541.42	-0.09	0.08
C O	542.55	-0.28	-0.12
H F	694.23	-0.59	-0.25
F ₂	696.69	-0.69	-0.35
MAD	-	0.28	0.24

Table C53: *CEBE results (eV) from density functional ω B97; the Chong test set is used and the ionized atom is in bold font.*

Molecule	Exp ⁹⁷	$\delta(\omega$ B97)	$\delta(\omega$ B97 _r)
C ₂ H ₂	290.82	0.64	0.69
C H ₄	290.91	0.01	0.06
C H ₃ OH	292.42	0.09	0.14
C H ₃ CN	292.45	0.42	0.47
C H ₃ CN	292.98	-0.00	0.05
H CN	293.40	0.25	0.30
H ₂ CO	294.47	0.18	0.23
C O	296.21	0.52	0.57
C O ₂	297.69	0.28	0.33
N H ₃	405.56	-0.04	0.05
C H ₃ CN	405.64	-0.12	0.09
H CN	406.78	0.06	0.15
N NO	408.71	0.08	0.17
N ₂	409.98	-0.01	0.08
N NO	412.59	0.36	0.45
C H ₃ OH	539.11	-0.48	-0.31
H ₂ CO	539.48	-0.55	-0.38
H ₂ O	539.90	-0.42	-0.25
C O ₂	541.28	-0.22	-0.05
N NO	541.42	-0.20	-0.03
C O	542.55	-0.40	-0.23
H F	694.23	-0.78	-0.44
F ₂	696.69	-0.84	-0.50
MAD	-	0.30	0.26

Table C54: *CEBE results (eV) from density functional ω B97X; the Chong test set is used and the ionized atom is in bold font.*

Molecule	Exp ⁹⁷	$\delta(\omega$ B97X)	$\delta(\omega$ B97X _r)
C ₂ H ₂	290.82	0.77	0.82
C H ₄	290.91	0.15	0.20
C H ₃ OH	292.42	0.20	0.25
C H ₃ C N	292.45	0.56	0.61
C H ₃ CN	292.98	0.10	0.15
H CN	293.40	0.38	0.43
H ₂ C O	294.47	0.30	0.35
C O	296.21	0.65	0.70
C O ₂	297.69	0.44	0.49
N H ₃	405.56	0.11	0.20
C H ₃ C N	405.64	-0.01	0.08
H CN	406.78	0.18	0.28
N NO	408.71	0.26	0.35
N ₂	409.98	0.14	0.23
N NO	412.59	0.46	0.55
C H ₃ O H	539.11	-0.31	-0.14
H ₂ C O	539.48	-0.40	-0.23
H ₂ O	539.90	-0.24	-0.07
C O ₂	541.28	-0.04	0.14
N NO	541.42	0.00	0.17
C O	542.55	-0.29	-0.12
H F	694.23	-0.59	-0.25
F ₂	696.69	-0.70	-0.36
MAD	-	0.32	0.31

Table C55: *CEBE results (eV) from density functional ω B97X-D; the Chong test set is used and the ionized atom is in bold font.*

Molecule	Exp ⁹⁷	$\delta(\omega$ B97X-D)	$\delta(\omega$ B97X-D _r)
C ₂ H ₂	290.82	0.63	0.68
C H ₄	290.91	0.03	0.07
C H ₃ OH	292.42	0.05	0.10
C H ₃ C N	292.45	0.44	0.49
C H ₃ C N	292.98	-0.07	-0.02
H CN	293.40	0.27	0.32
H ₂ C O	294.47	0.16	0.21
C O	296.21	0.52	0.56
C O ₂	297.69	0.28	0.34
N H ₃	405.56	-0.05	0.04
C H ₃ C N	405.64	-0.22	-0.13
H C N	406.78	0.01	0.09
N NO	408.71	0.10	0.19
N ₂	409.98	-0.01	0.08
N NO	412.59	0.17	0.26
C H ₃ O H	539.11	-0.49	-0.32
H ₂ C O	539.48	-0.59	-0.42
H ₂ O	539.90	-0.41	-0.24
C O ₂	541.28	-0.22	-0.05
N NO	541.42	-0.15	0.02
C O	542.55	-0.47	-0.30
H F	694.23	-0.80	-0.46
F ₂	696.69	-0.95	-0.61
MAD	-	0.31	0.26

Table C56: *CEBE results (eV) from density functional BPW91; the Chong test set is used and the ionized atom is in bold font.*

Molecule	Exp ⁹⁷	$\delta(\text{BPW91})$	$\delta(\text{BPW91}_r)$
C ₂ H ₂	290.82	0.09	0.14
C H ₄	290.91	-0.54	-0.49
C H ₃ O H	292.42	-0.59	-0.54
C H ₃ C N	292.45	-0.27	-0.22
C H ₃ C N	292.98	-0.76	-0.71
H CN	293.40	-0.36	-0.32
H ₂ C O	294.47	-0.53	-0.48
C O	296.21	-0.38	-0.33
C O ₂	297.69	-1.00	-0.95
N H ₃	405.56	-0.58	-0.49
C H ₃ C N	405.64	-0.79	-0.70
H CN	406.78	-0.48	-0.39
N N O	408.71	-0.71	-0.62
N ₂	409.98	-0.64	-0.55
N N O	412.59	-0.90	-0.81
C H ₃ O H	539.11	-0.91	-0.74
H ₂ C O	539.48	-0.88	-0.71
H ₂ O	539.90	-0.89	-0.72
C O ₂	541.28	-0.70	-0.53
N N O	541.42	-0.47	-0.30
C O	542.55	-0.79	-0.62
H F	694.23	-1.19	-0.85
F ₂	696.69	-1.26	-0.92
MAD	-	0.68	0.57

Table C57: *CEBE results (eV) from density functional TPSSh; the Chong test set is used and the ionized atom is in bold font.*

Molecule	Exp ⁹⁷	$\delta(\text{TPSSh})$	$\delta(\text{TPSSh}_r)$
C ₂ H ₂	290.82	0.58	0.64
C H ₄	290.91	0.01	0.06
C H ₃ OH	292.42	0.02	0.07
C H ₃ C N	292.45	0.29	0.34
C H ₃ C N	292.98	-0.21	-0.16
C HN	293.40	0.20	0.25
C H ₂ C O	294.47	0.10	0.15
C O	296.21	0.28	0.33
C O ₂	297.69	-0.18	-0.13
N H ₃	405.56	-0.07	0.02
C H ₃ C N	405.64	-0.20	-0.11
C HN	406.78	0.04	0.13
N NO	408.71	-0.03	0.06
N ₂	409.98	0.01	0.10
N NO	412.59	-0.07	0.02
C H ₃ O H	539.11	-0.40	-0.23
C H ₂ O	539.48	-0.41	-0.24
C H ₂ O	539.90	-0.36	-0.19
C O ₂	541.28	-0.14	0.03
N NO	541.42	0.08	0.25
C O	542.55	-0.27	-0.19
H F	694.23	-0.58	-0.24
F ₂	696.69	-0.51	-0.17
MAD	—	0.22	0.18

Table C58: *CEBE results (eV) from density functional M11; the Chong test set is used and the ionized atom is in bold font.*

Molecule	Exp ⁹⁷	$\delta(\text{M11})$	$\delta(\text{M11}_r)$
C ₂ H ₂	290.82	0.84	0.89
C H ₄	290.91	0.06	0.11
C H ₃ OH	292.42	0.19	0.24
C H ₃ CN	292.45	0.42	0.48
C H ₃ CN	292.98	0.23	0.28
C HN	293.40	0.51	0.56
C H ₂ CO	294.47	0.37	0.42
C O	296.21	0.68	0.73
C O ₂	297.69	0.56	0.61
N H ₃	405.56	0.08	0.17
C H ₃ CN	405.64	0.21	0.30
C HN	406.78	0.40	0.49
N NO	408.71	0.41	0.50
N ₂	409.98	0.39	0.48
N NO	412.59	0.73	0.82
C H ₃ OH	539.11	0.03	0.20
C H ₂ CO	539.48	0.03	0.20
C H ₂ O	539.90	-0.07	0.10
C O ₂	541.28	0.14	0.31
N NO	541.42	0.20	0.37
C O	542.55	0.25	0.42
H F	694.23	0.21	0.13
F ₂	696.69	0.02	0.36
MAD	–	0.32	0.40

Table C59: *CEBE results (eV) from density functional M11-L; the Chong test set is used and the ionized atom is in bold font.*

Molecule	Exp ⁹⁷	$\delta(\text{M11-L})$	$\delta(\text{M11-L}_r)$
C ₂ H ₂	290.82	1.10	1.15
C H ₄	290.91	0.21	0.26
C H ₃ OH	292.42	0.40	0.45
C H ₃ C N	292.45	0.63	0.68
C H ₃ C N	292.98	0.53	0.58
C HN	293.40	0.74	0.79
C H ₂ C O	294.47	0.65	0.70
C O	296.21	0.64	0.69
C O ₂	297.69	0.76	0.81
N H ₃	405.56	0.46	0.55
C H ₃ C N	405.64	0.45	0.54
C HN	406.78	0.68	0.77
N NO	408.71	0.72	0.81
N ₂	409.98	0.65	0.74
N NO	412.59	0.92	1.01
C H ₃ O H	539.11	0.65	0.82
C H ₂ C O	539.48	0.51	0.68
C H ₂ O	539.90	0.57	0.74
C O ₂	541.28	0.84	1.01
N NO	541.42	1.09	1.26
C O	542.55	0.52	0.69
H F	694.23	0.66	1.00
F ₂	696.69	0.46	0.80
MAD	–	0.65	0.76

Table C60: *CEBE results (eV) from density functional SOGGA11; the Chong test set is used and the ionized atom is in bold font.*

Molecule	Exp ⁹⁷	$\delta(\text{SOGGA11})$	$\delta(\text{SOGGA11}_r)$
C ₂ H ₂	290.82	0.97	1.02
C H ₄	290.91	-0.10	-0.05
C H ₃ OH	292.42	-0.20	-0.15
C H ₃ CN	292.45	0.35	0.40
C H ₃ CN	292.98	0.10	0.15
C HN	293.40	0.44	0.49
C H ₂ CO	294.47	-0.06	-0.01
C O	296.21	0.33	0.38
C O ₂	297.69	-0.32	-0.27
N H ₃	405.56	0.10	0.19
C H ₃ CN	405.64	0.21	0.30
C HN	406.78	0.46	0.55
N NO	408.71	0.19	0.28
N ₂	409.98	0.44	0.53
N NO	412.59	0.16	0.25
C H ₃ OH	539.11	-0.07	0.10
C H ₂ CO	539.48	-0.02	0.22
C H ₂ O	539.90	-0.05	0.12
C O ₂	541.28	0.23	0.40
N NO	541.42	0.68	0.85
C O	542.55	0.32	0.49
H F	694.23	-0.29	0.05
F ₂	696.69	-0.41	-0.07
MAD	-	0.28	0.32

Table C61: *CEBE results (eV) from density functional SOGGA11X; the Chong test set is used and the ionized atom is in bold font.*

Molecule	Exp ⁹⁷	$\delta(\text{SOGGA11X})$	$\delta(\text{SOGGA11X}_r)$
C ₂ H ₂	290.82	0.46	0.51
C H ₄	290.91	-0.23	-0.18
C H ₃ OH	292.42	-0.10	-0.05
C H ₃ C N	292.45	0.20	0.25
C H ₃ CN	292.98	-0.16	-0.11
H C N	293.40	0.15	0.20
H ₂ C O	294.47	0.08	0.13
C O	296.21	0.46	0.51
C O ₂	297.69	0.35	0.40
N H ₃	405.56	-0.27	-0.18
C H ₃ C N	405.64	-0.30	-0.21
H C N	406.78	-0.08	0.01
N NO	408.71	0.13	0.22
N ₂	409.98	-0.01	0.08
N NO	412.59	0.39	0.48
C H ₃ O H	539.11	-0.69	-0.52
H ₂ C O	539.48	-0.77	-0.60
H ₂ O	539.90	-0.65	-0.48
C O ₂	541.28	-0.37	-0.20
N NO	541.42	-0.28	-0.11
C O	542.55	-0.55	-0.38
H F	694.23	-1.00	-0.66
F ₂	696.69	-0.93	-0.59
MAD	-	0.37	0.31

Table C62: *CEBE results (eV) from density functional B3LYPV1R; the Chong test set is used and the ionized atom is in bold font.*

Molecule	Exp ⁹⁷	$\delta(\text{B3LYPV1R})$	$\delta(\text{B3LYPV1R}_r)$
C ₂ H ₂	290.82	0.68	0.73
C H ₄	290.91	0.06	0.11
C H ₃ OH	292.42	0.05	0.10
C H ₃ C N	292.45	0.41	0.46
C H ₃ C N	292.98	-0.07	-0.02
C HN	293.40	0.34	0.39
C H ₂ C O	294.47	0.19	0.24
C O	296.21	0.53	0.58
C O ₂	297.69	0.21	0.26
N H ₃	405.56	-0.08	0.01
C H ₃ C N	405.64	-0.23	-0.14
C HN	406.78	0.04	0.13
N NO	408.71	0.09	0.18
N ₂	409.98	0.04	0.13
N NO	412.59	0.07	0.09
C H ₃ O H	539.11	-0.55	-0.38
C H ₂ O	539.48	-0.56	-0.39
C H ₂ O	539.90	-0.44	-0.27
C O ₂	541.28	-0.22	-0.05
C NO	541.42	-0.08	0.09
C O	542.55	-0.37	-0.20
H F	694.23	-0.73	-0.39
F ₂	696.69	-0.85	-0.51
MAD	–	0.30	0.25

Table C63: *CEBE results (eV) from density functional B3LYPV3; the Chong test set is used and the ionized atom is in bold font.*

Molecule	Exp ⁹⁷	(δ (B3LYPV3))	δ (B3LYPV3 _r)
C ₂ H ₂	290.82	0.57	0.62
C H ₄	290.91	-0.05	0.00
C H ₃ OH	292.42	-0.06	-0.01
C H ₃ CN	292.45	0.30	0.35
C H ₃ CN	292.98	-0.18	-0.13
H CN	293.40	0.23	0.28
H ₂ C O	294.47	0.08	0.13
C O	296.21	0.42	0.47
C O ₂	297.69	0.09	0.14
N H ₃	405.56	-0.19	-0.10
C H ₃ C N	405.64	-0.34	-0.25
H CN	406.78	-0.07	0.02
N NO	408.71	-0.02	0.07
N ₂	409.98	-0.07	0.02
N NO	412.59	-0.04	0.05
C H ₃ O H	539.11	-0.66	-0.49
H ₂ C O	539.48	-0.67	-0.50
H ₂ O	539.90	-0.55	-0.38
C O ₂	541.28	-0.33	-0.16
N NO	541.42	-0.19	-0.02
C O	542.55	-0.48	-0.31
H F	694.23	-0.85	-0.51
F ₂	696.69	-0.97	-0.63
MAD	-	0.32	0.25

Table C64: *CEBE results (eV) from density functional B3P86V1R; the Chong test set is used and the ionized atom is in bold font.*

Molecule	Exp ⁹⁷	$\delta(\text{B3P86V1R})$	$\delta(\text{B3P86V1R}_r)$
C ₂ H ₂	290.82	0.62	0.68
C H ₄	290.91	-0.07	-0.02
C H ₃ OH	292.42	-0.05	0.00
C H ₃ C N	292.45	0.32	0.36
C H ₃ C N	292.98	-0.13	-0.08
H CN	293.40	0.24	0.29
H ₂ C O	294.47	0.09	0.14
C O	296.21	0.40	0.45
C O ₂	297.69	0.06	0.10
N H ₃	405.56	-0.12	-0.03
C H ₃ C N	405.64	-0.22	-0.13
H CN	406.78	0.03	0.12
N NO	408.71	0.06	0.15
N ₂	409.98	0.00	0.09
N NO	412.59	0.07	0.16
C H ₃ O H	539.11	-0.49	-0.32
H ₂ C O	539.48	-0.52	-0.35
H ₂ O	539.90	-0.46	-0.29
C O ₂	541.28	-0.20	-0.03
N NO	541.42	-0.05	0.12
C O	542.55	-0.36	-0.19
H F	694.23	-0.77	-0.43
F ₂	696.69	-0.78	-0.44
MAD	-	0.27	0.22

Table C65: *CEBE results (eV) from density functional B3P86V5; the Chong test set is used and the ionized atom is in bold font.*

Molecule	Exp ⁹⁷	$\delta(\text{B3P86V5})$	$\delta(\text{B3P86V5}_r)$
C ₂ H ₂	290.82	0.51	0.56
C H ₄	290.91	-0.18	-0.13
C H ₃ OH	292.42	-0.16	-0.11
C H ₃ C N	292.45	0.20	0.25
C H ₃ CN	292.98	-0.24	-0.19
H CN	293.40	0.13	0.18
H ₂ C O	294.47	-0.02	0.03
C O	296.21	0.29	0.34
C O ₂	297.69	-0.06	-0.01
N H ₃	405.56	-0.23	-0.14
C H ₃ C N	405.64	-0.33	-0.24
H CN	406.78	-0.08	0.01
N NO	408.71	-0.06	0.03
N ₂	409.98	-0.11	-0.02
N NO	412.59	-0.05	0.04
C H ₃ O H	539.11	-0.61	-0.44
H ₂ C O	539.48	-0.63	-0.46
H ₂ O	539.90	-0.57	-0.40
C O ₂	541.28	-0.31	-0.14
N NO	541.42	-0.17	0.01
C O	542.55	-0.47	-0.30
H F	694.23	-0.89	-0.55
F ₂	696.69	-0.90	-0.56
MAD	—	0.31	0.22

Appendix D

Appendix to Chapter 5

D1 Relative Energies of Flat and Bent Ionophores

Table D1: *Relative energies (in kJ/mol) of flat and bent geometries of crown ether ionophores.*

Molecule	Flat	Bent
18C – O ₀ S ₆	0	6.7
18C – O ₁ S ₅	0.5	0
18C – O ₂ S ₄ – meta	11.6	0
18C – O ₂ S ₄ – ortho	0	13.8
18C – O ₂ S ₄ – para	0	17.7
18C – O ₃ S ₃ – 1, 1, 1	0	7.3
18C – O ₃ S ₃ – 2, 1	0	0
18C – O ₃ S ₃ – 3	0	15.9
18C – O ₄ S ₂ – meta	4.7	0
18C – O ₄ S ₂ – ortho	0	7.0
18C – O ₄ S ₂ – para	0	0
18C – O ₅ S ₁	0	11.4
18C – O ₆ S ₀	0	24.8

D2 Relative Energies of Ionophore Isomers

Table D2: *Relative energies (in kJ/mol) of crown ether ionophore isomers.*

Molecule	ortho	meta	para
18C – O ₂ S ₄	0.4	0	11.2
18C – O ₄ S ₂	6.7	5.9	0

Molecule	1,1,1	2,1	3
18C – O ₃ S ₃	16.8	0.0	14.9

D3 Binding Affinities of Ionophores with Metal Incorporated

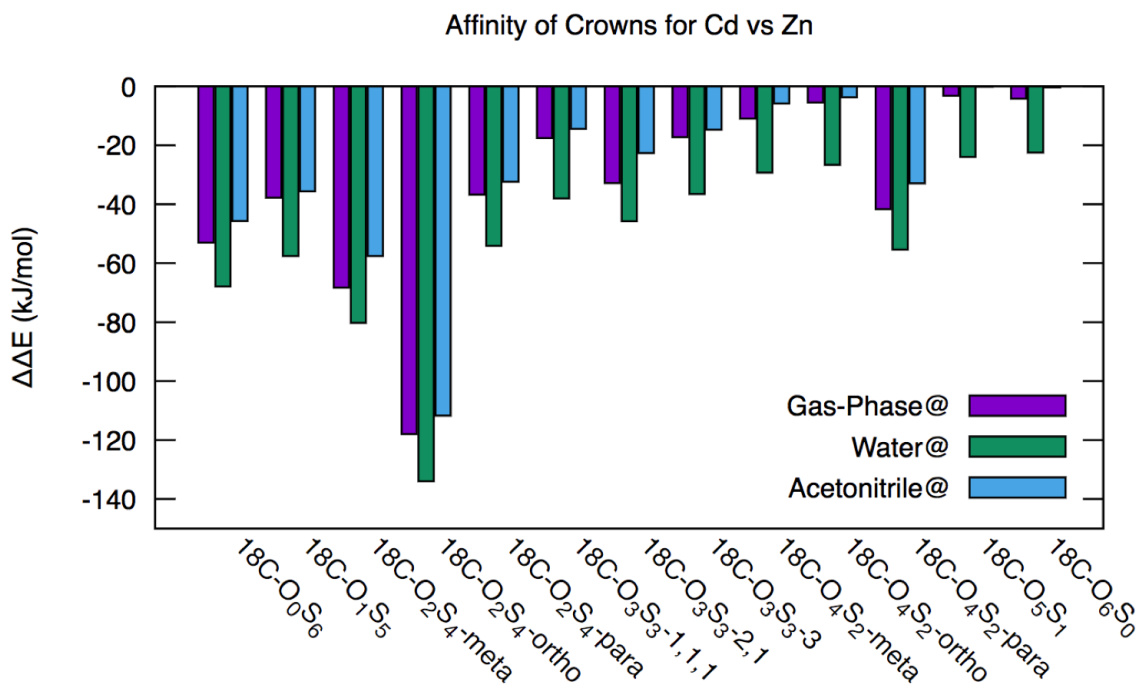


Figure D1: *Binding affinity for Cd²⁺ over Zn²⁺. A negative binding affinity ($\Delta\Delta E_{rxn}$) indicates that Cd has a higher affinity for the crown than Zn.*

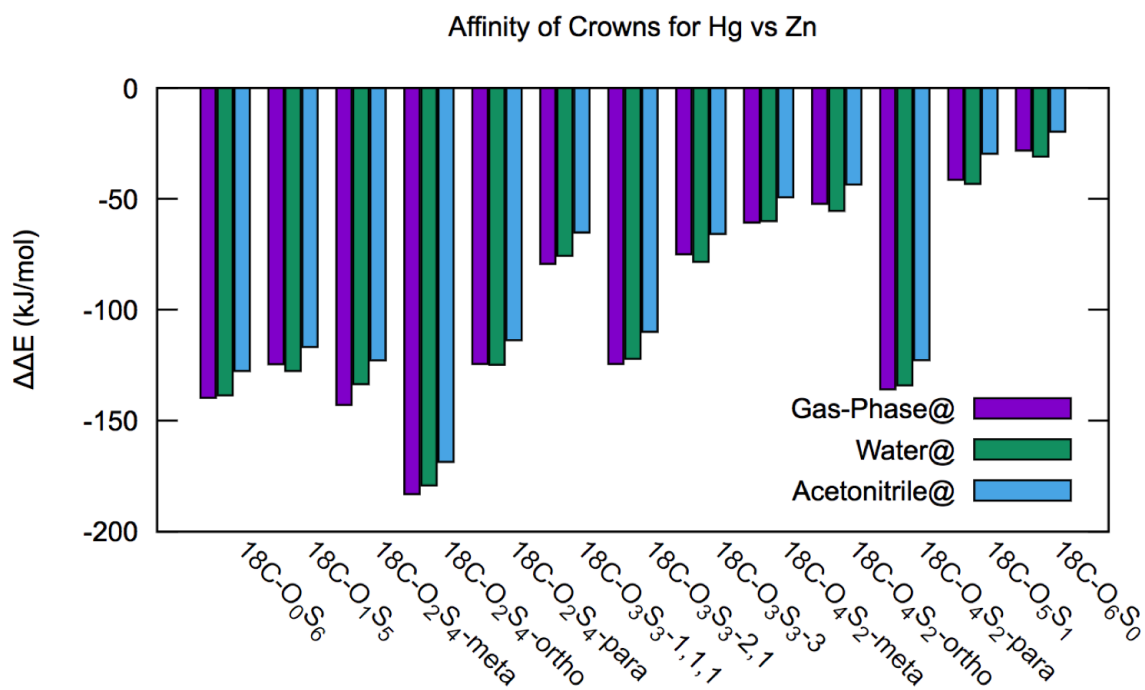


Figure D2: Binding affinity for Hg^{2+} over Zn^{2+} . A negative binding affinity ($\Delta\Delta E$) indicates that Hg has a higher affinity for the crown than Zn.

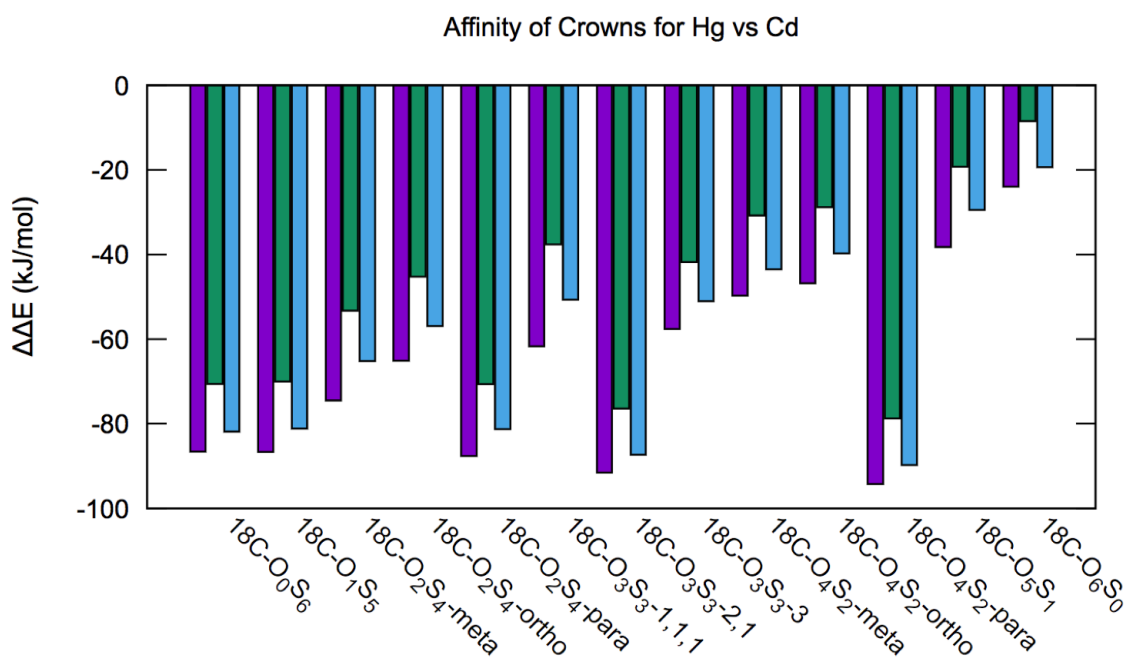


Figure D3: Binding affinity for Hg^{2+} over Cd^{2+} . A negative binding affinity ($\Delta\Delta E$) indicates that Hg has a higher affinity for the crown than Cd.

D4 Relative Energies of Chemosensor Isomers

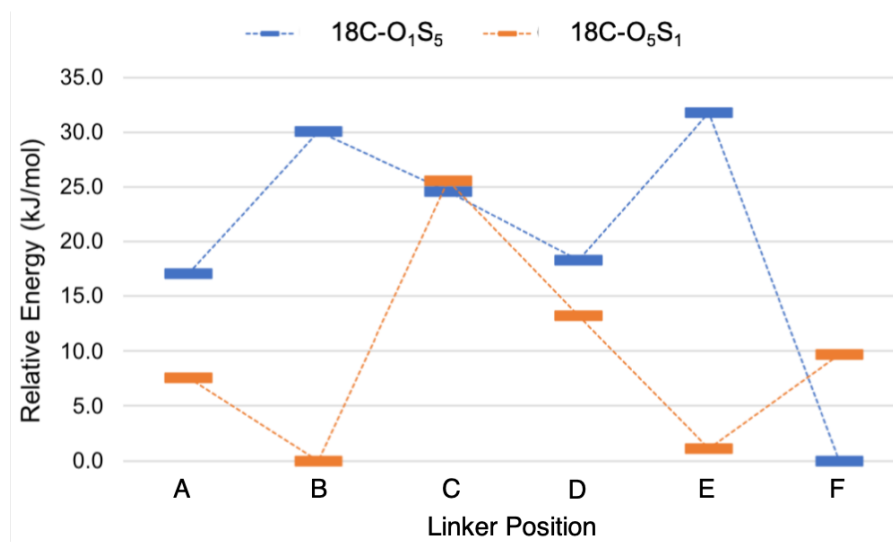


Figure D4: The relative energy (kJ/mol) for each isomer is compared to the position of the benzene linker for 18C-O₅S₁ and 18C-O₁S₅. The lowest energy compounds are 18C-O₅S₁-**B** and **E**, and 18C-O₁S₅-**F**.

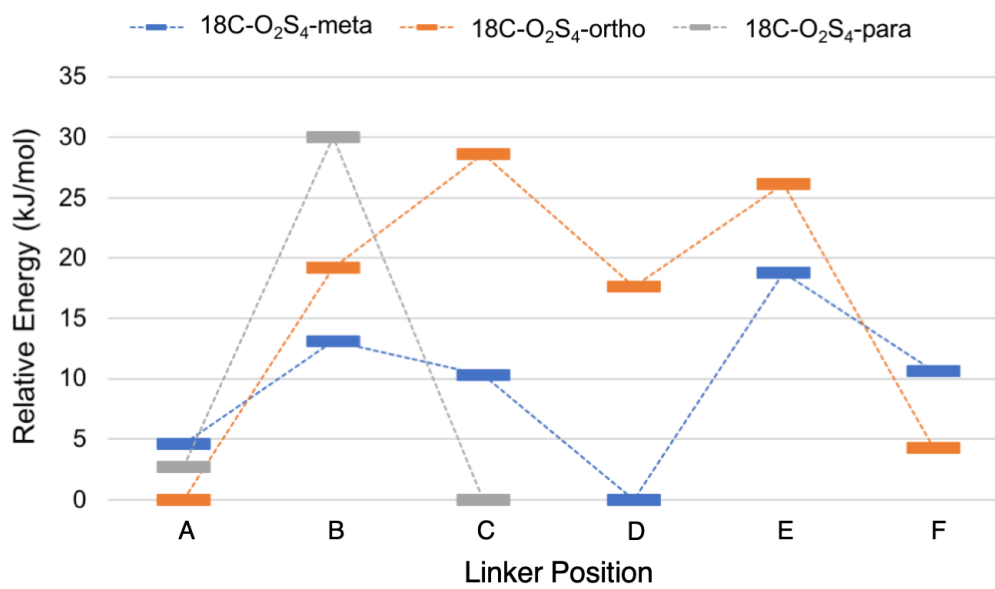


Figure D5: The relative energy (kJ/mol) for each isomer is compared to the position of the benzene linker for 18C-O₂S₄. The lowest energy compounds are 18C-O₂S₄-meta-**D**, 18C-O₂S₄-ortho-**A**, and 18C-O₂S₄-para-**C** and **A**.

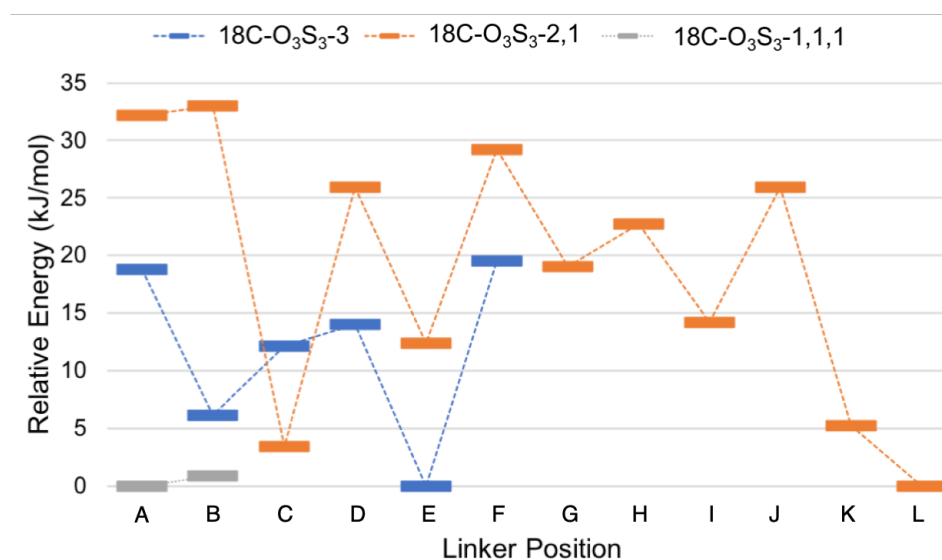


Figure D6: The relative energy (kJ/mol) for each isomer is compared to the position of the benzene linker for 18C-O₃S₃. The lowest energy compounds are 18C-O₂S₄-3-E, 18C-O₂S₄-2,1-L, and 18C-O₂S₄-1,1,1-A and -B.

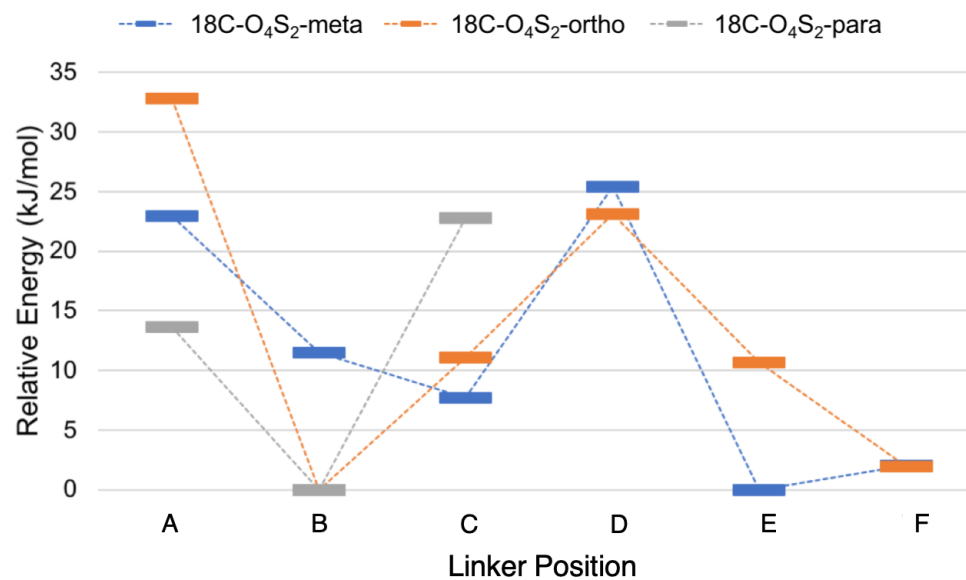


Figure D7: The relative energy (kJ/mol) for each isomer is compared to the position of the benzene linker for 18C-O₄S₂. The lowest energy compounds are 18C-O₄S₂-meta-E, 18C-O₄S₂-ortho-B, and 18C-O₂S₄-para-B.

D5 Rotation of BODIPY

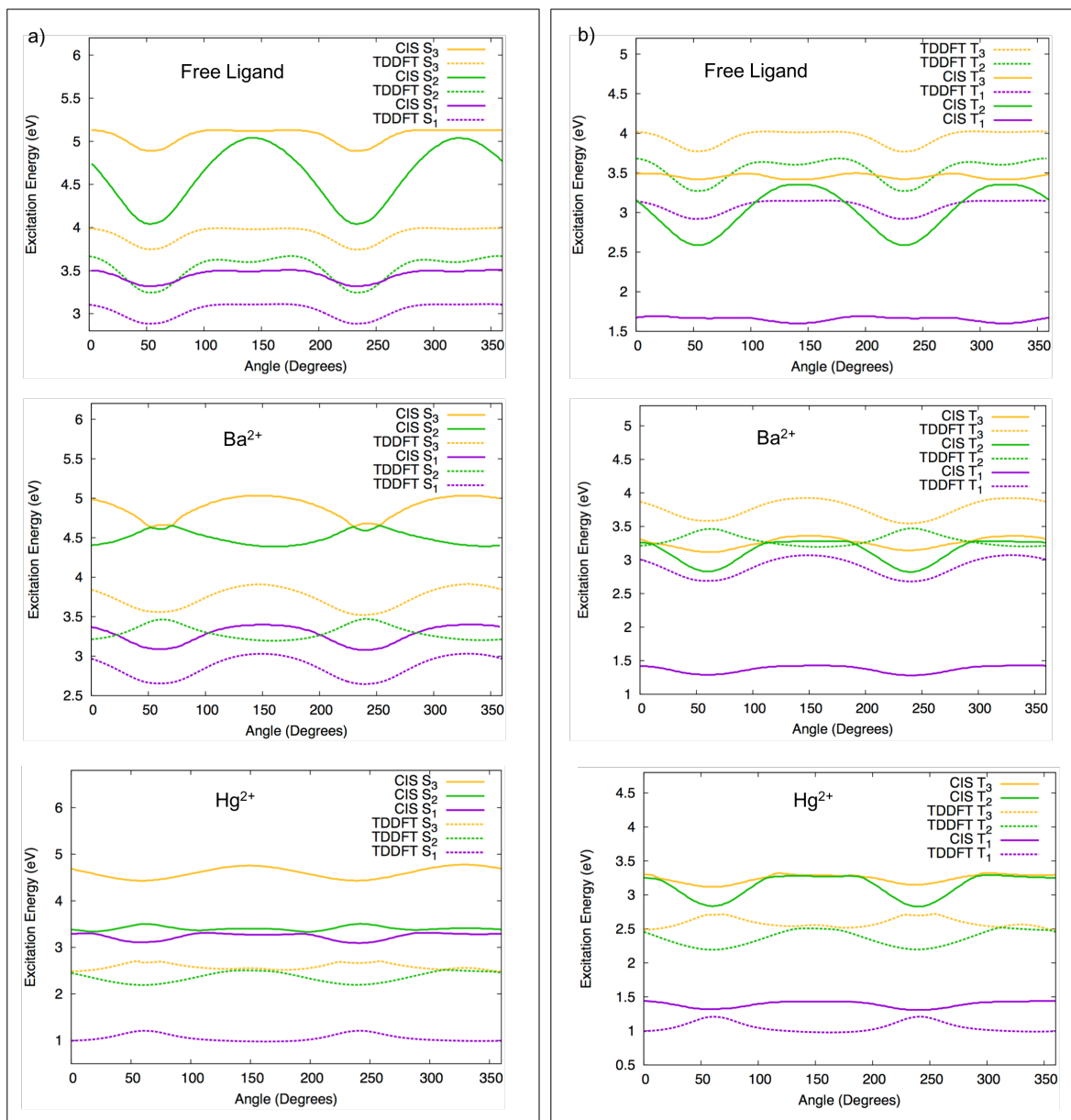


Figure D8: A plot of excitation energy as a function of BODIPY-linker angle. a) Energies of the lowest three singlet excited states, calculated with CIS and the MCP-DZP basis set for light atoms and MCP-TZP for any metal ions and TD-DFT(PBE0) with the same basis set, for the free ligand (top), ligand with Ba²⁺ (middle), and ligand with Hg²⁺ (bottom). b) Energies of the lowest three triplet excited states, calculated with CIS/6-31G(d) and TD-DFT(PBE0)/6-31G(d), for the free ligand (top), ligand with Ba²⁺ (middle), and ligand with Hg²⁺ (bottom).

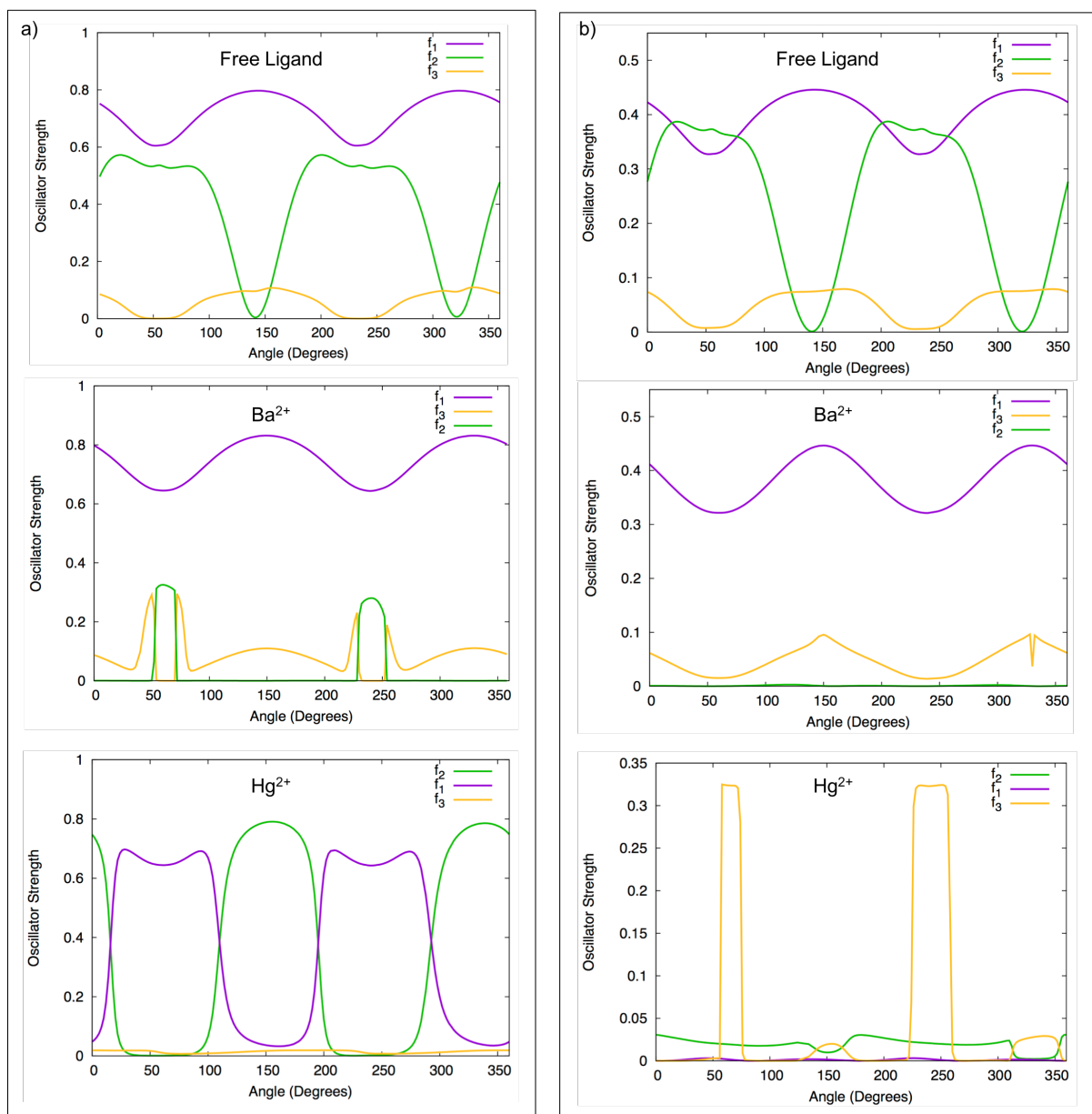


Figure D9: A plot of oscillator strength as a function of BODIPY-linker angle. a) Oscillator strengths of the lowest three singlet excited states, calculated with CIS and the MCP-DZP basis set for light atoms and MCP-TZP for any metal ions and TD-DFT(PBE0) with the same basis set, for the free ligand (top), ligand with Ba^{2+} (middle), and ligand with Hg^{2+} (bottom). b) Oscillator strengths of the lowest three triplet excited states, calculated with CIS and TD-DFT(PBE0), for the free ligand (top), ligand with Ba^{2+} (middle), and ligand with Hg^{2+} (bottom).